

Fundamental studies on the heterogeneously catalyzed dehydrogenation reactions of hydrogen carrier molecules

Grundlagenforschung zu heterogen katalysierten
Dehydrierungsreaktionen von
Wasserstoffspeichermolekülen

Der Naturwissenschaftlichen Fakultät
der Friedrich-Alexander-Universität Erlangen-Nürnberg

zur

Erlangung des Doktorgrades Dr. rer. nat.

vorgelegt von

Philipp Alois Norbert Bachmann

aus Aschaffenburg

Als Dissertation genehmigt von der Naturwissenschaftlichen Fakultät
der Friedrich-Alexander-Universität Erlangen-Nürnberg

Tag der mündlichen Prüfung: 09.10.2019

Vorsitzender des Promotionsorgans: Prof. Dr. Georg Kreimer

Gutachter: PD Dr. Christian Papp

Prof. Dr. Jörg Libuda

Table of contents

1. Introduction.....	1
2. Fundamentals and techniques.....	7
2.1 X-ray photoelectron spectroscopy.....	7
2.2 Synchrotron radiation	12
2.3 Temperature Programmed Desorption	14
2.4 Near Edge X-ray Absorption Fine Structure.....	16
3. General experimental setup.....	18
3.1 Synchrotron UHV machine setup.....	18
3.2 TPD UHV machine setup	19
4. Indole, Indoline and Octahydroindole on Pt(111).....	21
4.1 Introduction	22
4.2 Specific experimental setup.....	24
4.3 Results and discussion.....	25
4.3.1 Indole	25
4.3.2 Indoline	29
4.3.3 Octahydroindole	32
4.3.4 Comparison of indole, indoline, octahydroindole and H ₁₂ -N-ethylcarbazole	37
4.4 Conclusion	43
5. 2-methylindole, 2-methylindoline and 2-methyloctahydroindole on Pt(111).....	45
5.1 Introduction	46
5.2 Specific experimental setup.....	47
5.3 Results and discussion.....	49
5.3.1 2-methylindole (2-MI).....	49
5.3.2 2-methylindoline (2-MINI)	55
5.3.3 2-methyloctahydroindole (2-MOHI)	58
5.3.4 Comparison of the 2-methyl substituted and the unsubstituted, indole-based LOHC system	62
5.4 Conclusion	67
6. Indene, Indan and Hexahydroindan on Pt(111).....	71
6.1 Introduction	71
6.2 Specific experimental setup.....	72

6.3	Results and discussion.....	73
6.3.1	Indene	73
6.3.2	Indan	77
6.3.3	Hexahydroindan	79
6.3.4	Comparison of the homocyclic indene-based LOHC system with the heterocyclic indole-based LOHC system	83
6.4	Conclusion	84
7.	Formic acid decomposition on Pt(111) and Ni(111)	87
7.1	Introduction	87
7.2	Specific experimental setup	90
7.3	Results and discussion.....	91
7.3.1	Formic acid on Ni(111)	91
7.3.2	Formic acid on Pt(111)	97
7.4	Conclusion	103
8.	Formation of h-BN from Ammonia borane and Borazine on Ni(111).....	105
8.1	Introduction	106
8.2	Specific experimental setup	107
8.3	Results and discussion.....	108
8.3.1	Borazine.....	108
8.3.2	Ammonia borane	114
8.4	Conclusion	121
9.	Summary	123
10.	Zusammenfassung	127
11.	References.....	133
12.	Acknowledgements – Danksagung	145
Appendix A: Supplementary Data		A-1
Appendix B: Programs and Scripts.....		B-1
	IGOR scripts	B-1
	LabVIEW programs	B-14

1. Introduction

“[...] I believe that water will one day be employed as fuel, that hydrogen and oxygen which constitute it, used singly or together, will furnish an inexhaustible source of heat and light, of an intensity of which coal is not capable. Some day the coalrooms of steamers and the tenders of locomotives will, instead of coal, be stored with these two condensed gases, which will burn in the furnaces with enormous calorific power.”

— **Jules Verne**, *The Mysterious Island*, 1874.

“We are like tenant farmers chopping down the fence around our house for fuel when we should be using Nature's inexhaustible sources of energy — sun, wind and tide. [...] I'd put my money on the sun and solar energy. What a source of power! I hope we don't have to wait until oil and coal run out before we tackle that.”

— **Thomas Edison**, conversation with Henry Ford and Harvey Firestone, 1931.

These quotes, from the famous science fiction author Jules Verne and the electrical pioneer Thomas Edison, date back roughly 150 or 90 years, and yet, their statements are most relevant today. We now live in the modern world of the 21st century, and still we are degrading our nature by burning more fossil fuels than ever (see Figure 1). In fact, this has led to global warming and environmental pollution, now being among the major problems of humanity, largely caused by our energy needs and modern industry.^[1-3] By now, only first global effects of this manmade problem are visible, but in the long term it may harm our planet, climate and environment significantly, likely having a strong impact on the persistence of living organisms, including humans.^[4-7]

Only in recent years, political leaders around the world began to realize that we need to invest more in environmental protection, greenhouse gas reduction and clean energy production.^[8-10] This, however, is no easy task with the steadily growing world population and the associated energy demands. The strong increase in energy consumption in the past ~50 years is shown in Figure 1; this includes the world population increase of ~120% since 1965 as well as a ~60% energy consumption increase per capita.^[11-12] Thereby, fossil fuels (oil, coal and natural gas) make up ~85% of our global energy consumption as of 2018 (see Figure 2). Leaving out the 4% energy share of controversially discussed nuclear power, only 11% of energy

consumption go to renewable energy sources, considered “clean”. Admittedly, the share of renewable energy is rising fast in the last decade (see Figure 1 and Figure 2), but extrapolating the data with regard to the also rising energy demand, it still will take decades, until renewable energies reach the highest share.

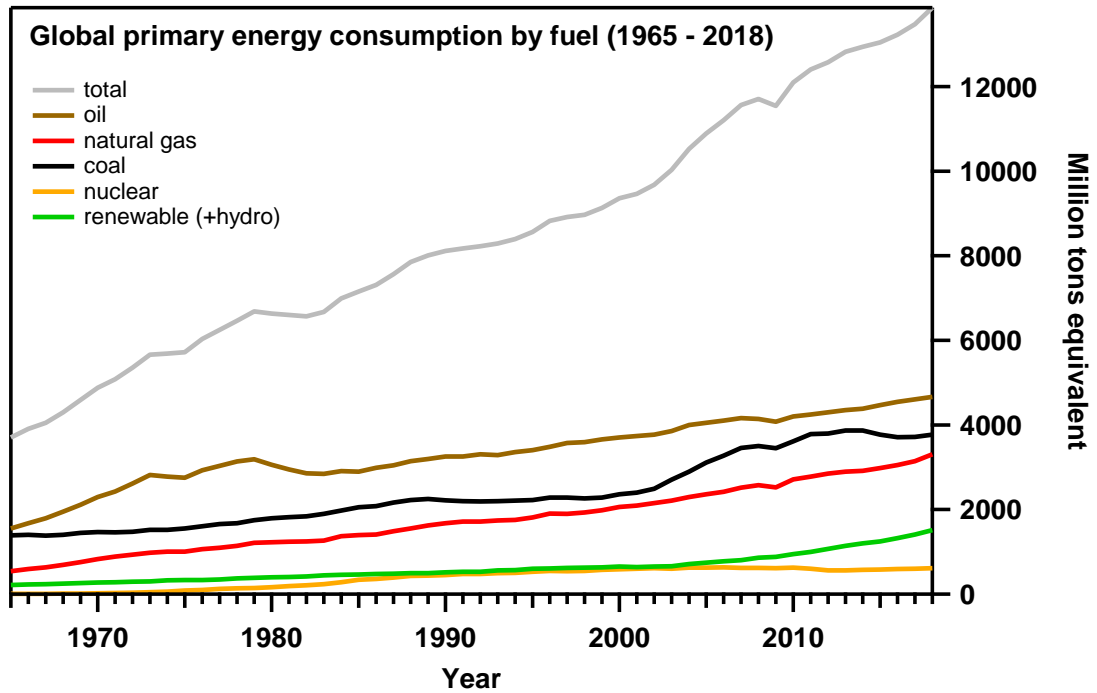


Figure 1: Global primary energy consumption by fuel source in million tons equivalent from 1965 – 2018.^[11]

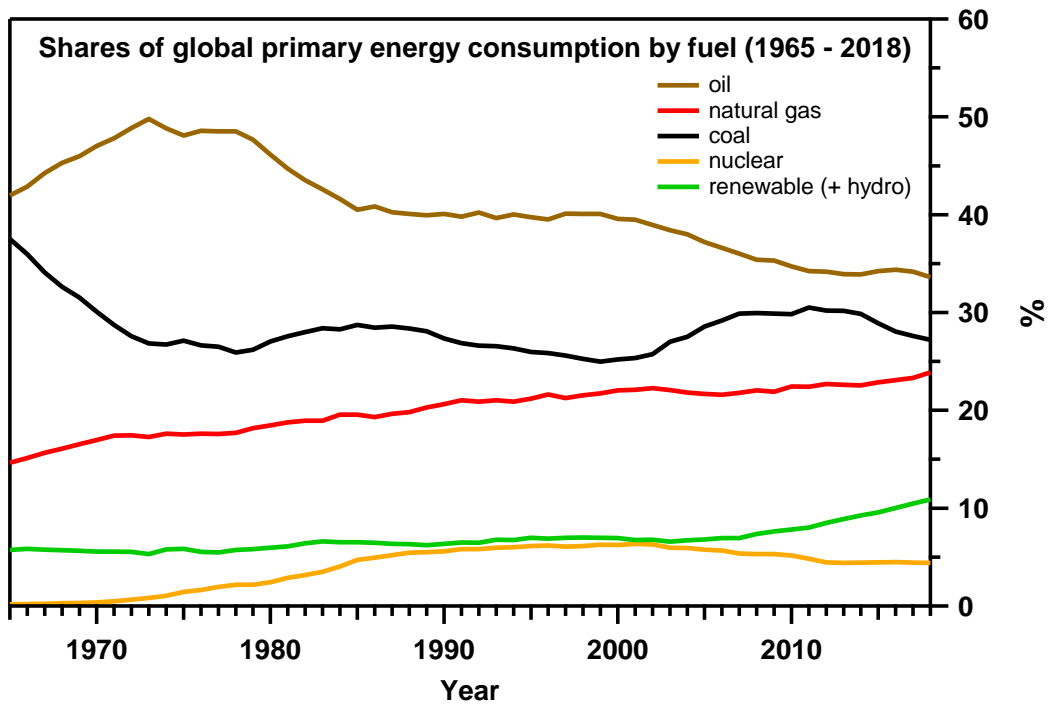


Figure 2: Shares of the global primary energy consumption by fuel source from 1965 – 2018.^[11]

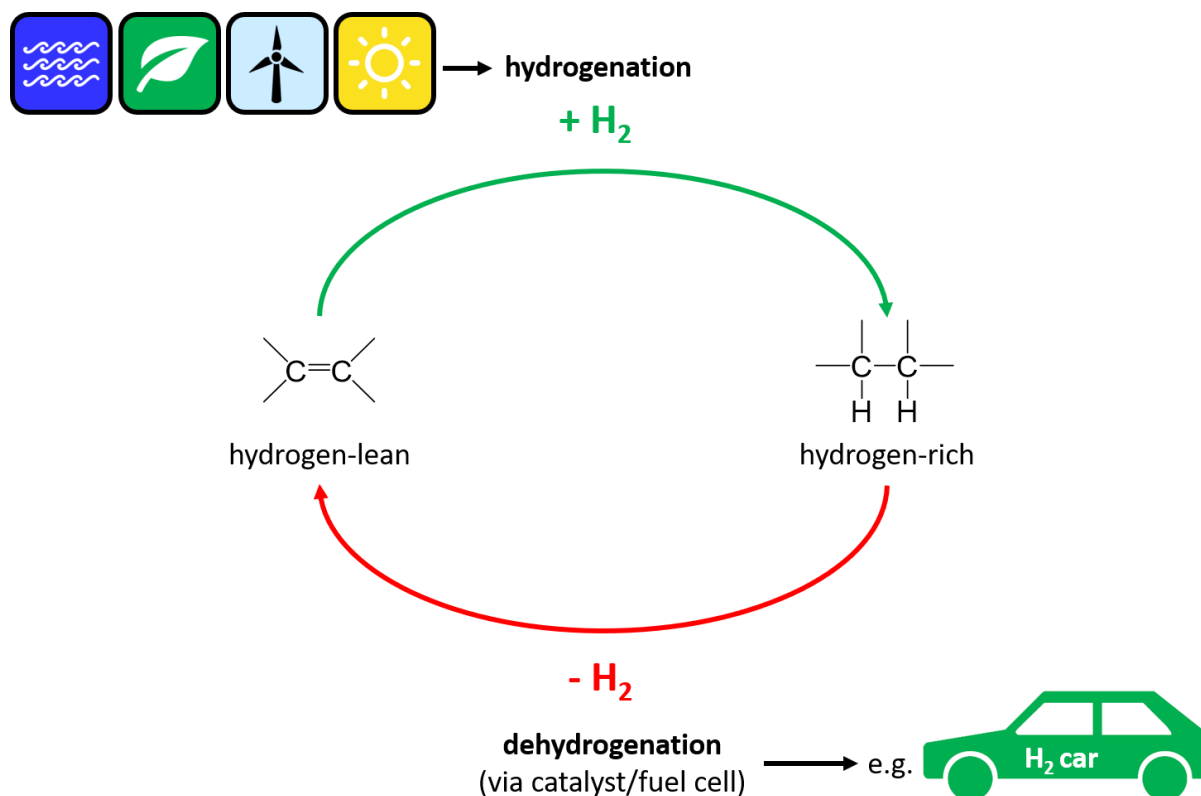
Nowadays, the biggest contributions to renewable energies come from biomass, hydroelectricity, solar and wind energy. Especially the share of the latter two is rising fast, as sun and wind energy can be considered inexhaustible and are comparably easy to use. However, one of the biggest challenges that come in hand with these renewable energy sources, is the place and time mismatch of energy production and consumption. In order to maintain a stable power supply, an extensive energy grid and decentralized, local energy storage systems are necessary. As an extension of existing electrical grids is expensive and controversial due to landscape alteration, energy storage solutions have gained high interest in the recent years. Especially chemical and electrochemical storage solutions aim to offer high density energy storage.

As a consequence of recent ecofriendly efforts, e.g. the uprise of the electric vehicles, powered electrochemically by lithium-ion batteries, is observed. While this progress is undoubtedly helping urban areas to become “greener”, the overall environmental record is barely changed, as electricity to charge these batteries is still mainly produced from fossil fuels as discussed above. Furthermore, the production of batteries from rare earth metals consumes large amounts of energy and has a high environmental impact^[13], not in said urban areas, but elsewhere, which is again hardly better in the big picture. Additionally, state of the art lithium-ion batteries struggle with safety issues like fire hazard and explosions when handled improperly or damaged.^[14-15]

The best-known chemical energy storage however is hydrogen. As lightest element, H₂ has an unmatched gravimetric energy storage density of 33 kWh/kg, but a very low volumetric storage density of 3 Wh/l.^[16-17] In order to use pure H₂ efficiently, either high pressure storage (up to 700 bar) or liquefaction at 20 K are necessary.^[16-17] Indeed, both methods are only suitable for very secure application environments, due to the high flammability of hydrogen and the (energetically) unfavorable storage conditions.

Storing hydrogen in a chemically bound state, however, can overcome these issues. A promising concept for that are so-called Liquid Organic Hydrogen Carriers (LOHCs), which can be de- and rehydrogenated catalytically, while maintaining their molecular framework.^[18] Ideally, LOHCs also possess certain physical and chemical properties, such as a low melting point, favorable thermodynamics and kinetics, large-scale availability and low toxicity.^[17-20]

A sketch of the de- and rehydrogenation cycle of a LOHC system is shown in Scheme 1:



Scheme 1: De- and rehydrogenation cycle of a LOHC system.

Such LOHC systems are i.e. the heterocyclic N-ethylcarbazole with its hydrogen-rich form H₁₂-N-ethylcarbazole (storage capacity of 5.8 wt% H₂)^[17, 21-29] or isomeric mixtures of dibenzyltoluenes with their hydrogen-rich H₁₈-dibenzyltoluene counterparts (storage capacity of 6.2 wt% H₂)^[30-36]. Conventional fossil fuels possess storage capacities higher than 10 wt% H₂ (total combustion). This value is significantly higher than the reversible storage capacity of LOHCs; however, these smaller values of ~6 wt% H₂ are still sufficient for realistic applications and LOHCs have a high potential to be a future alternative to our present-day battery technology regarding transportation solutions, capable of using the existing gas station networks with minor upgrades. Moreover, LOHCs represent a “green” solution to large-scale energy storage, capable of stabilizing the existing electrical grid with the rise and challenges of renewable energy production (see above). Also, decentralization of energy production and storage is a possible use-case scenario, decreasing the dependence on a huge and expensive energy network. In conclusion, LOHC systems, or hydrogen storage systems in general, have the potential to be a key technology towards a sustainable, “green” future.^[17]

For this work, the dehydrogenation behavior of several LOHC systems on model catalysts has been evaluated. The investigations have been conducted in ultra-high vacuum (UHV) using X-ray photoelectron spectroscopy (XPS) as main method. Together with other surface science methods, like temperature programmed desorption (TPD) and near angle X-ray absorption spectroscopy (NEXAFS), the temperature-induced reaction pathways and intermediates of single LOHC molecules on the catalysts are identified and their performance as LOHC systems is discussed.

An introduction to the fundamentals and the techniques used in this thesis is given in Chapter 2, and Chapter 3 describes the general experimental setup.

Chapter 4 discusses the dehydrogenation of the LOHC system indole, indoline and octahydroindole on Pt(111). For octahydroindole and indoline, dehydrogenation into an indole intermediate is found. Furthermore, all three molecules show deprotonation of the NH-group, ultimately forming a surface-bound indolide species, before the molecule framework decomposes into fragments.

Chapter 5 is a follow-up study to the results presented in Chapter 4, with the aim to further improve the dehydrogenation characteristics and obtain more stable intermediates, ultimately avoiding or delaying indolide formation. Hence, the dehydrogenation of the 2-methylindole, 2-methylindoline and 2-methyloctahydroindole LOHC system on Pt(111) is investigated in order to compare the performance of the system to the unsubstituted indole-based LOHC system and to determine the influence of substitution on the reaction pathway. Thereby, 2-methyloctahydroindole first dehydrogenates via two different π -allylic species into a 2-methylindoline intermediate, followed by a 2-methylindole intermediate. Analogous to the fully hydrogenated 2-methyloctahydroindole, 2-methylindoline first dehydrogenates into a 2-methylindole intermediate. Consecutively, all three molecules show deprotonation of the NH-group, ultimately forming a surface bound 2-methylindolide species, before the molecule framework decomposes into fragments.

Chapter 6 is about the dehydrogenation of the indene, indan, hexahydroindan LOHC system on Pt(111). This system basically is the homocyclic analog to the heterocyclic indole-based LOHC system. For hexahydroindan, dehydrogenation via an unspecified H_x-indan intermediate into an indenyl surface species is observed. For indan and indene, no dehydrogenation intermediate is observed before forming indenyl, which later decomposes into fragments.

Chapter 7 investigates the dehydrogenation behavior of formic acid on Pt(111) and Ni(111). Formic acid can also be considered as a LOHC molecule and is an important intermediate in steam reforming or the water-gas shift reaction. For Ni(111), adsorption of formic acid and partially dehydrogenated formate is observed, before dehydrogenation into the desorption products H₂O, CO and CO₂ takes place. On Pt(111), adsorption also leads to formic acid and formate on the surface, who then dehydrogenate into CO₂ as desorption product.

Chapter 8 discusses the formation of hexagonal boron nitride (h-BN) by dehydrogenation of ammonia borane and borazine on Ni(111). While ammonia borane can be considered as a solid hydrogen carrier with a large 19.6 wt% H₂ storage capacity, the focus in this study lies on the formation of h-BN, which is, as an insulating graphene analog, of high interest for semiconductor applications. For borazine, the dehydrogenation into disordered and defective boron nitride is observed, before formation of h-BN on the surface. Ammonia borane already partially dehydrogenates upon adsorption and then dehydrogenates into a borazine-like intermediate, before it follows the same reaction pathway as borazine.

Chapter 9 and 10 summarize the results of this thesis in English and German, respectively.

2. Fundamentals and techniques

2.1 X-ray photoelectron spectroscopy

Photoelectron spectroscopy is based on the effect, where an electron is ejected from a material upon irradiation with light. This so called photoelectric effect was first observed in 1887 by Hertz^[37] and described 1905 by Einstein^[38] using quantum mechanics. Photoelectron spectroscopy can be divided in two sections. While ultraviolet photoelectron spectroscopy (UPS) is based on low-energy irradiation ($h\nu < 100$ eV) where electrons are mainly emitted from valence band, X-ray photoelectron spectroscopy (XPS) utilizes high-energy irradiation ($h\nu > 100$ eV) to excite core level electrons.

To obtain XP spectra, one measures the kinetic energy of the emitted photoelectrons. When a sample with the work function ϕ_S is irradiated with electromagnetic radiation $h\nu$, electrons with the binding energy E_B , are excited and leave the sample with a kinetic energy E_{kin} :

$$E_{kin} = h\nu - E_B - \phi_S \quad (1)$$

With ϕ_S being usually unknown, the Fermi level E_F is commonly used as reference for E_{kin} and E_B . Therefore, the sample must be set to the same electric potential as the electron analyzer. Consequently, Equation 1 changes to

$$E_{kin,F} = h\nu - E_B \quad (2)$$

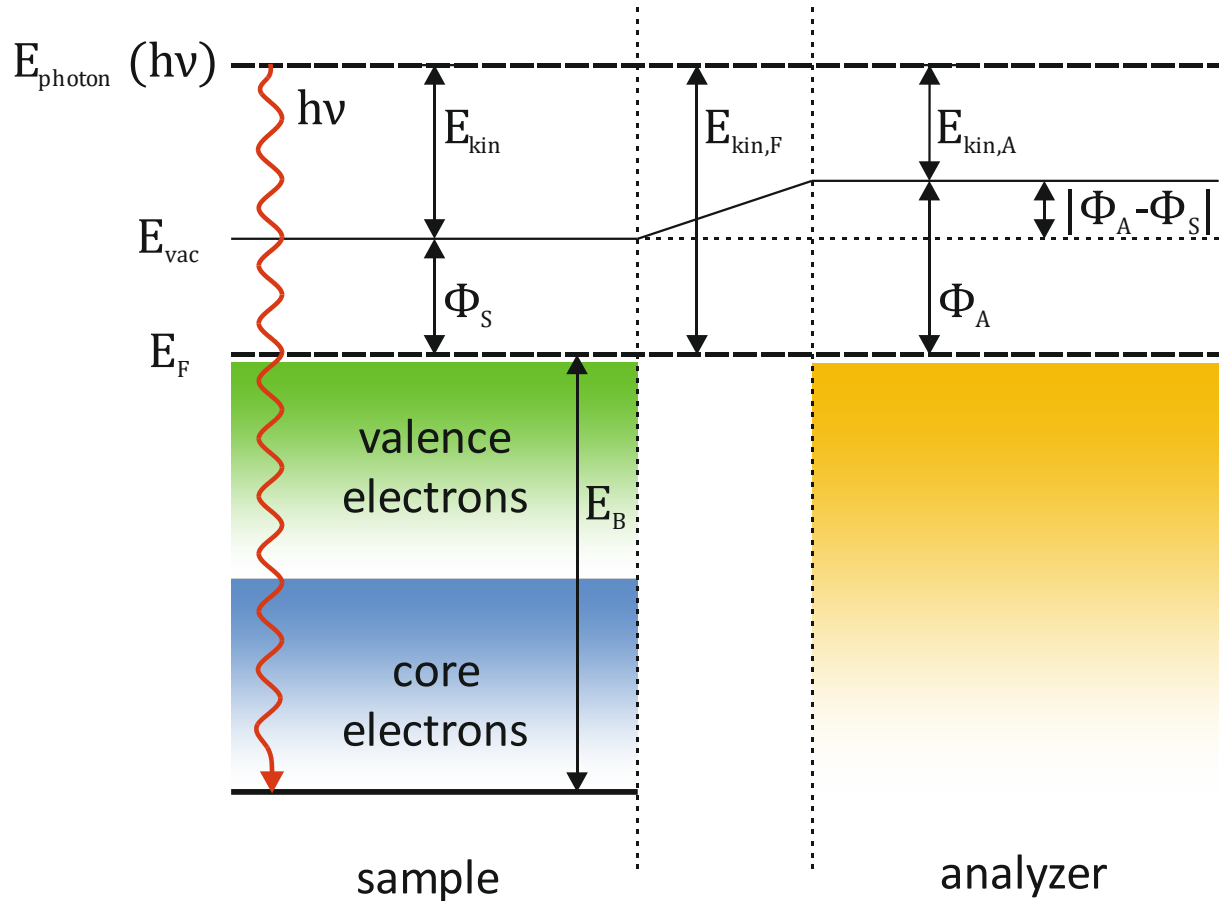
or

$$E_{kin,A} = h\nu - E_B - \phi_A \quad (3)$$

with the work function of the analyzer ϕ_A and the measured kinetic energy $E_{kin,A}$. A sketch of the relations in the photoemission process is given in Scheme 2.

Photoelectron spectroscopy in general is a very surface-sensitive method. Therefore, XPS is a widespread technique, often used in surface science to investigate surface physics and chemistry.^[39-40] The surface sensitivity depends on the probability of an electron to escape from a certain depth inside a sample and is determined by the inelastic mean free path λ_e (IMFP) of the electron, which again is a function of the kinetic energy of the electron and the nature of the sample. In laboratories, usually Al-K α or Mg-K α radiation with fixed excitation

energies of 1486.6 or 1253.6 eV, respectively, is used, which results in high kinetic energies for e.g. measurements of the C 1s core level (binding energy of ~280-290 eV). The escape depth then usually is about 15 Å. To increase the surface sensitivity, lower excitation energies are needed. This can e.g. be achieved with synchrotron radiation (see Chapter 2.2).^[41]

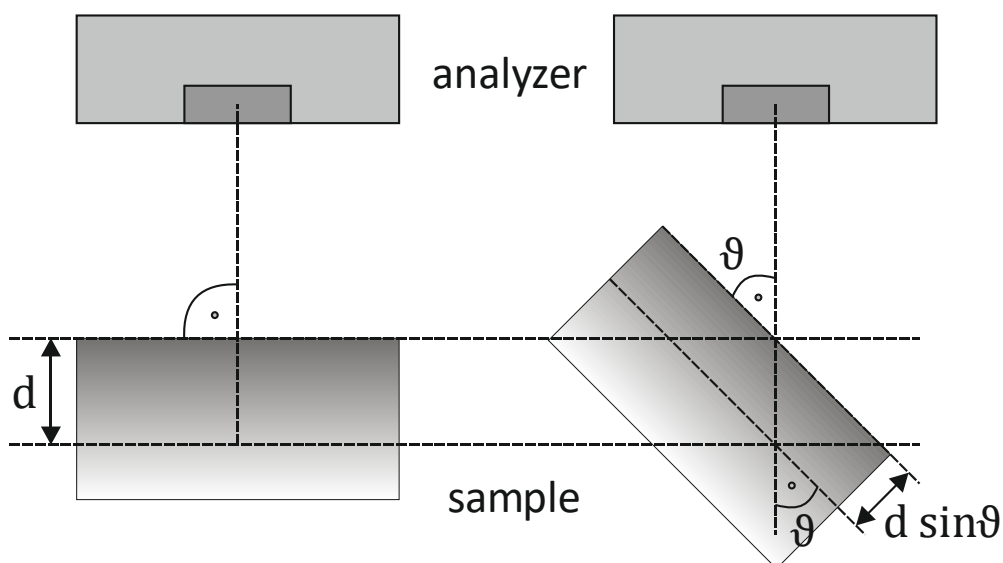


Scheme 2: Schematic of the energy levels for the photoemission process. Fermi level: E_F ; photon energy: E_{photon} ; kinetic energy of the electron in the vacuum: E_{kin} ; vacuum level: E_{vac} ; sample work function: Φ_S ; binding energy: E_B ; measured kinetic energy: $E_{kin,A}$ and the Fermi level correlated kinetic energy of the electron: $E_{kin,F}$. Φ_A is the work function of the analyzer.

Next to the nature of the material and the irradiation energy, the IMFP can also be tweaked by tilting the sample and thus changing the exit angle (see Scheme 3). Thereby, the exponential dependence of the signal intensity is described by:^[42]

$$I(d) = I_0 \cdot \exp\left(\frac{-d}{\lambda_e \sin\vartheta}\right) \quad (4)$$

with I as the signal intensity, d as the depth of penetration, λ_e as the inelastic mean free path of the electron, ϑ as the take-off angle and I_0 as the signal intensity at $d = 0$ and the take-off angle.



Scheme 3: Variation of the take-off angle in XPS. Left: Detection of photoelectrons normal to the surface. Right: Detection of electrons at a glancing angle with a reduced escape depth d depending on the take-off angle ϑ .

While the analyzer measures the kinetic energy of the emitted electrons, XP spectra are usually shown with the binding energy on the x axis increasing to the left, instead of the kinetic energy, which increases to the right.

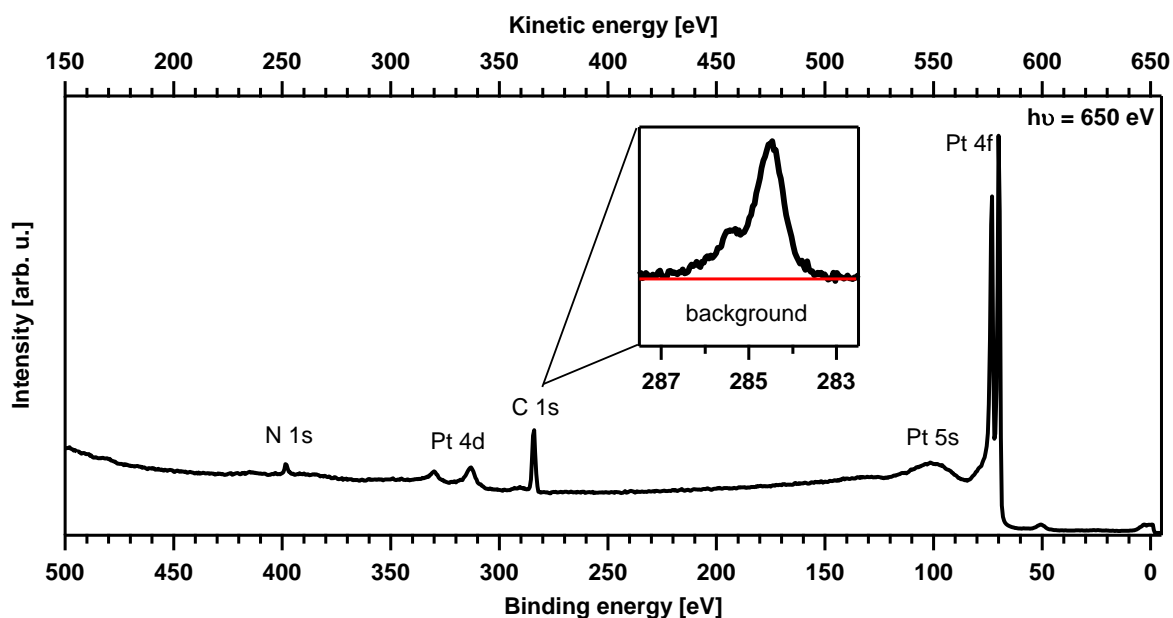


Figure 3: XPS survey of Pt(111) with a carbon and nitrogen containing adsorbate at $h\nu=650$ eV.

In Figure 3 an example XP spectrum of Pt(111) with adsorbates is shown. The relation given in Equation 3 translates the measured kinetic energy onto the binding energy scale. Different element and core level specific binding energy ranges are marked. Hence, this information

enables the qualitative determination of the elemental composition of the investigated surface.

Besides the elemental information, core level electrons can also give information on the chemical state of the atom and thus bonds in a molecule. The overall binding energy shift, also called chemical shift, arises due to superposition of initial and final state contributions.^[43-44] Thereby, the initial state (refer to Koopmans' theorem and frozen orbital approximation)^[39, 45] basically reflects the bonding situation in a molecule before photoexcitation and is influenced by, e.g., the oxidation state, geometry or the electronegativity of adjacent atoms. Furthermore, final state effects (after ionization) can induce additional shifts due to the relaxation of electrons. Consecutively, it is possible to distinguish different chemical species within a molecule or material, exhibiting shifts from tenths of an electronvolt (eV) up to several eV. For small shifts, an experimental setup with sufficient energy resolution (spectral line width of the incident irradiation and analyzer resolution) is crucial.

Next to the chemical shift, other final state effects can lead to additional peaks in a spectrum, so called satellites. They can appear due to the excitation of a second electron into an unoccupied state (shake up) or into vacuum (shake off), where the primary photoelectron loses energy, caused by inelastic interactions. This results in an apparently higher binding energy. Moreover, high resolution XP measurements can resolve the vibrational fine structure of simple, well defined adsorbate layers. This effect can be attributed to vibrational excitations in the ionic final state. The transition probability and intensity distribution of the vibrational lines corresponds to the Franck-Condon principle, which relates to the Born-Oppenheimer approximation.^[46] For example, C-H vibrational excitations are typically observed at ~ 400 meV higher binding energy than the corresponding adiabatic peak. The empirically found intensity ratio is ~ 0.17 per C-H bond.^[47]

Furthermore, quantitative analysis is also possible, as the XPS peak area is proportional to the abundance of an adsorbate. This is due to the photoemission cross section being independent from the chemical surrounding. However, photoelectron diffraction (PED)^[48] might have a non-neglectable impact on XPS signal intensities. In principle, PED is a scattering process, where the main photoelectron wave interferes with scattered electron waves in such way that it influences the detected intensities in dependence of the kinetic photoelectron energy and emission angle, which is especially a strong effect for kinetic energies of ~ 100 eV.^[49]

Quantitative analysis is done by integration of the peak intensity after subtraction of a background signal, which is caused by inelastically scattered electrons (intensity below individual peaks, see inset in Figure 3).^[50] To gain referenced quantitative information, the integrated intensities are typically calibrated to known structures, like CO on Pt(111), which amounts to 0.50 ML carbon (1 ML carbon = 1 carbon atom/Pt atom).^[51-52] Peak fitting usually was done using Doniach-Šunjić-profiles convoluted with a Gaussian function^[40, 53], after subtraction of a linear background. Additional information about raw data preparation, peak fitting and background subtraction methods are described in the PhD thesis of M. Kinne.^[51]

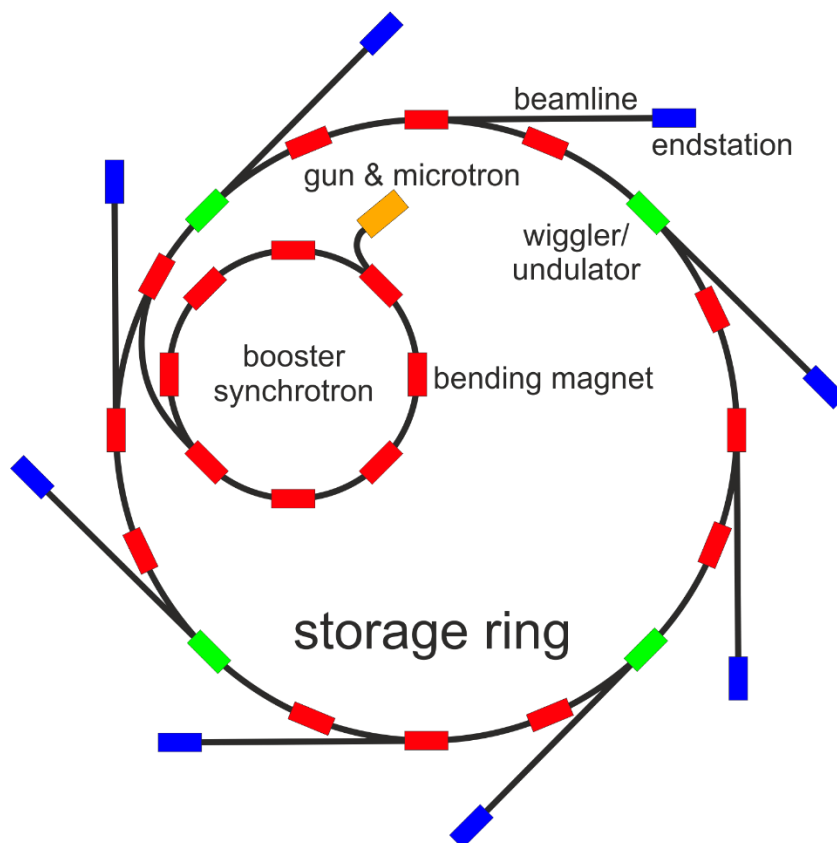
In this work, XPS mainly has been used to conduct isothermal adsorption experiments and consecutive temperature programmed XPS (TPXPS) of adsorbates on Pt(111) and Ni(111) single crystal surfaces.

2.2 Synchrotron radiation

Synchrotron radiation is the electromagnetic radiation that is emitted in tangential direction towards the motion direction of a charged particle with relativistic velocity, when it is deflected from a linear path. This effect is particularly efficient for electrons because of their small mass.^[41, 43] The lost energy per turn with a revolution time of $2\pi R/c$ is given by:^[54]

$$\Delta E_e = \frac{4\pi e^2}{3 R} \left[\frac{E}{mc^2} \right]^4 \quad (5)$$

with E as the electron energy, m as the electron mass, c as the speed of light, e as the particle charge and R as the radius of curvature.



Scheme 4: Schematic depiction of a synchrotron facility.

Nowadays, synchrotron radiation is produced in a dedicated storage ring connected to an upstream synchrotron (particle accelerator) and microtron/electron gun. The storage ring is equipped with different insertion devices that enable tunable radiation characteristics. The radiation is usually produced by different types of bending magnets, so called wigglers and

undulators. To keep a constant current, the storage ring is periodically injected with new electrons to compensate for the energy losses. A schematic depiction of a synchrotron facility is shown in Scheme 4.

Synchrotron radiation can be adjusted in a wide range from infrared to high energy X-ray radiation, which allows for broad scientific use.^[41, 54] The main advantages of a synchrotron light source versus a laboratory X-ray source for XPS are the very high intensity (several orders of magnitude higher) and the high brilliance of the radiation, which allows for fast and highly resolved measurements. Moreover, the radiation can be tuned to achieve e.g. pulsed or polarized light.^[41, 54]

In sum, synchrotron radiation is perfectly suited for in situ spectroscopy. For this thesis, the undulator beamlines U49-2 PGM 1/PGM 2 and UE56-2 PGM 2 at BESSY II (Berliner Elektronenspeicherring-Gesellschaft für Synchrotronstrahlung) of the HZB (Helmholtz Zentrum Berlin) were used to conduct XPS and NEXAFS experiments.

2.3 Temperature Programmed Desorption

Temperature programmed desorption (TPD), or sometimes also referred to as thermal desorption spectroscopy (TDS), is a widespread and valuable method, which utilizes a mass spectrometer to detect the thermally induced desorption of adsorbates and their fragments from a solid sample during heating.^[55-56] Usually, a linear heating ramp with a heating rate β of 2-10 K/s is used to obtain sharp desorption features in the resulting TPD spectra. The combination of TPXPS and TPD is perfectly suited for the observation of temperature-induced reactions, as both, the reaction of adsorbates on the catalyst and the desorption of reaction products to the gas phase can be monitored complementary. Especially regarding dehydrogenation reactions, TPD can give valuable insights into the desorption of formed hydrogen, which is only indirectly accessible in XPS. Assuming that readsorption on the sample surface can be ignored (due to an infinitely high pumping rate of the UHV chamber), the desorption rate is given with the Polanyi-Wigner equation:^[57-58]

$$r = -\frac{d\theta}{dt} = v(\theta)\theta^n e^{\left(-\frac{E_{des}(\theta)}{RT}\right)} \quad (6)$$

with r as the desorption rate, θ as the coverage (ML), t as the time, v as the preexponential desorption factor, n as the desorption order, E_{des} as the desorption activation energy, R as the gas constant and T as the temperature.

During desorption, different kinetics are observed. Zero-order kinetics ($n = 0$) have no coverage dependence and are observed for e.g. multilayer desorption. First-order kinetics describe the unimolecular desorption, where r is proportional to the number of adsorbed particles; the peak position is independent of θ . Second-order kinetics are present for recombinative desorption, where $r \sim \theta^2$ and the peak position is shifting to lower T with increasing θ , as observed for e.g. hydrogen desorption ($\text{H} + \text{H} \rightarrow \text{H}_2$).^[57]

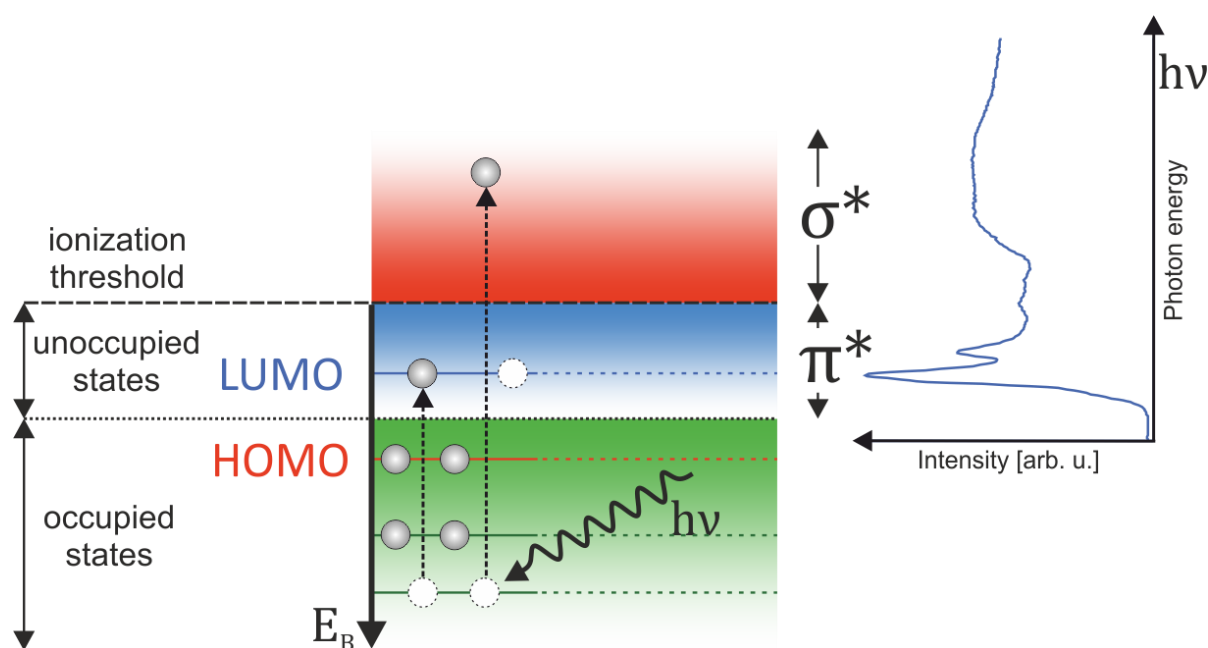
There are various modern and precise techniques for quantitative and qualitative analysis of TPD data, like the “leading edge method”. Still, the “Redhead analysis”^[59] is popular in surface science for a rough determination of the desorption parameters, although the error in E_{des} is often as high as $\pm 30\%$, due to the strong dependence on ν , which is usually assumed to be 10^{13} s^{-1} .^[57, 59] Here, the relation of desorption temperature and activation energy is given by:

$$E_{des} = RT_{max} \left[\ln \left(\frac{\nu T_{max}}{\beta} \right) - 3.46 \right] \quad (7)$$

with additionally T_{max} as the temperature of a desorption peak maximum.

2.4 Near Edge X-ray Absorption Fine Structure

Upon exposing a sample to X-rays, absorption of the radiation is observed. In contrast to XPS, where the excitation energy is constant, X-ray absorption spectroscopy (XAS) varies the excitation energy, to observe the change of absorption in the investigated energy range. Here, synchrotron radiation is needed for continuously scanning through an excitation energy range. For surface science, near edge absorption fine structure (NEXAFS) offers great potential for investigating e.g. the molecular orientation or characteristic valence states.



Scheme 5: Schematic description of X-ray absorption with the resulting electron excitation and production of a sample NEXAFS spectrum (right). Electron transitions into unoccupied states give π^* orbitals, while above the ionization threshold σ^* orbitals are found. LUMO: lowest unoccupied molecular orbital; HOMO: highest occupied molecular orbital.

In NEXAFS spectroscopy, the probability for a photon to be absorbed by a material drastically increases when the excitation energy approaches the binding energy value of a core level electron. This leads to a strong increase in X-ray absorption (absorption edge), which is due to the excitation of core level electrons into unoccupied states (LUMO) and to above the ionization threshold. The absorption edge is labeled according to the electron shells, i.e. K -edge for $1s$ electronic transitions or L_x -edge for $2s$, $2p$ transitions. For excitation energies just below the ionization threshold, the electron is not removed but instead transitions into a weakly bound orbital (unoccupied π^* orbitals) occur. Above the ionization threshold, mainly transitions into unbound σ^* orbitals take place.^[60-61] Usually, the photoabsorption is

monitored up to 30-50 eV above the absorption edge or ionization threshold. The principle is depicted in Scheme 5.

The observed resonance intensities of distinct orbitals depend on the density of unoccupied states and selection rules. Thereby, the angle of the incoming radiation and its polarization (orientation of the electric field or the X-rays) relative to the orientation of the orbitals in a molecule has a significant impact on the absorption probability and thus the outgoing NEXAFS spectrum. Consequently, the orientation of a molecule can be probed by either tilting the sample or changing the polarization of the incoming radiation, while measuring several spectra.^[61]

X-ray absorption generally can be measured either in transmission or electron yield mode. In electron yield mode, the absorption is determined by measuring the electrons that are ejected from the sample.^[61] In this work, especially partial electron yield was used, where in contrast to total electron yield, only electrons with a higher energy than the applied potential at the retardation optics can pass and are detected.

NEXAFS was used as complementary method to XPS in normal (0°) and grazing (70°) incidence to observe changes in the NEXAFS C *K*-edge π^* -region and thus determining e.g. orientation or aromaticity of adsorbate molecules. The X-ray intensity of the beamline and consecutively the electron yield is strongly dependent on the photon energy and synchrotron storage ring current, which is usually held constant. As the signal produced by (sub)monolayers coverages usually is very small compared to the photon flux variation, background correction is necessary to observe the actual absorption features. This is done by either subtraction or division of a reference spectrum of the clean substrate or an Au-coated grid in the beam path, simultaneously producing a reference during measurement of the adsorbate on the substrate.

3. General experimental setup

3.1 Synchrotron UHV machine setup

XPS and NEXAFS experiments were conducted at the beamlines U49-2 PGM 1 and UE56-2 PGM 1/2 at the synchrotron BESSY II of the Helmholtz-Zentrum Berlin (HZB). Therefore, a custom, transportable UHV apparatus^[62] was used (see Figure 4). The setup consists of a preparation chamber, an analysis chamber and a connected supersonic molecular beam chamber.



Figure 4: Picture of the original synchrotron UHV setup.

All three chambers are separated by gate valves. The preparation chamber accommodates LEED optics and several tools for sample preparation, such as a sputter gun, electron beam evaporators for metals/solids and dosing systems for more volatile substances. The analysis chamber houses the connection port for the beamline, a quadrupole mass spectrometer (QMS 200, Pfeiffer Vacuum), a partial electron yield (PEY) NEXAFS detector (details of the NEXAFS setup are already described elsewhere^[63]) and a hemispherical electron analyzer (Omicron EA 125 HR U7). Additionally, dosing facilities for liquids (e.g. LOHCs) or solids can be mounted. The sample is mounted to a manipulator at one end of the preparation chamber, which allows for the transfer of the sample between the preparation and the analysis chamber. The

manipulator is capable of translation in all three spatial directions as well as rotation around its main axis; the sample holder at the front of the manipulator can thereto be tilted perpendicular. Sample temperatures down to 100 K are achieved by liquid nitrogen cooling; a filament on the backside of the sample allows heating up to 600 K, without introducing disturbing electrical fields. Temperatures up to 1300 K are possible with direct resistive heating of the sample.

3.2 TPD UHV machine setup

TPD measurements were carried out in a different UHV setup ^[64-65] with only one main chamber (see Figure 5), having separately pumped dosing facilities and organic evaporators connected.

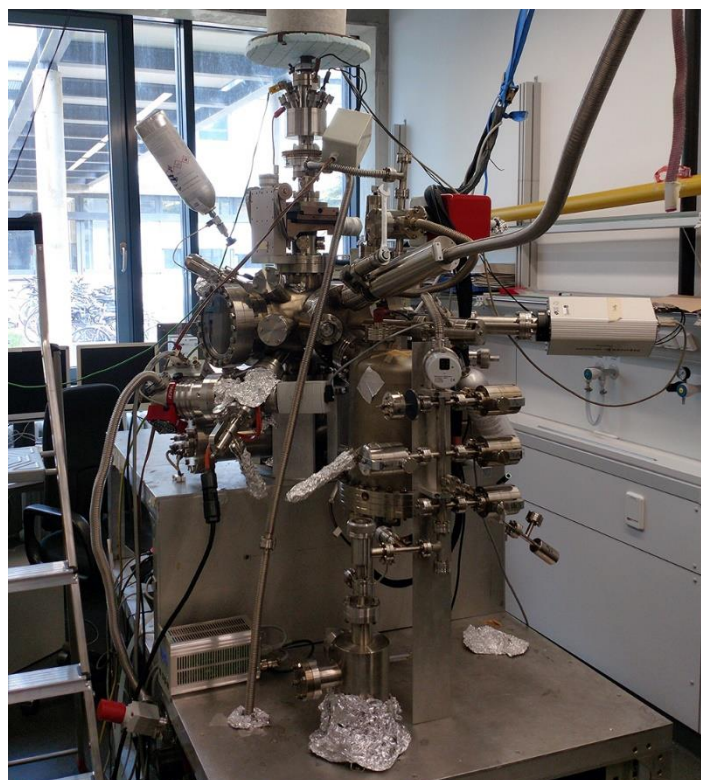


Figure 5: Picture of the TPD UHV machine setup.

The chamber itself is equipped with an Al $K\alpha$ X-ray source, an energy analyzer (CLAM 100 VG), LEED optics, a sputter gun as well as a QMS (QMS 200, Pfeiffer Vacuum) including a “Feulner cup”^[66]. Liquid nitrogen cooling allows for temperatures down to 90 K, while temperatures can be ramped up to 1300 K by resistive heating.

4. Indole, Indoline and Octahydroindole on Pt(111)

The results presented in this chapter have already been published^[67-68]; the content of this chapter is adapted from:

Dehydrogenation of the Liquid Organic Hydrogen Carrier System Indole/Indoline/Octahydroindole on Pt(111)

P. Bachmann, M. Schwarz, J. Steinhauer, F. Späth, F. Düll, U. Bauer, T. N. Silva, S. Mohr, C. Hohner, M. Scheuermeyer, P. Wasserscheid, J. Libuda, H.-P. Steinrück, C. Papp

The Journal of Physical Chemistry C **2018**, *122*, 4470-4479.

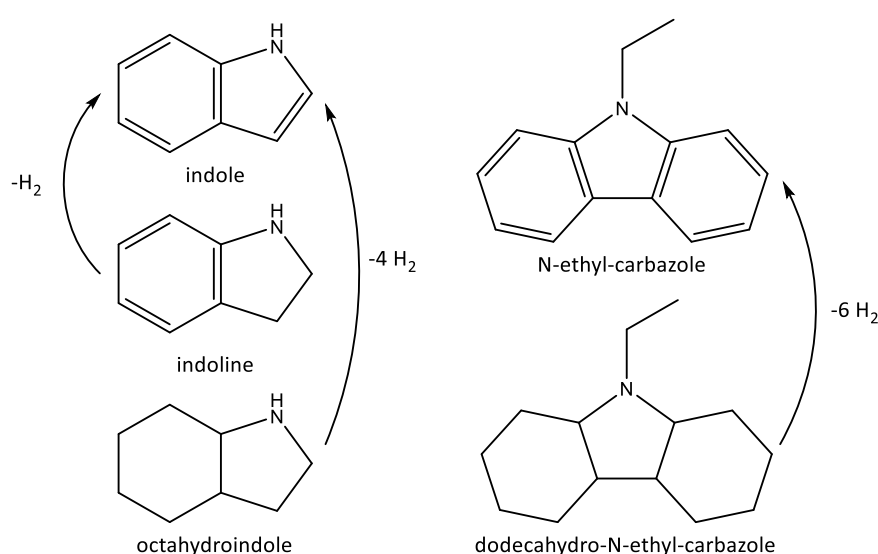
Reprinted (adapted) with permission. Copyright 2018 American Chemical Society.

Authorship: P. Bachmann (except IRAS part)

Indole derivatives are considered as promising Liquid Organic Hydrogen Carriers (LOHC) for renewable energy storage. Using X-ray photoelectron spectroscopy (XPS), Temperature Programmed Desorption (TPD) and Infrared Reflection Absorption Spectroscopy (IRAS), we investigated low temperature adsorption, and dehydrogenation during heating of indole, indoline and octahydroindole on Pt(111). For all three molecules, we find deprotonation of the NH bond above 270 K, accompanied with dehydrogenation of indoline and octahydroindole via an indole intermediate, resulting in an indolide species above 300 K. For octahydroindole, we also find a side reaction yielding small amounts of a π -allyl species between 170 and 450 K. Above 450 K, decomposition of the remaining indolide species takes place.

4.1 Introduction

With the global efforts towards mitigating climate change, renewable energy sources, in particular solar and wind energy, have become increasingly important for energy production. However, weather conditions and day/night cycles cause energy fluctuations and thus a mismatch in place and time regarding energy production and consumption. Consequently, an extensive electrical grid and large-scale energy storage is necessary to maintain a constant supply. Hydrogen is a most relevant candidate as energy vector, because it is easily available from electrolysis.^[16-17, 69] While the gravimetric energy storage density of H₂ is outstanding with 33 kWh/kg, its volumetric energy storage density with 3 Wh/L under ambient conditions is, however, poor.^[16-17] Therefore, very high pressures (up to 700 bar) or liquefied hydrogen (-253 °C), are necessary.^[16-17] These conditions and their potential risks are unfavorable for large scale, easy-to-use scenarios. Chemically stored hydrogen, particularly Liquid Organic Hydrogen Carrier (LOHC) systems, present a safer alternative to elemental dihydrogen. LOHCs are organic molecules, which can store hydrogen via a fully reversible, catalytic hydrogenation and dehydrogenation process, allowing for repeated cycles of (un)loading hydrogen, while maintaining the original carrier structure. A technically applicable LOHC system should feature appropriate physical and chemical properties, including thermal stability, suitable melting points, favorable hydrogenation thermodynamics, large scale availability, low toxicity, and a reasonable price.^[17-20]



Scheme 6: Left: Octahydroindole/indoline/indole LOHC system. Right: Dodecahydro-N-ethylcarbazole/N-ethylcarbazole LOHC system.

In the past, particularly N-heterocyclic compounds have been found to exhibit suitable LOHC properties.^[21, 70-71] One extensively studied candidate is the N-ethylcarbazole/dodecahydro-N-ethylcarbazole system (see Scheme 6) with a capacity of storing 5.8 wt% hydrogen.^[17, 21-29] Following this research, the structurally similar indole has recently become of interest for future LOHC systems, as this molecule and some of its derivatives are easily available; they possess preferential LOHC properties, such as low temperature dehydrogenation.^[72-74]

This chapter presents a detailed quantitative *in situ* study of indole, indoline and octahydroindole on a Pt(111) single-crystal surface as model catalyst in ultrahigh vacuum (UHV) to address their thermally induced dehydrogenation mechanisms on the molecular scale. In terms of a LOHC system, indole represents the hydrogen-lean carrier molecule, while octahydroindole is the hydrogen-rich counterpart. Indoline is a possible intermediate in the dehydrogenation reaction of octahydroindole to indole, and itself can be also considered as a hydrogen storage compound (see Scheme 6). In a previous study, we already investigated these molecules qualitatively using IRAS as main investigation method. Multilayer desorption was observed at 220 K for indole, 200 K for indoline and 185 K for octahydroindole. The remaining molecularly adsorbed monolayers show deprotonation of the NH group above 300 K. Dehydrogenation of indoline and octahydroindole is observed between 300 and 390 K, yielding an identical indolide surface species for indole and indoline above 300 K. Above 390 K, further dehydrogenation and decomposition occurs similarly for both molecules. Heating octahydroindole to 390 K yields a different intermediate, which originates from partial dehydrogenation of the 6-membered ring. Above 420 K, the same decomposition species as seen for indole and indoline forms.^[68] In this follow-up study, we used high-resolution X-ray photoelectron spectroscopy (XPS) and temperature programmed desorption (TPD), to follow the dehydrogenation and decomposition in more detail and in a quantitative fashion. We identify the individual reaction steps and surface species, including the dehydrogenation of octahydroindole and indoline to indole and further deprotonation into indolide with consecutive decomposition into fragments at higher temperatures. For octahydroindole, we also identified a π -allylic species.

4.2 Specific experimental setup

The XPS experiments were performed at the synchrotron BESSY II at beamlines U49-2 PGM-2 and UE56-2 PGM-2 using the synchrotron UHV machine (see Chapter 3.1). TPD experiments were performed in a separate TPD UHV machine (see Chapter 3.2).

The adsorption of indole/indoline/octahydroindole on Pt(111) was conducted using the vapor pressure of the substances. The heating rate was set to 0.5 K/s during TPXPS and 3 K/s for TPD. The carbon coverage on Pt(111) (1 carbon monolayer (C-ML) = 1 carbon atom / Pt atom) was calibrated by comparison to the well-known saturation surface coverage of carbon monoxide at 200 K, which leads to a $c(4\times 2)$ LEED pattern and amounts to 0.5 monolayers.^[52, 75-76] Molecule and nitrogen coverage (ML and N-ML) are derived from the carbon coverage. Peak fitting of the C 1s and N 1s spectra was done using Doniach-Šunjić-profiles^[53] convoluted with a Gaussian function. The C 1s and N 1s regions were measured at 380 and 500 eV with resolutions of 150 and 200 meV at an emission angle of 0° relative to the surface normal. Prior to each spectrum, the sample position is shifted to avoid beam damage. All spectra are referenced to the Fermi edge of Pt(111).

IRAS was recorded by M. Schwarz in an UHV system described elsewhere in detail (base pressure 1×10^{-10} mbar).^[77] The system is equipped with a vacuum Fourier-transform infrared (FTIR) spectrometer (Bruker Vertex 80v), several evaporator sources, two quadrupole mass spectrometers, and all required sample preparation and characterization methods. The IR spectra were acquired at a spectral resolution of 4 cm^{-1} . Previous to the deposition, a reference spectrum of the clean sample at the respective adsorption temperature was recorded. The octahydroindole monolayer spectrum was acquired under isothermal and steady state conditions. The molecules were continuously dosed at pressures of 1×10^{-7} mbar for 60 min. During the deposition, six spectra of 10 min were acquired. All spectra were identical for all experiments, confirming that steady state was reached.

Indole (99%) and indoline (99%) were purchased from Sigma-Aldrich. Octahydroindole (96%) was synthesized as described in a previous study.^[68]

4.3 Results and discussion

To analyze the adsorption and reaction of indole, indoline and octahydroindole on Pt(111), we use in-situ C 1s and N 1s high resolution X-ray photoelectron spectroscopy (XPS), temperature programmed XPS (TPXPS) and temperature programmed desorption (TPD) as main tools. In the following, we will concentrate on the adsorption and reaction of submonolayer coverages of the LOHC molecules as the multilayers have been shown to not react on the surface, but to desorb as intact molecules.^[68]

4.3.1 Indole

We first address indole, as it is the hydrogen-lean form of the LOHC systems indole/indoline and indole/octahydroindole. Understanding the surface chemistry and the spectral fingerprint of the hydrogen lean-carrier molecule is crucial to the analysis of the hydrogen-rich indoline and octahydroindole, as it is the designated product of the dehydrogenation process and its further decomposition on the catalyst limits the applicability of these systems as LOHC. Both, C 1s and N 1s regions were measured during exposure of indole at 140 K and consecutive heating. Selected spectra of the reaction of 1.00 L (C 1s) and 0.66 L (N 1s) are shown in Figure 6a and b, with the corresponding quantitative analyses in Figure 7a and b, respectively. During exposure to indole, we observe the growth of C 1s signals with a dominating peak at 284.5 eV, a smaller peak at 285.4 eV and a weak satellite shoulder at 286 eV. The relative height of these signals does not change during adsorption, suggesting molecular adsorption of indole, as was also shown in the previous IRAS study.^[68] Due to the complexity of the molecules, a straightforward assignment of the C 1s components to the eight carbon atoms is not possible. Nevertheless, when taking into account earlier data certain conclusions can be drawn: For the related molecules benzene or toluene, only one main peak is found at 284.5 eV, that is, at the same binding energy as the dominating peak of indole.^[23, 78-79] Furthermore, the carbon atoms in proximity to the electronegative nitrogen are expected at a higher binding energy, which would be in line with the smaller peak at 285.4 eV. This assignment of the two dominating peaks is further supported by their intensity ratio of approximately 6:2, which agrees with the nominal expectation (Insets in Figure 6).

In the N 1s region, we observe the growth of one peak at 399.0 eV, assigned to aminic nitrogen^[80-82]. This behavior again indicates that indole adsorbs molecularly. From NEXAFS data (see Figure 15 on page 42) and in agreement with IRAS^[68], we deduce that indole is lying flat on the Pt(111) surface, unlike structurally related pyrrole or pyridine molecules.^[83-84]

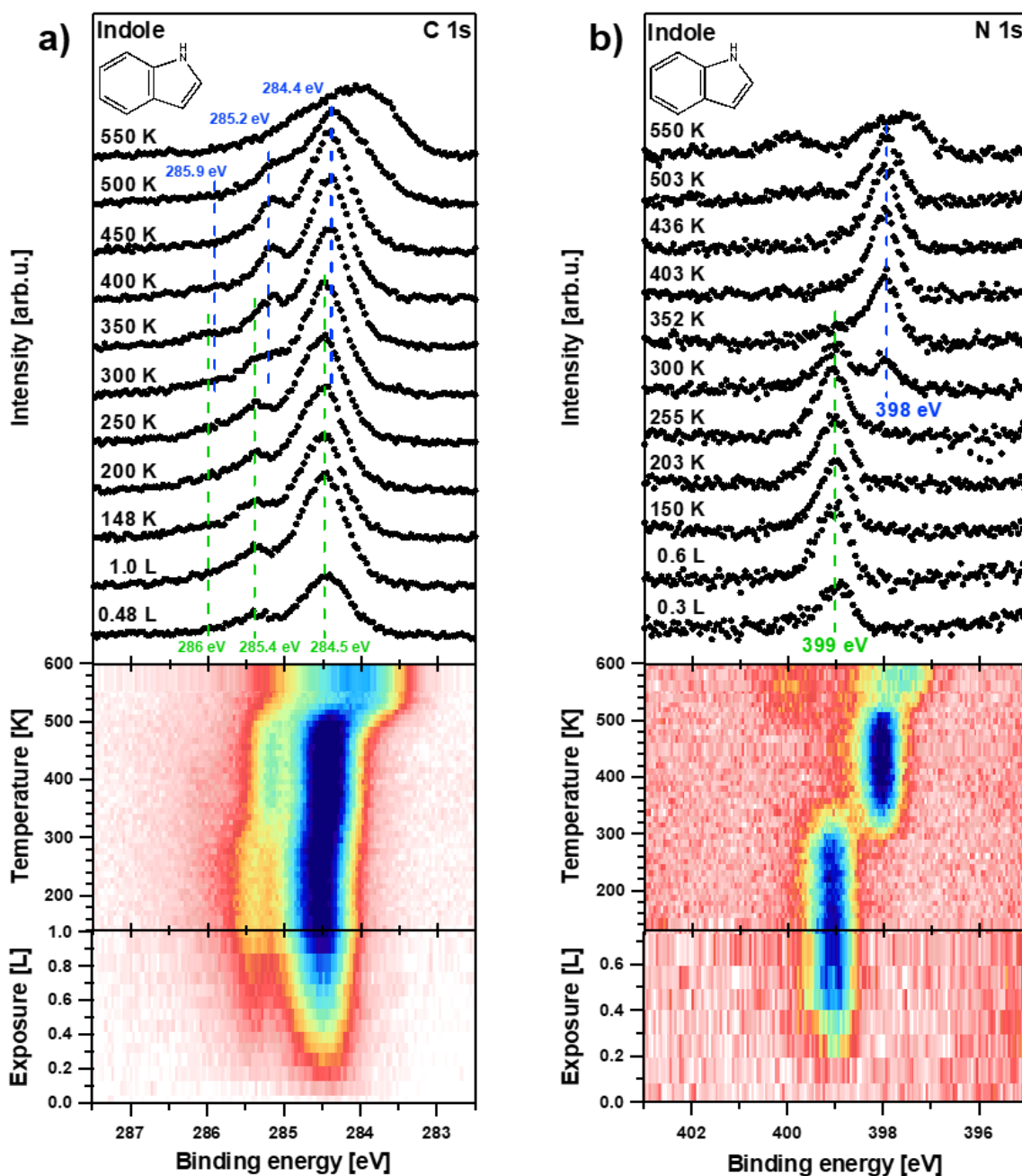


Figure 6: Selected C 1s (left, $h\nu=380$ eV) and N 1s (right, $h\nu=500$ eV) XP spectra (top) and density plots (bottom) of indole on Pt(111). Green: indole; blue: indolide.

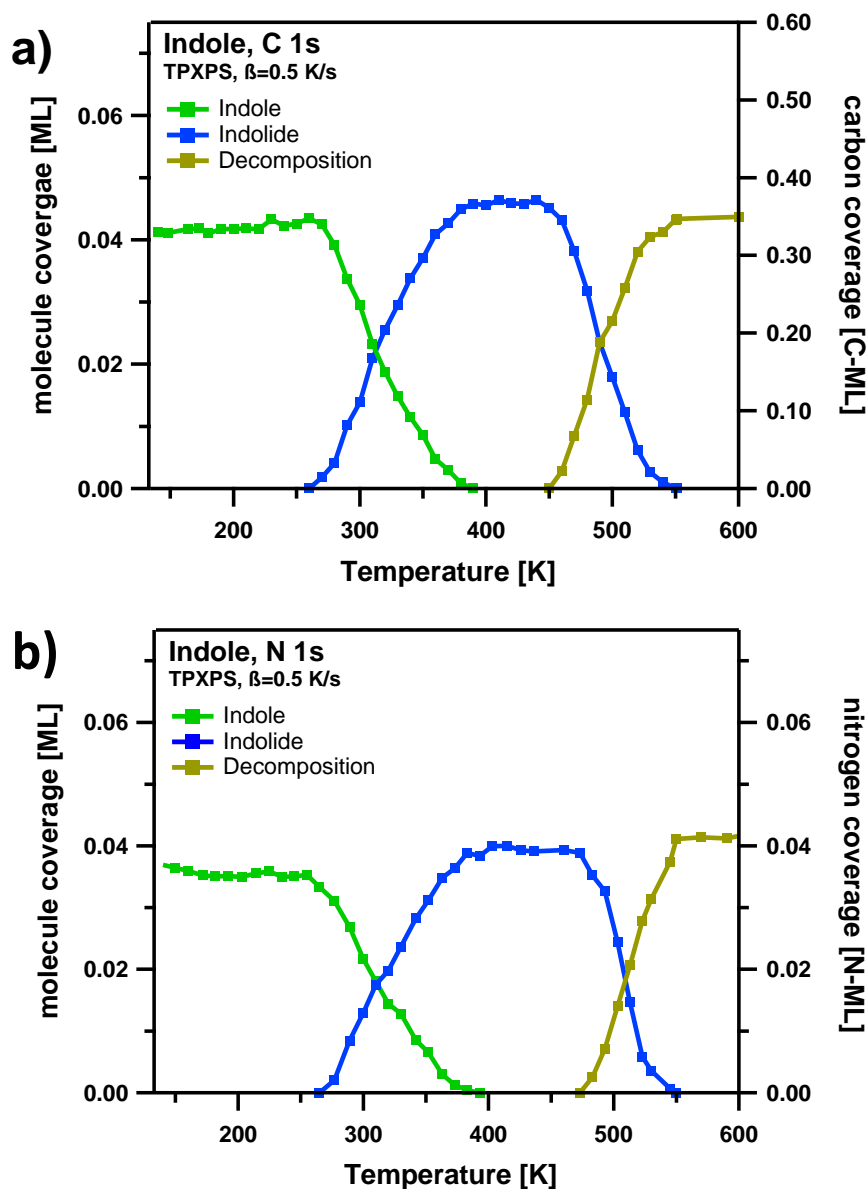


Figure 7: Quantitative analysis of the TPXPS experiments of indole on Pt(111) in the C 1s (a) and N 1s (b) regions shown in Figure 6.

To study the reaction of indole on the Pt(111) model catalyst, we performed TPXPS experiments. The sample is heated from 140-600 K with a linear heating ramp of 0.5 K/s while XP spectra are continuously recorded approximately every 10 K. Because a reaction is only expected to occur for molecules in direct contact with the surface, we focus on experiments in the monolayer regime. Upon heating, no reaction indicative changes occur up to 260 K in both the C 1s and N 1s core level. Indole is the only observed surface species, with a nearly constant coverage. Above 260 K, the indole peak at 399.0 eV in the N 1s region starts to decrease and vanishes at 390 K. It is replaced by a peak at 398.0 eV. The newly formed peak, with a shift of 1.0 eV to lower binding energy relative to indole, is attributed to a deprotonated aminic nitrogen, in agreement with previous studies of N-heterocyclic compounds^[26, 80-82, 85].

The resulting surface species is indolide. In the C 1s region, much smaller changes are observed along with the deprotonation step. The main peak at 284.5 eV peaks shifts to 284.4 eV, that is, to lower binding energies by 0.1 eV, and for the smaller peak at 285.4 eV a slightly larger shift of by 0.2 eV to 285.2 eV is found (see Figure 6). The proposed deprotonation is further confirmed by TPD measurements of H_2 $m/z=2$; in Figure 8, we observe a pronounced peak with a rate maximum at 350 K; the peak area corresponds to the desorption of ~ 1 hydrogen atom per molecule; the higher temperature as compared to the maximum rate in the XPS experiment (as estimated from the temperature of ~ 320 K, where 50% of indole is converted to indoline in Figure 7) is due to the higher heating rate in TPD. The low desorption intensity from 400 to 450 K is assigned to a small general increase in background pressure during heating and desorption.

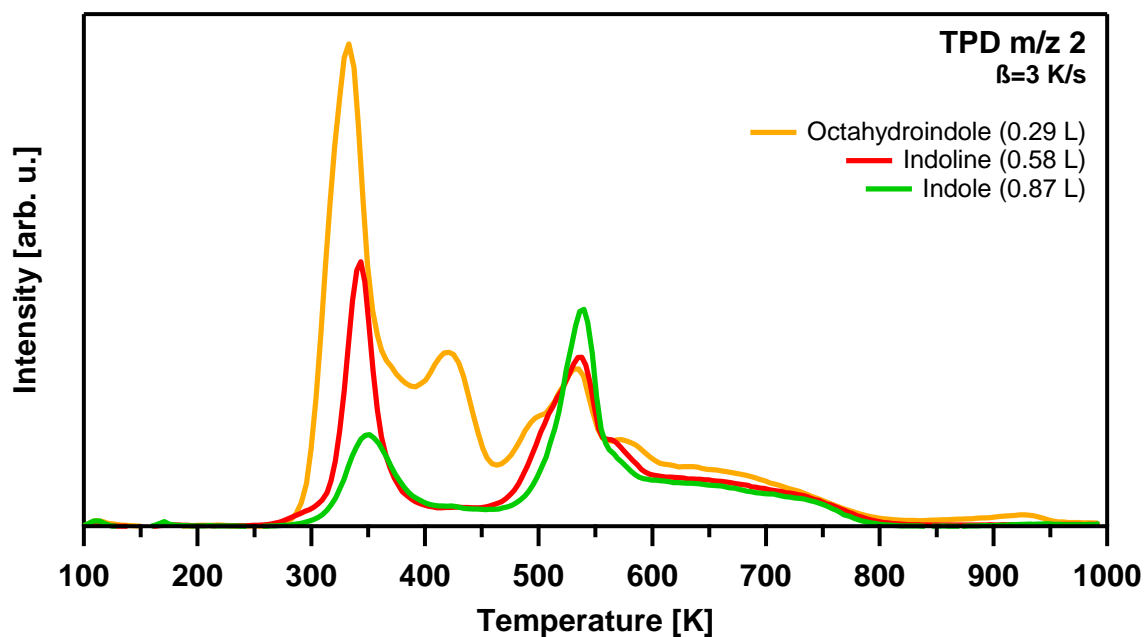


Figure 8: H_2 ($m/z=2$) TPD spectra of indole, indoline and octahydroindole on Pt(111), collected with a heating rate of 3 K/s.

Upon further heating, the N 1s and C 1s signals of the indolide species remain unchanged up to 450 K. Above this temperature, decomposition and fragmentation of the surface species starts with the highest reaction rate (inflection point) at ~ 500 K. While this transition is clearly visible in the N 1s spectra, the C 1s spectra show a significant broadening at this temperature. At 550 K, all indolide has decomposed. This decomposition reaction is also observed in TPD with a peak at 540 K for H_2 , again at higher temperatures than in XPS, due to the higher heating rate in TPD. Beyond 550 K, only undefined carbon and nitrogen fragments are identified in

XPS. We will not continue discussing these fragments as the decomposition of the hydrogen lean LOHC is an unwanted reaction and needs to be avoided in the LOHC storage cycle.

4.3.2 Indoline

Next, we want to study the hydrogen carrier molecule indoline, which is obtained from indole by partial hydrogenation of the five-membered ring (see Scheme 6). Indoline also is a possible intermediate in the dehydrogenation of the fully hydrogenated octahydroindole to indole, which will be discussed later. Indoline is interesting as LOHC, because its conversion to indole using different catalysts was shown to be fast, but has the drawback of only a small hydrogen storage capacity of 1.7%.^[86] In a previous study, molecular adsorption of indoline as intact molecule at low temperature has been shown with IRAS.^[68]

To study adsorption and reaction quantitatively and in more detail, we exposed the Pt(111) surface to 0.72 L (C 1s) and 0.84 L (N 1s) indoline at 140 K. Selected spectra collected during adsorption and subsequent TPXPS are shown in Figure 9a and b, with the quantitative analysis to the TPXPS displayed in Figure 10a and b, respectively. In the C 1s region, adsorption of indoline leads to the growth of a dominating peak at 284.3 eV along with a smaller peak at 285.4 eV and a weak shoulder at 285.9 eV. With increasing coverage, the peak shape does not change, but all peaks are slightly shifting towards higher binding energies, by 0.1 eV, to 284.4, 285.5 and 285.9 eV at 0.7 L, respectively. The peak shape and binding energy of the main peak of indoline after adsorption are very similar to indole, but the smaller peak at higher binding energy is significantly broader with its center at a higher binding energy (see Figure 14 and Table 2 on pages 40/41). In the N 1s region, indoline adsorption leads to a single peak at 399.5 eV, whose binding energy and shape remains unchanged with increasing coverage. Compared to indole, the indoline peak is shifted towards higher binding energies by 0.5 eV, reflecting the sensitivity of the N 1s level to different chemical surroundings in the 5-membered ring.

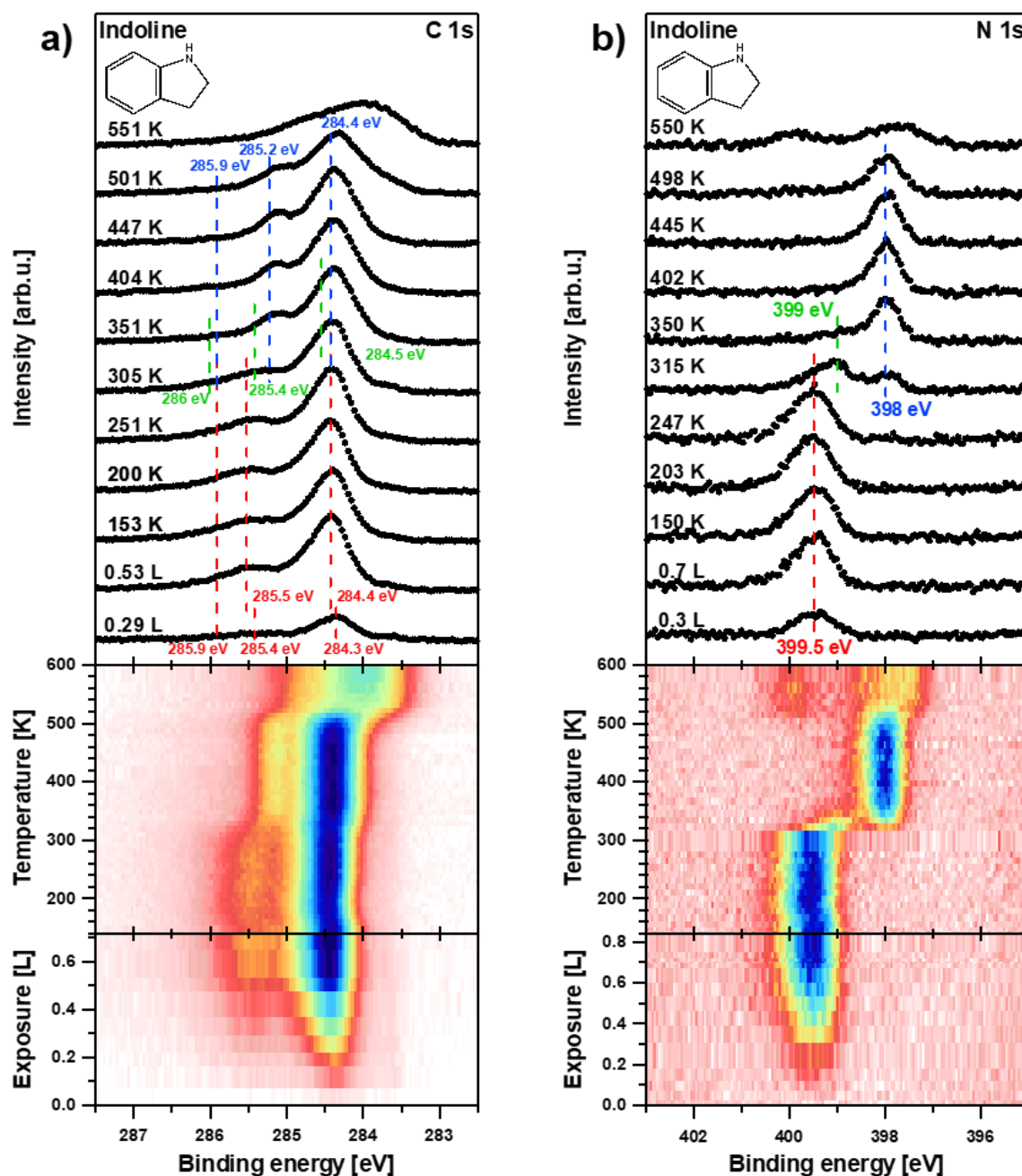


Figure 9: Selected C 1s (left, $h\nu=380$ eV) and N 1s (right, $h\nu=500$ eV) XP spectra (top) and density plots (bottom) of the adsorption and TPXPS of indoline on Pt(111). Red: indoline; green: indole; blue: indoline.

To study the thermal evolution of the adsorbed indoline layer, TPXPS experiments were performed in the N 1s and C 1s regions. In the C 1s region, up to 200 K only a small shift of 0.05 eV towards higher binding energies occurs (Figure 9a), while the N 1s region remains unchanged (Figure 9b); these minor changes might be related to reordering phenomena. No further changes in peak shape or signal intensity are observed in both core levels up to 270 K. Above 270 K, the indoline peak in the N 1s regions declines rapidly and vanishes at 330 K. Simultaneously, first a peak at 399.0 eV and 10 K later, a second peak at 398.0 eV develops.

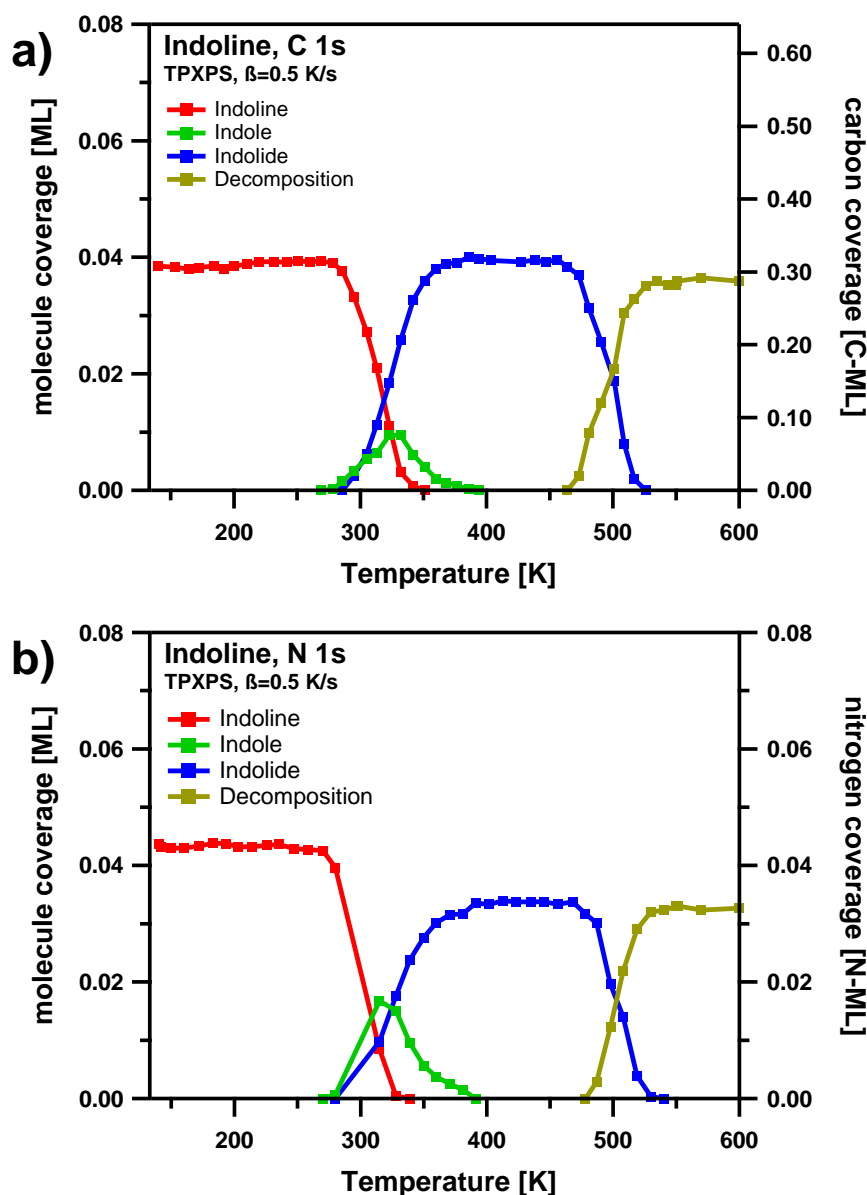


Figure 10: Quantitative analysis of the TPXPS experiments of indole on Pt(111) in the C 1s (a) and N 1s (b) regions shown in Figure 9.

The overall intensity decrease in the N 1s region (Figure 9, Figure 10) as compared to the C 1s region is likely caused by photoelectron diffraction effects which often occur at such low kinetic energies of the photoelectrons.^[85] From its binding energy, the peak at 399.0 eV is assigned to indole (see above), and thus indicates dehydrogenation of the five-membered ring; the peak at 398.0 eV is attributed to the deprotonated indolide species, that is, the same reaction intermediate discussed for indole. The indole peak at 399.0 eV is only found in a very narrow temperature window, that is, it reaches maximum intensity at ~315 K and quickly converts thereafter to the peak of the deprotonated indolide at 398.0 eV. The conversion from indole and indoline to the deprotonated indolide species is completed at 385 K. Thus, indole is only observed as an intermediate on the surface up to 385 K with a maximum coverage of

0.14 ML C at 330 K, see Figure 9 and Figure 10. In the C 1s region, these reaction steps are mirrored by changes in shape and height of the smaller peak at 285.5 eV and the flattening of the weak shoulder at 286 eV. The complexity of the C 1s spectra, in particular the relatively small changes for the different species, as compared to the N 1s region, introduces a larger error in the coverage and temperature values obtained, leading to the reaction temperature of indoline to indole of 275 K, being 15 K higher. Overall, the conversion from indoline to deprotonated indolide via indole goes along with a small shift of all peaks towards lower binding energies, leading to values of 284.4, 285.2 and 285.9 eV (Figure 9a), see also the thermal evolution of indole.

This dehydrogenation reaction is also reflected in the H₂ TPD spectra from the adsorbed indoline layer in Figure 8. The desorption maximum is found at 340 K, shifted to lower temperatures by 10 K as compared to 350 K for indole; this shift reflects the slightly earlier start of the reaction, also seen in TPXPS. From the integrated TPD area (see Figure A 1 in Appendix A), the peak at 340 K amounts for the desorption of 3 hydrogen atoms, which equals the NH deprotonation and the dehydrogenation of indoline at the five-membered ring into indole. Above 400 K, the C 1s and N 1s spectra of the remaining indolide are identical to the indole spectra beyond at the respective temperature, with the same decomposition products for temperatures above 450 K. The decomposition into C and N fragments at 550 K is again reflected in the TPD spectra with a desorption maximum at 540 K for m/z=2.

4.3.3 Octahydroindole

Last, we examined the adsorption and thermal evolution of octahydroindole, the fully hydrogenated form of indole. This molecule is very attractive as LOHC, as it has a large hydrogen storage capacity of 6.4%, which is significantly higher than that of indoline. The Pt(111) surface was exposed to 0.55 L (C 1s) and 0.90 L (N 1s) octahydroindole at 140 K. Selected spectra collected during adsorption and during heating are shown in Figure 11a and b, along with the corresponding quantitative analysis of the TPXPS in Figure 12a and b, respectively. In the C 1s region, adsorption leads to one broad peak at 284.4 eV with a smaller shoulder at 285.4 eV. With increasing coverage, the peaks shift by 0.4 eV, to 284.8 and 285.8 eV at 0.55 L; these values are ~0.4 eV higher than those found for indole and indoline. The broader peak shape is typical for saturated hydrocarbons, and is due to the weaker

surface interaction, leading to less defined carbon-substrate interactions. In the N 1s region, one peak develops at 399.5 eV; in addition, a weaker peak is seen at 401.0 eV. While the dominating peak is assigned to molecularly adsorbed octahydroindole, the smaller one could either be due to octahydroindole with a significantly different adsorption site or more likely due to the interaction with minor amounts of water leading to the protonation of the NH group, similar to reports on the protonation of other N-heterocyclic compounds at lower pH.^[87-88]

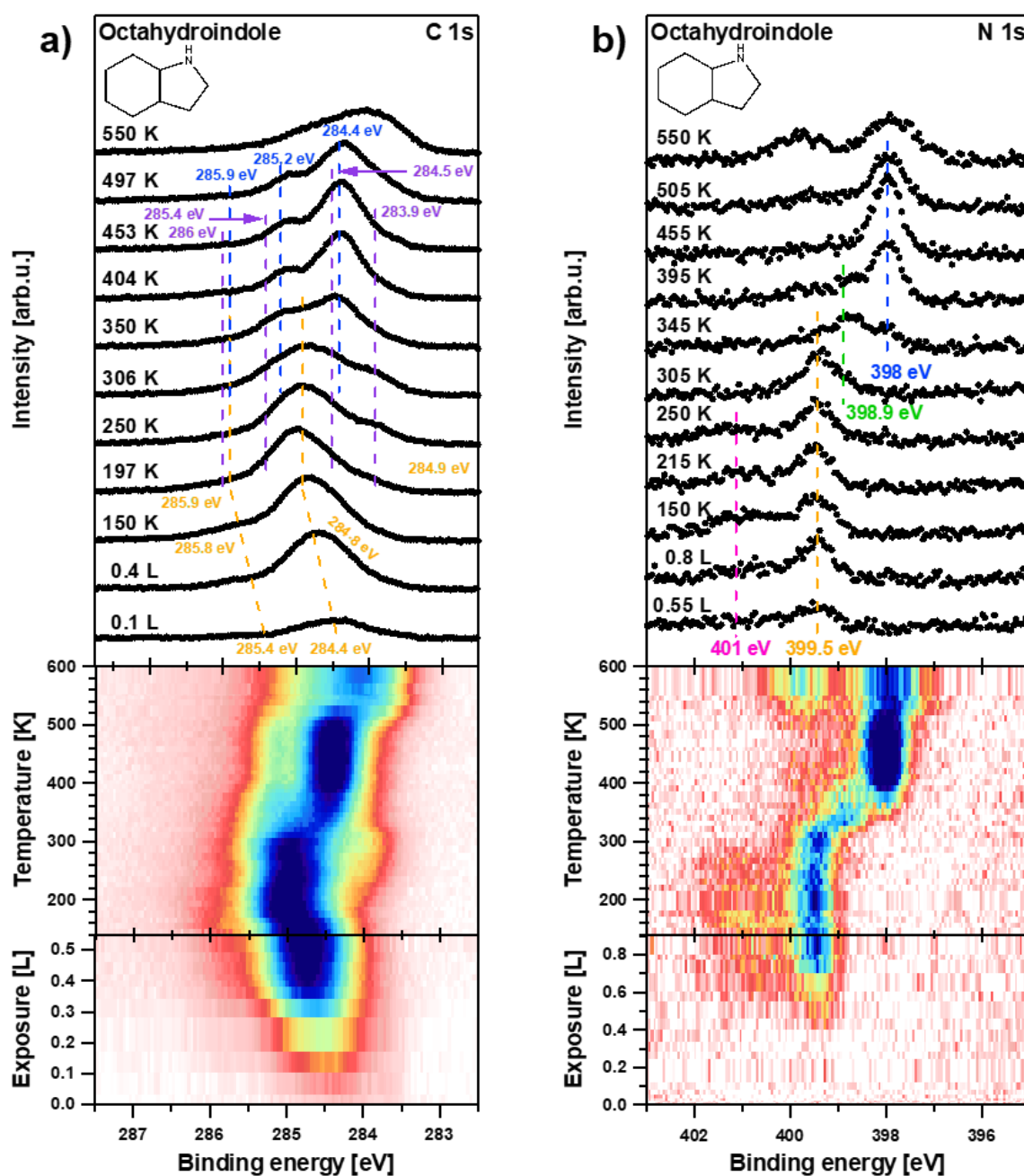


Figure 11: Selected C 1s (left, $h\nu=380$ eV) and N 1s (right, $h\nu=500$ eV) XP spectra (top) and density plots (bottom) of the adsorption and TPXPS of octahydroindole on Pt(111). Orange: octahydroindole; pink: octahydroindole (+OH), purple: π -allyl/indole, green: indole; blue: indolide.

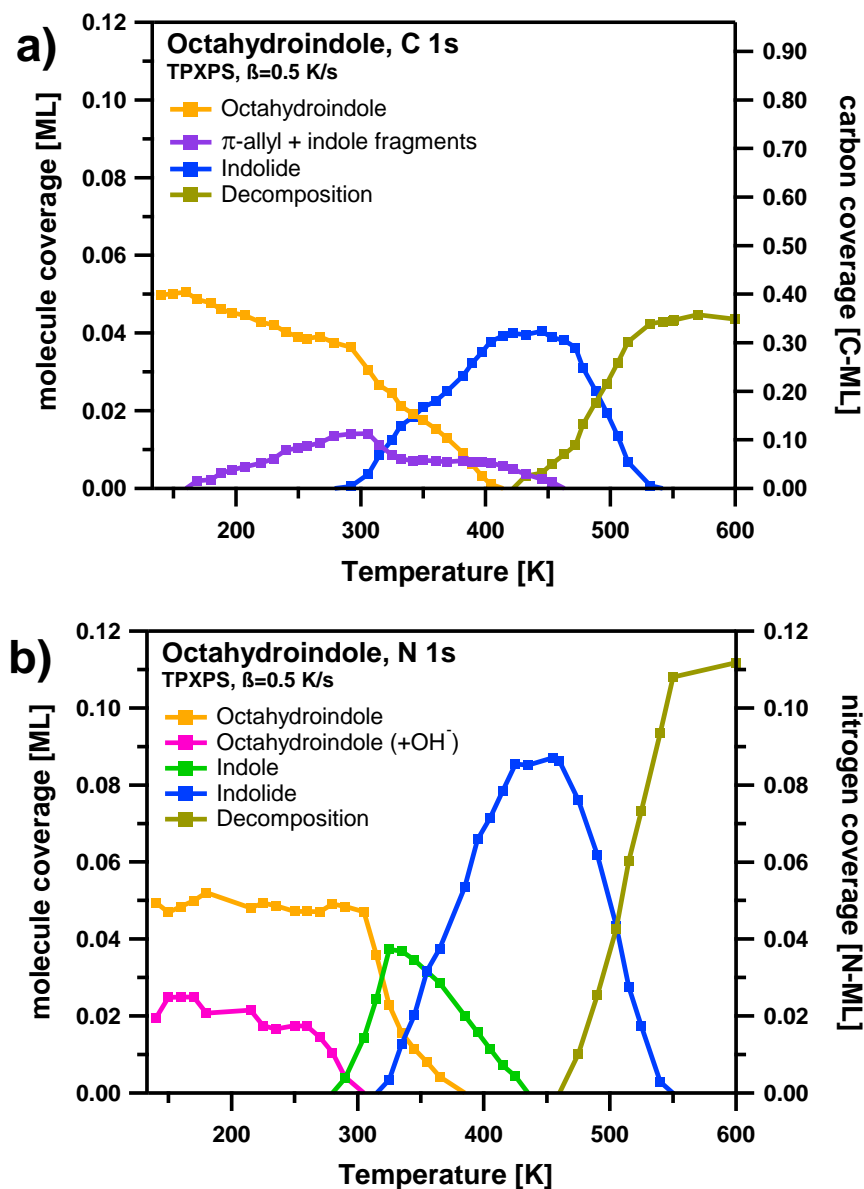


Figure 12: Quantitative analysis of the TPXPS experiments of octahydroindole on Pt(111) in the C 1s (a) and N 1s (b) regions shown in Figure 11.

This assignment is also in line with our IRAS data. We performed isothermal IRAS of a saturated octahydroindole monolayer on Pt(111) at 180 K (Figure 13). The spectrum is basically identical to the previously reported at 210 K sample temperature. We can identify CH stretching vibrations at 2935 and 2859 cm^{-1} , as well as CH_2 scissoring at 1463 and 1450 cm^{-1} . Further bands are found at lower wavenumbers; see Table 1 together with their assignment. All these bands can be assigned to molecular octahydroindole on the Pt(111) surface. As we have reported before, the only band missing is the NH stretching mode expected around 3300 cm^{-1} . Instead, we find a very broad feature at 2650 cm^{-1} , which we did not identify before due to its low intensity. The absence of a band around 3300 cm^{-1} and a band at this frequency is characteristic for secondary ammonium ions.^[89] This behavior strongly supports protonation

of octahydroindole. As proton source, we invoke water, which is a known contamination of octahydroindole.

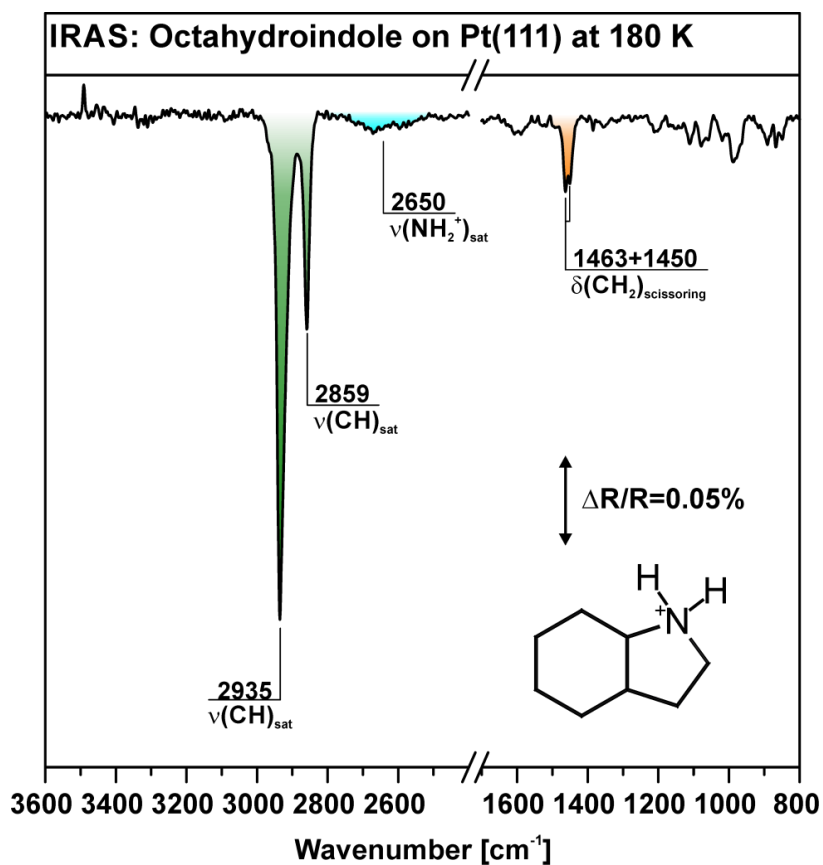


Figure 13: IR spectrum during continuous exposure of Pt(111) to octahydroindole at 180 K.

Band position in IRAS (cm ⁻¹)	Assignment
848, 868, 917, 987	$\nu(\text{CC}), \nu(\text{CN}), \delta(\text{CC}), \delta(\text{CH})$
1020	$\nu_{\text{as}}(\text{N1C2C3})$
1058, 1079	$\nu(\text{N1C7a}), \delta(\text{CH}_2)$
1110	$\nu(\text{CC}), \delta(\text{CH}_2)$
1211	$\delta(\text{CH}_2)_{\text{twisting}}$
1355, 1385	$\delta(\text{NH})$
1450, 1463	$\delta(\text{CH}_2)_{\text{scissoring}}$
2650	$\nu(\text{NH}_2^+)$
2859	$\nu(\text{C2H}), \nu(\text{C7aH})$
2935	$\nu(\text{CH}_2)$

Table 1: Assignment of IR-bands of octahydroindole at 180 K on Pt(111)

Thermal evolution of the hydrogen-rich system at submonolayer coverages is investigated by TPXPS in the C 1s and the N 1s regions. In the N 1s region, no change is observed upon heating until the decline of the peak at 401 eV between 280 and 300 K. Above 300 K, a steep decline of the octahydroindole peak at 399.5 eV is observed until it vanishes at 380 K. Simultaneously, a peak at 398.9 eV, develops, indicating the formation of indole (see above), and reaches its maximum at 320 K. Subsequently, indole reacts to form the already discussed indolide with a peak at 398.0 eV. This indolide species has its maximum coverage at 450 K; at this temperature indole has completely vanished. Decomposition of indolide to C- and N-fragments starts at 460 K and is completed at 550 K. The observed temperature dependent behavior in the N 1s region is consistent with the results found for indole and indoline described above, while the coverage increase above 540 K is due to electromagnetic stray fields, which sometimes occur during resistive heating.

In the C 1s TPXPS experiment, the temperature-induced changes are again more difficult to analyze. Upon heating to 180 K, the octahydroindole peaks at 284.8 and 285.8 eV shift to higher binding energies by 0.3 eV, while the peak shape changes due to the emergence of two new species. The peaks at 284.5/285.4 eV are attributed to small fractions of indole (see above); the new peak at 283.9 eV presumably is due to a π -allylic species. Such species have previously been reported for other cyclic compounds^[78, 90-91] The minor difference of the N 1s values of indole (398.9 eV here vs 399.0 eV for direct indole adsorption – see above) between 290 and 430 K might also be due to the formation of this π -allyl, compared to the “pure” indole experiment. Above 180 K, the C 1s region is difficult to interpret solely on the peak shape. To simplify the discussion and reduce the error bars in the complicated analysis, the indole and the π -allyl contributions are added in Figure 12. Between 290 and 310 K, the combined indole plus π -allyl C 1s signal reaches its maximum with 0.1 ML C. During this reaction, the octahydroindole coverage is slowly decreasing to 0.3 ML C at 290 K. Starting at 310 K, we observe the formation of indolide on the surface, associated with a drastic peak change towards lower binding energies, that is, 284.4, 285.2 and 285.9 eV at 400 K (Figure 11); these values are typical for indolide (compare with Figure 6 and Figure 14). Simultaneously, octahydroindole vanishes at 410 K, and the indole/ π -allyl species declines until 460 K, with a plateau of 0.05 ML C between 330 and 400 K. Indolide decomposition occurs between 450 and 530 K, in unison with the N 1s results and analogous to indole and indoline. Moreover, H₂ TPD (see Figure 8) indicates the loss of 9 hydrogen atoms up to 450 K during the

dehydrogenation and deprotonation of octahydroindole to indole and indolide with a desorption peak at 330 K; a smaller, second peak at 420 K, is attributed to the decomposition of the remaining π -allyl and indole, concomitant with the XP spectra. Analogous to indole and indoline, decomposition and fragmentation of the indolide is represented by a desorption peak at 540 K.

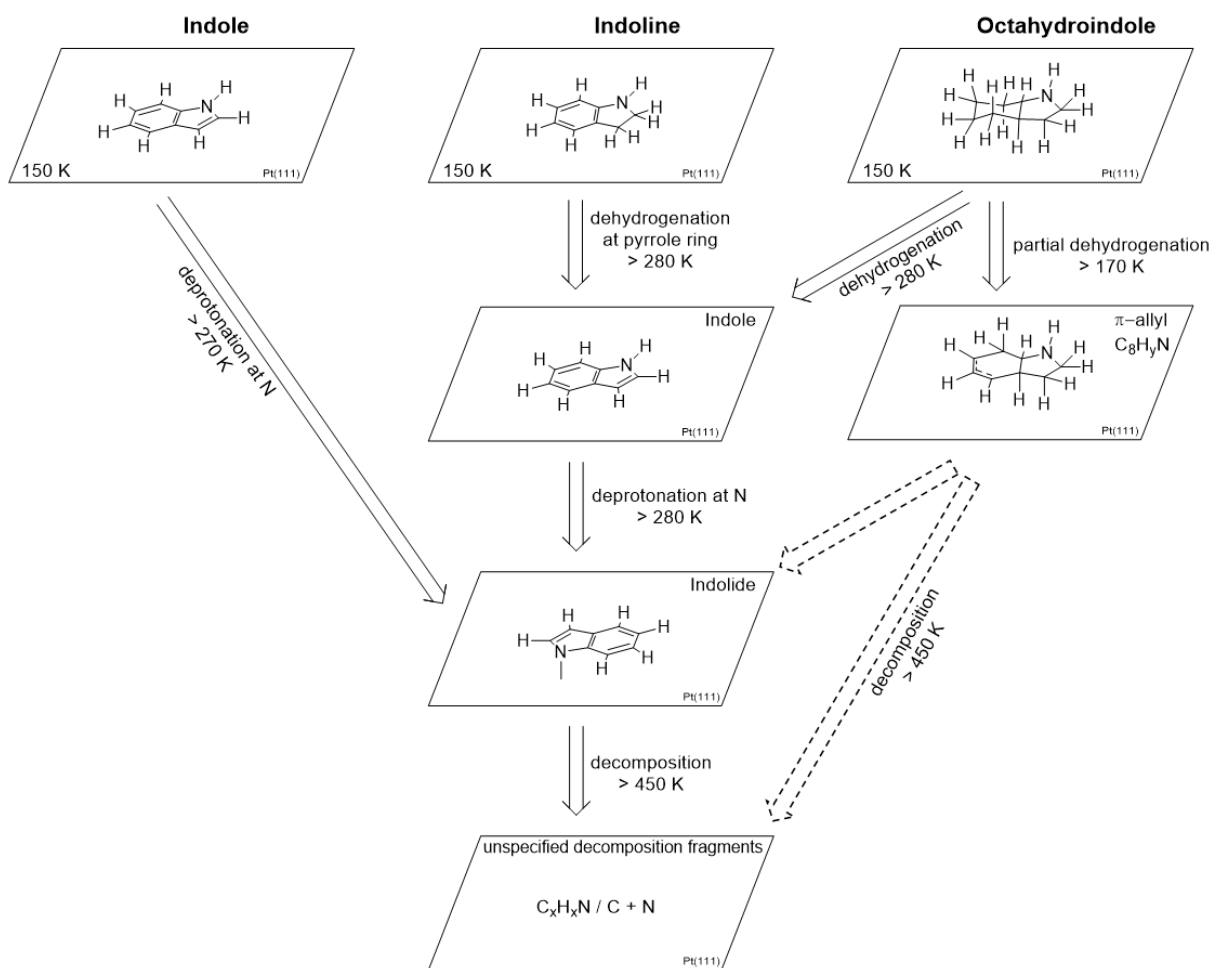
To further understand the adsorption geometry and to observe the conversion of octahydroindole to indole, we performed NEXAFS at the C K-edge and N K-edge of both molecules (see Figure 15 on page 42). For this purpose, we adsorbed multilayers of indole and octahydroindole at low temperature and then heated the sample to above the multilayer desorption temperatures. Spectra were taken at 230 and 420 K for octahydroindole and 260 and 420 K for indole in grazing (GI, 70°) and normal (NI, 0°) incidence. In the π^* region (284-292 eV), a large π^* contribution at 285 eV in GI and low π^* contribution in NI in this region shows the flat adsorption geometry of indole at 260 K. A similar behavior is reported for benzene, while pyridine, which is adsorbed with the ring being perpendicular to the surface, leads to the opposite behavior in grazing and normal incidence spectra.^[92] Octahydroindole, shows the opposite behavior, with low π^* contribution in GI and a distinct peak in NI at 230 K. Upon heating to 420 K, the octahydroindole C K-edge spectra become nearly identical to the indole spectra, which virtually stay unchanged from 260 to 420 K.

4.3.4 Comparison of indole, indoline, octahydroindole and H₁₂-N-ethylcarbazole

The comparison of the N 1s and C 1s spectra of indole, indoline and octahydroindole at three temperatures visualizes the differences of the three molecules (see Figure 14; also Table 2 for binding energies). At ~150 K clear differences are evident. At ~330 K, indole is observed as intermediate species for octahydroindole and indoline, while at ~400 K the spectra show the great conformity of all three molecules, which results from the similar reaction to the here present indolide species. For octahydroindole, small amounts of π -allyl are still observed at 400 K and 283.9 eV in the C 1s region, causing a slight broadening of the main peak. To reflect C 1s peak shape in a quantitative manner, 4 peaks for indole, indoline and indolide and 3 for octahydroindole are used to create an envelope, which is kept constant during fitting for the respective species.

Both, indoline and octahydroindole are a LOHC system with indole as the hydrogen-lean form (see also Scheme 7). The pair octahydroindole/indole offers a hydrogen storage capacity of 6.4%, while the pair indoline/indole only reaches 1.7%. While both pairs are promising LOHC candidates, our study shows several challenges that have to be mastered. On the one hand, there is no evidence of an indoline-like intermediate in the dehydrogenation of octahydroindole, but the formation of minority π -allyl species is proposed. On the other hand, we find the deprotonation of the NH group above ~ 300 K for all molecules, leading to an indolide surface species. Both effects are obstructive in terms of the LOHC system reversibility. The deprotonated molecule cannot desorb, as would be necessary in the catalytic reaction. Nevertheless, this deprotonation might be not as relevant at higher hydrogen pressures in technical catalysis, where in addition coadsorbed carbon or C_xH_y species might block the relevant active sites.

Overall, the octahydroindole and indoline LOHC systems show similarities to the previously investigated H_{12} -N-ethylcarbazole/N-ethylcarbazole system with 5.8% hydrogen storage capacity. Starting at 200 K, H_{12} -N-ethylcarbazole dehydrogenates into N-ethylcarbazole. Dealkylation into carbazole takes place above 390 K. Above 450 K, decomposition is observed.^[22-26] These steps can be seen analogous to the observed dehydrogenation of octahydroindole/indoline into indole above 280 K, the consecutive deprotonation above ~ 300 K into indolide and decomposition above ~ 450 K; thereby, indole only resembles a relatively short-lived intermediate in comparison to N-ethylcarbazole.



Scheme 7: Reaction pathways of indole, indoline and octahydroindole on Pt(111)

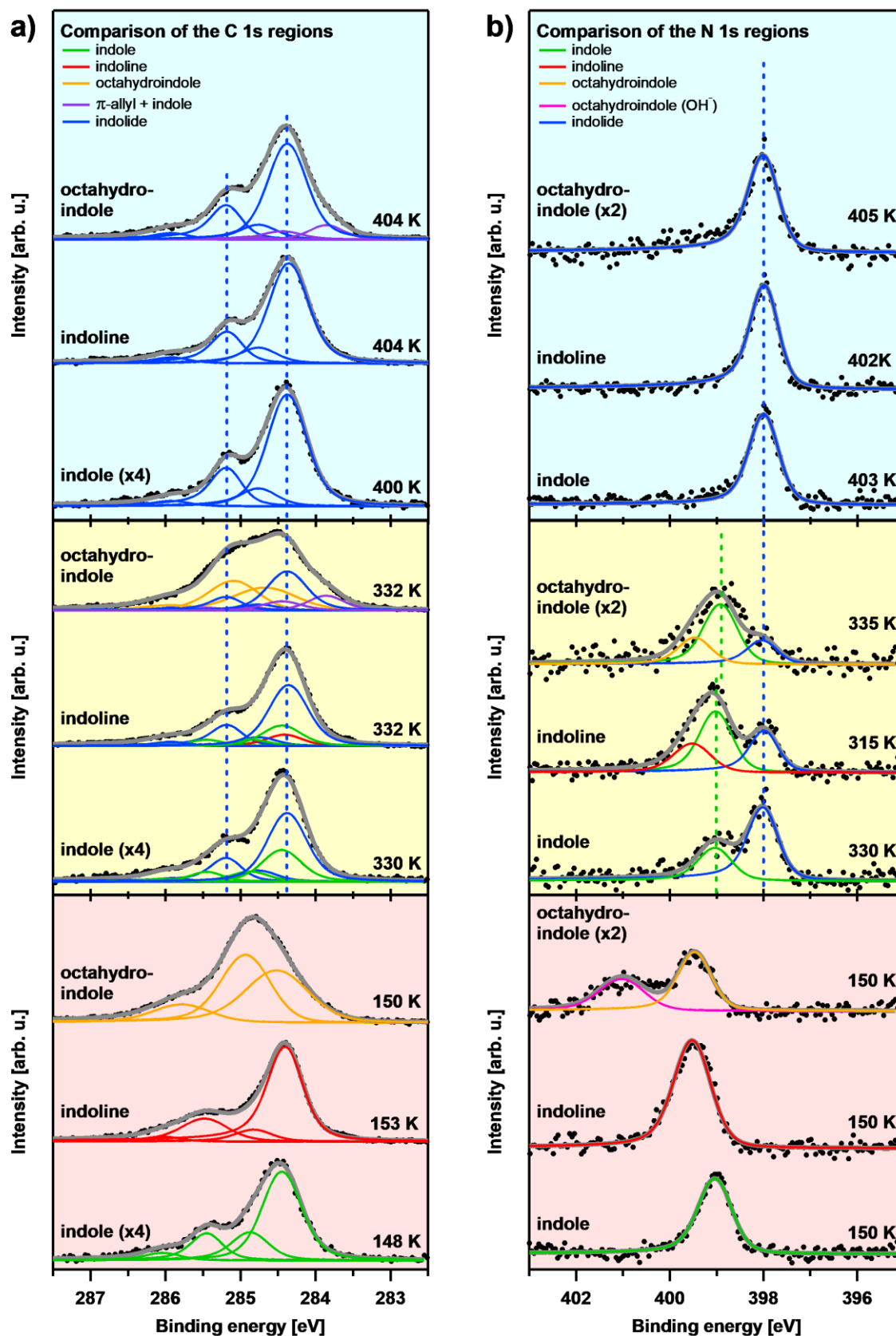


Figure 14: Comparison of the C 1s and N 1s regions of indole, indoline and octahydroindole at 150, 330 and 400K, including the fitted peaks of the single species with peak positions given in Table 2 (the number of peaks needed during fitting is up by 1 in the C 1s region in comparison to the visible and discussed peaks derived from the raw spectra). Orange: octahydroindole; red: indoline; green: indole; pink: octahydroindole (+OH⁻), purple: π -allyl/indole; blue: indolide; other: decomposition fragments.

Indole		Core level	Peak #	Binding energy (range) [eV]
Species	Indole	C 1s	1	284.5
			2	284.9
			3	285.4
			4	286.0
		N 1s	1	399.0
	Indolide	C 1s	1	284.4
			2	284.8
			3	285.2
			4	285.9
		N 1s	1	398.0

Indoline		Core level	Peak #	Binding energy (range) [eV]
Species	Indoline	C 1s	1	284.4 (284.3-284.4)
			2	284.8 (284.7-284.9)
			3	285.5 (285.4-285.5)
			4	286.0 (285.9-286.0)
		N 1s	1	399.5
	Indole	C 1s	1	284.5
			2	284.9
			3	285.4
			4	286.0
		N 1s	1	399.0
	Indolide	C 1s	1	284.4
			2	284.8
			3	285.2
			4	285.9
		N 1s	1	398.0

Octahydroindole		Core level	Peak #	Binding energy (range) [eV]
Species	Octahydro-indole	C 1s	1	284.5 (284.1-284.7)
			2	284.9 (284.5-285.1)
			3	285.8 (285.3-285.9)
		N 1s	1	399.5
			2	401.0
	Indole + π -allyl	C 1s	1	284.5
			2	284.9
			3	285.4
			4	286.0
			5	283.9
		N 1s	1	398.9
	Indolide	C 1s	1	284.4
			2	284.8
			3	285.2
			4	285.9
N 1s		1	398.0	

Table 2: Binding energies and binding energy ranges of the fitted peaks of indole, indoline and octahydroindole shown in Figure 14.

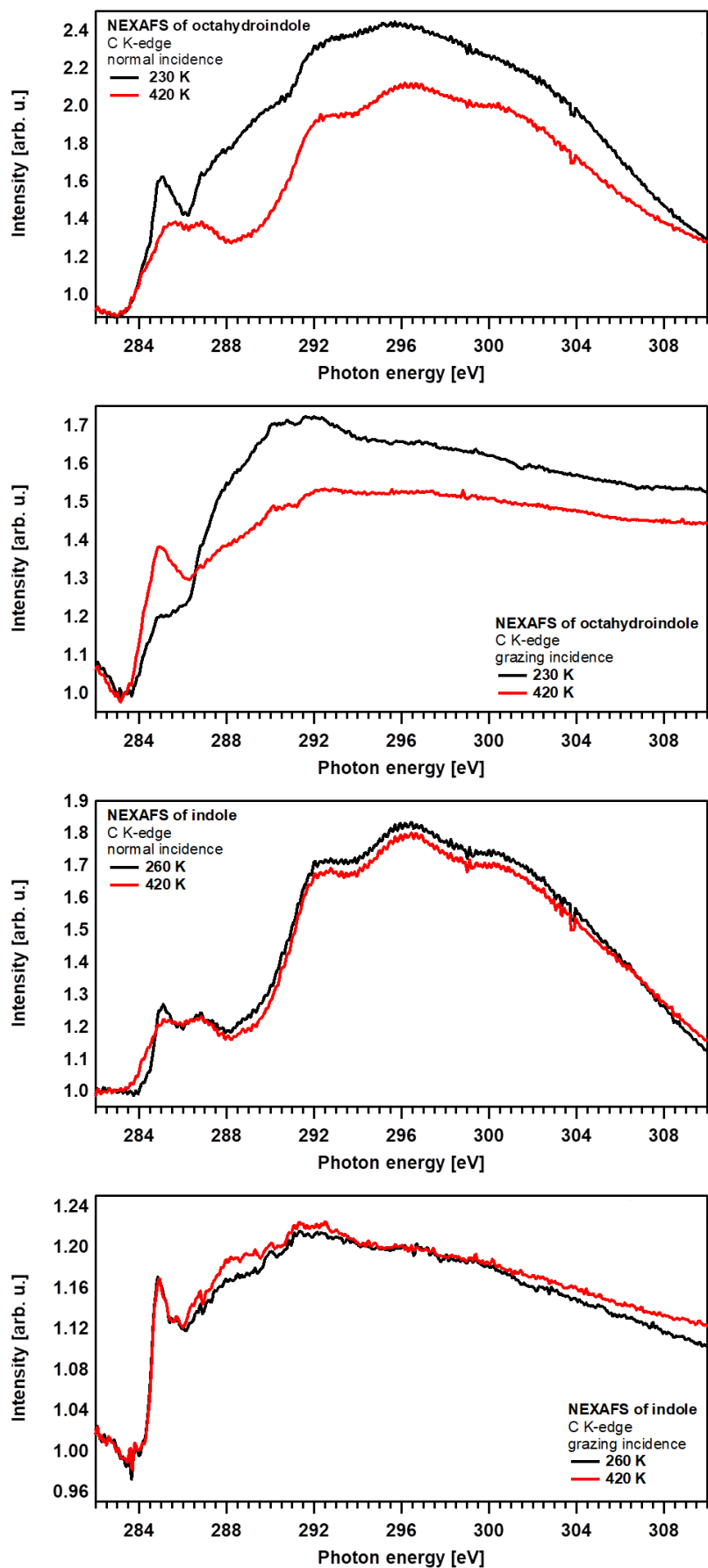


Figure 15: C K-edge grazing and normal incidence NEXAFS spectra at 230/260 and 420 K of indole and octahydroindole. The spectra were measured in partial electron yield (PEY) mode.

4.4 Conclusion

In conclusion, we performed a high resolution XPS study, assisted by TPD, of the surface reaction of the LOHC systems indole/indoline and indole/octahydroindole on Pt(111). We identified the following reaction steps of indoline and octahydroindole: First, both molecules dehydrogenate into an indole intermediate above 270 K, with a H₂ desorption maximum of 330 K for octahydroindole and 340 K for indoline. The second step is the nearly simultaneous deprotonation into an indolide species, which remains stable up to 540 K on the surface, before decomposition. Furthermore, partial protonation of octahydroindole is seen in presence of OH⁻ traces up to 290 K. Also, a π -allylic minority species is identified, which emerges from 170-450 K, during octahydroindole dehydrogenation. Under real catalytic conditions, the NH deprotonation reaction and decomposition needs to be avoided in order to form a functioning and efficient hydrogen storage cycle.

5. 2-methylindole, 2-methylindoline and 2-methyloctahydroindole on Pt(111)

The results presented in this chapter have been submitted^[93]; the content of this chapter is adapted from:

Dehydrogenation of the Liquid Organic Hydrogen Carrier System 2-methylindole/2-methylindoline/2-methyloctahydroindole on Pt(111)

P. Bachmann, J. Steinhauer, F. Späth, F. Düll, U. Bauer, R. Eschenbacher, F. Hemauer, M. Scheuermeyer, A. Bösmann, P. Wasserscheid, H.-P. Steinrück, C. Papp

- submitted

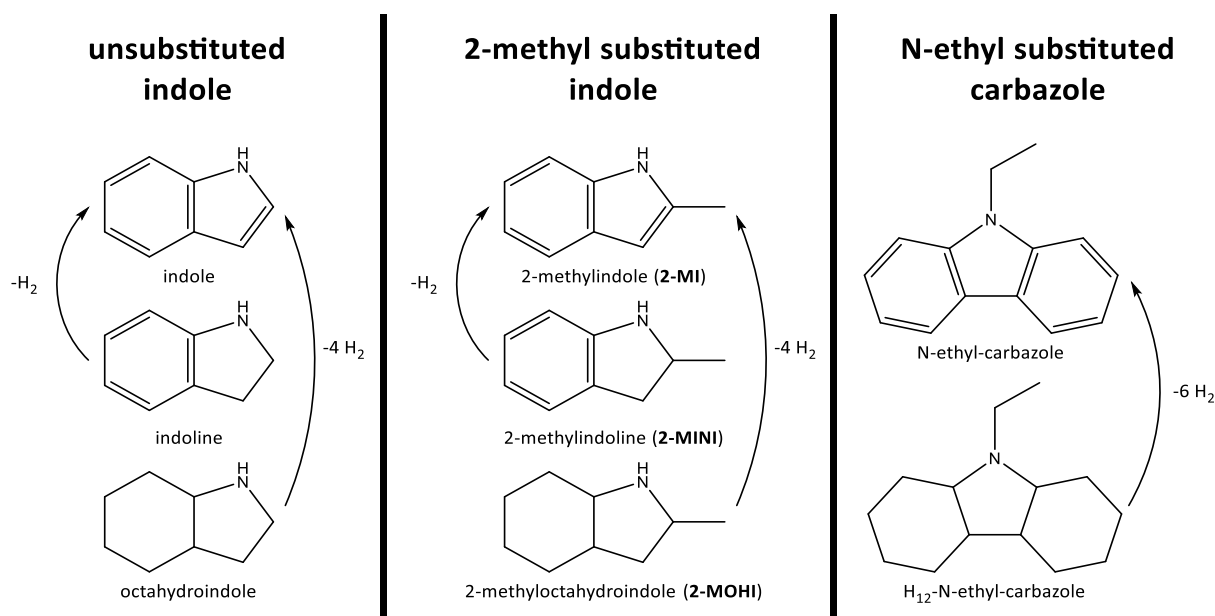
Authorship: P. Bachmann (except synthesis part)

Among other N-heterocycles, indole and its substituted derivatives, like methylindoles, are considered as promising Liquid Organic Hydrogen Carriers (LOHC) for the storage of hydrogen from renewable energy. We used X-ray Photoelectron Spectroscopy (XPS) and Temperature Programmed Desorption (TPD) to investigate the low temperature adsorption and consecutive dehydrogenation reaction during heating of 2-methylindole, 2-methylindoline and 2-methyloctahydroindole on Pt(111) and their viability as LOHC system. For all H_x-2-methylindoles, we find deprotonation at the NH bond starting between 240 to 300 K, resulting in a 2-methylindolide species. Simultaneously or before this reaction step, the dehydrogenation of 2-methyloctahydroindole via 2-methylindoline and 2-methylindole intermediates, is observed at slightly different temperatures. For 2-methyloctahydroindole, we also find π -allyl intermediates above 230 K. Starting at ~390 K, decomposition of the remaining 2-methylindolide species takes place under the conditions of our surface science experiments.

5.1 Introduction

As outlined above, N-heterocyclic compounds exhibit suitable properties for LOHC applications.^[21, 70-71] In the past, especially the dodecahydro-N-ethylcarbazole/N-ethylcarbazole system (see Scheme 8, right panel) with a storage capacity of 5.8 wt% hydrogen has been studied.^[17, 21-29] Recently, also the structurally related indole and its derivatives have gained attention as potential LOHC systems. They are easily available and show advantageous LOHC properties, including favorable thermodynamics and kinetics for hydrogen release from perhydro indole compounds at comparably mild temperature conditions.^[72-74, 86]

In the previous chapter, the dehydrogenation of the indole, indoline and octahydroindole LOHC system (see Scheme 8, left) on Pt(111) was investigated using high resolution X-ray photoelectron spectroscopy (XPS), infrared reflection absorption spectroscopy (IRAS) and temperature-programmed desorption (TPD).^[67-68] Thereby, we found indoline and octahydroindole to dehydrogenate to form an indole intermediate above 270 K with consecutive deprotonation into an indolide species, which is observed up to 540 K on the surface, before it decomposes (see Chapter 4 for more details).^[67-68]



Scheme 8: LOHC systems. Left: indole / indoline / octahydroindole; middle: 2-methylindole (2-MI) / 2-methylindoline (2-MINI) / 2-methyloctahydroindole (2-MOHI); right: N-ethylcarbazole / H₁₂-N-ethylcarbazole.

In order to better understand the surface chemistry of indoles and possibly tweak the unwanted NH deprotonation reaction as well as the decomposition temperature, we sought to investigate methyl-substituted indole derivatives. Especially 2-methylindoline has gained

interest in the recent years, as it was shown to dehydrogenate into 2-methylindole fast and with high conversion rate in real catalysis using different heterogeneous and also homogeneous catalysts.^[94-98] Interestingly, however, there is barely information on the dehydrogenation of the fully hydrogenated 2-methyloctahydroindole.^[74]

In this chapter, a detailed quantitative *in situ* study on the dehydrogenation of the LOHC system 2-methylindole (2-MI), 2-methylindoline (2-MINI) and 2-methyloctahydroindole (2-MOHI), which is shown in Scheme 8 (center), is presented. This allows us to determine the influence of the substitution on the overall dehydrogenation reaction in comparison to the original indole system. Using high-resolution XPS and TPD, we follow the dehydrogenation and decomposition of the single molecules on Pt(111) in ultra-high vacuum (UHV). We identify individual reaction steps and surface species; this includes the dehydrogenation of 2-MOHI and 2-MINI to 2-MI and further deprotonation into 2-methylindolide (2-MID) with consecutive decomposition into fragments at higher temperatures. For 2-MOHI, we find π -allylic surface species and 2-MINI as intermediates.

5.2 Specific experimental setup

The XPS experiments were performed at the synchrotron BESSY II at beamline UE56-2 PGM-2 using the synchrotron UHV machine (see Chapter 3.1). TPD experiments were performed in a separate TPD UHV machine (see Chapter 3.2).

The adsorption of indole/indoline/octahydroindole on Pt(111) was conducted using the vapor pressure of the substances. The heating rate was set to 0.5 K/s during TPXPS and 3 K/s for TPD. All TPD spectra were background-corrected with a spectrum of the clean Pt crystal to account for the desorption of small amounts of hydrogen adsorbed from the background pressure. Due to slightly different coverages, the spectra are normalized to the peak at 480 K.

Adsorbate coverages on Pt(111) were calibrated by comparison to the well-known saturation coverage of carbon monoxide at 200 K, which leads to a c(4x2) LEED pattern and amounts to 0.5 carbon monolayers (1 carbon monolayer = 1 carbon atom / Pt atom).^[52, 75-76] The molecule coverage in monolayers (ML) is derived from the carbon coverage (1 ML = 9 carbon monolayers). Peak fitting of the C 1s and N 1s spectra was done using Doniach-Šunjić-profiles^[53] convoluted with a Gaussian function. The C 1s and N 1s regions were measured at 380 and 500 eV with resolutions of 150 and 200 meV at an emission angle of 0° relative to the

surface normal. Prior to each spectrum, the sample position is shifted to avoid beam damage. All spectra are referenced to the Fermi edge of Pt(111).

The investigated molecules 2-methylindole and 2-methylindoline were purchased from Sigma-Aldrich (purity >98%). The catalytic hydrogenation of 2-methylindole to 2-methyloctahydroindole was carried out over a 5 wt% Ru/Al₂O₃ catalyst at 413 K in a 300 mL Parr autoclave equipped with a gas entrainment stirrer. The autoclave was charged with a solution of 10 g 2-methylindole in 150 mL cyclohexane and 1 g catalyst. After sealing, the reactor was flushed three times with argon to remove air, and then flushed three times with hydrogen. After the reaction temperature was reached the hydrogen pressure was adjusted to 5 Mpa and kept constant over the duration of the reaction. After three hours, the autoclave was allowed to cool to room temperature, the hydrogen pressure released and the autoclave was flushed with argon. The solvent cyclohexane was removed with a rotary evaporator at reduced pressure. The 2-methyloctahydroindole was collected as a brownish liquid. The identity and purity of >98% of the material was confirmed via ¹H/¹³C-NMR and GC-MS.

5.3 Results and discussion

To analyze the adsorption and reaction of 2-methylindole (2-MI), 2-methylindoline (2-MINI) and 2-methyloctahydroindole (2-MOHI) on Pt(111), we use *in situ* high resolution XPS of the N 1s and C 1s core levels, temperature programmed XPS (TPXPS) and TPD. Calibrated coverage values (given in monolayers, ML) are used for quantitative comparison. Notably, the denoted gas exposures (given in Langmuir, L) during adsorption of the molecules are not necessarily comparable between each other, due to quite different pumping speeds of the different species and different ionization probabilities in the ion gauges. In the following, we will discuss the adsorption and temperature-induced reaction of the different molecules. We will focus on the N 1s region, and present the adsorption and thermal evolution in the multilayer and monolayer range. In addition, we will also discuss the corresponding C 1s spectra in the monolayer range. The C 1s spectra are significantly more complex than the N 1s spectra, due to the superposition of the signals of inequivalent carbon atoms in the individual molecules, yielding complex and broad peak structures. As a result, the C 1s spectra are challenging to analyze, especially quantitatively. Therefore, interpretation of the C 1s spectra relies on cross-referencing to the more distinct N 1s data. We will thus focus in the following on the quantitative analysis in the N 1s region. Finally, we will give a comparison of the 2-methyl-substituted system to the unsubstituted H_x-indole system.

5.3.1 2-methylindole (2-MI)

We first address 2-methylindole as the hydrogen-lean form of the LOHC system. To analyze the hydrogen-rich 2-MINI and 2-MOHI, it is crucial to understand the spectral fingerprint and surface reactions of 2-MI, which is the desired product from 2-MINI and 2-MOHI dehydrogenation. Furthermore, the irreversible decomposition of 2-methylindole on Pt(111) limits the temperature range for the applicability of the whole LOHC system.

The N 1s and C 1s regions were measured during exposure of Pt(111) to 2-methylindole at 140 K and subsequent heating. Selected XP spectra during adsorption and reaction of 0.23 ML (N 1s) and 0.05 ML (C 1s) are shown in Figure 16a and b, respectively, with the corresponding quantitative analysis of the N 1s region in Figure 17a. Notably, the denoted final coverage after adsorption for the N 1s measurements accounts for the signal of the multilayer plus the signal

of the monolayer (0.08 ML), which is partly damped (see below). To further illustrate the adsorption behavior, density plots, containing all recorded spectra of the N 1s and C 1s regions, are depicted in Figure 18a and b.

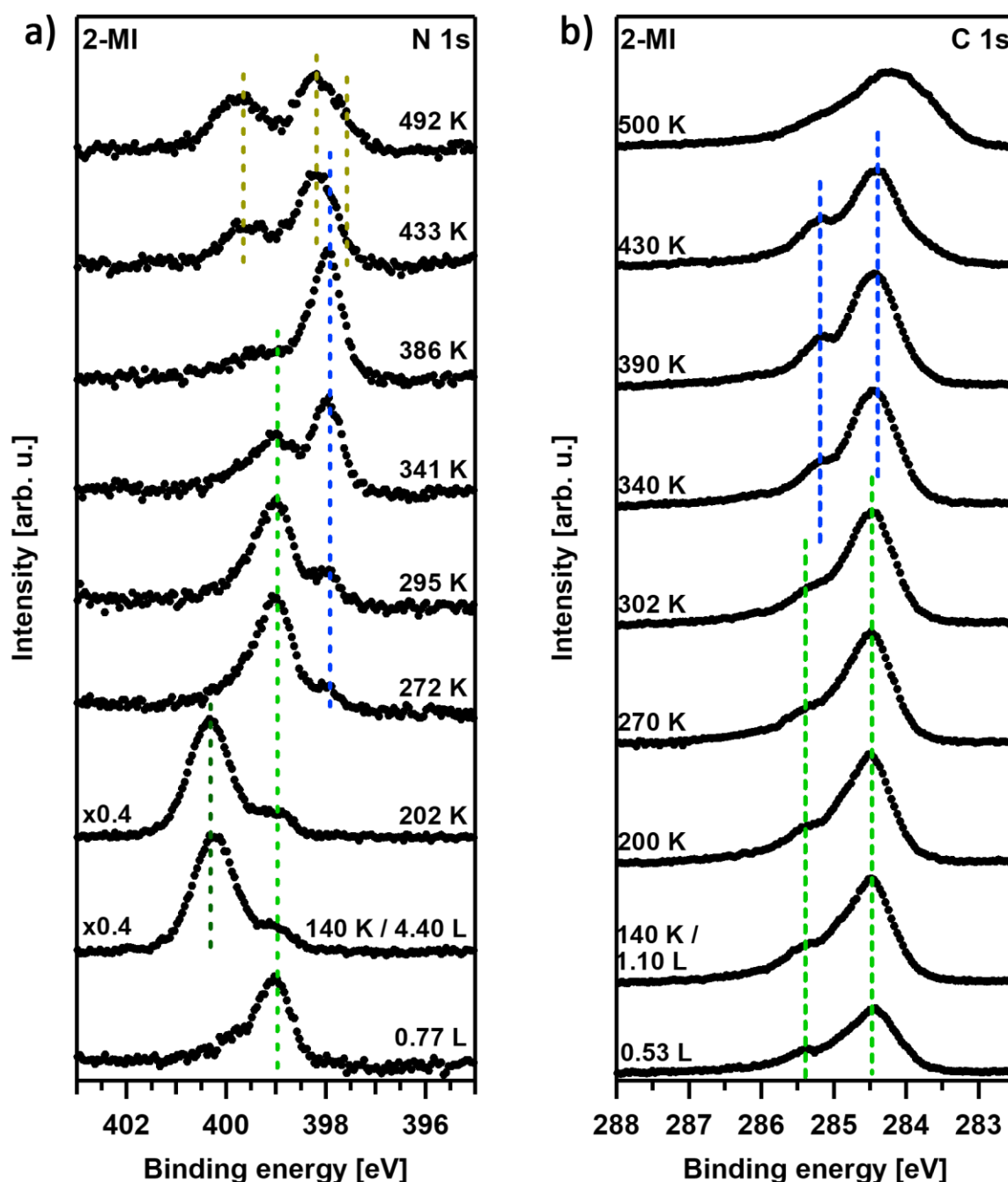


Figure 16: Selected N 1s (left, $h\nu=500$ eV) and C 1s (right, $h\nu=380$ eV) XP spectra of 2-methylindole on Pt(111). For the C 1s spectra, only the dominating features at the respective temperatures are highlighted. Green: 2-methylindole; dark green: 2-methylindol multilayer; blue: 2-methylindolide; ochre: decomposition.

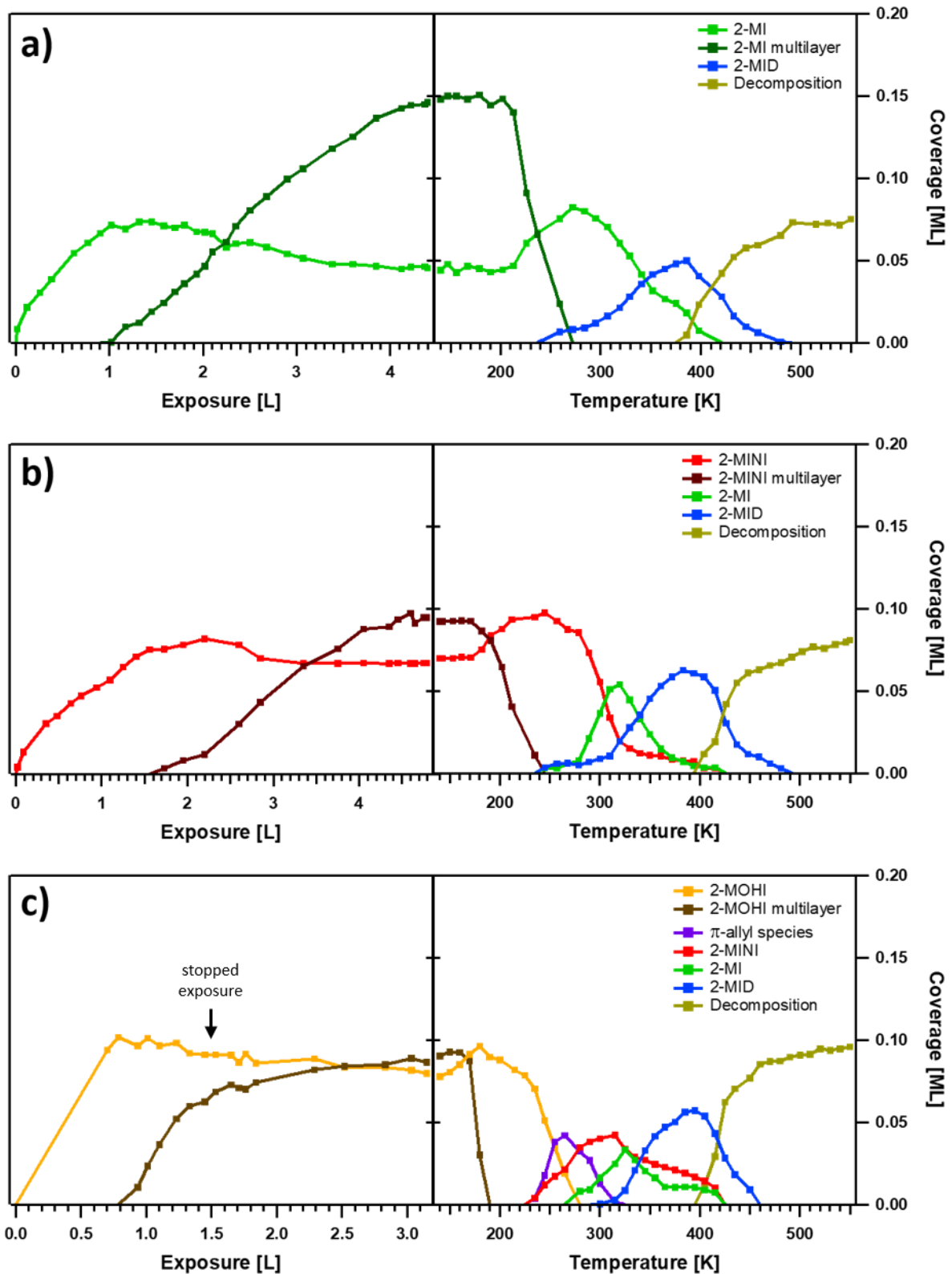


Figure 17: Quantitative analysis of the N 1s XPS experiments of 2-methylindole (a), 2-methylindoline (b) and 2-methyloctahydroindole (c) on Pt(111).

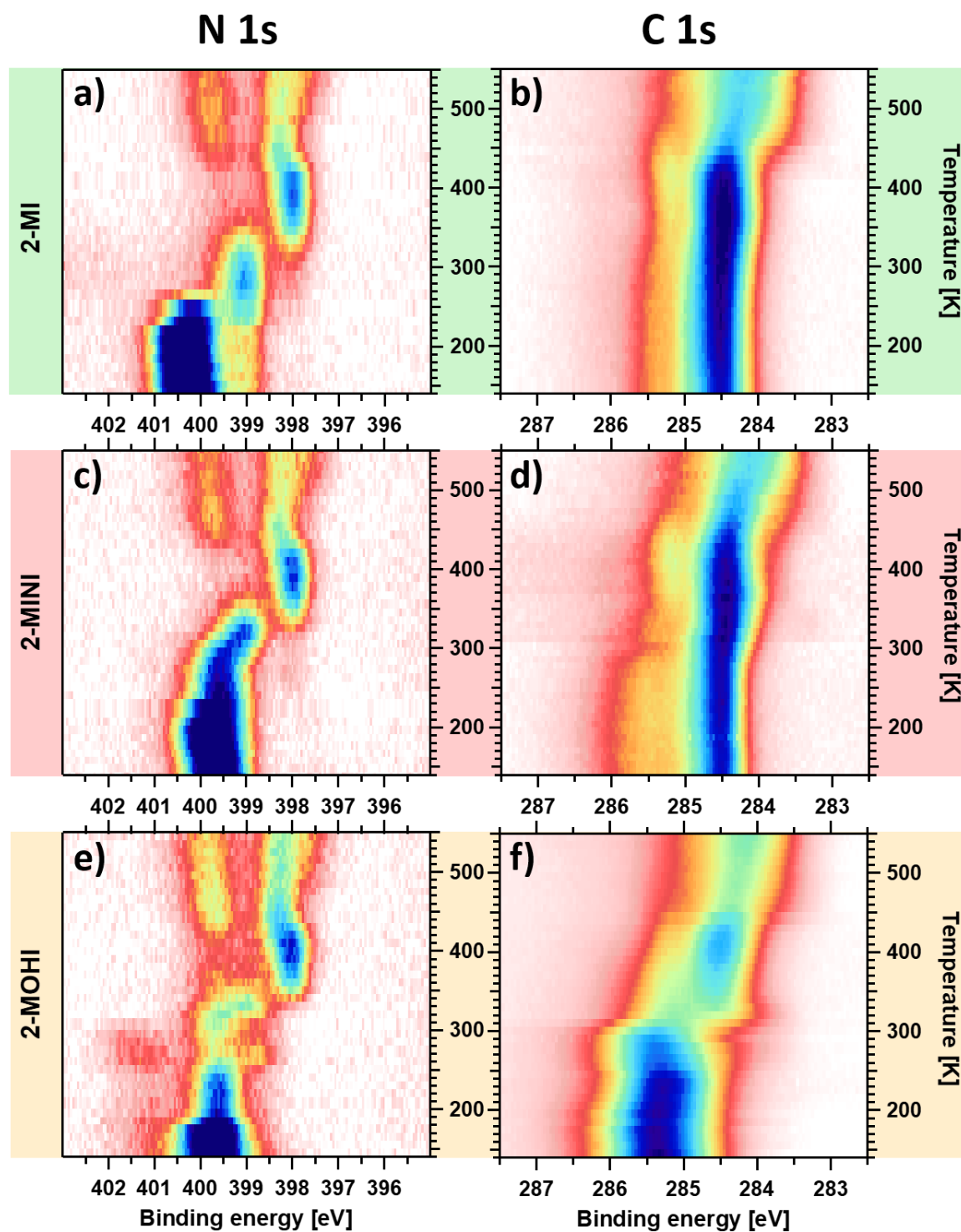


Figure 18: N 1s and C 1s density plots of the TPXPS experiments of 2-methylindole (a, b), 2-methylindoline (c, d) and 2-methyloctahydroindole (e, f).

In the N 1s region, the adsorption of 2-MI leads to the steady growth of one peak at 399.0 eV, which we assign to the aminic nitrogen^[80-82] of the molecularly adsorbed 2-MI. Above a coverage of 0.07 ML, an additional peak assigned to physisorbed multilayers is observed at 400.0 eV, and shifts to 400.3 eV at the end of the adsorption. The final coverage of the multilayer is ~0.15 ML; note that at this coverage the monolayer signal at 399.0 eV is dampened by 25% to ~0.05 ML.

The C 1s region shows a more complex and broad spectral fingerprint during adsorption, with a dominating peak at 284.4 eV accompanied by a shoulder at 284.9 eV, a smaller peak at 285.4 eV, and a very weak satellite at 286.0 eV, with no change in relative heights during adsorption. Due to the broad and unstructured nature of the spectrum, a straightforward assignment of the C 1s components to the nine carbon atoms is not possible. Nevertheless, when taking into account earlier data of indole on Pt(111)^[67-68], similarities are obvious and certain assumptions can be made: For the related molecules benzene or toluene, only one main peak is found at 284.5 eV, which is the same binding energy as observed for (non-methylated) indole, and very close to the value of 284.4 eV of the main 2-MI peak found here.^[23, 78, 99] Analogous to indole, the two carbon atoms in proximity to the electronegative nitrogen in 2-MI are expected to give signals at a higher binding energy, which would be in-line with the smaller peak at 285.4 eV. The remaining carbon atom in 3-position and the methyl carbon are also expected at slightly higher binding energy, in-line with the shoulder at 284.9 eV. These assignments are further supported by their expected intensity ratio of approximately 5:2:2 (for 284.4, 284.9 and 285.4 eV), which agrees with the integrated area of the fitted peaks (see Figure A 2 in Appendix A).

To study the reaction of 2-MI on the Pt(111) model catalyst, we subsequently performed TPXPS experiments. XP spectra were continuously recorded every ~10 K while the sample was heated from 140 to 550 K with a linear heating ramp of 0.5 K/s. In the N 1s region, up to 210 K no change is observed. Above this temperature, the multilayer signal starts to decline until it vanishes between 260 and 270 K, while the monolayer signal at 399 eV increases to 0.08 ML at 270 K, due to the reduced damping. The slightly larger monolayer coverage than observed at the onset of multilayer formation during adsorption (0.07 ML) indicates that the monolayer was not completed at this point. In the C 1s region, again no changes occur up to ~270 K, verifying that 2-MI is the only surface species. Above 270 K, the N 1s peak of 2-MI at 399.0 eV starts to decline, and vanishes at 420 K. Simultaneously, a new peak emerges at 398.0 eV, that

is, at 1.0 eV lower binding energy. This peak is attributed to the deprotonation of the aminic nitrogen in 2-MI, resulting in a 2-methylindolide (2-MID) surface species, bound to the surface via the nitrogen atom. This change in binding energy upon reaction was also observed in prior studies using indole and further N-heterocycles.^[67-68, 80-82]

In the C 1s region, the reaction from 2-MI to 2-MID leads to a small shift of all peaks to lower binding energies by 0.1 – 0.2 eV above 260 K, resulting in the new binding energies of 284.3, 284.7, 285.2 and 285.9 eV for 2-MID, and a subtle change in the overall spectral fingerprint (see Figure 16b and Figure 18b). 2-MID reaches its maximum coverage of 0.05 ML at 390 K (see Figure 17a) and then declines until 490 K. Also at 390 K, decomposition of the 2-MID species into unidentified carbon and nitrogen fragments starts. This is clearly visible by the formation of new peaks in the N 1s region at 397.6, 398.3 and 399.7 eV; the C 1s signal gets broader and more diffuse upon further heating. These fragments are not further discussed as the decomposition of the hydrogen-lean LOHC molecule is an unwanted reaction and needs to be avoided in a viable LOHC storage cycle.

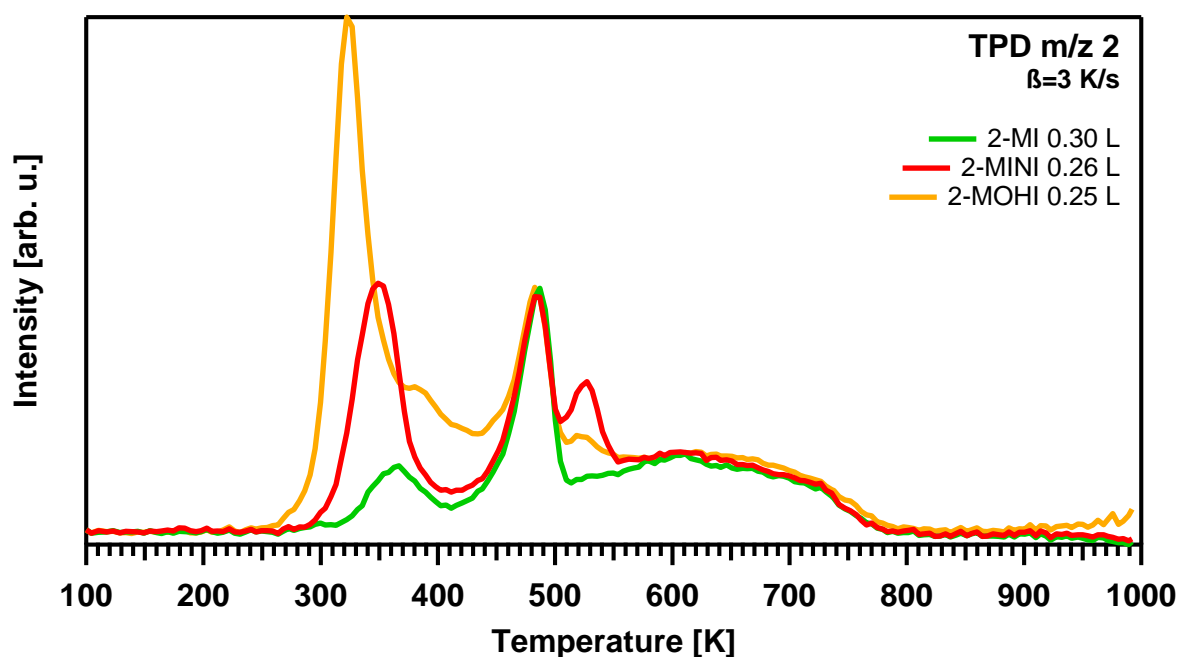


Figure 19: H₂ (m/z=2) TPD spectra of 2-methylindole, 2-methylindoline and 2-methyloctahydroindole on Pt(111), collected with a heating rate of 3 K/s.

The proposed deprotonation and decomposition of 2-MI is also confirmed by TPD measurements of H₂ (m/z=2) shown in Figure 19. We observe a pronounced peak with a rate maximum at 360 K, which corresponds to the loss of one hydrogen atom during the deprotonation at the nitrogen atom. The higher temperature of the rate maximum as

compared to the corresponding value of 340 K observed in the TPXPS experiment (temperature, where 50% of 2-MI is converted to 2-MID in Figure 19) is due to the higher heating rate of 3 K/s in TPD. The subsequent decomposition reaction is observed in TPD with a desorption maximum at 480 K for H₂. Above 800 K, no further H₂ desorption is observed.

In our experiments, we do not observe any evidence for the methyl-group to react or decompose before the general decomposition onset above 390 K. Upon demethylation, one would expect a change of the shoulder in the C 1s spectra at 284.9 eV, which we assigned to the bound methyl group; methyl on Pt(111) would be expected at ~282.5 eV, up to 280 K.^[47, 100] Additionally, we would expect the reaction and decomposition of the resulting indole or indolide species to be identical to the behavior observed in prior studies;^[67-68] however, the here observed behavior is different. Moreover, the integrated peak area in XPS is constant throughout the experiment, which indicates that there is no loss due to desorption of potentially formed methyl/methane. This is further supported by the absence of a corresponding signal ($m/z=15$) in the TPD measurements (Figure A 3 in Appendix A). There is also no evidence in the shown H₂ ($m/z=2$) TPD measurements for a dehydrogenation of the methyl group at temperatures below the general decomposition.

5.3.2 2-methylindoline (2-MINI)

Next, we investigate 2-methylindoline, which is obtained through hydrogenation of the 2-methylindole five-membered ring in 2 and 3-position (see Scheme 8). Although having only 1.5 wt% hydrogen storage capacity (2 hydrogen atoms per molecule), 2-MINI is not only interesting as possible LOHC intermediate in the 2-methyloctahydroindole dehydrogenation, but also due to its own capabilities as LOHC molecule, as demonstrated by some of us in a recent study using a homogeneous Ir-complex as dehydrogenation catalyst at comparably low temperatures.^[98] Furthermore, indoline/indole-based systems have been shown to exhibit favorable dehydrogenation characteristics using different catalysts.^[86, 101-102]

To study adsorption and reaction in detail, we measured N 1s and C 1s spectra during adsorption and reaction in the multilayer range (0.19 ML) and the monolayer range (0.04 ML), respectively, on Pt(111) at 140 K. Selected spectra collected during adsorption and subsequent TPXPS are shown in Figure 20a and b; the corresponding density plots are depicted in Figure 18c and d, and the quantitative analysis of the N 1s region in Figure 17b.

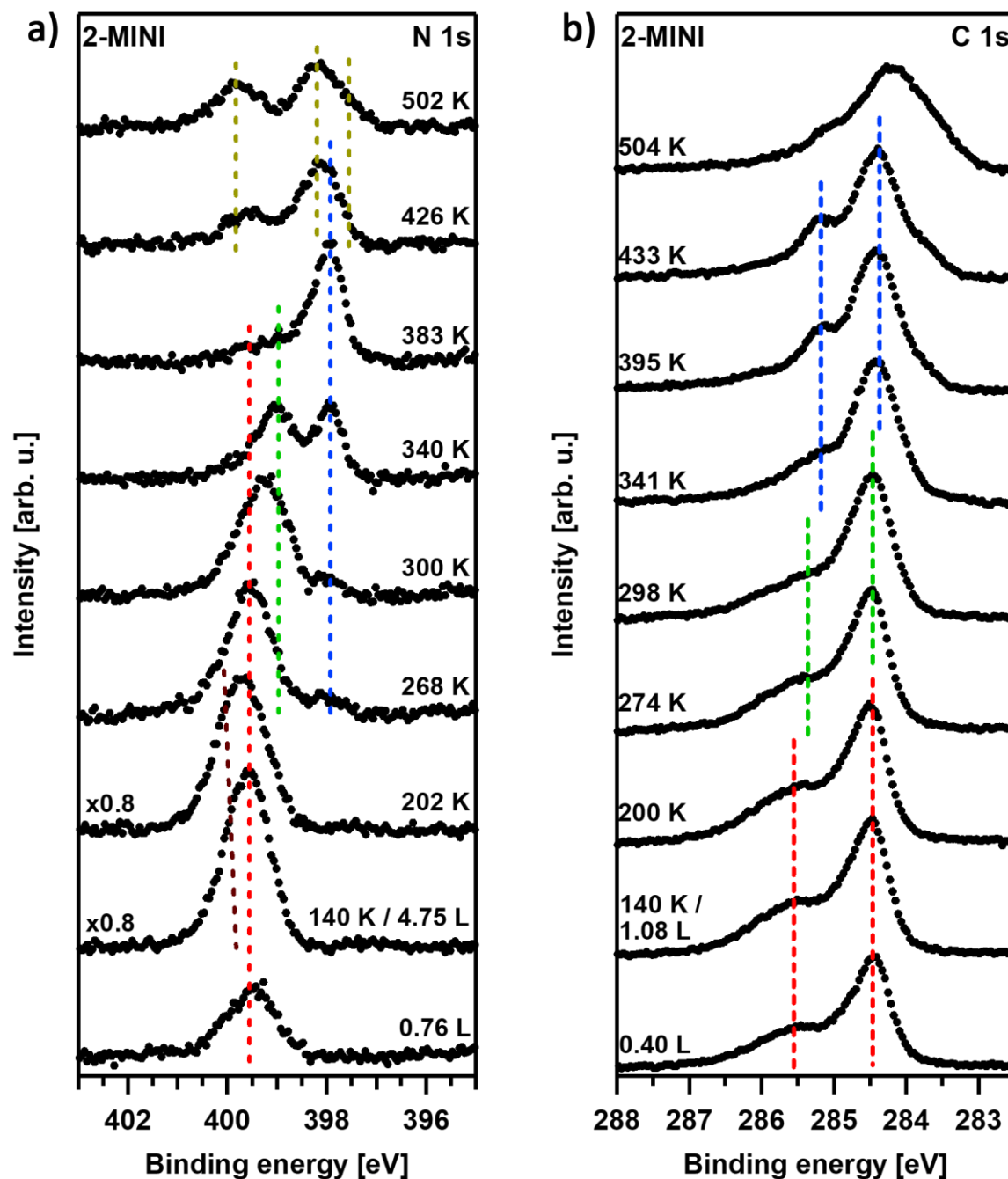


Figure 20: Selected N 1s (left, $h\nu=500$ eV) and C 1s (right, $h\nu=380$ eV) XP spectra of 2-methylindoline on Pt(111). For the C 1s spectra, only the dominating features at the respective temperatures are highlighted. Red: 2-methylindoline; dark red: 2-methylindoline multilayer; green: 2-methylindole; blue: 2-methylindoline; ochre: decomposition.

Adsorption of 2-MINI initially leads to one distinct N1s peak at 399.5 eV, which is assigned to the monolayer; its binding energy is 0.5 eV higher than observed for the monolayer of 2-MI. When the monolayer reaches a coverage of 0.08 ML, a second peak starts to rise at ~ 399.6 eV, very close to the monolayer signal. At the end of the adsorption experiment, the multilayer N 1s signal has shifted by 0.1 eV to 399.7 eV, and has reached a coverage of ~ 0.09 ML. Simultaneously, the monolayer N 1s signal is damped by 13%, from 0.08 ML to 0.07 ML. In the

C 1s region, we find again a main peak at 284.4 eV accompanied by a broad shoulder at 285.5 eV. With increasing coverage, both shift to higher binding energies by 0.1 eV, and are observed at 284.5 and 285.6 eV at the end of the adsorption experiment, at a final coverage of 0.04 ML. The overall spectral fingerprint of the 2-MINI C 1s region is similar to 2-MI. The main difference is that the shoulder at higher binding energy is broadened and shifted to 285.6 eV (see Figure 16b and Figure 20b).

Subsequently, we performed TPXPS experiments to study the thermal evolution of the adsorbed 2-methylindoline layer. In the N 1s region, multilayer desorption is observed from 170 to 240 K, which is ~40 K lower than for 2-MI (desorption onset at 210 K). The multilayer peak at 399.7 eV continually shifts towards 400.0 eV during heating. As consequence of the multilayer desorption, the monolayer signal at 399.5 eV rises due to the lower damping above 170 K, reaching ~0.10 ML at 250 K, which is ~0.02 ML higher than the value observed at the onset of multilayer formation during adsorption. Above 240 K, the 2-MINI signal in the N 1s region starts to decrease, while two new peaks at 399.0 and 398.0 eV rise. The peak at 399.0 eV is assigned to 2-MI and indicates dehydrogenation at the five-membered ring. The initially smaller peak at 398.0 eV indicates the virtually simultaneous deprotonation at the nitrogen atom, forming 2-MID, analogous to the already discussed 2-MI reaction (see above). The 2-MI peak at 399.0 eV reaches its maximum of ~0.05 ML at 320 K, before declining in favor of the 2-MID peak, which reaches its maximum of 0.06 ML above 370 K. Above 390 K, decomposition takes place as seen by the broadening of the peak structure. The remaining small 2-MINI and 2-MI signals vanish at 420 K, while 2-MID is gone at 500 K.

In the C 1s spectra of the 2-MINI submonolayer, no changes are seen up to ~250 K. Above this temperature, the observed changes support the results deduced from the N 1s spectra. With increasing temperature, the signal shape of 2-MINI (main peak/pronounced shoulder at 284.5/285.6 eV) steadily evolves towards the characteristic peak shape of 2-MI (main peak/weak shoulder at 284.4/285.4 eV) and 2-MID (main peak/small peak at 284.3/285.2 eV), similar to the already discussed 2-MI C 1s experiment (see Figure 16b or Figure 23 on page 66 for a comparison of selected spectra). Due to the complexity of the signal in this region, it is difficult to determine exact transition temperatures or fits, as the three different species 2-MINI, 2-MI and 2-MID occur never as single species on the surface. Similar to the N 1s region, the onset of the decomposition in the C 1s region is observed above 390 K, as the peaks start

to become broad. 2-MID vanishes until 500 K as indicated by the disappearance of the peak/shoulders above 285 eV.

The H₂-TPD spectrum of the adsorbed 2-MINI layer in Figure 19 reflects the dehydrogenation reaction observed in XPS. The first desorption maximum is found at 350 K. With the deprotonation at the nitrogen atom and the additional release of 2 hydrogen atoms at the five-membered ring, the integrated area of the 2-MINI peak is higher than for 2-MI by a factor of ~3; the maximum is found at 10 K lower temperature. Analogous to 2-MI, the decomposition of 2-MID into fragments is reflected by the desorption at 480 K and above.

5.3.3 2-methyloctahydroindole (2-MOHI)

Finally, we examined the adsorption and thermal evolution of the fully hydrogenated 2-methyloctahydroindole. With a significantly higher storage capacity of 5.7 wt% H₂, 2-MOHI is a highly attractive LOHC molecule.

We adsorbed MOHI on the Pt(111) at 140 K in the multilayer (0.19 ML) and monolayer range (0.10 ML), and subsequently heated the adsorbed layers, while performing XPS in the N 1s and C 1s regions, respectively. In Figure 21a and b, selected spectra of the adsorption and heating experiments are shown; the corresponding density plots are depicted in Figure 18e and f, and the quantitative analysis of the N 1s region in Figure 17c. After the end of the 2-MOHI exposure to Pt(111), which is indicated by an arrow in Figure 17c, the surface coverage continued to increase slowly, which is due to post adsorption of MOHI, because the pumping speed of the system for this molecule is very low.

In the N 1s region, three peaks are observed at low exposure. The dominating peak at 399.6 eV is assigned to molecularly adsorbed 2-MOHI. The peak at 401.0 eV is attributed to a protonation of the NH group, which results from the interaction with minor amounts of water. An analogous behavior was proposed for the previously investigated unsubstituted octahydroindole,^[67] and is in-line with reports of other N-heterocyclic compounds at low pH.^[87-88] For the sake of clarity, the intensity of these monolayer peaks at 399.6 and 401.0 eV are combined in Figure 17c. The third peak at 398.6 eV is comparably small and is most likely caused by impurities in the 2-MOHI sample, such as already decomposed or dehydrogenated

2-MOHI according to its similar binding energy to 2-MI; therefore, this minor contribution will not be further discussed.

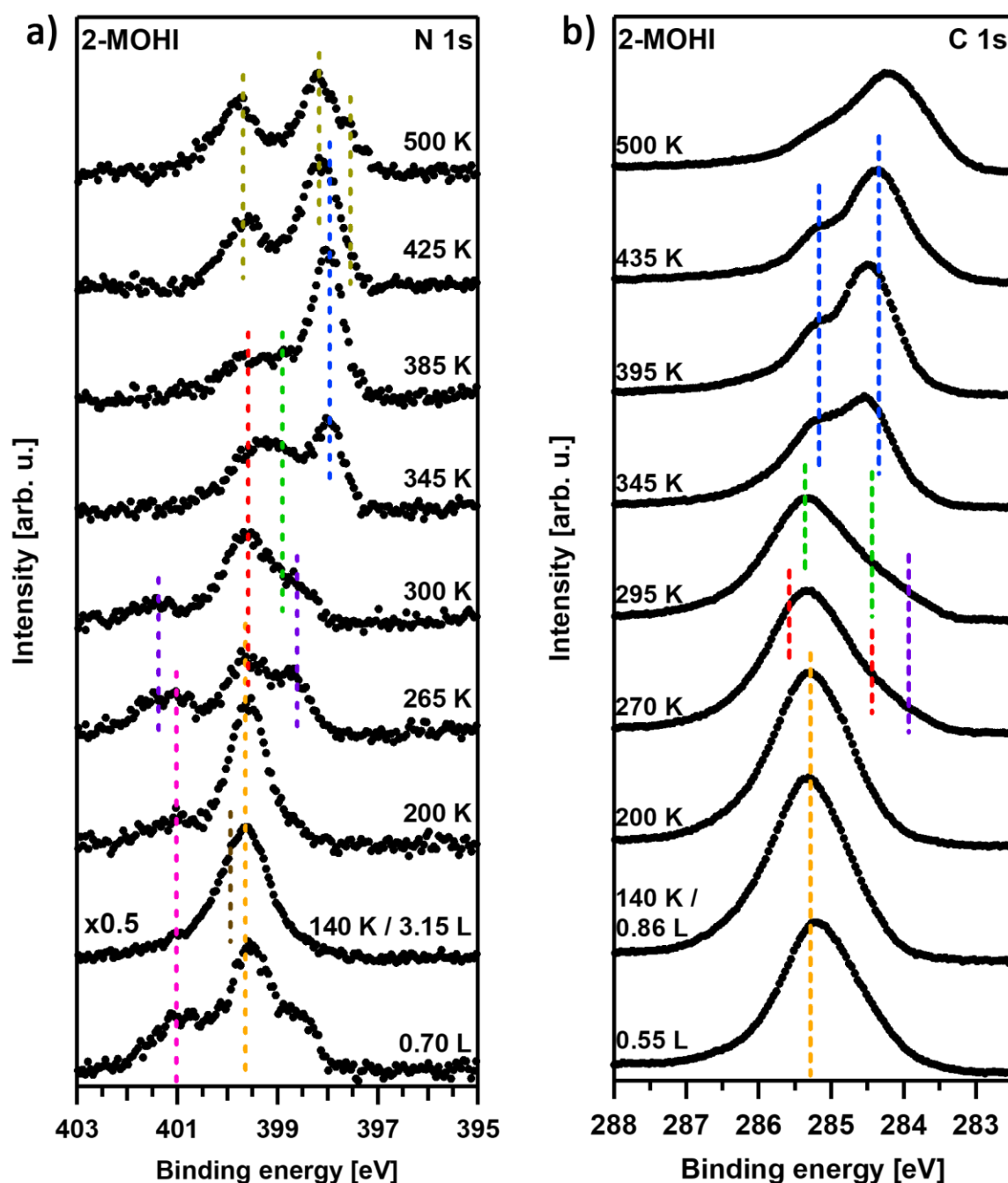


Figure 21: Selected N 1s (left, $h\nu=500$ eV) and C 1s (right, $h\nu=380$ eV) XP spectra of 2-methylindoline on Pt(111). For the C 1s spectra, only the dominating features at the respective temperatures are highlighted. Orange: 2-methyloctahydroindole; magenta: 2-methyloctahydroindole (+H₂O); brown: 2-methyloctahydroindole multilayer; purple: π -allyl species; red: 2-methylindoline; green: 2-methylindole; blue: 2-methylindoline; ochre: decomposition.

After saturation of the monolayer at 0.10 ML, an additional signal is observed at 399.9 eV, due to multilayer adsorption. With increasing multilayer coverage, the monolayer signals at 399.6 and 401 eV get damped. In the C 1s region, adsorption of 2-MOHI leads to one initial broad

peak at 284.8 eV at the beginning of the adsorption (data not shown), shifting to 285.3 eV. The overall peak shape is quite different to that of 2-MI or 2-MINI. This behavior is attributed to the fact that saturated hydrocarbons usually possess a weaker and less specific interaction with the surface, which leads to less defined adsorption sites and surface orientations, in turn resulting in the broad peak shape seen for 2-MOHI.

The thermal evolution of the hydrogen-rich 2-MOHI is again investigated by TPXPS. In the N 1s region, rapid multilayer desorption is observed from 160 to 190 K. Thereby, the multilayer peak slightly shifts from 399.9 to 399.8 eV. Simultaneously, the damping of the monolayer signals at 399.6 and 401.0 eV gets reversed, causing a rise from 0.08 to 0.10 ML at 200 K. Between 200 and 230 K, the monolayer of 2-MOHI signals slowly decreases to 0.08 ML, due to further desorption. Above 230 K, the decline of the monolayer signals accelerates, until both vanish at 270 K. Simultaneously, new peaks emerge at 401.3, 399.6 and 398.6 eV. We attribute the peaks at 401.3 and 398.6 eV to two different π -allyl intermediate species, being partially dehydrogenated at the six-membered ring. The peak at 399.6 eV is assigned to 2-MINI (compare to the value of 399.5 eV in the 2-MINI experiment; see also Table 3 on page 65 for a comparison of binding energies of single species across all experiments). This assignment indicates that dehydrogenation first takes place at the six-membered ring, which is also supported by the observed formation of π -allyl intermediates.

Such π -allylic species have previously been reported also for other cyclic compounds.^[78, 90-91] The occurrence of such intermediate species in the thermal evolution of 2-MOHI, in contrast to the 2-MINI experiment, is attributed to the stronger π -interactions of 2-MINI with the Pt(111) surface. One could speculate that the N 1s binding energy increases with the distance of the nitrogen atom to the surface. This concurs e.g. with our observation that for a higher degree of hydrogenation, which leads to an increased surface distance in the monolayers, a higher binding energy is observed (2-MOHI: 399.6 eV; 2-MINI: 399.5 eV, 2-MI: 399.0 eV; and in all cases we find higher binding energies for the multilayers); a similar behavior is observed for other molecules.^[84, 103-105] Thus, we propose that the two π -allyls possess either a down-tilted (401.3 eV) or up-tilted (398.6 eV) methyl-group with regard to the sample surface, which could explain the large binding energy difference of both peaks to each other and to the 2-MOHI/2-MINI signals. In Figure 17c, both π -allyls are combined for clarity and reach a maximum coverage of 0.04 ML at ~270 K, before vanishing above 300 K (see also discussion of C 1s region below). The minor difference of the N 1s values of 2-MINI (399.6 eV here vs

399.5 eV for the pure 2-MINI adsorption – see above) might be due to the formation of the π -allyls or minor byproducts. The 2-MINI intermediate reaches its maximum of 0.04 ML at \sim 300 K. Meanwhile, two new peaks at 398.9 and 398.0 eV show up above 270 and 300 K, respectively. The first peak is attributed to the further dehydrogenated 2-MI intermediate, with its binding energy also being slightly lower (by 0.1 eV) than the value of 399.0 eV observed for the pure 2-MI adsorption. The second peak at 398.0 eV is again attributed to 2-MID, with the deprotonated nitrogen atom, as seen for the 2-MI and 2-MINI TPXPS experiments. 2-MI reaches its maximum of 0.03 ML at \sim 330 K, before declining until \sim 420 K. 2-MID is present up to 460 K, with its maximum coverage of 0.06 ML at \sim 390 K. At this temperature, the onset of decomposition into fragments is observed, as indicated by the rise of three new peaks, which are not further discussed as the focus lies on the selective dehydrogenation reaction of the LOHC molecule.

In the C 1s region, no changes are observed up to 200 K (Figure 21b). In contrast to the N 1s region, with clearly separated peaks and large shifts, the changes in the C 1s region above 200 K are initially rather subtle. From 200 to 230 K, the broad peak at 285.3 eV is shifted very slightly to 285.2 eV, without changes in the shape or height. Between 230 and 270 K, a shoulder develops at \sim 284.0 eV, while the main peak shifts from 285.2 to 285.4 eV. The shoulder at 284.0 eV is characteristic for the π -allyl formation and similar to what has been observed for unsubstituted octahydroindole, or methylcyclohexane and dicyclohexylmethane.^[67, 78] Referring to the prior discussed observations in the N 1s region, the overall change represents the reaction and dehydrogenation of 2-MOHI to 2-MINI and π -allylic intermediates. Above 270 K, major changes are observed in the C 1s region. The broad peak at 285.4 eV strongly decreases up to 300 K and is replaced by a new double peak structure with maxima at \sim 284.6 and \sim 285.1 eV. This change is attributed to the further dehydrogenation, and thus formation of 2-MI and 2-MID. Increasing the temperature up to 390 K, the overall signal shifts to slightly lower binding energies and becomes very similar to the peak shape of 2-MID in the 2-MI and 2-MINI TPXPS experiments; here, the main peak is found at 284.3 eV and a small peak at 285.2 eV. The somewhat higher intensity of the peak at 285.2 eV can most likely be explained by the coexistence of other species, like 2-MINI and 2-MI, still being present on the surface (see N 1s region, Figure 17c). Above 390 K, the peak ratio and positions continue to become even more similar to the known pure 2-MID structure,

and finally and the overall signal structure becomes indistinct due to the onset of the decomposition.

Our H₂-TPD results shown in Figure 19 agree with the conclusions derived from XPS; they indicate the loss of 9 hydrogen atoms up to ~450 K. Thereby, we observe a main desorption peak at 320 K with a shoulder at 360 - 380 K. In comparison to the 2-MI and 2-MINI TPD results, the much larger peak at 320 K is attributed to the dehydrogenation of 2-MOHI to the π -allylic species and to 2-MINI, while the shoulder matches the further dehydrogenation and deprotonation to 2-MID. Analogous to the 2-MI and 2-MINI TPD spectra, decomposition and fragmentation of 2-MID is represented by desorption peaks at 480 K and above. In agreement to the XPS results, the stepwise dehydrogenation in TPD emphasizes that dehydrogenation first takes place at the six-membered ring, followed by the dehydrogenation of the five-membered ring. This behavior is interesting, since for the larger H₁₂-N-ethylcarbazole, dehydrogenation first takes place at the activated five-membered ring on Pt(111).^[23, 25-26]

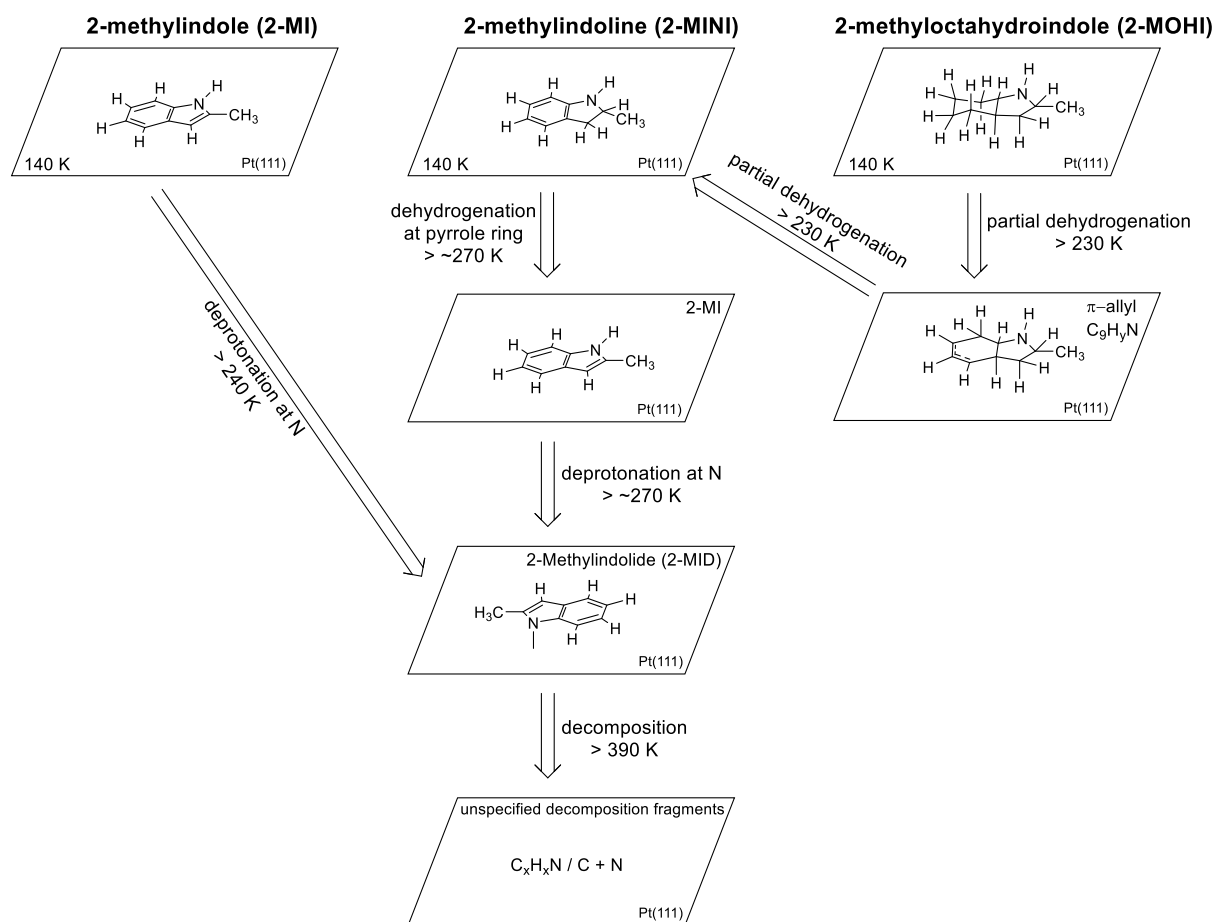
5.3.4 Comparison of the 2-methyl substituted and the unsubstituted, indole-based LOHC system

In the following, we will give a short comparison of the here discussed 2-methyl substituted to the unsubstituted indole-based LOHC system which is discussed in Chapter 4.^[67-68] Overall, the dehydrogenation reactions of both systems are very similar:

Both octahydroindole and indoline dehydrogenate into an indole intermediate above 270 K, which decomposes at ~430 K for octahydroindole and ~390 K for indoline. Simultaneously, above 270 K (320 K for octahydroindole) deprotonation of the NH-group starts, forming an indolide surface species, which starts to decompose above ~460 K and finally vanishes at ~540 K. Moreover, for octahydroindole, partial protonation of the NH-group is seen in presence of OH- traces, and a π -allylic minority species is found in the temperature range of 170 to 450 K during octahydroindole dehydrogenation.^[67-68] A more detailed discussion is given in Chapter 4: Indole, Indoline and Octahydroindole on Pt(111).

For the 2-methyl substituted system, all 2-MI, 2-MINI and 2-MOHI show deprotonation of the NH-group, starting at 240-260 K for 2-MI and 2-MINI, and ~320 K for 2-MOHI. For 2-MINI and 2-MOHI in parallel to deprotonation also dehydrogenation to 2-MI intermediates occurs,

resulting in a 2-MID species above 300 K; for 2-MOHI also 2-MINI is observed as intermediate, along with two different π -allyl intermediates above 250 K, with an either up or down tilted methyl group. Decomposition of 2-MID starts above 390 K, with 2-MI and 2-MINI being observed up to 420 K and 2-MID up to \sim 490 K. A summary of the single reaction steps, selected spectra and binding energies of the 2-methyl substituted LOHC system are given in Scheme 9, Figure 17, Figure 23 and Table 3 on the following pages.



Scheme 9: Reaction pathways of 2-MI, 2-MINI and 2-MOHI on Pt(111).

Analogous to octahydroindole, partial protonation of the NH-group is observed. Notably, we did not find indications of a demethylation reaction before decomposition. In addition to the similar reaction pathways, the overall N 1s and C 1s peak shape and positions as well as the observed shifts are very similar in both LOHC systems.^[67]

While both systems follow the same overall dehydrogenation and decomposition route with (2-methyl)indole and (2-methyl)indolide intermediates, we also observe several distinct differences between the substituted and the pure indole system, which are caused by introduction of the methyl-group in 2-position. First, the onset of the decomposition is seen \sim 70 K earlier for the 2-methyl substituted system (\sim 390 vs \sim 460 K), indicating a lower thermal

stability than the unsubstituted system. Furthermore, in contrast to indoline and octahydroindole, the dehydrogenation of 2-MINI and 2-MOHI to 2-MI or 2-MID is not entirely completed at the onset of decomposition. 2-MINI and 2-MOHI are in small amounts observed up to ~420 K (see Figure 17, Figure 22 and Figure 23), limiting the capabilities of the 2-methyl substituted LOHC system under the given experimental conditions. However, partial dehydrogenation of 2-MOHI to 2-MINI might represent a good LOHC system by avoiding the unwanted reaction to 2-MID and decomposition. Second, we observe a 2-MINI intermediate in the 2-MOHI dehydrogenation while in the octahydroindole dehydrogenation no indoline intermediate was observed. This indicates that the dehydrogenation of 2-MOHI starts at the six-membered ring first. Also, while the decline of both 2-MINI and indoline starts at ~270 K, smaller amounts of 2-MINI are observed up to ~70 K higher than indoline (~420 K vs ~350 K), suggesting a stabilizing effect of the methyl-group in the hydrogenated 5-membered ring of 2-MINI, possibly due to electronic and steric reasons. Third, we propose two different π -allylic intermediates (up/down tilted methyl group) during 2-MOHI dehydrogenation. In the case of octahydroindole, only one π -allylic species is observed due to the missing methyl group. Interestingly we observe strong shifts of the N 1s signals for the π -allyl intermediates of 2-MOHI in comparison to octahydroindole, which might be due to differences in the N-Pt bond distance.

Finally, the investigated 2-methyl substituted LOHC system (as well as the pure indole LOHC system) also shows similarities to the previously investigated and well established H₁₂-N-ethylcarbazole/N-ethylcarbazole system.^[22-26] The dehydrogenation above 200 K and dealkylation above 390 K of H₁₂-N-ethylcarbazole with the following decomposition above 450 K can be seen analogous to the main reaction pathway observed for 2-MOHI/2-MINI. However, for H₁₂-N-ethylcarbazole no π -allylic intermediates are found and its dehydrogenation sequence (first five-membered, then six-membered ring) is different (see discussion of 2-MOHI above).

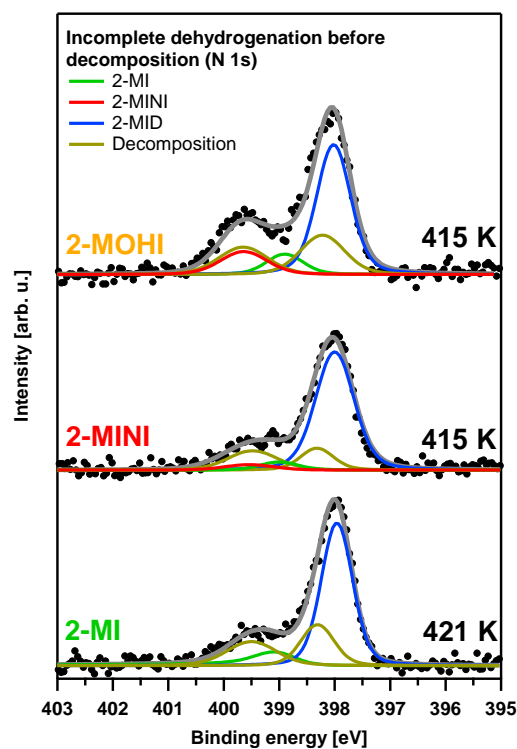


Figure 22: Comparison of the N 1s regions of 2-methylindole (2-MI), 2-methylindoline (2-MINI), and 2-methyloctahydroindole (2-MOHI) at ~415 K. The fitted peaks of the single species show slightly incomplete dehydrogenation of the molecules at the onset of the decomposition. Red: 2-MINI; green: 2-MI; blue: 2-methylindolide (2-MID); ocher: Decomposition fragments.

Species	2-MI Binding energy (multilayer) [eV]	2-MINI Binding energy (multilayer) [eV]	2-MOHI Binding energy (multilayer) [eV]
2-MI	399.0 (400.0 – 400.3)	399.0	389.9
2-MINI	-	399.5 (399.6 – 400.0)	399.6
2-MOHI	-	-	399.6 + 401.0 (399.8 – 399.9)
2-MID	398.0	398.0	398.0
allyl	-	-	398.6 + 401.3

Table 3: Binding energies of the observed species within the 2-MI, 2-MINI and 2-MOHI N 1s experiments.

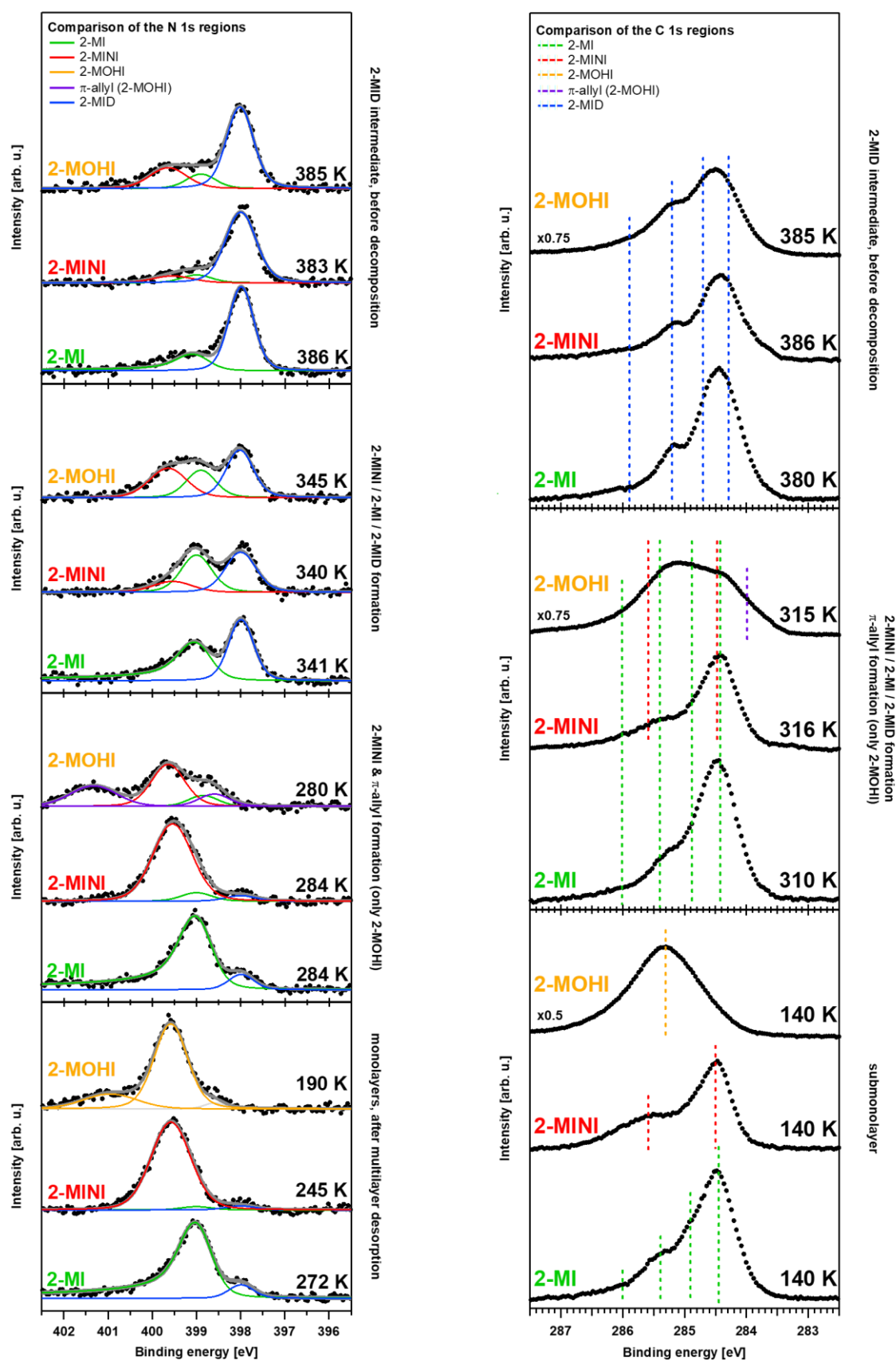


Figure 23: Comparison of the N 1s and C 1s regions of 2-methylindole (2-MI), 2-methylindoline (2-MINI), and 2-methyloctahydroindole (2-MOHI) at selected temperatures, depicting important reaction steps and intermediates. Additionally, the N 1s spectra include fitted peaks of the single species. In the C 1s region, the visible peaks of the main species at the specified temperature are marked by lines. Orange: 2-MOHI; red: 2-MINI; green: 2-MI; purple: π -allyl (2-MOHI); blue: 2-methylindoline (2-MID).

5.4 Conclusion

We performed a combined high resolution XPS and TPD study of the surface reactions of the LOHC system 2-methylindole/2-methylindoline/2-methyloctahydroindole on Pt(111). For the hydrogen-lean 2-methylindole, starting above 240 K we first observe deprotonation of the NH-group, resulting in 2-methylindolide, which then declines with the onset of the decomposition at 390 K until it vanishes at 490 K. The partially hydrogenated 2-methylindoline starts to dehydrogenate into 2-methylindole at 240 K, and otherwise shares the same reaction path as 2-methylindole. For the hydrogen-rich 2-methyloctahydroindole a more complex reaction is seen: First, it partly dehydrogenates at the six membered-ring to form two different π -allylic intermediate species before forming 2-methylindoline. Thereafter, it continues the same stepwise dehydrogenation to 2-methylindole and the deprotonation of the NH-group to form 2-methylindolide, before it finally decomposes into fragments. The NH deprotonation is an unwanted reaction that needs to be avoided in real catalytic conditions in order to form an efficient hydrogen storage cycle.

Overall, the system behaves very similar to the unsubstituted indole LOHC system, although there are some noteworthy differences: The onset of decomposition is observed ~ 70 K earlier for the 2-methyl substituted system than for the unsubstituted indole system, making the substituted system thermally less stable. Furthermore, dehydrogenation of the hydrogen-rich molecules is not yet complete at the onset of decomposition. Also, 2-methylindoline is observed up to ~ 70 K higher than indoline during dehydrogenation. The TPXPS of 2-methyloctahydroindole reveals three stable dehydrogenation intermediates, that is, two different π -allylic species and a 2-methylindoline intermediate, which are not observed for octahydroindole. Because of this, we can clearly distinguish that the six-membered ring in 2-methyloctahydroindole is dehydrogenated first, followed by the five-membered ring; the latter corresponds to the dehydrogenation of 2-methylindoline.

To summarize, the 2-methyl substituted LOHC system seems to be less stable than the pure indole system on Pt(111) in terms of the temperature range and thus applicability. Still, the substitution shows a strong influence on the stability of reaction intermediates. Taking this into account, 2-MOHI and 2-MINI might represent a good LOHC pair, avoiding the unwanted reaction to 2-MID and decomposition, by only partial de/rehydrogenation. This knowledge

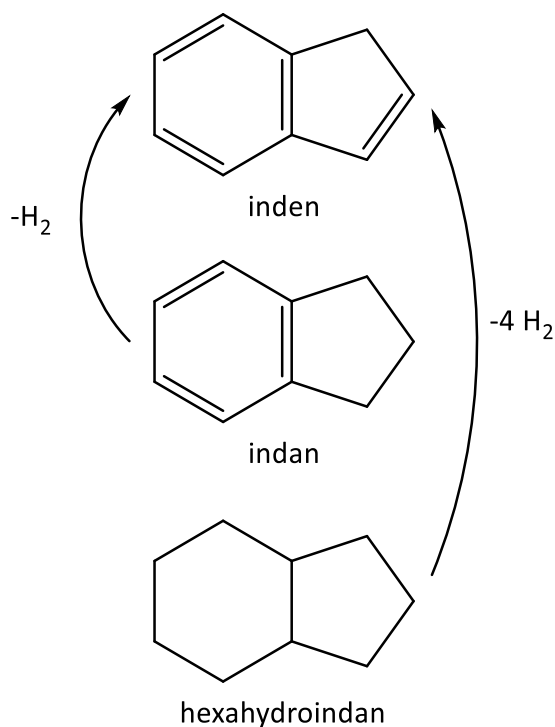
combined with further studies on similar systems can be used to specifically tailor more suitable LOHC systems in the future.

6. Indene, Indan and Hexahydroindan on Pt(111)

6.1 Introduction

In the past, mainly homocyclic molecules containing six-membered rings or N-heterocycles have been investigated regarding their capabilities as LOHC systems. Especially N-ethylcarbazole and derivatives^[17, 21-29] as well as (substituted) indoles^[67-68, 72-74, 93] (see Chapter 4 and Chapter 5) are promising and thoroughly investigated N-heterocycles, showing preferential dehydrogenation behavior at low temperatures due to the influence of the heteroatom. But also homocycles have been shown to exhibit excellent dehydrogenation characteristics. Here, isomeric dibenzyltoluenes gained high attention as hydrogen carrier in the last years, being widely available and showing very favorable dehydrogenation characteristics.^[30-36]

Based on previous research, indene, indan and hexahydroindan (see Scheme 10) gained our attention as possible LOHC system. Indene is basically the homocyclic analog to indole and the hydrogen-rich form hexahydroindan has, in terms of LOHC systems, a very high storage capacity of 6.5 wt% hydrogen. Furthermore, all three molecules are already liquid at room temperature, simplifying the applicability of the system.



Scheme 10: The indene/indan/hexahydroindan-based LOHC system.

In this chapter, a detailed quantitative *in-situ* study of indene, indan and hexahydroindan on a Pt(111) single-crystal surface as model catalyst is presented in order to address their thermally induced dehydrogenation mechanisms on the molecular scale. In terms of a LOHC system, indene represents the hydrogen-lean carrier molecule, while hexahydroindan is the hydrogen-rich counterpart. Indan is a possible intermediate in the dehydrogenation reaction of hexahydroindan to indene, and itself can be also considered as a hydrogen storage compound (see Scheme 10), which could also form the LOHC (sub)systems indene/indan or indan/octahydroindole.

Using high-resolution XPS and TPD, we follow the dehydrogenation and decomposition of the single molecules on Pt(111) in UHV. Consecutively, we identify individual reaction steps and surface species; this includes the dehydrogenation of hexahydroindan, indan and indene, ultimately forming an indenyl surface species, which then decomposes at higher temperatures. Moreover, for hexahydroindan, an unspecified H_x -indan intermediate is observed.

6.2 Specific experimental setup

The XPS experiments were performed at the synchrotron BESSY II at beamline UE56-2 PGM 2 using the synchrotron UHV machine (see Chapter 3.1). TPD experiments were performed in a separate TPD UHV machine (see Chapter 3.2).

The adsorption of indene/indan/hexahydroindan on Pt(111) was conducted using the vapor pressure of the substances. The heating rate was set to 0.5 K/s during TPXPS up to 550 K, above this temperature, the sample was heated resistively in steps of 25-50 K. For TPD a heating rate of 3 K/s was used. All TPD spectra were background-corrected with a spectrum of the clean Pt crystal to account for the desorption of small amounts of hydrogen adsorbed from the background pressure. Due to different coverages, the spectra are normalized to the peak at 580 K.

Adsorbate coverages on Pt(111) were calibrated by comparison to the well-known saturation coverage of carbon monoxide at 200 K, which leads to a $c(4 \times 2)$ LEED pattern and amounts to 0.5 carbon monolayers (1 carbon monolayer = 1 carbon atom / Pt atom).^[52, 75-76] Peak fitting of the C 1s spectra was done using Doniach-Šunjić-profiles^[53] convoluted with a Gaussian

function. The C 1s region was measured at 380 eV with a resolution of 150 meV at an emission angle of 0° relative to the surface normal. Prior to each spectrum, the sample position is shifted to avoid beam damage. All spectra are referenced to the Fermi edge of Pt(111).

6.3 Results and discussion

6.3.1 Indene

First, we address indene as the hydrogen-lean carrier molecule of the LOHC system (see Scheme 10). As indene is the desired dehydrogenation product of the hydrogen-rich indan or hexahydroindan, it is crucial to understand the surface chemistry and the spectral fingerprint of indene. Furthermore, the stability of indene on the Pt(111) model catalyst limits the overall stability of the proposed LOHC system.

The C 1s region was measured during exposure of indene to Pt(111) at 110 K and subsequent heating. Selected XP spectra including fits during the reaction of 0.24 C-ML indene are shown in Figure 24 at the top with density plots, containing all recorded spectra of the adsorption and reaction, below. The corresponding quantitative analysis is shown in Figure 25. Note, that the fitted envelopes presented in Figure 24 are used as a quantitative measure of the chemical species only and thus have no direct physical origin. The discussed binding energies below always refer to the peak positions of the fitted envelopes.

The adsorption of 0.54 L indene leads to the steady growth of a main peak at 284.4 eV accompanied by a smaller shoulder at 284.1 eV (both green in Figure 24) , reaching a submonolayer coverage of 0.24 C-ML at the end of the adsorption (see Figure 25). Both signals are assigned to the molecular adsorption of indene on Pt(111).

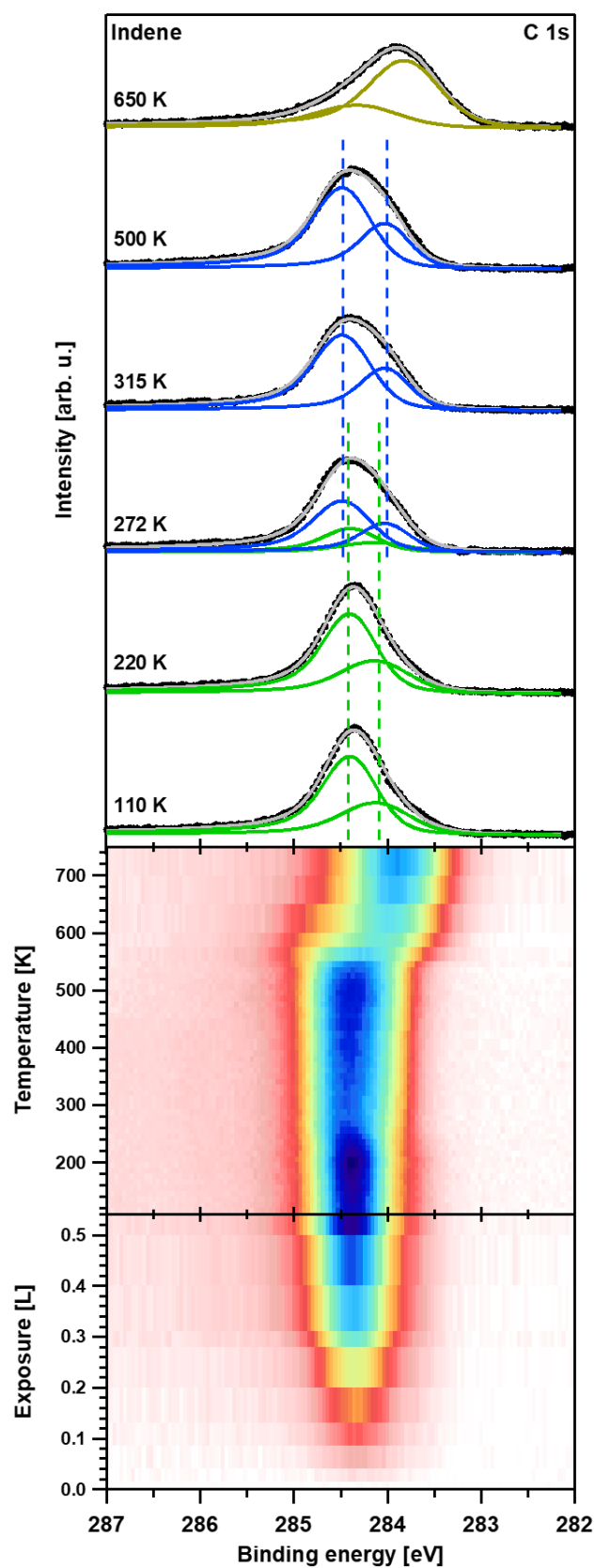


Figure 24: Selected C 1s XP spectra including fits (top) and density plots (bottom) of indene on Pt(111). Green: indene; blue: indenyl; other: decomposition.

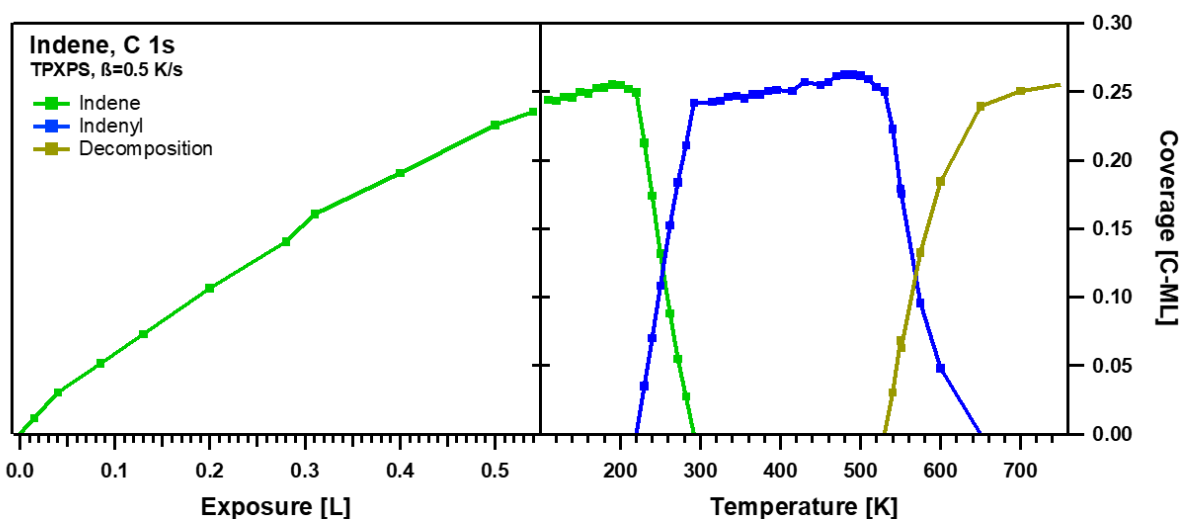


Figure 25: Quantitative analysis of the C 1s XPS experiments of indene on Pt(111) shown in Figure 24.

Consecutively, to study the temperature-induced reaction of indene, a TPXPS experiment was performed. Upon heating, no changes occur up to 220 K while the coverage increases very slightly to ~ 0.25 C-ML, possibly due to a minor coverage gradient on the crystal, which is observed by shifting the sample after each spectrum to avoid beam damage. Above ~ 220 K, the overall signal shape starts to broaden. This is reflected by the development of two new peaks at 284.4 and 284.0 eV (both blue in Figure 24), reaching ~ 0.25 C-ML at 300 K. These peaks are assigned to the abstraction of one hydrogen at the CH_2 -group in the five-membered ring of indene, forming an indenyl surface species (also see discussion of the $m/z=2$ TPD data below). The original indene peaks decline up to 300 K. Above 300 K, the indenyl signals remain virtually unchanged up to ~ 530 K. Above this temperature, decomposition into unspecified fragments takes place, with the indenyl signals declining until ~ 650 K. The spectral fingerprint further broadens and shifts to lower binding energies, with two new peaks emerging at 283.8 and 284.3 eV, which will not be further discussed as the decomposition of the hydrogen-lean LOHC molecule is an unwanted reaction and needs to be avoided in order to maintain a viable LOHC storage cycle.

The proposed dehydrogenation of the CH_2 -group at the five-membered ring of indene, forming indenyl, is also confirmed by TPD measurements of H_2 ($m/z=2$), shown in Figure 26. A first small peak with a desorption maximum at ~ 300 K, corresponding to the loss of one hydrogen atom, indicates the formation of the indenyl surface species. The observed temperature in TPD is ~ 50 K higher than the inflection point in TPXPS (250 K, where 50% of indene has reacted to indenyl), which is due to the desorption of H_2 on Pt(111) only taking

place above ~ 300 K for smaller coverages.^[106] The subsequent decomposition reaction is observed with a desorption maximum at 580 K. Above 800 K, no further H_2 desorption is observed.

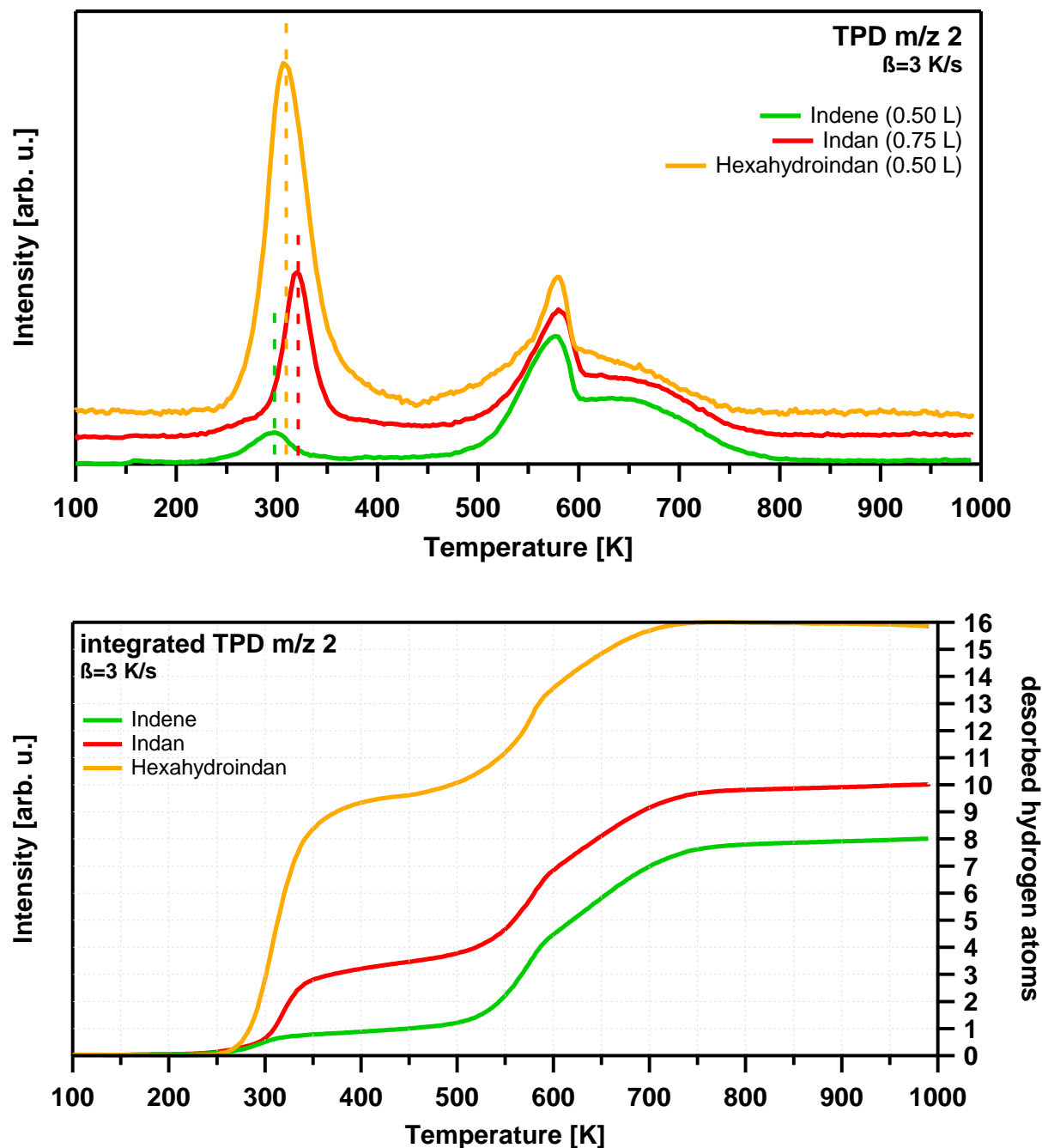


Figure 26: TPD of $m/z=2$ (H_2) of indene, indan and hexahydroindan on Pt(111) (top) with their integrated areas representing the amount of desorbed hydrogen (bottom).

6.3.2 Indan

Next, we discuss indan, which is obtained through hydrogenation of the five-membered ring in indene (see Scheme 10). Indan is not only a possible intermediate in the dehydrogenation of the fully hydrogenated hexahydroindan, it can also be considered itself as LOHC with 1.7 wt% hydrogen storage capacity in relation to the hydrogen lean indene. Therefore, the surface reaction and spectral fingerprint of indan is of high interest.

The C 1s region was measured during exposure of indan to Pt(111) at 130 K and subsequent heating. Selected XP spectra including fits during the reaction of 0.28 C-ML indan are shown in Figure 27 at the top with density plots, containing all recorded spectra of the adsorption and reaction, below. The corresponding quantitative analysis is shown in Figure 28. Again, the fitted envelopes presented in Figure 27 are used as a quantitative measure of the chemical species only and thus have no direct physical origin. The discussed binding energies below always refer to the peak positions of the fitted envelopes.

The adsorption of 0.23 L indan leads to the steady growth of one sharp peak at 284.2 eV (red in Figure 27), reaching a submonolayer coverage of 0.28 C-ML at the end of the adsorption (see Figure 28). This single peak is assigned to the molecular adsorption of indan on Pt(111). Compared to indene (284.1 and 284.4 eV), the single peak of indan is more narrow and its maximum is at a slightly lower binding energy.

After the adsorption, a TPXPS experiment was performed, to study the temperature-induced reaction of indan. Upon heating, no changes occur up to 240 K as the indan peak at 284.2 eV remains unchanged. Above this temperature, the overall signal shape starts to broaden. Analogous to the already discussed indene, the broadening is reflected by the development of two new peaks at 284.4 and 284.0 eV (both blue in Figure 27), which are again assigned to the indenyl surface species. This step represents the dehydrogenation of indan with the loss of three hydrogen atoms. The indan signal is gone until ~300 K, while the indenyl species reaches ~0.23 C-ML at this temperature. The ~20% decrease in coverage is most likely caused by molecular desorption of indan during the dehydrogenation as desorption of $m/z=118$ (indan) can also be observed in TPD at ~230 K (see Figure A 4 in Appendix A). The following course of reaction is very similar to indene. Both indenyl signals remain unchanged up to ~530 K. Above this temperature, decomposition into unspecified fragments takes place with

two new peaks emerging at 283.8 and 284.3 eV, which will not be further discussed. The indenyl signals declines until ~650 K.

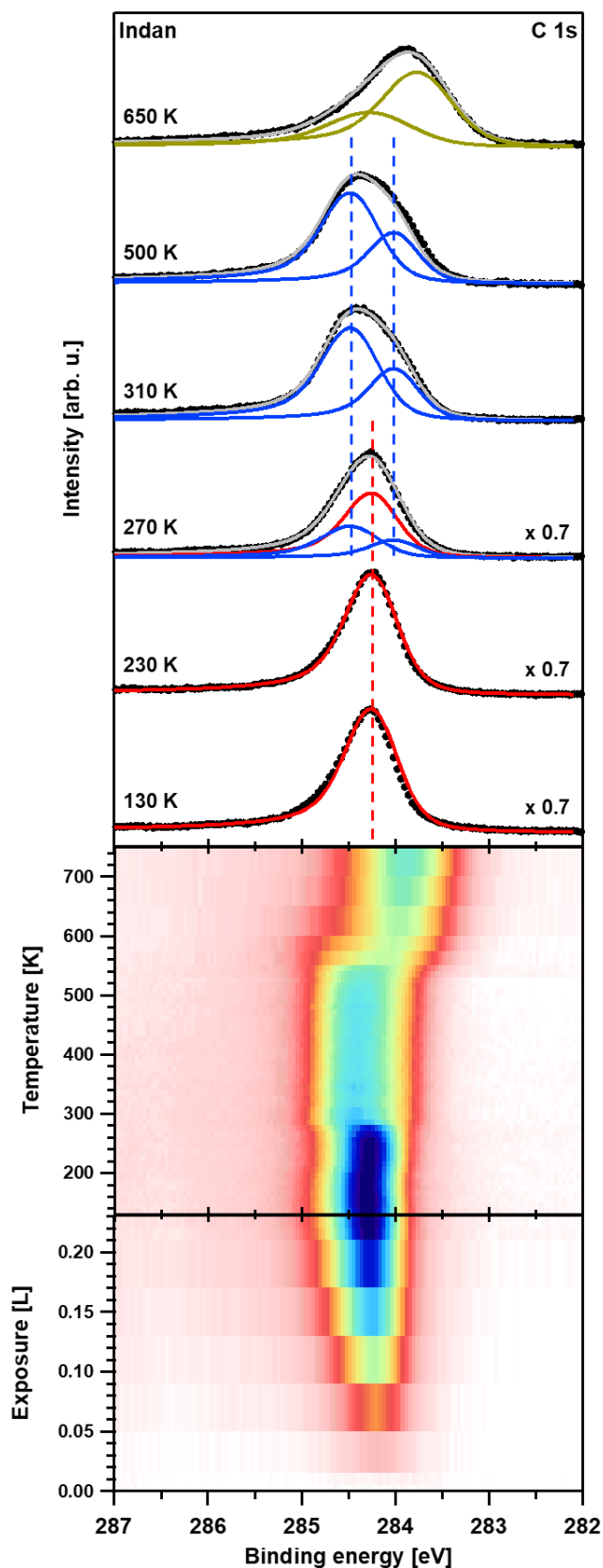


Figure 27: Selected C 1s XP spectra including fits (top) and density plots (bottom) of indan on Pt(111). Red: indan; green: indene; blue: indenyl; ocher: decomposition.

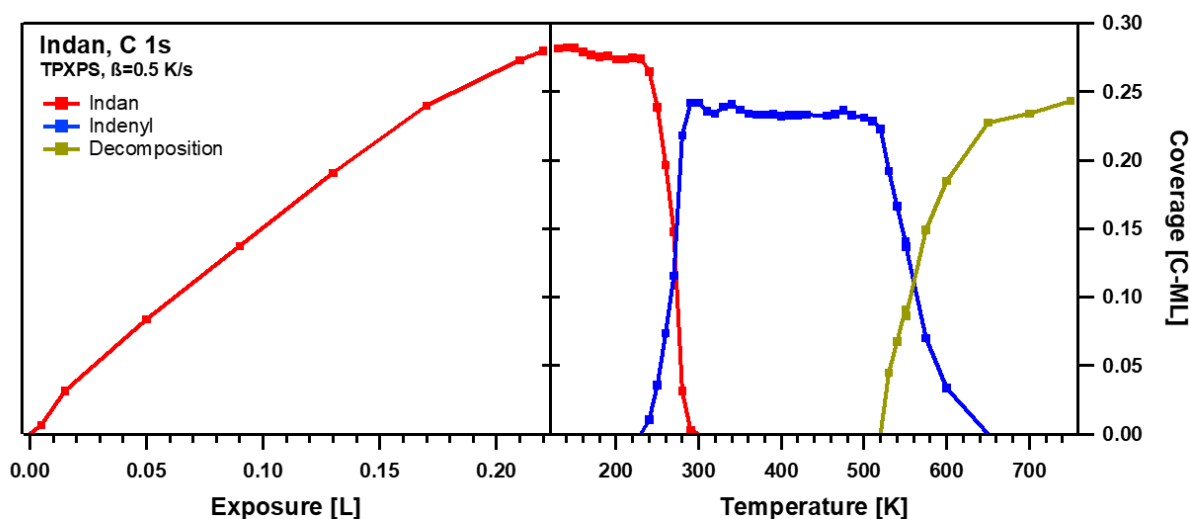


Figure 28: Quantitative analysis of the C 1s XPS experiments of indan on Pt(111) shown in Figure 27.

From XPS, the dehydrogenation order at the five-membered ring of indan cannot be determined. However, considering that the $m/z=2$ (H_2) TPD spectrum of indan in Figure 26 might be a linear combination of the indene TPD spectrum in the temperature range of 200-400 K, it can be assumed that first one hydrogen needs to split off in indan prior to the remaining two hydrogens. This is seen by the slope of the (integrated) indan TPD, which incorporates the intensity of the indene peak at ~ 300 K (green line in Figure 26), representing the desorption of one hydrogen, before reaching a maximum at 320 K, representing the desorption of two further hydrogens (red line in Figure 26) and thus the formation of the indenyl species. To verify this assumption, further experiments or DFT calculations are necessary. Analogous to indene, the subsequent decomposition reaction of the indenyl species is observed with a desorption maximum at 580 K. Above 800 K, no further H_2 desorption is observed.

6.3.3 Hexahydroindan

Finally, the adsorption and thermal evolution of the fully hydrogenated hexahydroindan is examined. With a significantly higher storage capacity of 6.5 wt% hydrogen, regarding the dehydrogenation to the hydrogen-lean indene, it is a highly attractive LOHC molecule.

The C 1s region was measured during exposure of 0.26 C-ML hexahydroindan to Pt(111) at 130 K and subsequent heating. Selected XP spectra including fits during the reaction of hexahydroindan are shown in Figure 29 at the top with density plots, containing all recorded

spectra of the adsorption and reaction, below. The corresponding quantitative analysis is shown in Figure 30. Again, the fitted envelopes presented in Figure 29 are used as a quantitative measure of the chemical species only and thus have no direct physical origin. The discussed binding energies below always refer to the peak positions of the fitted envelopes.

The adsorption of 0.25 L hexahydroindan leads to the steady growth of two convoluted peaks at 283.7 and 283.3 eV (orange in Figure 29), reaching a submonolayer coverage of 0.28 C-ML at the end of the adsorption (see Figure 30). Both peaks are assigned to the molecular adsorption of hexahydroindan on Pt(111) and are at significantly lower binding energies in comparison to indene (284.1 and 284.4 eV) or indan (284.2 eV).

Subsequently, a TPXPS experiment was performed, to study the temperature-induced dehydrogenation reaction of hexahydroindan. Upon heating, both hexahydroindan peaks at 283.7 and 283.3 eV start to shift slightly by 0.1 eV to lower binding energies, reaching 283.6 and 283.2 eV at 200 K. Above 200 K, a new peak (magenta in Figure 29 and Figure 30) arises at 283.9 eV, shifting the overall signal visibly to higher binding energies (see density plot in Figure 29), while the original hexahydroindan signals decline until 260 K. This new peak represents the continuous dehydrogenation of hexahydroindan and is labeled H_x-indan. It shifts by 0.1 eV to 284.0 eV at its maximum coverage of 0.16 C-ML at 250 K. As the H_x-indan peak is never isolated during its presence and is continually shifting, a distinct dehydrogenation reaction intermediate cannot be distinguished in the XPS data. From its binding energy range, however, it is quite possible, that very short lived π -allylic, indan or indene-like intermediates are present, similar to the structurally related octahydroindole/indole-based LOHC system discussed in Chapter 4.^[67] The H_x-indan signal then starts to decline above 250 K until it vanishes at ~300 K in favor of two new peaks at 284.0 and 284.4 eV, which emerge above 240 K and represent the dehydrogenated indenyl species, as seen for indene and indan. Indenyl reaches a maximum coverage of 0.17 C-ML (see Figure 30); the difference of ~40% to the starting coverage of 0.28 C-ML hexahydroindan is most likely explained by molecular desorption during the dehydrogenation process of hexahydroindan with $m/z=124$ (hexahydroindan) TPD spectra depicting desorption in the range from 200-300 K (see Figure A 5 in Appendix A). The consecutive reaction pathway of indenyl is equal to the already discussed indene and indan; indenyl remains unchanged up to ~530 K, where it starts to decompose into unspecified fragments. The indenyl signals then

declines until ~ 650 K. Both decomposition peaks again are observed at 283.8 and 284.3 eV and will not be further discussed.

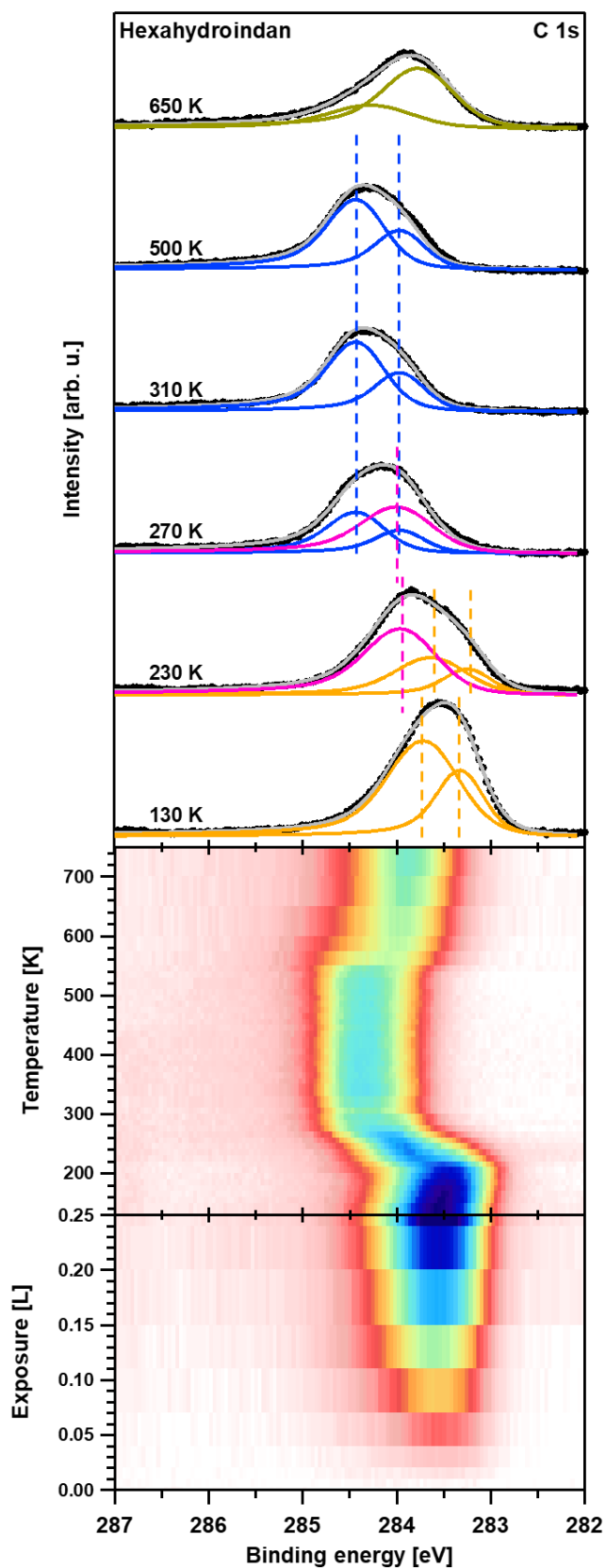


Figure 29: Selected C 1s XP spectra including fits (top) and density plots (bottom) of hexahydroindan on Pt(111). Orange: hexahydroindan; magenta: H_x-indan; green: indene; blue: indenyl; ocher: decomposition.

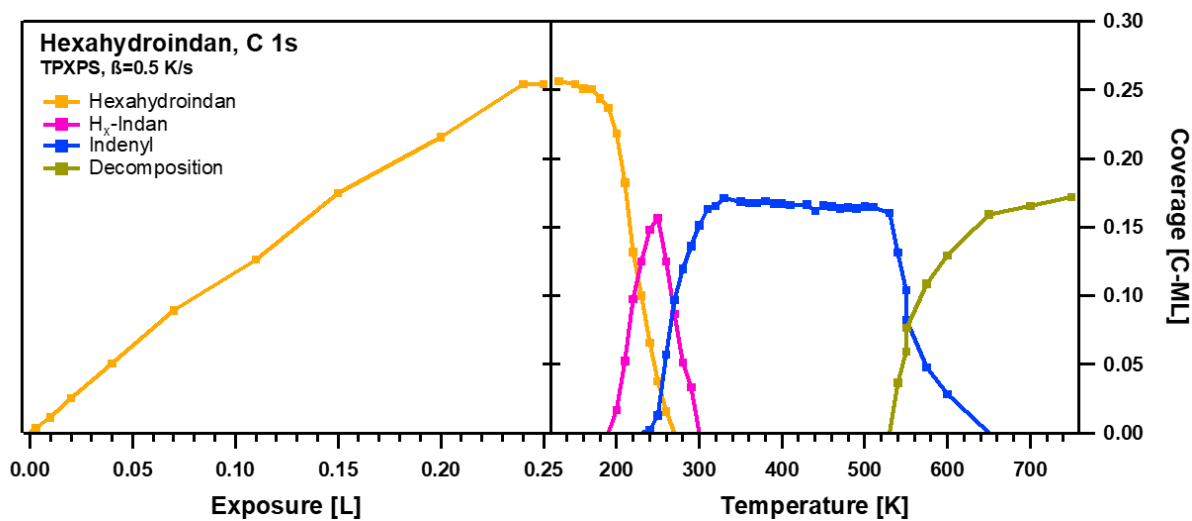
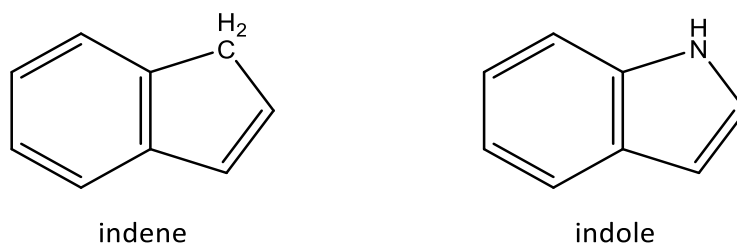


Figure 30: Quantitative analysis of the C 1s XPS experiments of hexahydroindan on Pt(111) shown in Figure 29.

Similar to the discussion for indan, the dehydrogenation order for hexahydroindan cannot be determined from the XPS data. However, again considering a strictly linear combination of the desorption features in the $m/z=2$ (H_2) TPD data shown in Figure 26, the following hypothetical dehydrogenation order, synthesized from the prior discussed indene and indan dehydrogenation, can be proposed. At 300 K, hexahydroindan has lost ~ 3 hydrogen atoms, which, following the above assumption, can possibly be attributed to the loss of one hydrogen at the five-membered ring, as initially observed for indene (green line in Figure 26) as well as the loss of two further hydrogens at the six-membered ring. To verify this assumption, further experiments or DFT calculations are necessary. Up to 400 K, the loss of another six hydrogen atoms is observed with a desorption maximum at ~ 310 K (orange line in in Figure 26), resulting in the indenyl intermediate. Analogous to indene and indan, the subsequent decomposition reaction of indenyl is observed with a desorption maximum at 580 K. Above 800 K, no further H_2 desorption is observed.

6.3.4 Comparison of the homocyclic indene-based LOHC system with the heterocyclic indole-based LOHC system

Indene is closely related to indole in terms of its molecular structure, with the only difference being the substitution of the CH₂-group in the five-membered ring of indene with an NH group for indole as shown in Scheme 11. Therefore, the differences of the respective LOHC systems are of high interest, as they basically outline the influence of the nitrogen substitution.



Scheme 11: Molecule structures of indene (left) and indole (right).

For octahydroindole and indoline, the dehydrogenation into an indole intermediate above 270 K is found. Simultaneously at 270 K, deprotonation of the NH group leads to an indolide species, which is observed up to 540 K on the surface, before it is completely decomposed (see Chapter 4 for a detailed discussion).

For indene, the dehydrogenation of the CH₂-group in the five-membered ring is observed above 220 K, forming an indenyl species. Indan dehydrogenates above 240 K, forming the same indenyl species; a stable dehydrogenation intermediate like indene is not observed. Hexahydroindan starts to dehydrogenate above 200 K into an unspecified H_x-indan intermediate, followed by the formation of indenyl above 240 K. For all three molecules, indenyl is observed up to 650 K, before it is completely decomposed.

Interestingly, a stable indan/indoline intermediate is neither observed for hexahydroindan nor octahydroindole, while 2-methylindoline is a stable intermediate in the dehydrogenation of 2-methyloctahydroindole (see also Chapter 5). Indole is observed as intermediate for indoline and octahydroindole dehydrogenation, while an analogous indene intermediate was not identified in the indan or hexahydroindan reaction. However, both systems ultimately form similar species with indenyl and indolide, emerging from the dehydrogenation of the CH₂-group in indene or the deprotonation of the substituted NH group equivalent in indole. Nevertheless, the formation of indenyl is observed up to ~50 K earlier (220 K for indene, 240 K for indan, hexahydroindan) than the formation of indolide (270 K), which in turn results in

lower dehydrogenation temperatures for the indene-based LOHC system. Beyond that, indenyl is observed up to ~110 K higher than indolide, which consecutively makes the whole indene-based LOHC system significantly more stable than the indole one.

However, outside of UHV, in real catalysis, this behavior might change and formation of the surface-bound indenyl or indolide species might not occur at all, which would be favorable for the technical applicability of these LOHC systems.

6.4 Conclusion

High resolution XPS and TPD experiments of the surface reactions of the LOHC system indene/indan/hexahydroindan on Pt(111) were performed.

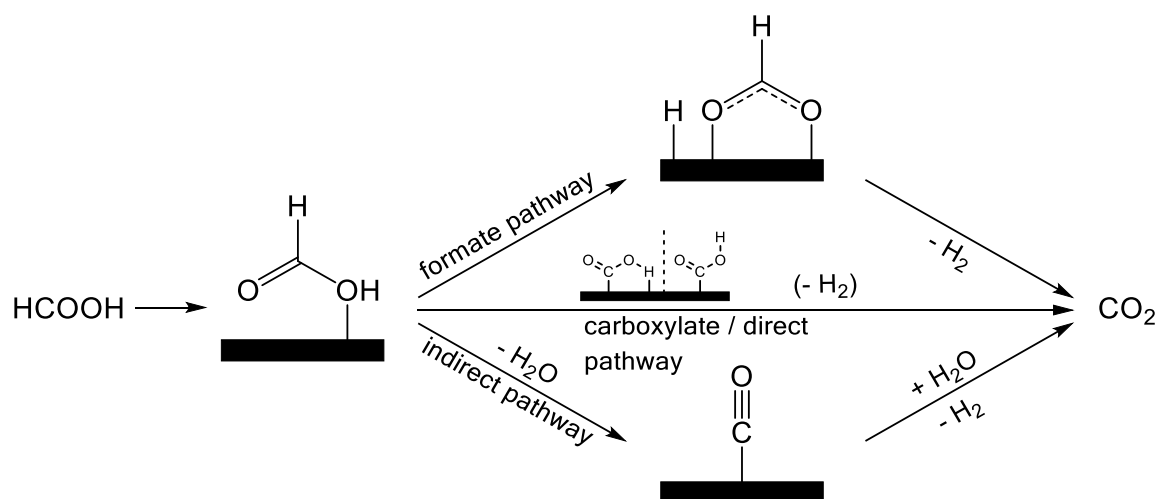
For the hydrogen-lean indene, the dehydrogenation of the CH₂-group to CH in the five-membered ring above ~220 K is observed, resulting in an indenyl surface species. Indan (partially hydrogenated at the five-membered ring) dehydrogenates above ~240 K, also forming indenyl; a stable intermediate like indene is not observed. Hexahydroindan dehydrogenates above ~200 K, forming a H_x-indan intermediate, followed by the formation of indenyl above ~240 K. Again, indene or indan are not observed as stable dehydrogenation intermediates in XPS. Decomposition of indenyl takes place above ~530 K and is completed until ~650 K for all three molecules. Above this temperature only fragments are left on the surface. In real catalytic conditions, dehydrogenation into the surface bound indenyl species needs to be avoided in order to form an efficient hydrogen storage cycle.

Overall, the homocyclic indene LOHC system is similar to the heterocyclic indole LOHC system (see Chapter 4). Indenyl can be seen as reaction analog to indolide. The main difference of both systems lies in the dehydrogenation and decomposition temperatures. The indene LOHC system dehydrogenates up to ~50 K earlier and indenyl is observed up to ~110 K higher than indolide, making it a very promising LOHC system to test in real catalytic conditions.

7. Formic acid decomposition on Pt(111) and Ni(111)

7.1 Introduction

The surface science of formic acid (HCOOH) has been extensively researched in the last decades with ongoing interest. Formic acid is nontoxic and basically decomposes either via dehydration ($\text{HCOOH} \rightarrow \text{CO} + \text{H}_2\text{O}$) or dehydrogenation ($\text{HCOOH} \rightarrow \text{CO}_2 + \text{H}_2$). As formic acid is also easy to store and handle, it has favorable properties to be a safe hydrogen carrier by catalytically induced de- and rehydrogenation.^[107-110] Formate (HCOO^-) and carboxylate ($^- \text{COOH}$) (see Scheme 12) are also intermediates in the important water-gas shift reaction^[108, 111-112] ($\text{CO} + \text{H}_2\text{O} \rightarrow \text{CO}_2 + \text{H}_2$), which produces hydrogen by reducing CO in syngas. Thus, the adsorption and reaction of formic acid on various catalytically active transition metal (oxide) surfaces has been studied^[113], utilizing surface science methods, including temperature programmed desorption (TPD)^[113-117], electron energy loss spectroscopy (EELS)^[113-114, 118-120], infrared spectroscopy, sum frequency generation (SFG)^[117, 121-122] and photoelectron spectroscopy (PES)^[123-126]. In the recent decade, particularly density functional theory (DFT) methods contributed to the investigation of the different mechanistic pathways of formic acid decomposition on metal surfaces to complement practical studies.^[127-131]



Scheme 12: Simplified illustration of possible formic acid oxidation pathways on metal surfaces.^[132]

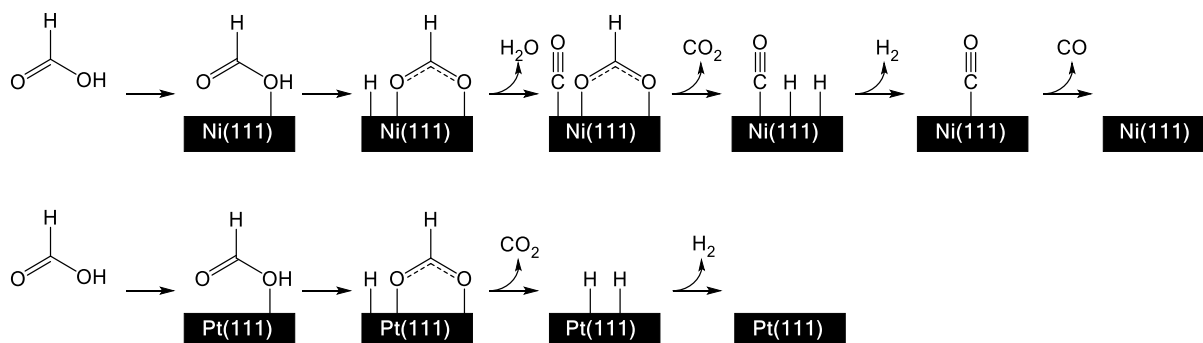
The reaction of formic acid was investigated on Pt(111) mainly using EELS and TPD. The saturation coverage on Pt(111) for the first layer is found to be 0.5 ML.^[133] Multilayer desorption is observed between 160-180 K^[118, 134] and first layer desorption of HCOOH is seen between 180-210 K^[116, 135-136]. The conversion of formic acid into formate occurs between 130-

170 K^[136], while formate desorbs from 170-260 K^[119, 136]. Carboxylate formation is not reported on Pt(111). As main reaction product CO₂ is identified at a desorption temperature of 260 K^[114, 116, 118-119, 134-137]. On Pt-O, next to bidentate/bridged formate, monodentate formate is reported to be stable below 130/170 K^[118-119, 134]. Above 170 K and on Pt(111), only bidentate/bridged formate is observed, as in EELS only the $\nu_s(\text{OCO})$ at 1330 cm⁻¹ is present, which is close to the one of the free formate ion at 1360 cm⁻¹. The asymmetric OCO at ~1600 cm⁻¹, which would indicate monodentate formate, is absent.^[118, 134] CO vibrations at 1640 and 1720 cm⁻¹ below 190 K, are attributed to molecularly adsorbed formic acid.^[116, 135] In contrast to practical results, DFT studies on the reaction of formic acid on Pt(111) are rather divergent towards the pathway of formic acid decomposition (see Scheme 12). Some studies find the formate pathway to be energetically favorable under gas-phase conditions^[127-128], predicting a bridged formate as well as a monodentate intermediate towards decomposition. However, other studies find the carboxylate pathway to be more favorable in gas phase^[48, 130-131] by as much as 0.48 eV^[130], while one study also finds favorable energetics for the formate pathway.^[131]

On Ni, a different reaction scheme is being reported. For Ni(110), EEELS and TDS show an initial reaction of formic acid to HCOO and HCO at 300 K followed by decomposition into CO on the surface at 330 K and desorption of CO₂ at 365 K.^[138] Using RAIRS, at 120 K and low coverage, $\nu_s(\text{OCO})$ at 1344 and 1364 cm⁻¹ are observed and attributed to possibly two different surface formates. At higher exposures, bands around 1600 and 1720 cm⁻¹ are assigned to $\nu_a(\text{OCO})$ and $\nu(\text{C=O})$ of formate and formic acid. Upon heating, the bands for formic acid disappear until 200 K. Starting at 285 K, decomposition of formate into CO is observed, while the $\nu_s(\text{OCO})$ is nearly gone at 300 K.^[139] TPD on Ni(110) reveals CO₂ desorbing at a peak temperature of 360 K, with small CO desorption at this temperature, and a main desorption peak at 410 K. IRAS shows a declining $\nu_s(\text{OCO})$ band at 1335 cm⁻¹, which vanishes until 360 K, with rising CO bands above 340 K.^[140] On Ni(111), CO₂ desorption is reported to take place at 360-370 K and CO desorption is observed from 430-450 K.^[122, 141] SFG with a pulsed laser to introduce a temperature jump, reveals the changes of $\nu(\text{CD})$ ^[122] and $\nu(\text{CH})$ ^[117] of bridged formate as well as $\nu_s(\text{OCO})$ ^[142]. A decrease is observed for $\nu(\text{CH})$ upon heating to 273 K.^[117] For $\nu(\text{CD})$ at 2160 cm⁻¹, also a decrease is observed above 275 K, while a new transient band at 2190 cm⁻¹ shows up, which is assigned to $\nu(\text{CD})$ of monodentate formate, before it decomposes into CO and CO₂.^[122] The decrease of the $\nu_s(\text{OCO})$ and $\nu(\text{CD})$ upon irradiation is suggested to be possibly

due to decomposition/desorption and/or a transient species like monodentate formate.^[142] DFT studies of formic acid on Ni(111) suggest that a bridged/bidentate formate species is energetically more stable than a monodentate species by 0.6-0.8 eV. However, they suggest a monodentate formate transition state during the decomposition of formate.^[129, 143]

In short, Scheme 13 summarizes the expected main reaction pathways for formic acid dehydrogenation/decomposition on Ni(111) and Pt(111):



Scheme 13: The expected main reaction pathways for formic acid dehydrogenation/decomposition on Ni(111) and Pt(111).

Herein, the thermal dehydrogenation, i.e. the hydrogen release, of formic acid has been investigated with high resolution XPS and NEXAFS in UHV using synchrotron radiation, as well as TPD. To obtain information on the surface processes, the C 1s and O 1s region were continually measured during the adsorption and consecutive heating of the molecules on the Ni(111) and the Pt(111) surfaces. NEXAFS spectra were recorded in normal and grazing incidence (0° and 70° with regard to the surface normal) at 140 and 190 K for the C K-edge and O K-edge.

7.2 Specific experimental setup

The XPS and NEXAFS experiments were performed at the synchrotron BESSY II at beamlines UE56-2 PGM 2 and U49-2 PGM 2 using the synchrotron UHV machine (see Chapter 3.1). TPD experiments were performed in a separate TPD UHV machine (see Chapter 3.2).

The adsorption of formic acid on Ni(111)/Pt(111) was done using the vapor pressure of the substances. The heating rate was set to 0.5 K/s during TPXPS and 3 K/s for TPD. The coverage (1 ML = 1 carbon/oxygen atom/Ni atom) on Ni(111) was calibrated by comparison to the well-known saturation surface coverage of benzene at 200 K, which leads to a $(\sqrt{7} \times \sqrt{7})R19.1^\circ$ LEED pattern.^[99, 144] For Pt(111), the coverage (1 ML = 1 carbon/oxygen atom/Pt atom) was calibrated by comparison to the well-known saturation surface coverage of carbon monoxide at 200 K, which leads to a $c(4 \times 2)$ LEED pattern and amounts to 0.50 monolayers.^[52, 75-76] Peak fitting of the C 1s and O 1s spectra was done using Doniach-Šunjić-profiles^[53] convoluted with a Gaussian function. The C 1s and O 1s regions were measured at 380 and 650 eV with resolutions of 150 meV (C 1s) and 200 meV (O 1s) for Ni(111) as well as Pt(111).

7.3 Results and discussion

7.3.1 Formic acid on Ni(111)

Spectra of the adsorption at 130 K and consecutive reaction during temperature programmed XPS for the C 1s and O 1s core levels of formic acid are shown in Figure 31a and b with the corresponding quantitative analysis in Figure 32. The C 1s and O 1s spectra were obtained in independent experiments and thus the final coverage is not identical.

In the C 1s region, the adsorption of 0.44 ML formic acid results in two main peaks at 289.5 and 287.5 eV. The broad peak at 289.5 eV is assigned to formic acid I and reaches ~0.14 ML. This assignment is based on previous XPS studies of formic acid on Cu(111) and Al(111), which assign the C 1s peak at higher binding energy to formic acid and the one at lower binding energy to formate.^[125-126] However, two main envelopes including an additional small satellite each due to vibrational splitting are needed to fit the signal at 287.5 eV, suggesting the existence of two different species. The vibrational satellites are located at a defined binding energy offset and height ratio to the parent peak.^[85] As there is only one known, bidentate formate species on Ni(111), the peak at 287.2 eV is assigned to formate, while the peak at 287.5 eV is proposed to be formic acid (labeled formic acid II below, bound e.g. similar to bidentate formate). A detailed discussion of the analysis that leads to these assignments is given below. However, the occurrence of two different formic acid species is unexpected and their differences cannot be explained within the scope of this study. Formate reaches ~0.14 ML at the end of the adsorption, while formic acid II reaches ~0.12 ML. A further small contribution at 285.3 eV with ~0.02 ML is attributed to carbon monoxide^[145], which is due to background adsorption of CO, which originates from the prior decomposition of formic acid on the chamber walls or other surfaces, which are at room temperature. Therefore, a slowly growing CO signal is seen during the adsorption of formic acid.

In the O 1s region, the adsorption of 0.52 ML formic acid leads to a peak at 531.7 eV with a broad shoulder at 532.7 eV. The first one is assigned to two species, formic acid I and formate (287.2 eV in the C 1s region), reaching ~0.33 ML; whereas the latter one represents the formic acid II species (287.5 eV in the C 1s region) with ~0.19 ML. The assignment here is based on the comparison to the C 1s experiments of formic acid and previous studies on Cu(111)^[125], as well as the TPXPS experiment discussed below.

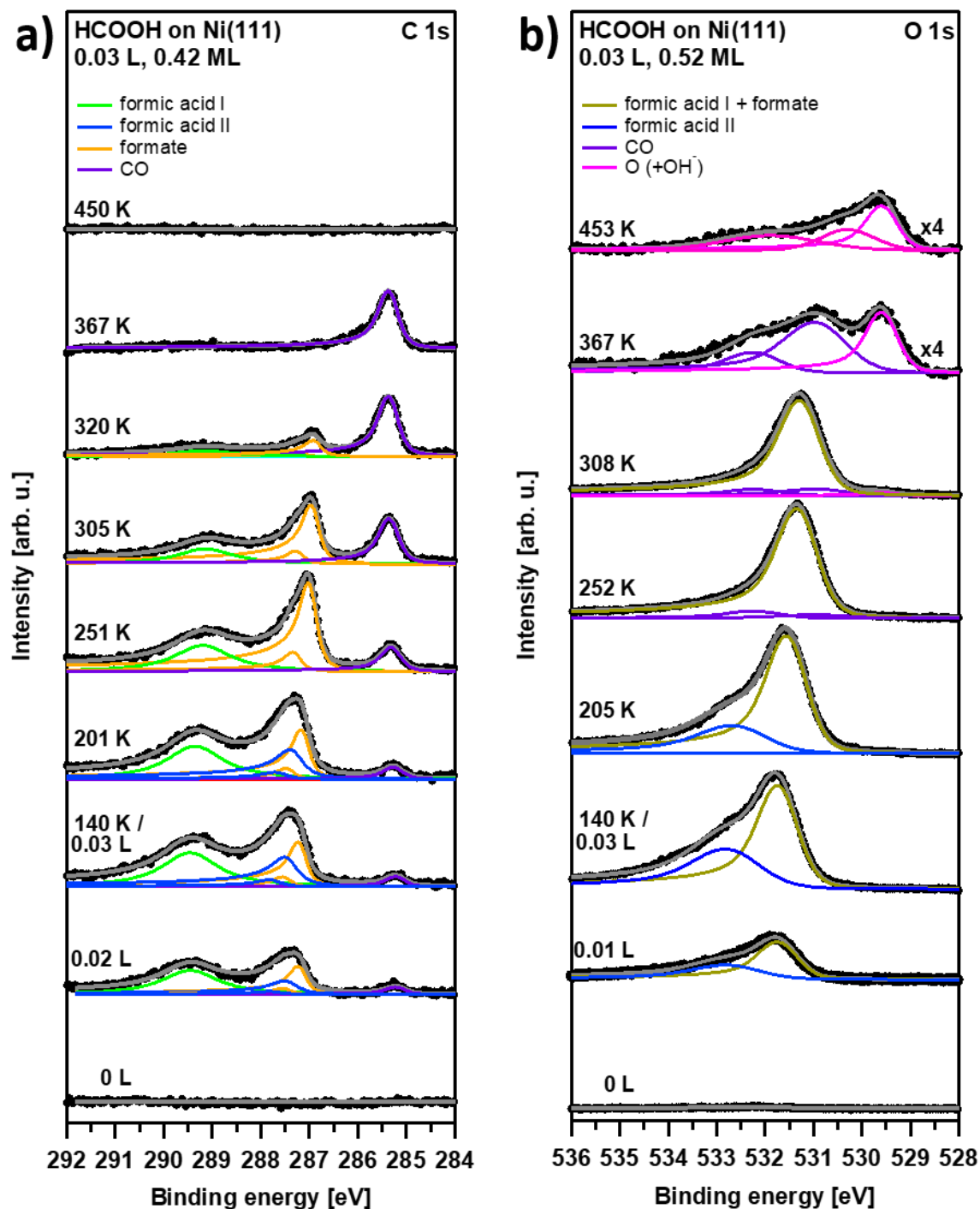


Figure 31: Selected spectra including fits of formic acid during adsorption and heating on Ni(111) including fits. a) C 1s region, b) O 1s region.

For coverages higher than 0.50 ML, formation of multilayers is found, with steadily growing peaks above 289.5 eV in the C 1s region and above 533.0 eV in the O 1s region (see Figure A 6 and Figure A 7 in Appendix A). In the 1.0 L TPD spectra of m/z 46 and 44 in Figure 33, multilayer desorption of formic acid on Ni(111) is observed below 200 K, with a desorption temperature of 165 K. (As the XPS and TPD experiments were performed in different UHV setups with different pressure gauges, the exposures are not comparable).

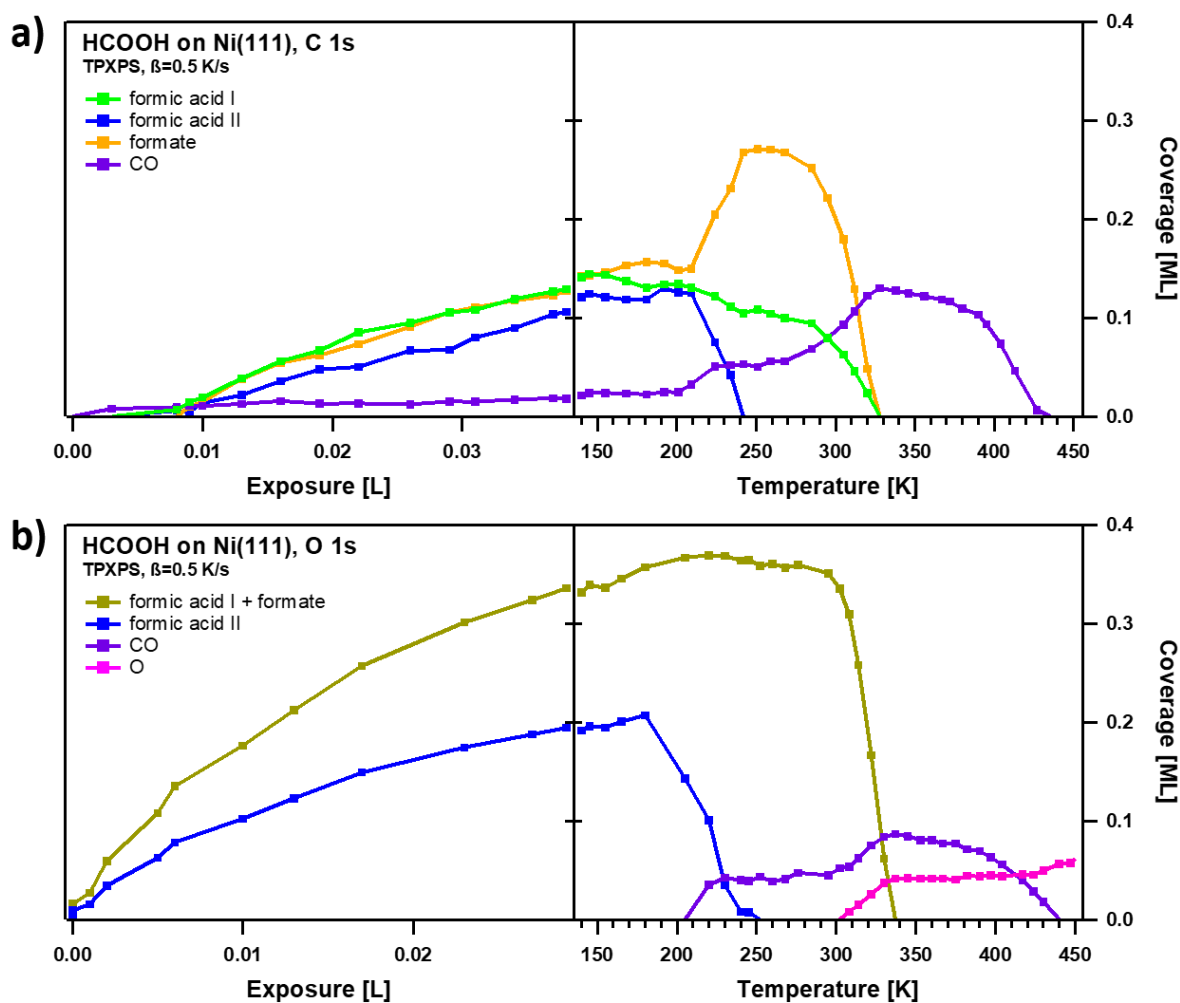


Figure 32: Quantitative analysis of the XPS experiments of formic acid on Ni(111) shown in Figure 31. a) C 1s region, b) O 1s region.

In the C 1s region (see Figure 31a and Figure 32a), upon heating, formic acid II at 287.5 eV starts to decline above 210 K until it vanishes at 240 K. The strong change in FWHM of the overall signal at ~ 287.5 eV during the decline of formic acid II serves also as an indication for the existence of two different species. Meanwhile, the formate peak shifts from 287.2 towards 287.0 eV and increases to a maximum of ~ 0.27 ML at 240 K. The CO signal increases from ~ 0.02 to ~ 0.05 ML in this temperature range, while the coverage of formic acid I decreases slightly and reaches a plateau at 250 K with ~ 0.10 ML. This behavior is best seen in the quantitative analysis shown in Figure 32a. In combination with the below discussed O 1s and TPD data, the observed changes in the temperature range from 210-250 K in the C 1s region can be explained by the partial dehydration of formic acid II, forming instantly desorbing H_2O (see TPD of m/z 18 in Figure 33) and CO in the process. Furthermore, the partial interconversion of formic acid I and II to formate affirm the peak assignment.

Starting at 280 K, the peak intensities of the remaining formic acid I and formate species start to decline rapidly, until they are gone at ~330 K. This step depicts the partial desorption and expected dehydrogenation of formic acid and formate to CO₂ (see also TPD of m/z 44 and m/z 46 in Figure 33) and CO.^[117, 131, 141] From 280 to 330 K, the overall coverage decreases by ~0.30 ML due to desorption. Meanwhile, an increase of the CO peak at 285.3 eV is found above 280 K up to a maximum of 0.13 ML at 330 K, which is then the only carbon species left on the surface.

In the O 1s region a decrease of the formic acid II species at 532.7 eV is observed upon heating above 180 K until it vanishes at 250 K (see Figure 32b), leading to a 33% decrease of the total O 1s coverage. The decline is analog to the decline of formic acid II in C 1s region and therefore also affirms the peak assignment. At the same time, the peak at 531.7 eV, representing formate and formic acid I, increases up to ~0.37 ML. Thereby, the peak is shifting continually towards 531.3 eV at 250 K (see Figure 31b). Furthermore, the formation of CO is observed above 200 K with two new broad peaks at 531.0 eV and 532.2 eV, reaching a plateau of ~0.05 ML above 230 K.^[145] As discussed for the C 1s region, these changes reflect the partial dehydration of formic acid II and the conversion of formic acid I and II to formate. However, the conversion to formate is not as pronounced in the O 1s region (see Figure 32b) as formic acid I and formate are not resolved and therefore their interconversion is not visible in the spectra. This again supports the peak assignment in the O 1s region.

Above 280 K, the formic acid I/formate peak at 531.3 eV declines rapidly, continually shifting to 531.1 eV, until it vanishes at 340 K. Analog to the C 1s region, this step depicts the desorption and dehydrogenation of formic acid and formate to CO₂ and CO.^[117, 131, 141] As a consequence thereof, the CO signal increases from ~0.05 to ~0.09 ML at 340 K. Furthermore, a new peak at 529.6 eV emerges above 300 K, which is assigned to oxygen on the Ni(111) surface, reaching 0.04 ML at 340 K.^[146-148] The behavior of CO formation and desorption in the O 1s region is very similar to the one observed for the C 1s region above. From ~340-400 K, CO intensity can be considered constant until CO desorbs between 400 and 440 K.^[117, 141, 145] After CO desorption, two very small peaks become evident at 530.3 and 531.9 eV, which are persistent well beyond 500 K. As known from the C 1s experiment, above 440 K, no carbon species are present on the surface. Therefore, these small contributions are assigned to further oxygen, oxide or hydroxide species on the surface.^[149]

The TPD spectra (see Figure 33) are in agreement with the XPS results. For coverages below 0.50 L, a desorption maximum of 240 K is visible for H₂O (m/z 18). The desorption of formic acid (m/z 46) and CO₂ (m/z 44) is observed at 330 K. The presence of both desorption peaks at this temperature also affirms the peak assignment in XPS, with formic acid I still being present at higher temperatures next to formate. At 340 K, H₂ (m/z 2) desorption is observed, followed by the CO desorption (m/z 28) maximum at 420 K. The small contribution at 330 K for the m/z 28 spectra is also be attributed to CO₂ desorption.

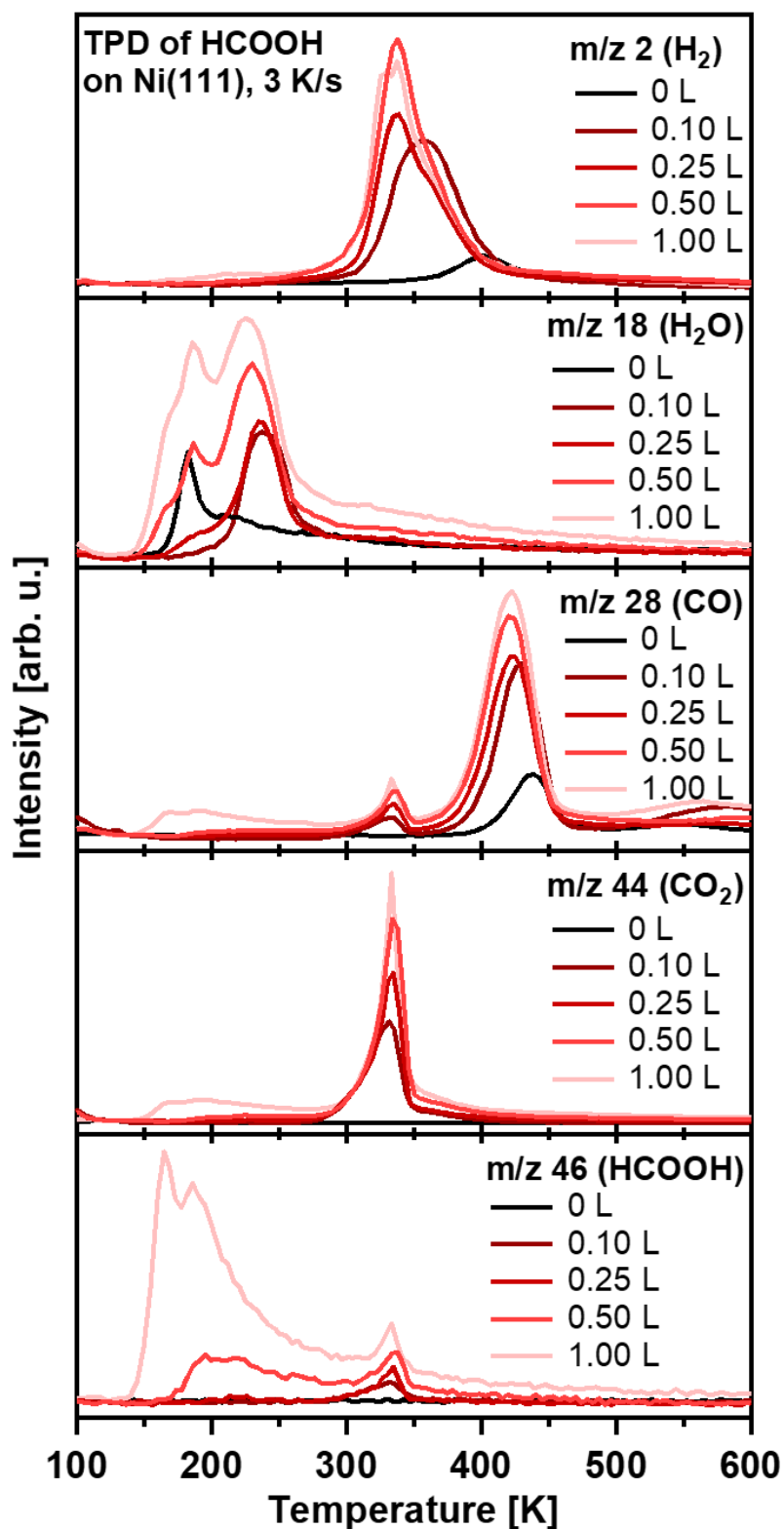


Figure 33: TPD spectra of m/z 2, 18, 28, 44 and 46 of formic acid on Ni(111) with exposures from 0-1.0 L.

7.3.2 Formic acid on Pt(111)

Spectra and fits of the adsorption and consecutive reaction of formic acid on Pt(111) during TPXPS for the two core level regions are shown in Figure 34a and b. The adsorption leads to peaks at 289.0 and 287.3 eV in the C 1s region and 531.6 and 532.7 eV in the O 1s region. The TPXPS measurements were conducted directly after the adsorption experiments, however postadsorption of formic acid leads to an increase in coverage between the adsorption and the TPXPS experiments (see Figure 35). Again, the C 1s and O 1s spectra were obtained in independent experiments and thus the final coverages are not identical.

Analogous to Ni(111), the peak at 289.0 eV and ~ 0.15 ML is assigned to adsorbed formic acid I, whereas the peak at 287.3 eV corresponds to two different species; formate at 287.2 and formic acid II at 287.5 eV, each accompanied with an additional small satellite due to vibrational splitting.^[85] Formate and formic acid II reach ~ 0.05 ML and ~ 0.08 ML, respectively. In the O 1s region, two signals are observed at 531.6 and 533.1 eV. Also based on the findings for Ni(111), the peak at 531.5 eV is assigned to formic acid I and formate, while the peak at 533.1 eV is assigned to formic acid II. Formic acid I and formate reach ~ 0.17 ML after until the start of the TPXPS, whereas formic acid II reaches ~ 0.08 ML.

For coverages higher than ~ 0.50 ML, formation of multilayers is found, where steadily growing peaks above 289.0 eV in the C 1s region and above 532.8 eV in the O 1s region are observed (see Figure A 8 and Figure A 9 in Appendix A). The TPD spectra of m/z 44 and 46 (Figure 36) show the multilayer desorption of formic acid on Pt(111) for exposures of 0.75 L and above.

In the C 1s spectra (Figure 34a and Figure 35a), no changes indicative of a reaction are observed below 160 K. Above this temperature, formic acid I at 289.0 eV and formic acid II at 287.5 eV start to decrease to ~ 0.07 and ~ 0.03 ML, while the formate signal increases to a maximum of ~ 0.08 ML at 180 K (see Figure 35a). This step indicates a partial conversion of formic acid to formate and also molecular desorption of formic acid, as the overall coverage decreases by $\sim 38\%$ until 180 K (see also TPD of m/z 46 in Figure 36). While the coverage of formic acid II remains at a plateau of ~ 0.03 ML up to ~ 210 K, formic acid I and formate continue to decline. Until ~ 220 K, all three signals are gone due to desorption of formic acid and CO_2 . Unlike for Ni(111), no formation of CO is observed on Pt(111).

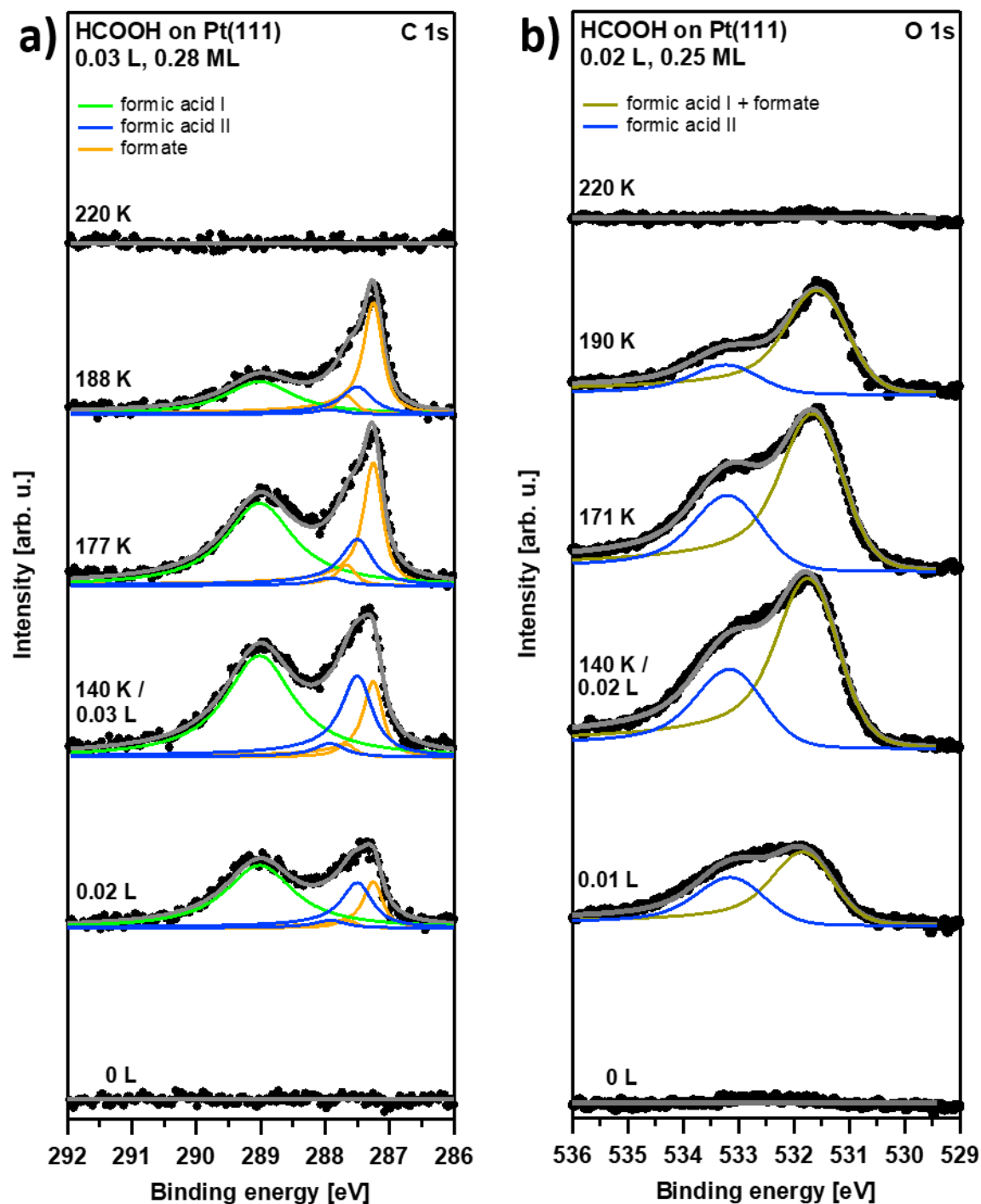


Figure 34: Selected spectra including fits of formic acid during adsorption and heating on Pt(111) including fits. a) C 1s region, b) O 1s region.

This desorption behavior is especially seen in the TPD spectra in Figure 36. Formic acid (m/z 46) shows a sharp desorption peak at 200 K, with a shoulder up to 250 K, while CO_2 (m/z 44) shows an initial desorption peak at 250 K for 0.1 L exposure. The difference of ~ 30 K compared to the TPXPS experiments can be explained by the different heating rates and might also be coverage-related; the observed reaction, however, is the same. At higher exposures, an additional peak at 200 K occurs for m/z 44. H_2 (m/z 2) desorption takes place at 350 K, after

formic acid/formate is completely desorbed, in line with desorption of molecular hydrogen on Pt(111) which is only observed above 300 K for smaller coverages.^[106] In contrast to Ni(111), no conversion to carbon monoxide is observed on Pt(111). TPD shows only a small amount of CO desorbing at 450 K for 0.1-1.0 L, which is slightly higher than the amount from a clean crystal and equals to less than 0.05 ML when compared to the 0.50 ML CO spectrum. CO likely originates from the decomposition of formic acid into CO at the chamber walls and adsorption on the sample during the experiment. In agreement to these results, using TPD, formic acid/formate was reported to desorb dimeric before 180 K, monomeric from 180-250 K and also as CO₂ above 200 K on Pt(111).^[116, 135]

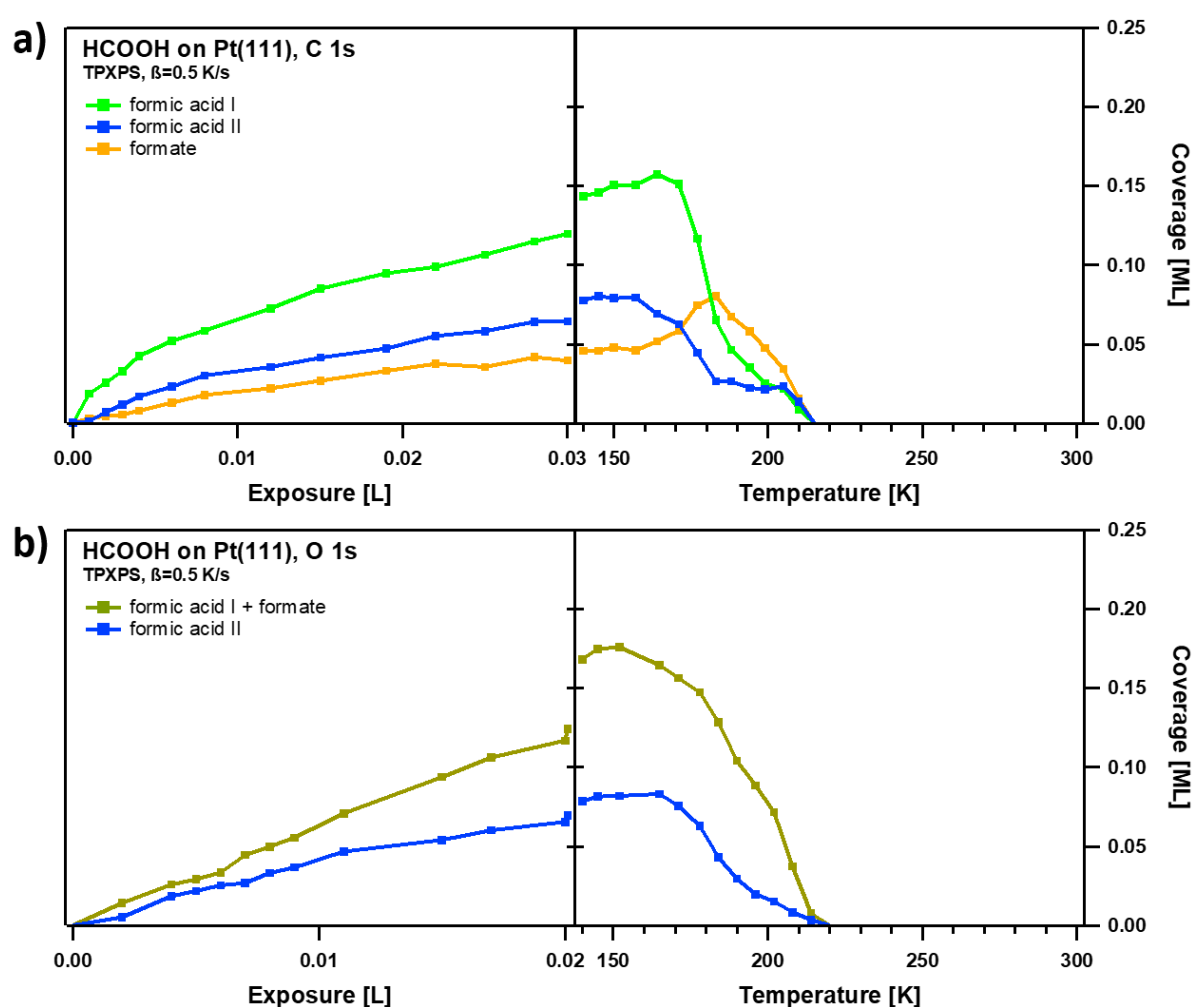


Figure 35: Quantitative analysis of the XPS experiments of formic acid on Ni(111) shown in Figure 34. a) C 1s region, b) O 1s region.

In the O 1s region (see Figure 34b and Figure 35b), up to 170 K, no major changes are observed. Above this temperature, both, the formic acid II peak at 533.1 eV and the formic acid I/formate peak at 531.6 eV start to continually decline until vanishing at ~220 K,

while slightly shifting to 533.2 and 531.5 eV, respectively. The coverage slope during the decline is very similar to what is observed in the C 1s region (compare Figure 35a and b) and in summary, the O 1s region shows the same behavior for formic acid as seen in the C 1s region. No apparent conversion to CO is observed. A CO₂ surface species does not exist on Pt(111) at the given temperatures.^[150-151]

In addition to XPS and TPD, NEXAFS of formic acid on Pt(111) at 140 K and 190 K was conducted in order to determine the adsorption geometry of formic acid. The C K-edge and O K-edge spectra are shown in Figure 37 and Figure 38, respectively. The normal incidence C K-edge spectra in Figure 37a show nearly no change in the π^* -region at 288 eV and a decrease of 25% in the σ^* -region beyond 290 eV from 150 to 190 K. In grazing incidence, the π^* -region is decreased by 60% (Figure 37b) and the σ^* -region only slightly upon heating. In the O K-edge spectra, a similar behavior is observed. The π^* -signal at 533 eV decreases by 30% from 150 to 190 K in normal incidence (Figure 38a), while the σ^* -region beyond 535 eV is decreased by 60%. The grazing incidence spectra (Figure 38b) show a decrease of 75% from 150 to 190 K in the two π^* -peaks at 532 and 534 eV, while the latter one also shifts to 533 eV upon heating and the σ^* -region is decreased by 60%. Combining these findings, it can be assumed, that formic acid/formate adsorbs rather disordered on the surface at 150 K, while at 190 K, it is most likely standing upright and bound perpendicular to the surface.

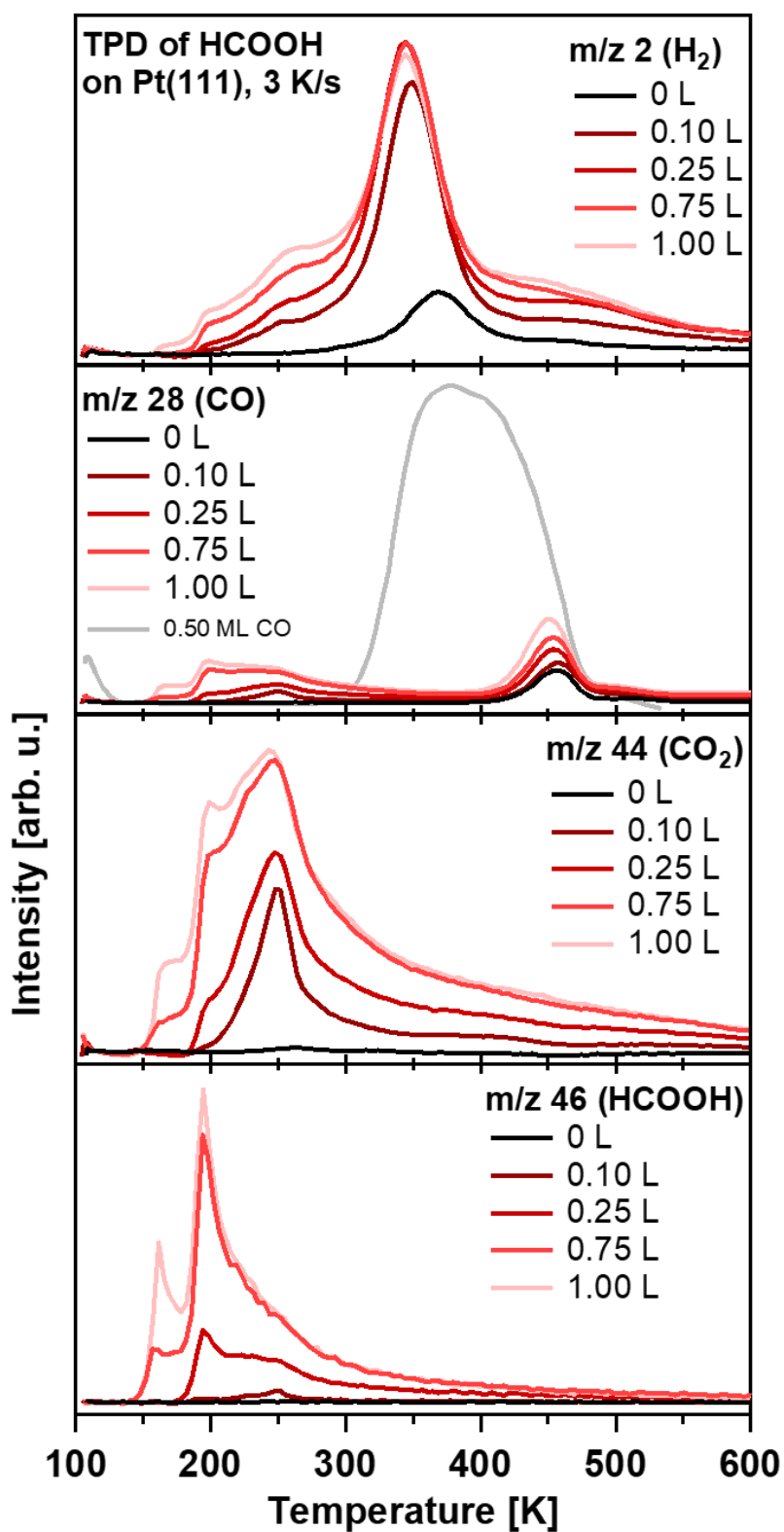


Figure 36: TPD spectra with m/z 2, 28, 44 and 46 of formic acid on Pt(111) with exposures from 0.1-1.0 L.

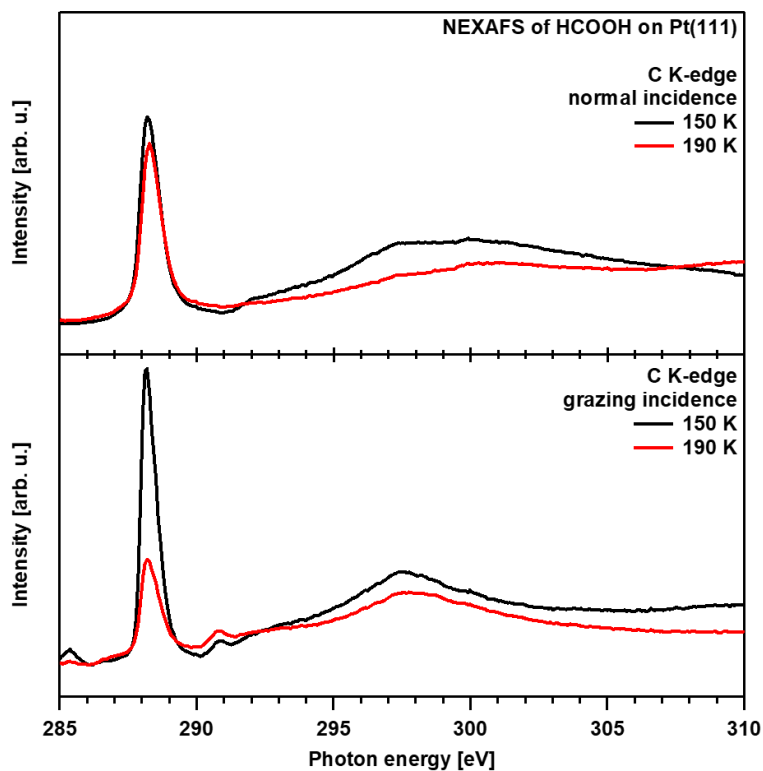


Figure 37: C K-edge NEXAFS of formic acid on Pt(111) at 150 and 190 K in normal (0°) and grazing (70°) incidence.

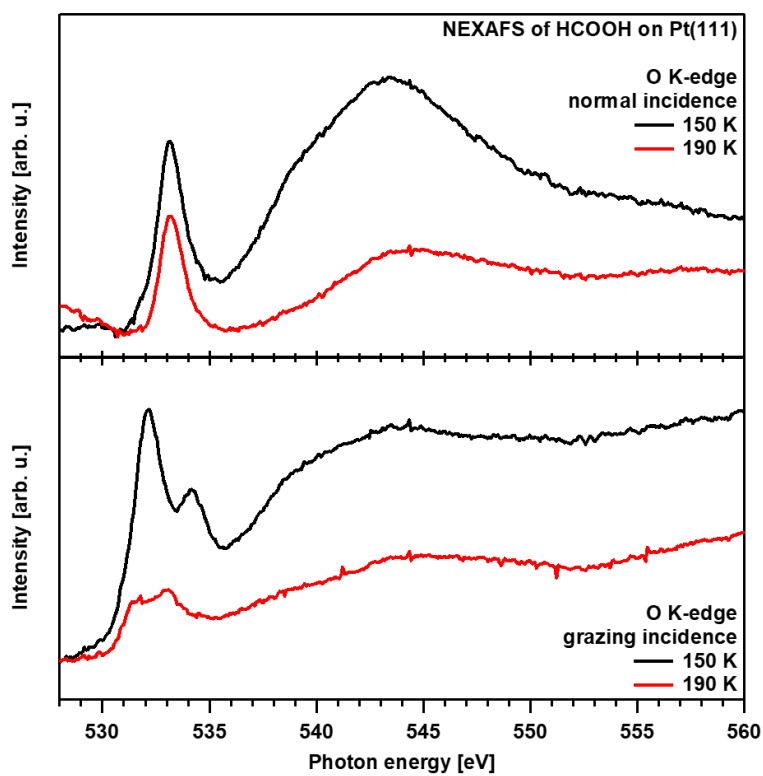


Figure 38: O K-edge NEXAFS of formic acid on Pt(111) at 150 and 190 K in normal (0°) and grazing (70°) incidence.

7.4 Conclusion

The adsorption and consecutive reaction of formic acid on Pt(111) and Ni(111) in UHV has been investigated using high-resolution XPS, TPD and NEXAFS. Comparing the XPS experiments on both surfaces, two different formic acid species and a formate species are found upon adsorption at low temperature on both surfaces. However, different temperature-induced reaction and decomposition pathways are observed on Ni(111) and Pt(111).

The occurrence of two different formic acid species is unexpected, but within the scope of this study, repeatable behavior on two different crystals throughout several experiments. Still, it has no influence on the general dehydrogenation behavior observed here, which is in line with previous studies.

On Ni(111), a partial conversion of the formic acid I and II to formate is observed above 210 K. Meanwhile, formic acid II also partially dehydrates, forming CO and instantly desorbing H₂O below 240 K. Above this temperature the remaining formic acid I and formate dehydrogenate into CO and instantly desorbing CO₂ until 330 K, accompanied by partial molecular desorption of formic acid. The desorption of CO is observed until 440 K.

On Pt(111), also a partial conversion of formic acid to formate is observed above 160 K in XPS. Thereafter, next to molecular desorption of formic acid, all species dehydrogenate into the desorption product CO₂ by 220 K, which is also in agreement to the obtained TPD results. NEXAFS suggests a disordered adsorption geometry of formic acid/formate on Pt(111) at 150 K, while the spectra at 190 K indicate perpendicular bound formic acid/formate.

8. Formation of h-BN from Ammonia borane and Borazine on Ni(111)

The results presented in this chapter have already been published^[152]; the content of this chapter is adapted from:

A HR-XPS study of the formation of h-BN on Ni(111) from the two precursors ammonia borane and borazine

P. Bachmann, F. Düll, F. Späth, U. Bauer, H.-P. Steinrück and C. Papp

The Journal of Chemical Physics, **2018**, *149* (16), 164709.

Reprinted (adapted) with permission. Copyright 2018 AIP Publishing.

Authorship: P. Bachmann

Together with borazine, ammonia borane is a prominent precursor molecule for the formation of hexagonal boron nitride, which is of high interest as 2D-material and graphene analogue. Ammonia borane also is a possible solid hydrogen carrier for renewable energies with high storage density. Using X-ray photoelectron spectroscopy and temperature-programmed desorption, we investigated low-temperature adsorption and dehydrogenation during heating of borazine and ammonia borane on Ni(111) to form h-BN. For borazine, we observe the formation of disordered boron nitride above 300 K, which starts to form hexagonal boron nitride above 600 K. Ammonia borane shows multiple dehydrogenation steps at the boron and nitrogen atoms up to 300 K. This results in various BH_xNH_y species, including borazine-like intermediates, before the formation of disordered boron nitride and finally hexagonal boron nitride, analogous to the borazine decomposition.

8.1 Introduction

Hexagonal boron nitride (h-BN) has become a material of high interest in recent years. Being an isoelectronic graphene analogue, with alternating nitrogen and boron atoms in a 2D honeycomb structure^[153-155], it exhibits various favorable chemical and physical properties, enabling e.g. applications as lubricant or as anti-oxidation coating.^[156-159] Although the structures of h-BN and graphene are similar, their electronic properties are very different. While graphene is a zero bandgap semi-metal with excellent electrical properties^[160], h-BN is an insulator with a wide band gap of ~ 5 eV.^[161-163] Combining these properties, graphene and h-BN make up an ideal pair for novel electronic devices.^[164] Additionally, the properties and ultimately the applications of such 2D-layers can be tweaked by further functionalization, like hydrogenation or oxidation.^[165-166]

There are many known routes for the synthesis of h-BN, mainly involving pyrolysis of boron- and nitrogen-containing reactants^[167], including ammonia borane (AB, BH_3NH_3) and borazine (BHNH)₃. These also exhibit interesting properties of their own. Borazine is structurally very similar to benzene^[168], but with a different, sometimes controversial, degree of aromaticity.^[169] The solid AB is isoelectric to ethane and has attracted interest as possible hydrogen storage material, with 19.6 wt% H_2 storage capacity.^[170-173] While this storage capacity is nearly unmatched, the formation of boron nitride upon total dehydrogenation is a drawback, as the latter is energetically very stable and it thus is challenging to regenerate AB by hydrogenation. Therefore, selective dehydrogenation and hydrogenation catalysts for AB and its decomposition products, which include polyaminoboranes and borazine-like structures, are of high interest.^[174-183]

In this chapter a detailed *in situ* study of the formation of h-BN submonolayers from AB and borazine on a Ni(111) single-crystal surface in ultrahigh vacuum (UHV) is presented. While h-BN is usually prepared at high temperatures from these precursors,^[153, 167, 184-185] the main goal of this study is the investigation of the temperature-induced reaction steps towards h-BN. To be able to follow the individual reaction steps, the molecules were adsorbed at low temperature and the dehydrogenation and decomposition of both h-BN precursors upon heating was monitored *in situ* by XPS in a quantitative fashion. We identified the individual reaction steps and surface species during adsorption and heating, including the

dehydrogenation of AB and borazine, leading to the formation of disordered boron nitride and later h-BN.

8.2 Specific experimental setup

The XPS experiments were performed at the synchrotron BESSY II at beamlines U49-2 PGM-2 and UE56-2 PGM-2 using the synchrotron UHV machine (see Chapter 3.1). TPD experiments were performed in a separate TPD UHV machine (see Chapter 3.2).

The adsorption of ammonia borane on Ni(111) was conducted with a solid evaporator, heated to 50 °C; for borazine, the dosing system, using the vapor pressure of the substance, was utilized. The heating rate during TPXPS was set to 0.5 K/s for borazine and 0.2 K/s for ammonia borane. The nitrogen and boron coverages at the end of the independent N 1s and B 1s adsorption experiments of AB and borazine on Ni(111) were calibrated using the known saturation coverage of a closed hexagonal boron nitride (h-BN) layer in the N 1s region, which equals to 1 N-ML and 1 B-ML on Ni(111)^[154] (see Figure 45, page 120). Thereby, 1 N-ML (1 B-ML) corresponds to 1 nitrogen (boron) atom / Ni atom. Peak fitting of the B 1s and N 1s spectra was done using Doniach-Šunjić-profiles^[53] convoluted with a Gaussian function. The B 1s and N 1s regions were measured at 380 and 500 eV with resolutions of 200 meV at an emission angle of 0° relative to the surface normal. Prior to each spectrum, the sample position is shifted to avoid beam damage. All spectra are referenced to the Fermi edge of Ni(111).

Ammonia borane (97%) was purchased from Sigma-Aldrich. Borazine was self-synthesized according to Wideman and Sneddon.^[186]

8.3 Results and discussion

To analyze the formation of h-BN by adsorption and reaction of ammonia borane and borazine on Ni(111), we use in situ high-resolution XPS of the B 1s and N 1s core levels, temperature programmed XPS (TPXPS), and temperature programmed desorption (TPD). In the following, we will concentrate on the temperature-induced reaction of the molecules and the similarities of their decomposition pathways, ultimately forming hexagonal boron nitride.^[153-154, 165, 187]

8.3.1 Borazine

We first address the cyclic reactant borazine, (B₃NH₃)₃, and its temperature-induced decomposition. Borazine is a common precursor to h-BN and a possible reaction product in the temperature-induced decomposition of ammonia borane. Therefore, it is crucial to understand its surface chemistry and spectral fingerprint, in order to analyze the reaction of ammonia borane.

We measured both B 1s and N 1s regions during exposure of Ni(111) to borazine at 140 / 130 K and consecutive heating. Selected spectra of the adsorption and reaction of 1.17 L (B 1s) and 1.28 L (N 1s) are depicted in Figure 39a and b, while spectra including fitted envelopes are provided in Figure 40a and b with binding energies given in Table 4 (page 119). The corresponding quantitative analyses are shown in Figure 41a and b, respectively. Additionally, selected XP-spectra including fitted envelopes are provided in. During exposure to borazine, we observe the growth of one B 1s peak at 189.4 eV and one N 1s peak 398.6 eV (both indicated in green). The onset of multilayer formation is observed at ~0.5 L. In the B 1s region, this is evident from one additional signal at 190.0 eV (blue), which shifts to 190.3 eV at the highest exposure of 1.17 L. In the N 1s region, a multilayer peak at 399.2 eV and an accompanying shoulder at 398.1 eV (both blue) are seen, damping the N 1s monolayer signal by 25% at 1.28 L. The origin of the shoulder is unclear at the moment. In the B 1s, no significant damping is observed, which is attributed to a smaller coverage in the respective experiment and the larger inelastic mean free path of the photoelectrons (190 eV for the B 1s region (hν=380 eV) vs 100 eV in the N 1s region (hν=500 eV)). The coverages at the end of the independent adsorption experiments amount to 0.39 B-ML in the B 1s experiment and 0.47 N-ML in the N 1s experiment. The significantly smaller total coverage in the B 1s

experiment is due to the higher adsorption temperature (140 K vs 130 K for the N 1s region), which leads to partial desorption of the multilayer.

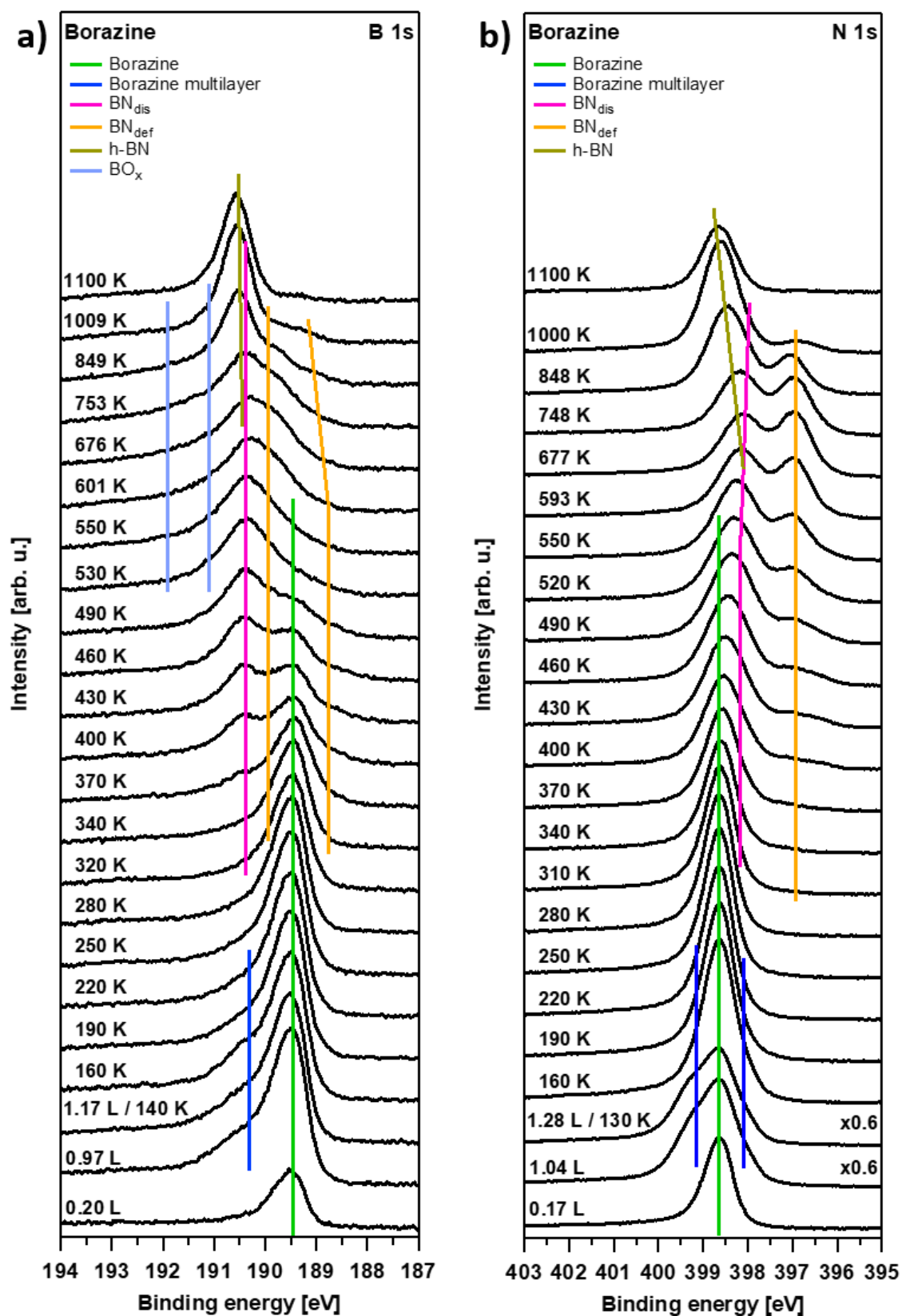


Figure 39: Selected B 1s (a, $h\nu = 380$ eV) and N 1s (b, $h\nu = 500$ eV) XPS spectra of the adsorption and TPXPS of borazine on Ni(111).

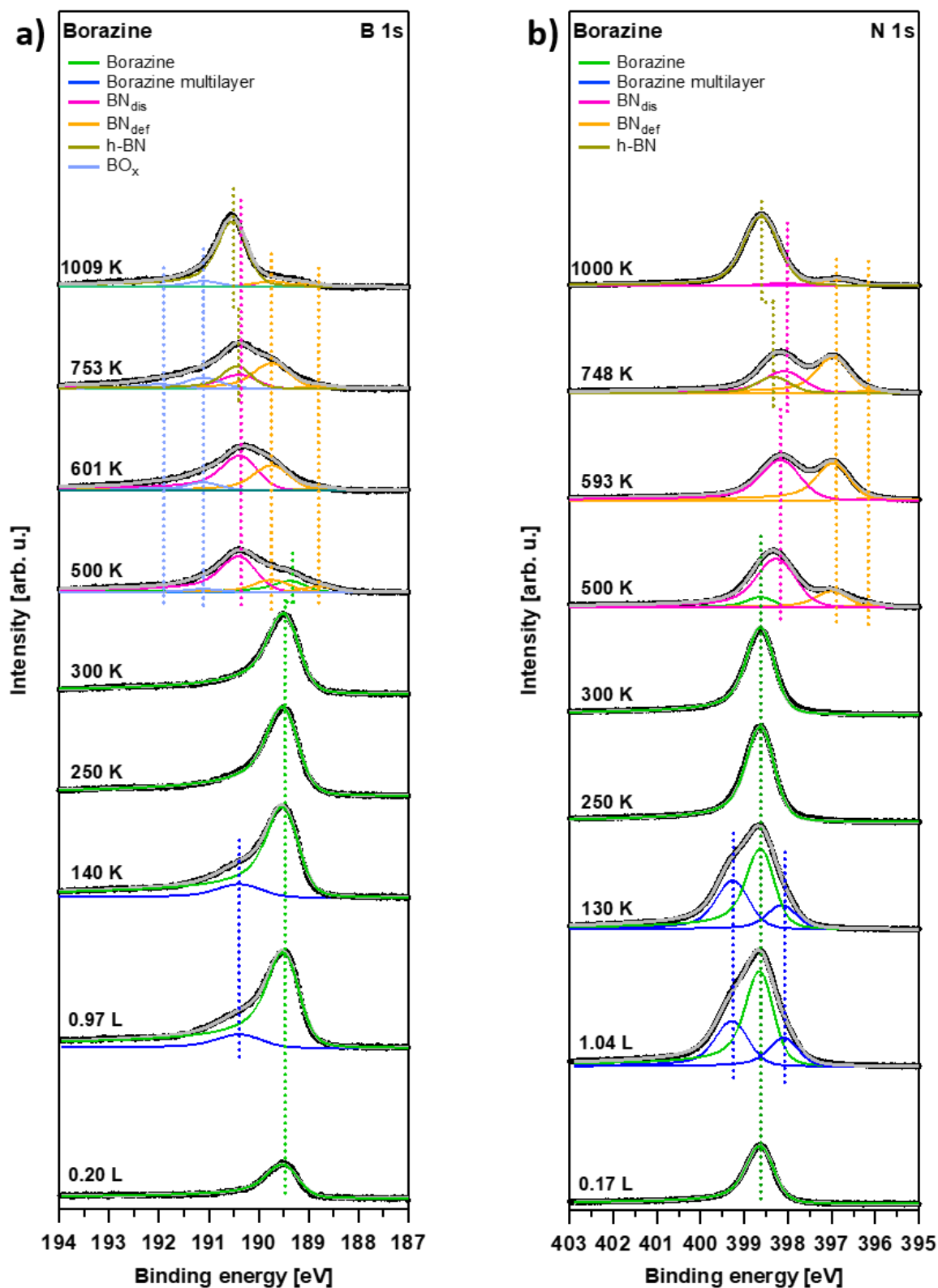


Figure 40: Selected B 1s (a, $h\nu = 380$ eV) and N 1s (b, $h\nu = 500$ eV) XPS spectra of the adsorption and TPXPS of borazine on Ni(111) including fits.

To study the dehydrogenation reaction of borazine and the consequent submonolayer formation of h-BN on Ni(111), we performed TPXPS experiments. The sample is heated from 140 to 550 K with a linear heating ramp of 0.5 K/s while XP spectra are continuously recorded approximately every 10 K. Above 550 K, the sample is resistively heated with larger temperature steps. Upon heating, a decrease of the multilayer signal due to desorption is observed in both B 1s and N 1s core levels up to 250 K. Simultaneously, the damping of the N 1s monolayer signal is reversed. Upon heating to 300 K, the borazine monolayer signals in the N 1s and B 1s regions then slightly decrease, likely due to further desorption of borazine. Starting at 300 K, major changes in the N 1s and B 1s spectra indicate the onset of borazine decomposition.

In the N 1s region, two new peaks emerge at lower binding energies, which are related to boron nitride forming on the surface. The dominating peak at 398.2 eV (pink) is assigned to disordered boron nitride (BN_{dis}) structures in the forming surface mesh, and the peak at 396.9 eV (ochre) to defective and ill-terminated disordered boron nitride (BN_{def}) with missing BN bonds in the mesh.^[153, 155, 188-189] We suggest that the binding energy decreases with the number of defects, that is, the peak at 396.9 eV is due to nitrogen with two boron neighbors and a further very small contribution (not highlighted in Figure 39b for clarity) at 396.1 eV is due to only one boron neighbor. The borazine signal declines until ~ 560 K, while the disordered boron nitride signals grow with increasing temperature. BN_{dis} reaches its highest coverage with 0.19 N-ML (see Figure 41b) at 500 K, then starts to decrease above 540 K, and shifts by 0.2 eV to lower binding energies. BN_{def} reaches its highest coverage of 0.15 N-ML at ~ 620 K. Above 620 K, a new peak develops at 398.2 eV (olive), which is assigned to hexagonal boron nitride (h-BN). This behavior is expected, because higher temperatures are needed for defects to disappear to form a well-ordered h-BN layer. The decomposition of borazine into boron nitride is further supported by TPD measurements of H_2 ($m/z = 2$) in Figure 42, which show a pronounced peak with a rate maximum at 360 K and a tail reaching up to 600 K. This behavior is consistent with the decomposition of borazine up to ~ 600 K, as seen in the TPXPS. The N 1s signal of h-BN^[165, 187, 190] steadily grows above 620 K, reaching ~ 0.22 N-ML at 1050 K while shifting towards 398.6 eV. Simultaneously, the disordered boron nitride species declines up to 1100 K. At this temperature, h-BN is not stable anymore, as the coverage is already declining.

The B 1s region above 300 K shows matching results. The monolayer signal at 189.4 eV decreases to vanish until 600 K, while shifting by 0.1 eV to 189.3 eV. Simultaneously, three new peaks emerge. The fast-growing peak at 190.4 eV (pink) is assigned to BN_{dis} , while the two smaller peaks at 189.7 and 188.7 eV (both ochre) are attributed to the disordered defective BN_{def} . Analogous to the N 1s region, we suggest the peaks at 189.7 and 188.7 eV to be due to boron with two and one nitrogen neighbors, respectively. At ~ 530 K, BN_{dis} reaches its maximum coverage of ~ 0.15 B-ML and BN_{def} amounts to 0.06 B-ML, see Fig. 2a. At higher temperatures, the BN_{dis} peak at 190.4 eV starts to decrease and slowly shifts to 190.3 eV. Simultaneously, the BN_{def} peaks at 188.7 eV continues to grow up to 0.10 B-ML at 650 K, and shifts to 188.8 eV. Starting at 620 K, a new signal evolves at 190.4 eV (olive), due to h-BN. It steadily grows and continually shifts to 190.5 eV at 1050 K.^[165, 187, 190] At the same time, the BN and BN_{def} peaks further decline up to 1100 K with the BN_{def} peak further shifting towards 189.0 eV. In agreement with the N 1s results, the h-BN signal starts to decrease above 1050 K also in the B 1s region.

Starting at 500 K, two additional signals appear at higher binding energies of 191.1 and 191.9 eV, (both light blue) reaching a maximum coverage of ~ 0.05 B-ML above 550 K. These peaks are assigned to boron oxides^[191-192], which form due to oxygen on the surface, which arises from small impurities like H_2O in borazine or oxygen from the Ni bulk. These boron oxide signals disappear from 900 to 1100 K (not shown in Figure 41a for clarity).

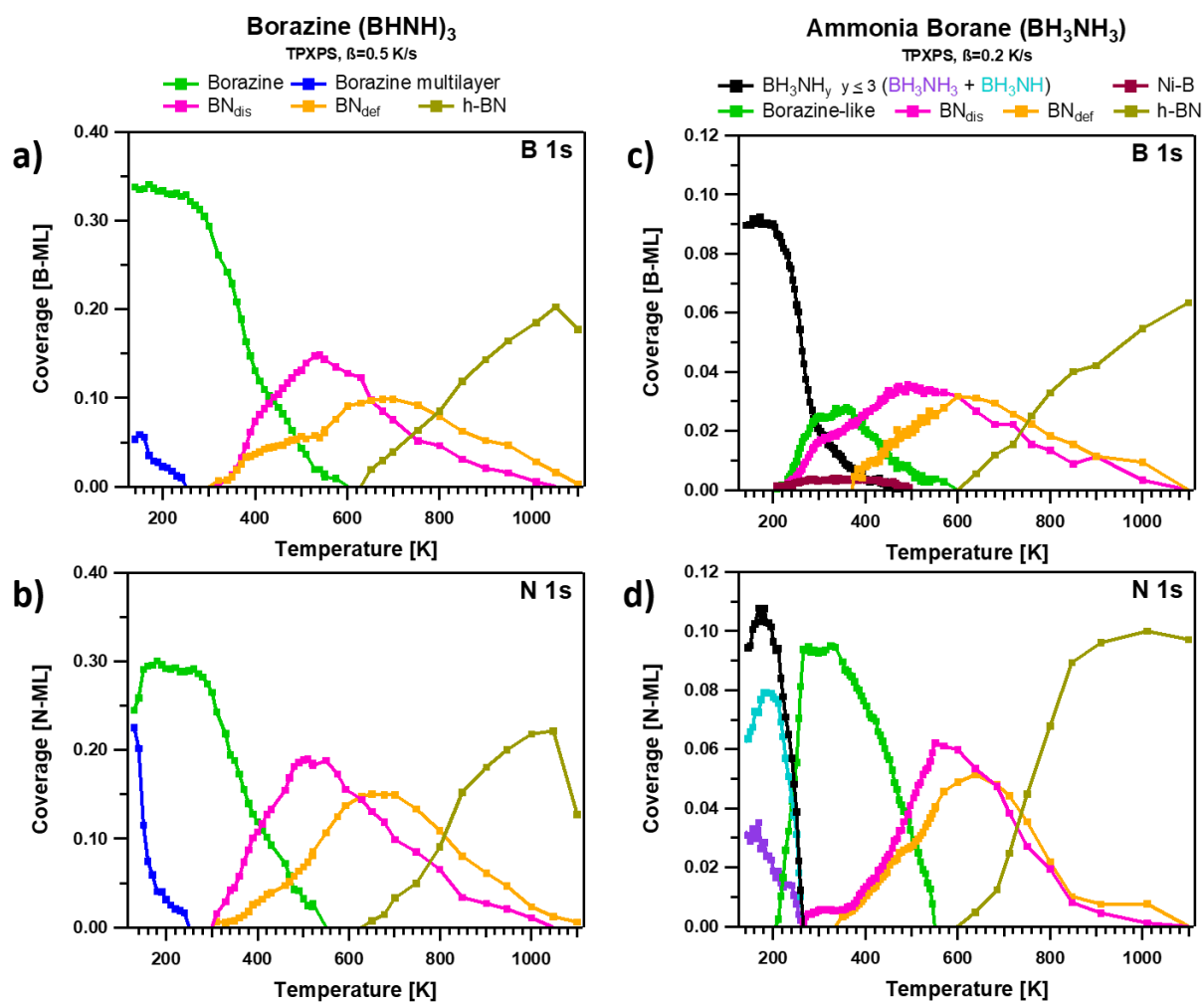


Figure 41: Quantitative analysis of the B 1s and N 1s region TPXPS experiments of borazine (a, b) and ammonia borane (c, d) shown in Figure 39 and Figure 43.

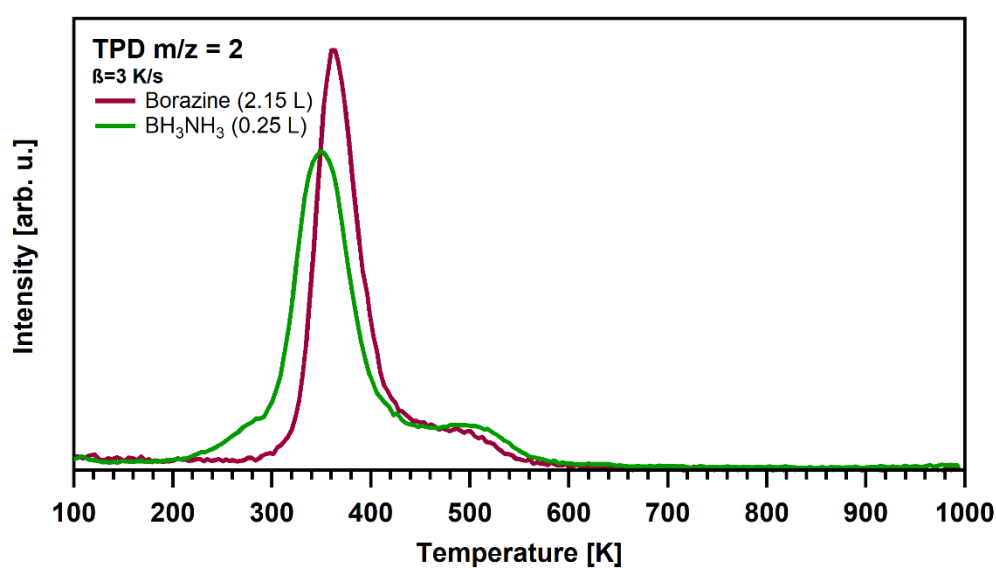


Figure 42: H₂ (m/z = 2) TPD spectra of ammonia borane and borazine on Ni(111), collected at a heating rate of 3 K/s.

8.3.2 Ammonia borane

With the knowledge from the temperature-induced reaction and decomposition of borazine leading to h-BN, and of the thereby identified reaction intermediates, we then examined the hydrogen-rich ammonia borane (AB) as precursor for the formation of a h-BN submonolayer. The Ni(111) surface was exposed to ~ 1.15 L AB at 130 K, in both, the B 1s and N 1s experiments, which yielded a submonolayer coverage. Selected spectra collected during adsorption and during heating are shown in Figure 43a and b; spectra including fitted envelopes are provided in Figure 44a and b with binding energies given in Table 4 (page 119). The corresponding quantitative analysis of TPXPS is shown in Figure 41c and d.

In the B 1s region, adsorption leads to one sharp and steadily growing peak at 188.4 eV (black), reaching a coverage of 0.09 B-ML at the highest exposure. In the N 1s region, we find the growth of two distinct peaks at 398.8 (cyan) and 400.9 eV (violet), shifting by 0.1 eV to 398.7 and 400.8 eV by the end of the exposure. Until 0.2 L, their coverage is about equal, but at higher exposures the peak at 398.7 eV dominates, yielding a ratio of ~ 1.6 at the highest exposure of 1.13 L, which amounts to 0.10 N-ML. We propose that the peak at 400.8 eV is due to intact AB and that the peak at 398.7 eV due to BH_3NH ; this partially dehydrogenated species is directly formed upon adsorption at 130 K. The observed chemical shift of 2.1 eV is in line with shifts in the range of 1 eV per split-off hydrogen atom from a nitrogen atom observed for N-heterocyclic compounds and ammonia.^[67, 193] Nevertheless, we cannot completely rule out the main peak at 398.7 eV being a BH_3NH_2 species.

The thermal evolution after the adsorption experiments is investigated by TPXPS with a heating rate of 0.2 K/s; above 550 K, again resistive heating is used, as described for the borazine experiments. Upon heating to 150 K, the N 1s signal of BH_3NH at 398.7 eV shifts to 398.6 eV, and slightly increases at the cost of the BH_3NH_3 peak at 400.8 eV. We attribute this shift to the increasing amount of coadsorbed hydrogen on the surface, which stems from AB dehydrogenation during adsorption and heating to 150 K. Between 150 and 180 K, the BH_3NH peak shifts from 398.6 to 398.9 eV, while still increasing on behalf of the AB peak. It reaches a maximum coverage of 0.08 N-ML at 180 K. We attribute the observed shift of 0.3 eV due to the desorption of significant amounts of coadsorbed H_2O between 160 and 180 K^[194], which was an inevitable impurity during AB adsorption. Above 180 K, the BH_3NH peak shifts to a slightly lower binding energy of 398.8 eV. It declines together with the AB peak at 400.8 eV

until 260 K. Simultaneously, starting at 200 K due to the further dehydrogenation of AB, a new peak emerges at 398.5 eV (green), which reaches its maximum coverage of 0.09 N-ML at 270 K; see Figure 41d. We assign this peak to a borazine-like species (BH_xNH , with $x \leq 2$), mostly having only one hydrogen left at both the boron and the nitrogen atom. The binding energy of 398.5 eV is very similar to the 398.6 eV observed for borazine, emphasizing the similarities of the nitrogen bonding environment. Similar reaction behavior and borazine-like intermediates are observed in ambient pressure pyrolysis of AB.^[170, 173, 195]

Starting at ~ 260 and 340 K (see Figure 41d), the growth of two new peaks at 398.2 (pink) and 397.0 eV (ochre) is observed, respectively, while the borazine-like peak declines until 550 K. In analogy to the situation for borazine, these peaks are assigned to BN_{dis} and BN_{def} , respectively, representing the end of the dehydrogenation process around 550 K. Notably, BN_{dis} is observed ~ 40 K earlier than for borazine, which likely is due to the lower surface coverage in the AB experiment. The additional small contribution at 396.1 eV, observed during borazine dehydrogenation, is not distinguishable for AB, possibly due to the significant lower surface coverage. The TPD measurements of H_2 ($m/z = 2$) of AB in Figure 42 visualize the hydrogen loss over a broad temperature range with a desorption maximum at 350 K and a tail up to 580 K, accompanied by a small feature at ~ 290 K. The dehydrogenation of AB and the desorption maximum are in line with the discussed XPS data, considering hydrogen desorption only takes place above 290 K on Ni(111).^[196]

BN_{dis} and BN_{def} reach their maximum coverages of 0.06 and 0.05 N-ML at 550 and 620 K, respectively, before declining up to 1100 K; BN_{dis} shifts by 0.2 eV to lower binding energy. Simultaneously to the decrease of the BN_{dis} and BN_{def} peaks, the h-BN peak at 398.4 eV (olive) develops above ~ 600 K, and shifts to 398.6 eV at 1000 K with a coverage of 0.10 N-ML. Only above 1100 K, the signal of h-BN declines (not shown). The decline of the h-BN signal in the borazine experiments at the highest temperature (last data point in Figure 41) might be correlated with the higher coverage; alternatively, since the two substances were not part of the same measurement series, also small differences in the attachment of the thermocouple and annealing time at the highest temperature may contribute.

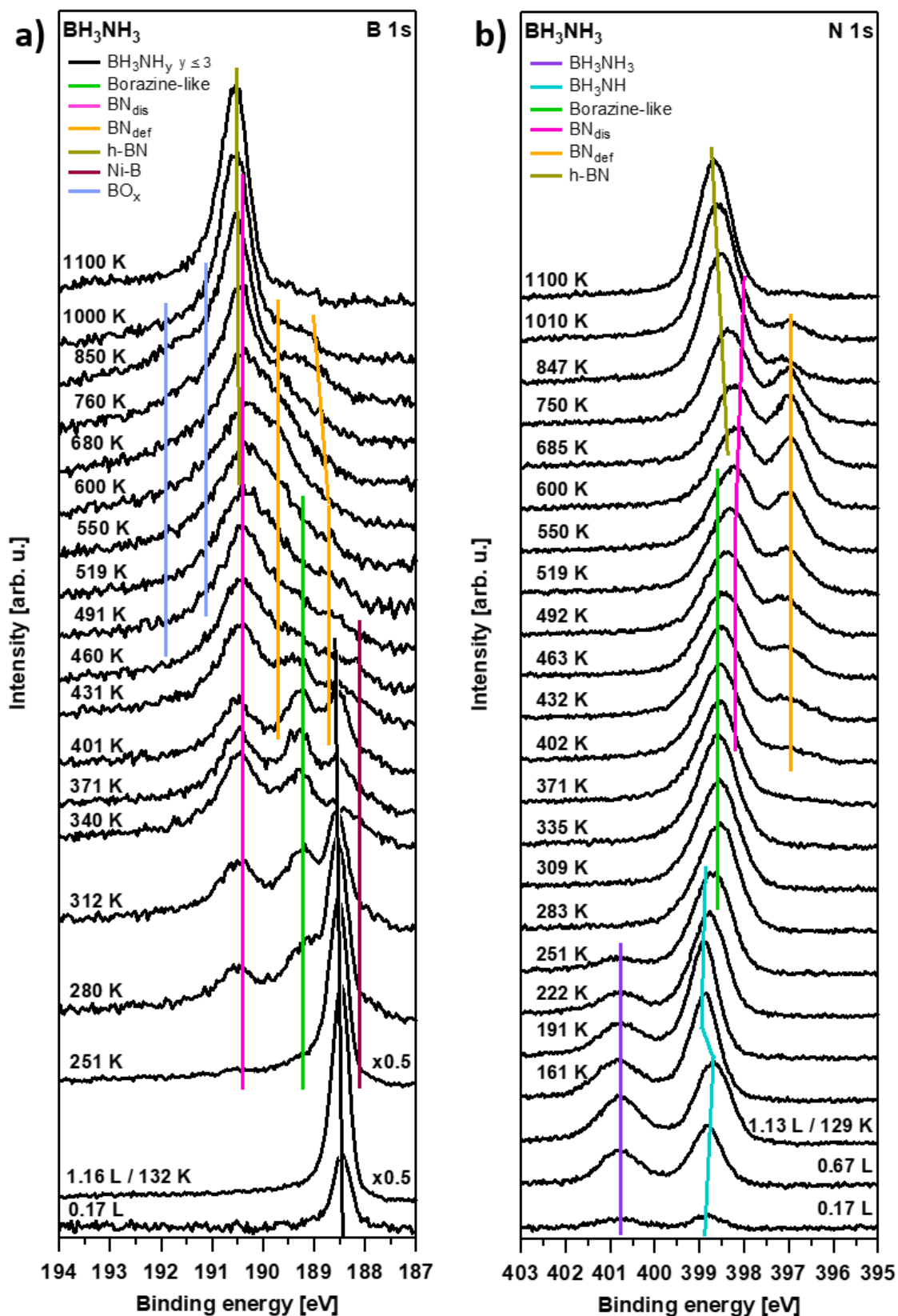
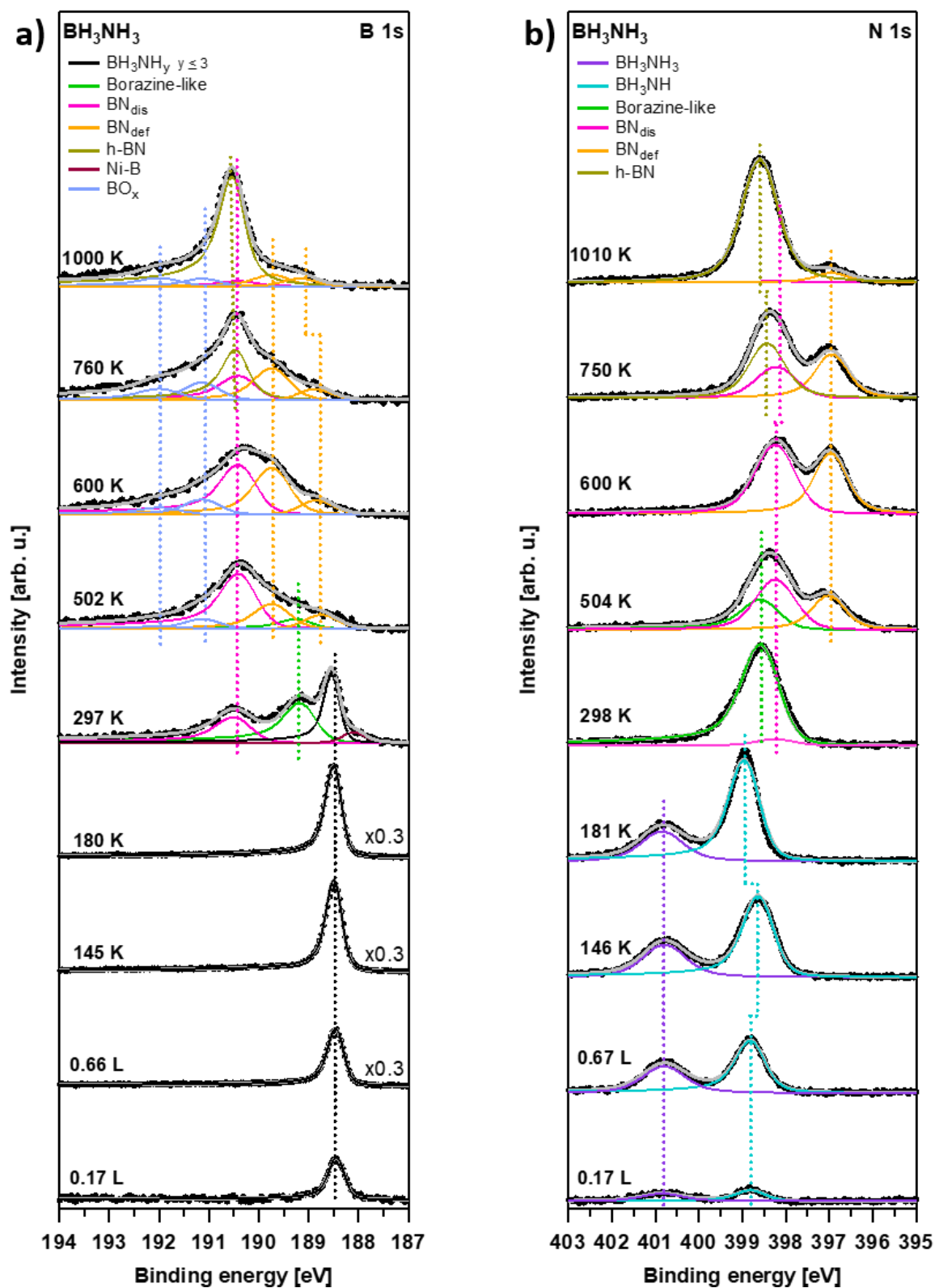


Figure 43: Selected B 1s (a, $h\nu = 380$ eV) and N 1s (b, $h\nu = 500$ eV) XPS spectra of the adsorption and TPXPS of ammonia borane on Ni(111).



In the B 1s region, the single peak at 188.4 eV (black) observed upon AB adsorption is assigned to both AB and BH₃NH. The observation of only one peak, in contrast to the two peaks in the N 1s spectra indicates that the B 1s binding energy is not sensitive to the number of hydrogens bound to the nitrogen. Upon heating, no changes were observed in the B 1s region until ~200 K, in contrast to the N 1s region. Above 200 K, we find the simultaneous development of two distinct new peaks, while the overall coverage decreases by ~20%. This is possibly due to photoelectron diffraction effects, as no signal reduction is observed in the N 1s region. The signal at 189.2 eV (green) is attributed to the borazine-like species, with its binding energy close to the one of borazine at 189.4 eV. The peak at 190.4 eV (pink) is assigned to BN_{dis}, as for borazine decomposition. Notably, it is observed already at ~70 K lower temperature than for borazine (see Figure 41), indicating that neat borazine is more stable towards BN formation and emphasizing a complex dehydrogenation pathway of AB, as resembled in ambient pressure pyrolysis.^[170, 173] The very small contribution at 188.1 eV (brown) is attributed to minor amounts of a Ni-B alloy^[191], reaching only 0.004 B-ML over the course of its existence up to 500 K.

While the borazine-like species and BN_{dis} grow rapidly up to ~0.03 and ~0.02 B-ML at 300 K, the BH₃NH signal severely decreases from 0.09 to 0.02 B-ML, while shifting by 0.1 eV to 188.5 eV; it finally vanishes at 470 K. The borazine-like species also shifts by 0.1 eV to 189.2 eV above 300 K, while remaining at nearly constant coverage up to 370 K, before it starts to decline up to 600 K, in favor of two new peaks at 189.7 and 188.7 eV (both ochre). These peaks are attributed to BN_{def}, and were also observed during the borazine TPXPS (see Figure 39, Figure 40, Figure 41). Above 600 K, again the h-BN signal at 190.4 eV (olive) starts to grow, at the cost of the declining signals of the BN_{dis} and BN_{def} until 1100 K; the BN_{def} signal at 188.7 shifts by 0.3 eV up to 189.0 eV, while the h-BN signal shifts by 0.1 eV to 190.5 eV. Notably, at 400 K, additional signals at 191.9 and 191.1 eV (both light blue) emerge, which are assigned to boron oxides forming due to oxygen contaminations on the surface, as already described for borazine above. The boron oxide reaches its maximum at ~900 K, before also declining until 1100 K, where h-BN is the only species left with a coverage of ~0.06 B-ML.

Overall, the decomposition pathways of borazine and AB show great similarities, as the reactions of both precursors follow the same pathway, especially above 300 K, where equal intermediates exist with BN_{dis} and BN_{def}, eventually leading to h-BN. Also, the existence of the

borazine-like species in the AB decomposition process strongly suggests that ring formation is favored for AB decomposition and thus borazine is a possible reaction intermediate.

Species	Core level	Peak #	Borazine Binding energy (range) [eV]	AB Binding energy (range) [eV]
Borazine multilayer	B 1s	1	190.0 (190.0-190.3)	-
	N 1s	1	398.1	-
		2	399.2	-
Borazine monolayer	B 1s	1	189.4 (189.3-189.4)	-
	N 1s	1	398.6	-
BH ₃ NH _y (y ≤ 3)	B 1s	1	-	188.4 (188.4-188.5)
BH ₃ NH ₃	N 1s	1	-	400.8
BH ₃ NH	N 1s	1	-	398.7 (398.6-398.7)
Borazine-like	N 1s	1	-	398.9 (398.8-398.9)
Borazine-like	B 1s	1	-	189.1 (189.1-189.2)
BN _{dis}	B 1s	1	190.4 (190.3-190.4)	190.4
	N 1s	1	398.2 (398.0-398.2)	398.2 (398.1-398.2)
BN _{def}	B 1s	1	188.7 (188.7-189.0)	188.7 (188.7-189.0)
		2	189.7	189.7
	N 1s	1	396.9 (396.8-396.9)	397.0 (396.9-397.0)
		2	396.1	-
B _x O _y	B 1s	1	191.1	191.1
		2	191.9	191.9
h-BN	B 1s	1	190.4 (190.4-190.5)	190.4 (190.4-190.5)
	N 1s	1	398.3 (398.3-398.6)	398.3 (398.3-398.7)
Ni-B	B 1s	1	-	188.1

Table 4: Binding energies and binding energy ranges of the fitted peaks of borazine and ammonia borane as shown in Figure 40 and Figure 44.

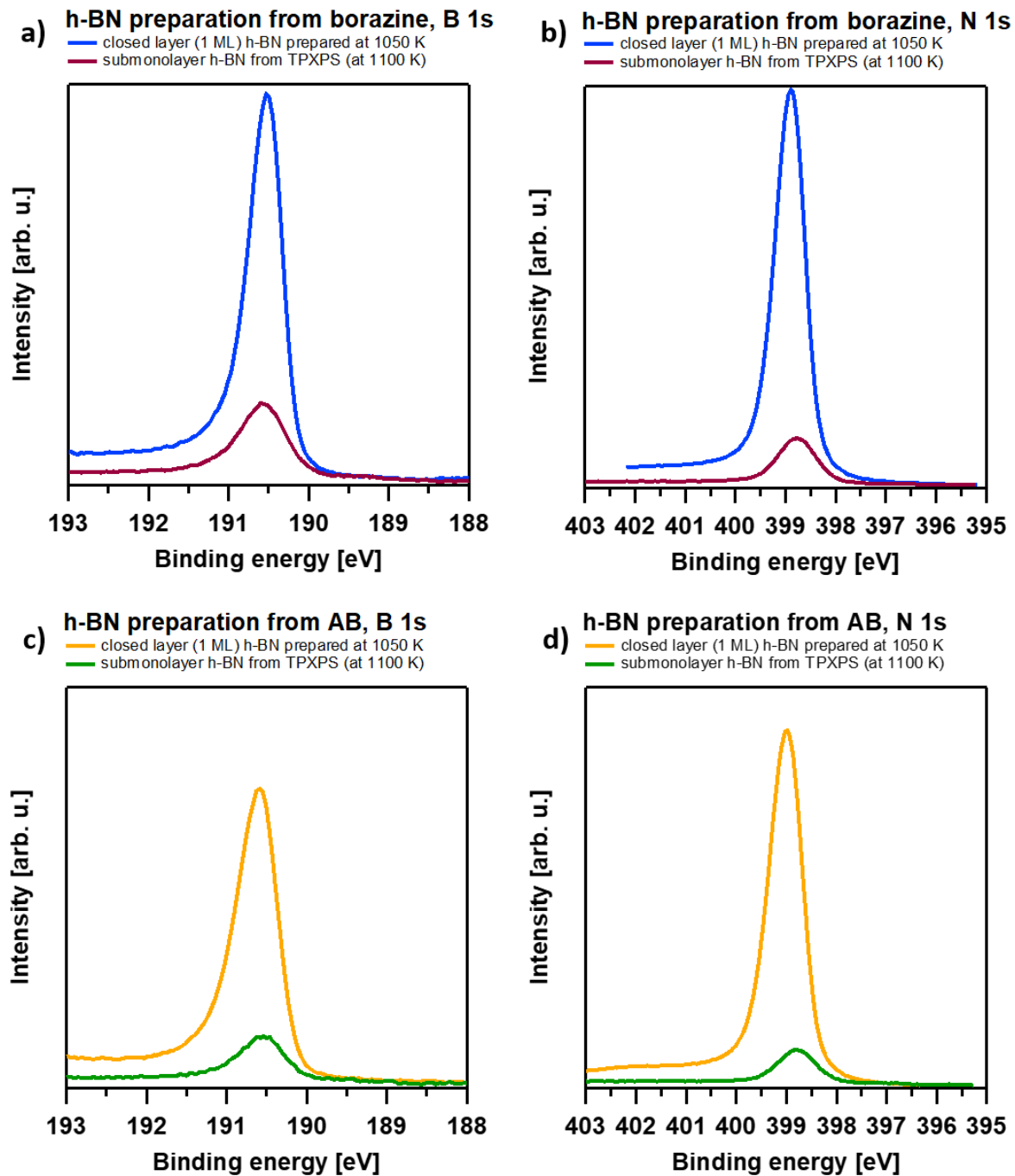


Figure 45: Comparison of h-BN preparations from borazine (a, b) and ammonia borane (c, d) in the B 1s and N 1s regions.

8.4 Conclusion

We performed a high-resolution XPS study, assisted by TPD, of the formation of h-BN submonolayers from ammonia borane and borazine on Ni(111). While h-BN is usually prepared at high temperatures from these precursors (see Figure 45), the main goal of this study is the investigation of the temperature-induced reaction steps towards h-BN. Thereby, we identified disordered BN_{dis} and defective BN_{def} upon heating borazine to above 300 K, which then are converted to h-BN above 600 K. For ammonia borane, a more complex reaction scheme is observed. Dehydrogenation of AB already occurs upon adsorption, resulting in a BH_3NH species, next to molecularly adsorbed AB. While AB is declining up to 260 K upon heating, BH_3NH loses hydrogen also at the boron atom, forming borazine-like species. While BN_{dis} formation is already observed between 230 and 260 K, that is, at lower temperatures than for borazine, BN_{def} formation takes place above 340 K. Both are again converted to h-BN above 600 K. Besides the main reaction to h-BN, we observe minor formation of Ni-B between 200 and 500 K. To finally conclude, we find a nearly identical onset of h-BN formation at ~ 600 K for both ammonia borane and borazine.

9. Summary

Liquid Organic Hydrogen Carriers are a promising approach in order to store energy in form of hydrogen. In the past, investigations on, e.g., the LOHC systems N-ethylcarbazole/H₁₂-N-ethylcarbazole and dibenzyltoluene/H₁₈-dibenzyltoluene have shown that this kind of energy storage is possible and sustainable towards a “green” future, possibly being a key technology for the success of renewable energy distribution and storage. Following these accomplishments, the dehydrogenation of several LOHC systems has been investigated and evaluated within this thesis, using model catalysts and surface science methods like XPS. Thereby, the focus especially lies on the investigation of LOHC systems containing N-heterocyclic and homocyclic five- and six-membered rings, as molecules containing these building blocks, including the examples stated above, usually exhibit favorable dehydrogenation characteristics.

The first LOHC system discussed in this thesis consists of the hydrogen-lean carrier molecule indole, the partially hydrogenated indoline (hydrogenated at the five-membered ring) and the fully hydrogenated octahydroindole. The adsorption and temperature-induced reaction of the molecules on Pt(111) was investigated using a combination of XPS, TPD, IRAS and NEXAFS. As seen in XPS, octahydroindole and indoline dehydrogenate into an indole intermediate above 270 K. Nearly simultaneously, at 270 K, deprotonation of the NH-group of indole takes place as observed by XPS, forming an indolide species, which is observed up to 540 K on the surface, before the decomposition of the molecular framework into fragments starts. Moreover, upon adsorption of octahydroindole, XPS and IRAS show partial protonation of the NH-group up to 290 K in presence of OH⁻ traces. Also, in the C 1s region, a π -allylic minority species is identified for octahydroindole, which exists from 170-450 K, during dehydrogenation. An indoline intermediate is not observed. To form an efficient and functioning hydrogen storage cycle, deprotonation of the NH-group must be avoided in real catalysis. There, due to other boundary conditions, irreversible binding of indole to the surface and the resulting formation of indolide may possibly not even take place.

Following the successful investigation of the indole-based LOHC system, the influence of substitution was examined by studying the adsorption and temperature-induced dehydrogenation of 2-methylindole, 2-methylindoline and 2-methyloctahydroindole on Pt(111) using XPS and TPD. While this LOHC system shows many similarities to the

unsubstituted indole system, there are some distinct differences regarding the stability of reaction intermediates and the reaction pathway. For the hydrogen-lean 2-methylindole, the deprotonation of the NH-group takes place above 240 K, resulting in a 2-methylindolide species, which is observed up to 490 K. Thereafter, only decomposition fragments are left. Dehydrogenation of the partially hydrogenated 2-methylindoline (hydrogenated at the five-membered ring) takes place above 240 K, forming a 2-methylindole intermediate. Afterwards, the same reaction path as for 2-methylindole is observed. The reaction of the fully hydrogenated 2-methyloctahydroindole is more complex. First, it partly dehydrogenates at the six membered-ring above 230 K to form two different π -allylic intermediate species, where the methyl-group is supposedly either up or down tilted in regard to the surface. Nearly simultaneously, a 2-methylindoline intermediate emerges. Above 270 K, a 2-methylindole intermediate is observed, before deprotonation of the NH-group leads to 2-methylindolide, which then decomposes until 490 K. Again, the deprotonation of the NH-group is an unwanted reaction that needs to be avoided in real catalytic conditions. Compared to the unsubstituted indole LOHC system, here decomposition is observed at significantly lower temperature and the overall system is less stable. In contrast, however, 2-methylindoline is observed as a stable intermediate. Still, the outcome of this study is highly interesting, as 2-methylindoline is known to react at favorably low temperatures in real catalysis. However, 2-methyloctahydroindole might be an even better candidate, as shown here with the six-membered ring of 2-methyloctahydroindole being dehydrogenated before the five-membered ring of 2-methylindoline in UHV.

Based on the studies of indoles, the adsorption and temperature-induced dehydrogenation reaction of the LOHC system indene, indan and hexahydroindan was investigated using XPS and TPD. This system can be seen as homocyclic analog to the heterocyclic indoles. Consecutively, familiar reaction steps are found. For the hydrogen-lean carrier molecule indene, the dehydrogenation of the CH₂-group to CH in the five-membered ring is observed above 220 K. This results in an indenyl surface species, which is basically an indolide analog. Dehydrogenation of the partially hydrogenated indan (hydrogenated at the five-membered ring) also leads to indenyl above 240 K; indene is not observed as a dehydrogenation intermediate. The fully hydrogenated hexahydroindan starts to dehydrogenate above 200 K, forming an unspecified H_x-indan intermediate, followed by the formation of the indenyl species above 240 K. The mutual indenyl species of all three molecules is observed up to 650K.

Above this temperature only fragments are left on the surface. As for the indoles, the formation of the indenyl species should be avoided in real catalysis in order to form an efficient hydrogen storage cycle. Surprisingly, this LOHC system performs very well compared to the indole LOHC system, dehydrogenating up to ~50 K earlier and indenyl being observed up to ~110 K higher than indolide, making it a very promising LOHC system to test in real catalytic conditions.

Apart from the cyclic LOHC systems, the adsorption and temperature-induced dehydrogenation of formic acid was studied on Pt(111) and Ni(111) using XPS, TPD and NEXAFS. Next to its capabilities as LOHC molecule, formic acid is also an intermediate in highly important industrial processes like steam reforming or the water-gas shift reaction. The adsorption behavior of formic acid is similar on both surfaces, finding two different formic acid species and formate upon adsorption. The reaction pathways are, however, different for Ni(111) and Pt(111). On Ni(111), heating above 210 K leads to the partial dehydration of one formic acid species, forming CO and instantly desorbing H₂O, while also partial conversion of the two different formic acid species to formate is observed until 240 K. Above this temperature, molecular desorption, dehydrogenation into CO and instantly desorbing CO₂ takes place until 330 K. Thereafter, CO desorbs until 440 K. On Pt(111), partial conversion of formic acid to formate is seen above 160 K. Afterwards, formic acid either desorbs molecularly or dehydrogenates and desorbs as CO₂ by 220 K, as does formate. Furthermore, NEXAFS suggests a disordered adsorption geometry of formic acid/formate on Pt(111) at 150 K, while indicating a rather perpendicular adsorption geometry at 190 K.

Last, ammonia borane and borazine were used to study the temperature-induced formation of h-BN on Ni(111). The focus here lies on the reaction pathway towards the formation of h-BN, which is an insulating graphene analog and therefore of high interest for semiconductor applications. However, ammonia borane also can be considered as solid hydrogen carrier with an excellent 19.6 wt% H₂ storage capacity. For borazine, the dehydrogenation into disordered and defective boron nitride is observed above 300 K, which then start to form h-BN above 620 K. Ammonia borane is already partially dehydrogenated at the nitrogen atom upon adsorption, resulting in a BH₃NH species. Above 200 K, dehydrogenation into a borazine-like intermediate is observed. In the range from 200-340 K, first the onset of disordered and later defective boron nitride is found. Above 600 K, h-BN is formed on the surface from these species.

Overall, this thesis especially contributes to the better understanding of the dehydrogenation surface reactions of LOHC systems using model catalysts in UHV. For future applications in real catalysis, it is crucial to understand the influence of e.g. heteroatoms or substitution towards the dehydrogenation behavior and stability of LOHCs. Establishing a comprehensive knowledge in this field will help us to find new LOHC systems, tune them and optimize their efficiency. In the long term, this will lead to new technologies, enabling a sustainable way for energy storage, which is necessary for a global change to renewable energy sources.

10. Zusammenfassung

Flüssige organische Wasserstoffträger (LOHCs) sind ein vielversprechender Ansatz, um Energie in Form von Wasserstoff zu speichern. In der Vergangenheit wurden bereits LOHC-Systeme wie z.B. N-Ethylkarbazol/H₁₂-N-Ethylkarbazol und Dibenzyltoluol/H₁₈-Dibenzyltoluol untersucht, mit dem Ergebnis, dass diese Art der Energiespeicherung zu einer „grünen“ Zukunft beitragen kann. LOHCs sind dabei nachhaltig und möglicherweise eine zukünftige Schlüsseltechnologie für die erfolgreiche Verteilung und Speicherung erneuerbarer Energien. Aufbauend auf diese vorangegangenen Studien wurde im Rahmen dieser Arbeit die Dehydrierung mehrerer LOHC-Systeme untersucht, wobei oberflächensensitive Methoden wie XPS verwendet wurden. Dabei lag das Hauptaugenmerk auf der Untersuchung von Molekülen die N-heterozyklische als auch homozyklischen Sechs- und Fünfringe enthalten, da diese oft sehr gute Dehydrierungseigenschaften aufweisen (siehe Beispiele oben).

Das erste in dieser Arbeit beschriebene LOHC-System setzt sich aus wasserstoffarmen Trägermolekül Indol, dem am Fünfring teilhydrierten Indolin und dem vollhydrierten Oktahydroindol zusammen. Die Adsorption sowie die temperaturinduzierte Reaktion der Moleküle auf Pt(111) wurde mit einer Kombination aus XPS, TPD, IRAS und NEXAFS untersucht. Mittels XPS ist oberhalb von 270 K die Dehydrierung von Oktahydroindol und Indolin zu einem Indol-Intermediat zu sehen. Nahezu gleichzeitig bei 270 K findet die Deprotonierung der NH-Gruppe von Indol statt. Dabei wird eine Indolidspezies gebildet, die bis 540 K beobachtet werden kann. Oberhalb dieser Temperatur liegen lediglich Fragmente vor; das Molekülgerüst wird zerstört. Des Weiteren zeigen XPS und IRAS während der Adsorption von Oktahydroindol eine partielle Protonierung der NH-Gruppe unterhalb von 290 K in Gegenwart von kleineren Mengen an OH⁻. In der C 1s Region von Oktahydroindol wird als Minoritätsspezies auch ein π -allyl identifiziert, welches während der Dehydrierung zwischen 170 und 450 K auftritt. Ein Indolin-Intermediat wird nicht beobachtet. Um einen effizienten und funktionierenden Wasserstoffspeicherzyklus zu bilden, muss die Deprotonierung der NH-Gruppe in der Realkatalyse vermieden werden. Allerdings findet dort aufgrund anderer Randbedingungen eine irreversible Bindung von Indol an die Oberfläche und die daraus resultierende Bildung von Indolid möglicherweise gar nicht erst statt.

Nach der erfolgreichen Untersuchung des Indol-basierten LOHC-Systems wurden die Auswirkungen einer Substitution anhand der Adsorption und temperaturinduzierten

Dehydrierung von 2-Methylindol, 2-Methylindolin und 2-Methyloktahydroindol auf Pt(111) mittels XPS und TPD im folgenden Kapitel besprochen. Während dieses LOHC-System viele Ähnlichkeiten mit dem unsubstituierten Indol-LOHC-System aufweist, gibt es einige deutliche Unterschiede bei der Stabilität der Reaktionszwischenprodukte und dem Reaktionsweg. Für das wasserstoffarme Trägermolekül 2-Methylindol findet die Deprotonierung der NH-Gruppe oberhalb von 240 K statt, was zu einer 2-Methylindolid-Spezies führt, die bis zu 490 K beobachtet werden kann. Bei höherer Temperatur liegen nur noch Zersetzungsfragmente auf der Oberfläche vor. Die Dehydrierung von 2-Methylindolin erfolgt oberhalb von 240 K unter Bildung eines 2-Methylindol-Zwischenprodukts. Danach gleicht der Reaktionsweg dem des 2-Methylindols. Die Reaktion von 2-Methyloktahydroindol ist komplexer. Zuerst dehydriert es oberhalb von 230 K teilweise am Sechsring und bildet dabei zwei verschiedene π -allyl-Intermediate. Wahrscheinlich ist bei diesen die Methylgruppe in Bezug zur Oberfläche jeweils entweder nach oben oder nach unten geneigt. Nahezu gleichzeitig entsteht ein 2-Methylindolin-Intermediat. Oberhalb von 270 K wird dann 2-Methylindol als Zwischenprodukt beobachtet, bevor die Deprotonierung der NH-Gruppe zu 2-Methylindolid führt, das sich anschließend bis 490 K zersetzt. Auch in diesem LOHC System ist die Deprotonierung der NH-Gruppe eine unerwünschte Nebenreaktion, die in der Realkatalyse vermieden werden sollte. Im Vergleich zum unsubstituierten Indol-LOHC-System ist hier zudem eine deutlich frühere Zersetzung des Trägermoleküls zu sehen, was das Gesamtsystem fragiler macht. Andererseits wird hier 2-Methylindolin jedoch als stabiles Zwischenprodukt beobachtet. Das Ergebnis dieser Untersuchungen ist von großem Interesse, da in der Realkatalyse bereits gezeigt wurde, dass 2-Methylindolin bei niedrigen Temperaturen und günstigen Reaktionsbedingungen mit hohem Umsatz de- und rehydriert werden kann. Wie hier gezeigt, könnte das vollhydrierte 2-Methyloktahydroindol jedoch ein noch besserer LOHC Kandidat sein, da der Sechsring unter den verwendeten Bedingungen zuerst, und somit vor dem Fünfring, dehydriert wird.

Basierend auf den Ergebnissen zu Indolen wurde anschließend die Adsorption und temperaturinduzierte Dehydrierungsreaktion des LOHC-Systems Inden, Indan und Hexahydroindan mittels XPS und TPD untersucht. Die Molekülstruktur dieses Systems stellt das homozyklische Pendant zu den Indol-Heterozyklen dar. Folglich werden hier ähnliche Reaktionsschritte gefunden. Oberhalb von 220 K wird für das wasserstoffarme Trägermolekül Inden die Dehydrierung der CH₂-Gruppe zu CH im Fünfring beobachtet. Dies führt zu einer

Indenyl-Oberflächenspezies, die im Grunde genommen ein Analogon zum Indolid ist. Die Dehydrierung von dem am Fünfring teilhydrierten Indan führt oberhalb von 240 K auch zu Indenyl. Während dieses Dehydrierungsschrittes wird Inden nicht als Zwischenprodukt beobachtet. Beim vollhydrierten Hexahydroindan beginnt die Dehydrierung schon oberhalb von 200 K, wobei zuerst ein nicht näher spezifizierbares H_x-Indan-Zwischenprodukt auftritt. Anschließend folgt die Bildung des Indenyls oberhalb von 240 K. Die gemeinsame Indenylspezies aller drei Moleküle ist bis 650 K präsent. Über dieser Temperatur bleiben nur Fragmente auf der Oberfläche zurück. Analog zum Indolid bei den Indolen sollte die Bildung der Indenylspezies in der Realkatalyse vermieden werden, um einen effizienten Wasserstoffspeicherzyklus zu bilden. Überraschenderweise zeigt sich das Inden-LOHC-System im Vergleich zum Indol-LOHC-System bereits im UHV als sehr leistungsfähig. Die Dehydrierungsreaktion tritt ~50 K früher auf und Indenyl ist bis zu ~110 K stabiler als Indolid, was dieses System zu einem guten Kandidaten für realkatalytische Untersuchungen macht.

Abseits der zyklischen LOHC-Systeme wurde auch die Adsorption und temperaturinduzierte Dehydrierung von Ameisensäure auf Pt(111) und Ni(111) mit XPS, TPD und NEXAFS untersucht. Neben den Eigenschaften als LOHC als LOHC-Molekül ist Ameisensäure auch ein Zwischenprodukt bei wichtigen industriellen Prozessen wie der Dampfreformierung oder der Wasser-Gas-Shift-Reaktion. Das Adsorptionsverhalten von Ameisensäure ist auf beiden Oberflächen ähnlich, wobei zwei verschiedene Ameisensäurespezies und ein Formiat bei der Adsorption gefunden werden. Die Reaktionswege auf Ni(111) und Pt(111) sind jedoch unterschiedlich. Auf Ni(111) führt das Heizen über 210 K zur teilweisen Dehydratisierung einer Ameisensäurespezies unter Bildung von CO und sofortiger Desorption des gebildeten H₂O. Zudem wird bis 240 K auch eine teilweise Umwandlung von beiden Ameisensäurespezies zu Formiat beobachtet. Anschließend folgt bis 330 K die molekulare Desorption von Ameisensäure sowie die Dehydrierung von Ameisensäure und Formiat zu CO und sofort desorbierendem CO₂. Danach findet die Desorption von CO bis 440 K statt. Auf Pt(111) ist oberhalb von 160 K eine teilweise Umwandlung von Ameisensäure zu Formiat zu beobachten. Danach desorbiert Ameisensäure entweder molekular oder dehydriert und desorbiert wie Formiat bis 220 K als CO₂. NEXAFS deutet auf eine ungeordnete Adsorptionsgeometrie von Ameisensäure/Formiat auf Pt(111) bei 150 K hin, während bei 190 K eine eher senkrechte Adsorptionsgeometrie vorliegt.

Zuletzt wurde die temperaturinduzierte Bildung von hexagonalem Bornitrid (h-BN) aus Aminoboran und Borazin auf Ni(111) untersucht. Der Schwerpunkt dieser Studie liegt auf dem Reaktionsweg zur Bildung von h-BN, einem Isolator und Graphen-Analogen, das für Halbleiteranwendungen von großem Interesse ist. Aminoboran gilt allerdings auch als fester Wasserstoffträger mit einer exzellenten Speicherkapazität von 19,6 Gew.-% Wasserstoff. Bei Borazin wird oberhalb von 300 K eine Dehydrierung in ungeordnetes sowie defektes Bornitrid beobachtet. Anschließend bildet sich oberhalb von 620 K h-BN. Aminoboran wird bereits bei der Adsorption teilweise am Stickstoffatom dehydriert, was zu einer BH_3NH -Spezies führt. Im weiteren Reaktionsverlauf wird oberhalb von 200 K dann eine Dehydrierung zu einem borazinähnlichen Zwischenprodukt beobachtet. Nachfolgend wird zwischen 200 und 340 K zunächst das Entstehen von ungeordnetem und später auch defektem Bornitrid festgestellt. Aus diesen beiden Spezies bildet sich dann oberhalb von 600 K h-BN, welches bis über 1000 K stabil bleibt.

Insgesamt trägt diese Arbeit insbesondere zum besseren Verständnis der Dehydrierungsflächenreaktionen von LOHC-Systemen im UHV unter Verwendung von Modellkatalysatoren bei. Für zukünftige Anwendungen in der Realkatalyse ist es entscheidend, den Einfluss von z.B. Heteroatomen oder Substituenten in Bezug auf das Dehydrierungsverhalten und die Stabilität von LOHCs zu bestimmen. Durch die Erweiterung des Kenntnisstandes auf diesem Gebiet können wir zukünftig neue LOHC-Systeme entwickeln und deren Effizienz optimieren. Dies führt letztendlich zu neuen Technologien, mit denen die notwendige nachhaltige Energiespeicherung für den globalen Umstieg auf erneuerbare Energien bereitgestellt werden kann.

11. References

- [1] Vitousek, P. M., Beyond Global Warming: Ecology and Global Change. *Ecology* **1994**, *75*, 1861-1876.
- [2] Lashof, D. A.; Ahuja, D. R., Relative contributions of greenhouse gas emissions to global warming. *Nature* **1990**, *344*, 529-531.
- [3] Ramanathan, V.; Feng, Y., Air pollution, greenhouse gases and climate change: Global and regional perspectives. *Atmos. Environ.* **2009**, *43*, 37-50.
- [4] Hughes, L., Biological consequences of global warming: is the signal already apparent? *Trends in Ecology & Evolution* **2000**, *15*, 56-61.
- [5] Root, T. L.; Price, J. T.; Hall, K. R.; Schneider, S. H.; Rosenzweig, C.; Pounds, J. A., Fingerprints of global warming on wild animals and plants. *Nature* **2003**, *421*, 57-60.
- [6] Dai, A., Increasing drought under global warming in observations and models. *Nature Climate Change* **2012**, *3*, 52.
- [7] Alan Pounds, J.; Bustamante, M. R.; Coloma, L. A.; Consuegra, J. A.; Fogden, M. P. L.; Foster, P. N.; La Marca, E.; Masters, K. L.; Merino-Viteri, A.; Puschendorf, R., et al., Widespread amphibian extinctions from epidemic disease driven by global warming. *Nature* **2006**, *439*, 161-167.
- [8] Meinshausen, M.; Meinshausen, N.; Hare, W.; Raper, S. C. B.; Frieler, K.; Knutti, R.; Frame, D. J.; Allen, M. R., Greenhouse-gas emission targets for limiting global warming to 2 °C. *Nature* **2009**, *458*, 1158.
- [9] Falkner, R., The Paris Agreement and the new logic of international climate politics. *International Affairs* **2016**, *92*, 1107-1125.
- [10] Grubb, M.; Vrolijk, C.; Brack, D.; Affairs, R. I. o. I.; Forsyth, T.; Energy; Programme, E., The Kyoto Protocol: A Guide and Assessment, Energy and Environmental Programme, Royal Institute of International Affairs, **1999**.
- [11] BP Statistical Review of World Energy 2019; BP p.l.c.: London, **2019**.
- [12] World Population Prospects: The 2017 Revision; United Nations, Department of Economic and Social Affairs, Population Division: New York, **2017**.
- [13] Peters, J. F.; Baumann, M.; Zimmermann, B.; Braun, J.; Weil, M., The environmental impact of Li-Ion batteries and the role of key parameters – A review. *Renewable and Sustainable Energy Reviews* **2017**, *67*, 491-506.
- [14] Lisboa, D.; Snee, T., A review of hazards associated with primary lithium and lithium-ion batteries. *Process Saf. Environ. Prot.* **2011**, *89*, 434-442.
- [15] Wang, Q.; Ping, P.; Zhao, X.; Chu, G.; Sun, J.; Chen, C., Thermal runaway caused fire and explosion of lithium ion battery. *J. Power Sources* **2012**, *208*, 210-224.
- [16] Eberle, U.; Felderhoff, M.; Schüth, F., Chemical and Physical Solutions for Hydrogen Storage. *Angew. Chem. Int. Ed.* **2009**, *48*, 6608-6630.
- [17] Preuster, P.; Papp, C.; Wasserscheid, P., Liquid Organic Hydrogen Carriers (LOHCs): Toward a Hydrogen-free Hydrogen Economy. *Acc. Chem. Res.* **2017**, *50*, 74-85.
- [18] Teichmann, D.; Arlt, W.; Wasserscheid, P.; Freymann, R., A future energy supply based on Liquid Organic Hydrogen Carriers (LOHC). *Energ. Environ. Sci.* **2011**, *4*, 2767-2773.
- [19] Teichmann, D.; Stark, K.; Müller, K.; Zottl, G.; Wasserscheid, P.; Arlt, W., Energy storage in residential and commercial buildings via Liquid Organic Hydrogen Carriers (LOHC). *Energ. Environ. Sci.* **2012**, *5*, 9044-9054.
- [20] He, T.; Pei, Q.; Chen, P., Liquid organic hydrogen carriers. *J. Energ. Chem.* **2015**, *24*, 587-594.
- [21] Papp, C.; Wasserscheid, P.; Libuda, J.; Steinrück, H.-P., Liquid Organic Hydrogen Carriers: Surface Science Studies of Carbazole Derivatives. *Chem. Rec.* **2014**, *14*, 879-896.
- [22] Amende, M.; Gleichweit, C.; Schernich, S.; Höfert, O.; Lorenz, M. P. A.; Zhao, W.; Koch, M.; Obesser, K.; Papp, C.; Wasserscheid, P., et al., Size and Structure Effects Controlling the

- Stability of the Liquid Organic Hydrogen Carrier Dodecahydro-N-ethylcarbazole during Dehydrogenation over Pt Model Catalysts. *J. Phys. Chem. Lett.* **2014**, *5*, 1498-1504.
- [23] Amende, M.; Gleichweit, C.; Werner, K.; Schernich, S.; Zhao, W.; Lorenz, M. P. A.; Höfert, O.; Papp, C.; Koch, M.; Wasserscheid, P., et al., Model Catalytic Studies of Liquid Organic Hydrogen Carriers: Dehydrogenation and Decomposition Mechanisms of Dodecahydro-N-ethylcarbazole on Pt(111). *ACS Catal.* **2014**, *4*, 657-665.
- [24] Amende, M.; Schernich, S.; Sobota, M.; Nikiforidis, I.; Hieringer, W.; Assenbaum, D.; Gleichweit, C.; Drescher, H.-J.; Papp, C.; Steinrück, H.-P., et al., Dehydrogenation Mechanism of Liquid Organic Hydrogen Carriers: Dodecahydro-N-ethylcarbazole on Pd(111). *Chem. Eur. J.* **2013**, *19*, 10854-10865.
- [25] Gleichweit, C.; Amende, M.; Bauer, U.; Schernich, S.; Höfert, O.; Lorenz, M. P. A.; Zhao, W.; Müller, M.; Koch, M.; Bachmann, P., et al., Alkyl chain length-dependent surface reaction of dodecahydro-N-alkylcarbazoles on Pt model catalysts. *J. Chem. Phys.* **2014**, *140*, 204711.
- [26] Gleichweit, C.; Amende, M.; Schernich, S.; Zhao, W.; Lorenz, M. P. A.; Höfert, O.; Brückner, N.; Wasserscheid, P.; Libuda, J.; Steinrück, H.-P., et al., Dehydrogenation of Dodecahydro-N-ethylcarbazole on Pt(111). *ChemSusChem* **2013**, *6*, 974-977.
- [27] Sobota, M.; Nikiforidis, I.; Amende, M.; Zanón, B. S.; Staudt, T.; Höfert, O.; Lykhach, Y.; Papp, C.; Hieringer, W.; Laurin, M., et al., Dehydrogenation of Dodecahydro-N-ethylcarbazole on Pd/Al₂O₃ Model Catalysts. *Chem. Eur. J.* **2011**, *17*, 11542-11552.
- [28] Sotoodeh, F.; Huber, B. J. M.; Smith, K. J., Dehydrogenation kinetics and catalysis of organic heteroaromatics for hydrogen storage. *Int. J. Hydrog. Energy* **2012**, *37*, 2715-2722.
- [29] Sotoodeh, F.; Smith, K. J., Kinetics of Hydrogen Uptake and Release from Heteroaromatic Compounds for Hydrogen Storage. *Ind. Eng. Chem. Res.* **2010**, *49*, 1018-1026.
- [30] Amende, M.; Kaftan, A.; Bachmann, P.; Brehmer, R.; Preuster, P.; Koch, M.; Wasserscheid, P.; Libuda, J., Regeneration of LOHC dehydrogenation catalysts: In-situ IR spectroscopy on single crystals, model catalysts, and real catalysts from UHV to near ambient pressure. *Appl. Surf. Sci.* **2016**, *360*, 671-683.
- [31] Brückner, N.; Obesser, K.; Bösmann, A.; Teichmann, D.; Arlt, W.; Dungs, J.; Wasserscheid, P., Evaluation of Industrially Applied Heat-Transfer Fluids as Liquid Organic Hydrogen Carrier Systems. *ChemSusChem* **2014**, *7*, 229-235.
- [32] Fikrt, A.; Brehmer, R.; Milella, V.-O.; Müller, K.; Bösmann, A.; Preuster, P.; Alt, N.; Schlücker, E.; Wasserscheid, P.; Arlt, W., Dynamic power supply by hydrogen bound to a liquid organic hydrogen carrier. *Appl. Energy* **2017**, *194*, 1-8.
- [33] Geburtig, D.; Preuster, P.; Bösmann, A.; Müller, K.; Wasserscheid, P., Chemical utilization of hydrogen from fluctuating energy sources – Catalytic transfer hydrogenation from charged Liquid Organic Hydrogen Carrier systems. *Int. J. Hydrog. Energy* **2016**, *41*, 1010-1017.
- [34] Jorschick, H.; Preuster, P.; Dürr, S.; Seidel, A.; Müller, K.; Bösmann, A.; Wasserscheid, P., Hydrogen storage using a hot pressure swing reactor. *Energ. Environ. Sci.* **2017**, *10*, 1652-1659.
- [35] Markiewicz, M.; Zhang, Y. Q.; Bösmann, A.; Brückner, N.; Thöming, J.; Wasserscheid, P.; Stolte, S., Environmental and health impact assessment of Liquid Organic Hydrogen Carrier (LOHC) systems – challenges and preliminary results. *Energ. Environ. Sci.* **2015**, *8*, 1035-1045.
- [36] Müller, K.; Aslam, R.; Fischer, A.; Stark, K.; Wasserscheid, P.; Arlt, W., Experimental assessment of the degree of hydrogen loading for the dibenzyl toluene based LOHC system. *Int. J. Hydrog. Energy* **2016**, *41*, 22097-22103.
- [37] Hertz, H., Ueber einen Einfluss des ultravioletten Lichtes auf die elektrische Entladung. *Ann. Phys.* **1887**, *267*, 983-1000.
- [38] Einstein, A., Über einen die Erzeugung und Verwandlung des Lichtes betreffenden heuristischen Gesichtspunkt. *Ann. Phys.* **1905**, *322*, 132-148.
- [39] van der Heide, P., X-ray Photoelectron Spectroscopy: An introduction to Principles and Practices, John Wiley & Sons, **2011**.
- [40] Hüfner, S., Photoelectron Spectroscopy - Principles and Applications, Springer-Verlag: Berlin Heidelberg, **2013**.
- [41] Wiedemann, H., Synchrotron Radiation, Springer-Verlag: Berlin Heidelberg, **2003**.

- [42] Seah, M. P.; Dench, W. A., Quantitative electron spectroscopy of surfaces: A standard data base for electron inelastic mean free paths in solids. *Surf. Interface Anal.* **1979**, *1*, 2-11.
- [43] Willmott, P., An Introduction to Synchrotron Radiation: Techniques and Applications, John Wiley & Sons: Chichester, **2011**.
- [44] Suga, S.; Sekiyama, A., Photoelectron Spectroscopy, Springer-Verlag: Berlin Heidelberg, **2014**.
- [45] Koopmans, T., Über die Zuordnung von Wellenfunktionen und Eigenwerten zu den Einzelnen Elektronen Eines Atoms. *Physica* **1934**, *1*, 104-113.
- [46] Wedler, G.; Freund, H. J., Lehrbuch der Physikalischen Chemie, Wiley-VCH: Weinheim, **2012**.
- [47] Steinrück, H.-P.; Fuhrmann, T.; Papp, C.; Tränkenschuh, B.; Denecke, R., A detailed analysis of vibrational excitations in x-ray photoelectron spectra of adsorbed small hydrocarbons. *J. Chem. Phys.* **2006**, *125*, 204706.
- [48] Yoo, J. S.; Abild-Pedersen, F.; Nørskov, J. K.; Studt, F., Theoretical Analysis of Transition-Metal Catalysts for Formic Acid Decomposition. *ACS Catal.* **2014**, *4*, 1226-1233.
- [49] Woodruff, D. P.; Bradshaw, A. M., Adsorbate structure determination on surfaces using photoelectron diffraction. *Reports on Progress in Physics* **1994**, *57*, 1029.
- [50] Briggs, D.; Seah, P., Practical Surface Analysis: Auger and X-ray photoelectron spectroscopy, Wiley, **1990**.
- [51] Kinne, M., Kinetische Untersuchungen von Oberflächenreaktionen mittels hochaufgelöster Röntgen-Photoelektronenspektroskopie - Oxidation von CO auf Pt(111) und zugehörige Elementarschritte. *Ph. D. thesis, Universität Erlangen-Nürnberg* **2004**.
- [52] Kinne, M.; Fuhrmann, T.; Whelan, C. M.; Zhu, J. F.; Pantförder, J.; Probst, M.; Held, G.; Denecke, R.; Steinrück, H.-P., Kinetic parameters of CO adsorbed on Pt(111) studied by in situ high resolution x-ray photoelectron spectroscopy. *J. Chem. Phys.* **2002**, *117*, 10852-10859.
- [53] Doniach, S.; Sunjic, M., Many-electron singularity in X-ray photoemission and X-ray line spectra from metals. *J. Phys. C* **1970**, *3*, 285.
- [54] Mobilio, S.; Boscherini, F.; Meneghini, C., Synchrotron Radiation: Basics, Methods and Applications, Springer Berlin Heidelberg, **2015**.
- [55] Kolasinski, K. W., Surface Science: Foundations of Catalysis and Nanoscience, John Wiley & Sons: Chichester, **2012**.
- [56] Gross, J. H., Massenspektrometrie - Ein Lehrbuch, Springer Spektrum: Berlin Heidelberg, **2013**.
- [57] Niemantsverdriet, J. W., Spectroscopy in Catalysis, Wiley-VCH: Hoboken, **2007**.
- [58] Cassuto, A.; King, D. A., Rate expressions for adsorption and desorption kinetics with precursor states and lateral interactions. *Surf. Sci.* **1981**, *102*, 388-404.
- [59] Redhead, P. A., Thermal desorption of gases. *Vacuum* **1962**, *12*, 203-211.
- [60] Lehmann, J.; Solomon, D.; Brandes, J.; Fleckenstein, H.; Jacobson, C.; Thieme, J., *Synchrotron-Based Near-Edge X-Ray Spectroscopy of Natural Organic Matter in Soils and Sediments*. In: Biophysico-Chemical Processes Involving Natural Nonliving Organic Matter in Environmental Systems, Senesi, N.; Xing, B.; Huang, P. M., Eds. John Wiley & Sons: Chichester, **2009**.
- [61] Stöhr, J., NEXAFS Spectroscopy, Springer-Verlag: Berlin Heidelberg, **1992**.
- [62] Denecke, R.; Kinne, M.; Whelan, C. M.; Steinrück, H.-P., In-situ core-level photoelectron spectroscopy of adsorbates on surfaces involving a molecular beam - general setup and first experiments. *Surf. Rev. Lett.* **2002**, *09*, 797-801.
- [63] Gleichweit, C., Dehydrogenation of Liquid Organic Hydrogen Carriers on Model Catalyst Surfaces. *Ph. D. thesis, Universität Erlangen-Nürnberg* **2015**.
- [64] Braun, W.; Steinrück, H. P.; Held, G., The surface geometry of carbonmonoxide and hydrogen co-adsorbed on Ni{111}. *Surf. Sci.* **2005**, *574*, 193-204.
- [65] Held, G.; Uremović, S.; Stellwag, C.; Menzel, D., A low-energy electron diffraction data acquisition system for very low electron doses based upon a slow scan charge coupled device camera. *Rev. Sci. Instrum.* **1996**, *67*, 378-383.
- [66] Feulner, P.; Menzel, D., Simple ways to improve "flash desorption" measurements from single crystal surfaces. *J. Vac. Sci. Technol.* **1980**, *17*, 662-663.
- [67] Bachmann, P.; Schwarz, M.; Steinhauer, J.; Späth, F.; Düll, F.; Bauer, U.; Nascimento Silva, T.; Mohr, S.; Hohner, C.; Scheuermeyer, M., et al., Dehydrogenation of the Liquid Organic

- Hydrogen Carrier System Indole/Indoline/Octahydroindole on Pt(111). *J. Phys. Chem. C* **2018**, *122*, 4470-4479.
- [68] Schwarz, M.; Bachmann, P.; Silva, T. N.; Mohr, S.; Scheuermeyer, M.; Späth, F.; Bauer, U.; Düll, F.; Steinhauer, J.; Hohner, C., et al., Model Catalytic Studies of Novel Liquid Organic Hydrogen Carriers: Indole, Indoline and Octahydroindole on Pt(111). *Chem. Eur. J.* **2017**, *23*, 14806-14818.
- [69] Müller, B.; Arlt, W.; Wasserscheid, P., A new concept for the global distribution of solar energy: energy carrying compounds. *Energ. Environ. Sci.* **2011**, *4*, 4322-4331.
- [70] Crabtree, R. H., Nitrogen-Containing Liquid Organic Hydrogen Carriers: Progress and Prospects. *ACS Sustain. Chem. Eng.* **2017**, *5*, 4491-4498.
- [71] Bourane, A.; Elanany, M.; Pham, T. V.; Katikaneni, S. P., An overview of organic liquid phase hydrogen carriers. *Int. J. Hydrog. Energy* **2016**, *41*, 23075-23091.
- [72] Cui, Y.; Kwok, S.; Bucholtz, A.; Davis, B.; Whitney, R. A.; Jessop, P. G., The effect of substitution on the utility of piperidines and octahydroindoles for reversible hydrogen storage. *New J. Chem.* **2008**, *32*, 1027-1037.
- [73] Dong, Y.; Yang, M.; Yang, Z.; Ke, H.; Cheng, H., Catalytic hydrogenation and dehydrogenation of N-ethylindole as a new heteroaromatic liquid organic hydrogen carrier. *Int. J. Hydrog. Energy* **2015**, *40*, 10918-10922.
- [74] Li, L.; Yang, M.; Dong, Y.; Mei, P.; Cheng, H., Hydrogen storage and release from a new promising Liquid Organic Hydrogen Storage Carrier (LOHC): 2-methylindole. *Int. J. Hydrog. Energy* **2016**, *41*, 16129-16134.
- [75] Bondino, F.; Comelli, G.; Esch, F.; Locatelli, A.; Baraldi, A.; Lizzit, S.; Paolucci, G.; Rosei, R., Structural determination of molecules adsorbed in different sites by means of chemical shift photoelectron diffraction: c(4x2)-CO on Pt(111). *Surf. Sci.* **2000**, *459*, L467-L474.
- [76] Zasada, I.; van Hove, M. A., Refinement of the Pt(111)+c(4x2)-2CO Structure Using Automated Tensor LEED. *Surf. Rev. Lett.* **2000**, *07*, 15-19.
- [77] Desikusumastuti, A.; Staudt, T.; Happel, M.; Laurin, M.; Libuda, J., Adsorption and reaction of NO₂ on ordered alumina films and mixed baria–alumina nanoparticles: Cooperative versus non-cooperative reaction mechanisms. *J. Catal.* **2008**, *260*, 315-328.
- [78] Gleichweit, C.; Amende, M.; Höfert, O.; Xu, T.; Späth, F.; Brückner, N.; Wasserscheid, P.; Libuda, J.; Steinrück, H.-P.; Papp, C., Surface Reactions of Dicyclohexylmethane on Pt(111). *J. Phys. Chem. C* **2015**, *119*, 20299-20311.
- [79] Papp, C.; Fuhrmann, T.; Tränkenschuh, B.; Denecke, R.; Steinrück, H. P., Site selectivity of benzene adsorption on Ni(111) studied by high-resolution x-ray photoelectron spectroscopy. *Phys. Rev. B* **2006**, *73*, 235426.
- [80] Gottfried, J. M.; Flechtner, K.; Kretschmann, A.; Lukasczyk, T.; Steinrück, H.-P., Direct Synthesis of a Metalloporphyrin Complex on a Surface. *J. Am. Chem. Soc.* **2006**, *128*, 5644-5645.
- [81] Hasik, M.; Bernasik, A.; Drelinkiewicz, A.; Kowalski, K.; Wenda, E.; Camra, J., XPS studies of nitrogen-containing conjugated polymers–palladium systems. *Surf. Sci.* **2002**, *507*, 916-921.
- [82] Kang, E. T.; Neoh, K. G.; Tan, K. L., The intrinsic redox states in polypyrrole and polyaniline: A comparative study by XPS. *Surf. Interface Anal.* **1992**, *19*, 33-37.
- [83] Tourillon, G.; Raaen, S.; Skotheim, T. A.; Sagurton, M.; Garrett, R.; Williams, G. P., A near edge X-ray absorption fine structure study of the adsorption of pyrrole and N-methylpyrrole on Pt(111): Orientation and dissociation of the adsorbed molecules. *Surf. Sci. Lett.* **1987**, *184*, L345-L354.
- [84] Wöckel, C.; Eilert, A.; Welke, M.; Schöppke, M.; Steinrück, H.-P.; Denecke, R., Pyridine on flat Pt(111) and stepped Pt(355)—An in situ HRXPS investigation of adsorption and thermal evolution. *J. Chem. Phys.* **2016**, *144*, 014702.
- [85] Papp, C.; Steinrück, H.-P., In situ high-resolution X-ray photoelectron spectroscopy – Fundamental insights in surface reactions. *Surf. Sci. Rep.* **2013**, *68*, 446-487.
- [86] Moores, A.; Poyatos, M.; Luo, Y.; Crabtree, R. H., Catalysed low temperature H₂ release from nitrogen heterocycles. *New J. Chem.* **2006**, *30*, 1675-1678.

- [87] Benne, D.; Maccallini, E.; Rudolf, P.; Sooambar, C.; Prato, M., X-ray photoemission spectroscopy study on the effects of functionalization in fulleropyrrolidine and pyrrolidine derivatives. *Carbon* **2006**, *44*, 2896-2903.
- [88] Vernon, C. F.; Fawell, P. D.; Klauber, C., XPS investigation of the states of adsorption of aurocyanide onto crosslinked polydiallylamine and commercial anionexchange resins. *React. Polym.* **1992**, *18*, 35-45.
- [89] Bienz, S.; Bigler, L.; Fox, T.; Meier, H., 5.2 *Charakterisierung von Verbindungen*. 2016 ed.; Hesse, M.; Meier, H.; Zeeh, B., Eds. Georg Thieme Verlag: Stuttgart, **2016**; Vol. 9.
- [90] Xu, C.; Koel, B. E.; Newton, M. A.; Frei, N. A.; Campbell, C. T., Dehydrogenation of Methylcyclohexane on Pt(111). *J. Phys. Chem.* **1995**, *99*, 16670-16675.
- [91] Henn, F. C.; Diaz, A. L.; Bussell, M. E.; Hugenschmidt, M. B.; Domagala, M. E.; Campbell, C. T., Decomposition of cyclohexene on platinum (111): a BPTDS and HREELS study. *J. Phys. Chem.* **1992**, *96*, 5965-5974.
- [92] Horsley, J. A.; Stöhr, J.; Hitchcock, A. P.; Newbury, D. C.; Johnson, A. L.; Sette, F., Resonances in the K shell excitation spectra of benzene and pyridine: Gas phase, solid, and chemisorbed states. *J. Chem. Phys.* **1985**, *83*, 6099-6107.
- [93] Bachmann, P.; Steinhauer, J.; Späth, F.; Düll, F.; Bauer, U.; Eschenbacher, R.; Hemauer, F.; Scheuermeyer, M.; Bösmann, A.; Wasserscheid, P., et al., Dehydrogenation of the Liquid Organic Hydrogen Carrier System 2-methylindole/2-methylindoline/2-methyloctahydroindole on Pt(111). *J. Chem. Phys.* **2019**, *submitted*.
- [94] Hara, T.; Mori, K.; Mizugaki, T.; Ebitani, K.; Kaneda, K., Highly efficient dehydrogenation of indolines to indoles using hydroxyapatite-bound Pd catalyst. *Tetrahedron Lett.* **2003**, *44*, 6207-6210.
- [95] Kojima, M.; Kanai, M., Tris(pentafluorophenyl)borane-Catalyzed Acceptorless Dehydrogenation of N-Heterocycles. *Angew. Chem. Int. Ed.* **2016**, *55*, 12224-12227.
- [96] Xu, R.; Chakraborty, S.; Yuan, H.; Jones, W. D., Acceptorless, Reversible Dehydrogenation and Hydrogenation of N-Heterocycles with a Cobalt Pincer Catalyst. *ACS Catal.* **2015**, *5*, 6350-6354.
- [97] Yi, C. S.; Lee, D. W., Efficient Dehydrogenation of Amines and Carbonyl Compounds Catalyzed by a Tetranuclear Ruthenium- μ -oxo- μ -hydroxo-hydride Complex. *Organometallics* **2009**, *28*, 947-949.
- [98] Søggaard, A.; Scheuermeyer, M.; Bösmann, A.; Wasserscheid, P.; Riisager, A., Homogeneously-catalysed hydrogen release/storage using the 2-methylindole/2-methylindoline LOHC system in molten salt-organic biphasic reaction systems. *Chem. Commun.* **2019**, *55*, 2046-2049.
- [99] Papp, C.; Fuhrmann, T.; Tränkenschuh, B.; Denecke, R.; Steinrück, H. P., Site selectivity of benzene adsorption on Ni(111) studied by high-resolution x-ray photoelectron spectroscopy. *Phys. Rev. B* **2006**, *73*, 235426.
- [100] Fuhrmann, T.; Kinne, M.; Tränkenschuh, B.; Papp, C.; Zhu, J. F.; Denecke, R.; Steinrück, H. P., Activated adsorption of methane on Pt(111) - an *in situ* XPS study. *New J. Phys.* **2005**, *7*, 107-107.
- [101] Dean, D.; Davis, B.; Jessop, P. G., The effect of temperature, catalyst and sterics on the rate of N-heterocycle dehydrogenation for hydrogen storage. *New J. Chem.* **2011**, *35*, 417-422.
- [102] Brayton, D. F.; Jensen, C. M., Dehydrogenation of pyrrolidine based liquid organic hydrogen carriers by an iridium pincer catalyst, an isothermal kinetic study. *Int. J. Hydrog. Energy* **2015**, *40*, 16266-16270.
- [103] Bonello, J. M.; Lambert, R. M., The structure and reactivity of quinoline overlayers and the adsorption geometry of lepidine on Pt{111}: model molecules for chiral modifiers in enantioselective hydrogenation. *Surf. Sci.* **2002**, *498*, 212-228.
- [104] Sexton, B. A.; Avery, N. R., Coordination of acetonitrile (CH₃CN) to platinum (111): Evidence for an η^2 (C, N) species. *Surf. Sci.* **1983**, *129*, 21-36.
- [105] Shavorskiy, A.; Eralp, T.; Schulte, K.; Bluhm, H.; Held, G., Surface chemistry of glycine on Pt{111} in different aqueous environments. *Surf. Sci.* **2013**, *607*, 10-19.
- [106] Christmann, K.; Ertl, G.; Pignet, T., Adsorption of hydrogen on a Pt(111) surface. *Surf. Sci.* **1976**, *54*, 365-392.

- [107] Enthaler, S., Carbon Dioxide—The Hydrogen-Storage Material of the Future? *ChemSusChem* **2008**, *1*, 801-804.
- [108] Grasemann, M.; Laurenczy, G., Formic acid as a hydrogen source - recent developments and future trends. *Energ. Environ. Sci.* **2012**, *5*, 8171-8181.
- [109] Johnson, T. C.; Morris, D. J.; Wills, M., Hydrogen generation from formic acid and alcohols using homogeneous catalysts. *Chem. Soc. Rev.* **2010**, *39*, 81-88.
- [110] Joó, F., Breakthroughs in Hydrogen Storage—Formic Acid as a Sustainable Storage Material for Hydrogen. *ChemSusChem* **2008**, *1*, 805-808.
- [111] Ratnasamy, C.; Wagner, J. P., Water Gas Shift Catalysis. *Catal. Rev.* **2009**, *51*, 325-440.
- [112] Smith, R. J. B.; Loganathan, M.; Shantha Murthy, S., A Review of the Water Gas Shift Reaction Kinetics. *Int. J. Chem. React. Eng.* **2010**, *8*.
- [113] Columbia, M. R.; Thiel, P. A., The interaction of formic acid with transition metal surfaces, studied in ultrahigh vacuum. *J. Electroanal. Chem.* **1994**, *369*, 1-14.
- [114] Abbas, N.; Madix, R. J., Surface reaction modification: The effect of structured overlayers of sulfur on the kinetics and mechanism of the decomposition of formic acid on Pt(111). *Appl. Surf. Sci.* **1983**, *16*, 424-440.
- [115] Benziqer, J. B.; Schoofs, G. R., Influence of adsorbate interactions on heterogeneous reaction kinetics. Formic acid decomposition on nickel. *J. Phys. Chem.* **1984**, *88*, 4439-4444.
- [116] Columbia, M. R.; Crabtree, A. M.; Thiel, P. A., The temperature and coverage dependences of adsorbed formic acid and its conversion to formate on platinum(111). *J. Am. Chem. Soc.* **1992**, *114*, 1231-1237.
- [117] Kusafuka, K.; Noguchi, H.; Onda, K.; Kubota, J.; Domen, K.; Hirose, C.; Wada, A., Time-resolved study of formate on Ni(1 1 1) by picosecond SFG spectroscopy. *Surf. Sci.* **2002**, *502-503*, 313-318.
- [118] Avery, N. R., Adsorption of formic acid on clean and oxygen covered Pt(111). *Appl. Surf. Sci.* **1982**, *11*, 774-783.
- [119] Columbia, M. R.; Thiel, P. A., The stabilization of formate on Pt(111) by coadsorbed atomic oxygen. *Chem. Phys. Lett.* **1994**, *220*, 167-171.
- [120] Jones, T. S.; Ashton, M. R.; Richardson, N. V., An electron energy loss study of the surface formate species chemisorbed on Ni(110): Dipole, impact, and resonance scattering for adsorbate covered surfaces. *J. Chem. Phys.* **1989**, *90*, 7564-7576.
- [121] Bandara, A.; Kubota, J.; Wada, A.; Domen, K.; Hirose, C., Adsorption and decomposition of formic acid (DFOOD) on NiO(111) and Ni(111) surfaces probed by SFG. *Appl. Phys. B* **1999**, *68*, 573-578.
- [122] Hirose, C.; Bandara, A.; Katano, S.; Kubota, J.; Wada, A.; Domen, K., Sum-frequency generation study of reacting species at surfaces. *Appl. Phys. B* **1999**, *68*, 559-565.
- [123] Allen, G. C.; Tucker, P. M.; Capon, A.; Parsons, R., X-ray photoelectron spectroscopy of adsorbed oxygen and carbonaceous species on platinum electrodes. *J. Electroanal. Chem. Interfacial. Electrochem.* **1974**, *50*, 335-343.
- [124] Bowker, M.; Madix, R. J., XPS, UPS and thermal desorption studies of the reactions of formaldehyde and formic acid with the Cu(110) surface. *Surf. Sci.* **1981**, *102*, 542-565.
- [125] Bayer, A. Photoelektronenspektroskopische Untersuchungen ultradünner Metall-Schichten - Zn/Pd(111) und Zn/Cu(111) als Modellkatalysatoren der Methanolsynthese und Methanol-Dampfreformierung / Photoelectron Spectroscopic Investigations of Ultra Thin Metal Layers - Zn/Pd(111) and Zn/Cu(111) as Model Catalysts in Synthesis and Steam Reforming of Methanol. PhD Thesis, Universität Erlangen-Nürnberg, 2006.
- [126] Davies, P. R.; Roberts, M. W.; Shukla, N., The reactive chemisorption of formic acid at Al(111) surfaces and the influence of surface oxidation and coadsorption with water: a combined XPS and HREELS investigation. *J. Phys.: Condens. Matter* **1991**, *3*, S237.
- [127] Gao, W.; Keith, J. A.; Anton, J.; Jacob, T., Oxidation of formic acid on the Pt(111) surface in the gas phase. *Dalton Trans.* **2010**, *39*, 8450-8456.
- [128] Gao, W.; Song, E. H.; Jiang, Q.; Jacob, T., Revealing the Active Intermediates in the Oxidation of Formic Acid on Au and Pt(111). *Chem. Eur. J.* **2014**, *20*, 11005-11012.

- [129] Luo, Q.; Feng, G.; Beller, M.; Jiao, H., Formic Acid Dehydrogenation on Ni(111) and Comparison with Pd(111) and Pt(111). *J. Phys. Chem. C* **2012**, *116*, 4149-4156.
- [130] Qi, Y.; Gao, J.; Zhang, D.; Liu, C., Comparative theoretical study of formic acid decomposition on PtAg(111) and Pt(111) surfaces. *RSC Adv.* **2015**, *5*, 21170-21177.
- [131] Herron, J. A.; Scaranto, J.; Ferrin, P.; Li, S.; Mavrikakis, M., Trends in Formic Acid Decomposition on Model Transition Metal Surfaces: A Density Functional Theory study. *ACS Catal.* **2014**, *4*, 4434-4445.
- [132] Chen, Y. X.; Heinen, M.; Jusys, Z.; Behm, R. J., Kinetics and Mechanism of the Electrooxidation of Formic Acid—Spectroelectrochemical Studies in a Flow Cell. *Angew. Chem. Int. Ed.* **2006**, *45*, 981-985.
- [133] Silbaugh, T. L.; Karp, E. M.; Campbell, C. T., Energetics of Formic Acid Conversion to Adsorbed Formates on Pt(111) by Transient Calorimetry. *J. Am. Chem. Soc.* **2014**, *136*, 3964-3971.
- [134] Avery, N. R., Reaction of HCOOH with a Pt(111)-O surface; identification of adsorbed monodentate formate. *Appl. Surf. Sci.* **1983**, *14*, 149-156.
- [135] Columbia, M. R.; Thiel, P. A., The reaction of formic acid with clean and water-covered Pt(111). *Surf. Sci.* **1990**, *235*, 53-59.
- [136] Jensen, M. B.; Myler, U.; Thiel, P. A., Local and collective structure of formate on Pt(111). *Surf. Sci. Lett.* **1993**, *290*, L655-L661.
- [137] Columbia, M. R.; Crabtree, A. M.; Thiel, P. A., Chemical reactions between atomic oxygen and formic acid on Pt(111). *J. Electroanal. Chem.* **1993**, *351*, 207-226.
- [138] Madix, R. J.; Gland, J. L.; Mitchell, G. E.; Sexton, B. A., Identification of the intermediates in the dehydration of formic acid on Ni(110) by high resolution electron energy loss vibrational spectroscopy. *Surf. Sci.* **1983**, *125*, 481-489.
- [139] Haq, S.; Love, J. G.; Sanders, H. E.; King, D. A., Adsorption and decomposition of formic acid on Ni{110}. *Surf. Sci.* **1995**, *325*, 230-242.
- [140] Yamakata, A.; Kubota, J.; Kondo, J. N.; Hirose, C.; Domen, K.; Wakabayashi, F., In Situ Observation of the Dehydration of Formate on Ni(110). *J. Phys. Chem. B* **1997**, *101*, 5177-5181.
- [141] Benziqer, J. B.; Schoofs, G. R., Influence of adsorbate interactions on heterogeneous reaction kinetics. Formic acid decomposition on nickel. *J. Phys. Chem.* **1984**, *88*, 4439-4444.
- [142] Noguchi, H.; Okada, T.; Onda, K.; Kano, S. S.; Wada, A.; Domen, K., Time-resolved SFG study of formate on a Ni(1 1 1) surface under irradiation of picosecond laser pulses. *Surf. Sci.* **2003**, *528*, 183-188.
- [143] Catapan, R. C.; Oliveira, A. A. M.; Chen, Y.; Vlachos, D. G., DFT Study of the Water–Gas Shift Reaction and Coke Formation on Ni(111) and Ni(211) Surfaces. *J. Phys. Chem. C* **2012**, *116*, 20281-20291.
- [144] Steinrück, H. P.; Huber, W.; Pache, T.; Menzel, D., The adsorption of benzene mono- and multilayers on Ni(111) studied by TPD and LEED. *Surf. Sci.* **1989**, *218*, 293-316.
- [145] Held, G.; Schuler, J.; Sklarek, W.; Steinrück, H. P., Determination of adsorption sites of pure and coadsorbed CO on Ni(111) by high resolution X-ray photoelectron spectroscopy. *Surf. Sci.* **1998**, *398*, 154-171.
- [146] Domnick, R.; Held, G.; Witte, P.; Steinrück, H.-P., The transition from oxygen chemisorption to oxidation of ultra-thin Ni layers on Cu(111). *J. Chem. Phys.* **2001**, *115*, 1902-1908.
- [147] Kitakatsu, N.; Maurice, V.; Hinnen, C.; Marcus, P., Surface hydroxylation and local structure of NiO thin films formed on Ni(111). *Surf. Sci.* **1998**, *407*, 36-58.
- [148] Norton, P. R.; Tapping, R. L.; Goodale, J. W., A photoemission study of the interaction of Ni(100), (110) and (111) surfaces with oxygen. *Surf. Sci.* **1977**, *65*, 13-36.
- [149] Lorenz, M., Interaction of small molecules with thin NiO layers and related metal surfaces studied with high resolution X-ray photoelectron spectroscopy. *Ph. D. thesis, Universität Erlangen-Nürnberg* **2004**.
- [150] Freund, H. J.; Roberts, M. W., Surface chemistry of carbon dioxide. *Surf. Sci. Rep.* **1996**, *25*, 225-273.
- [151] Solymosi, F., The bonding, structure and reactions of CO₂ adsorbed on clean and promoted metal surfaces. *J. Mol. Catal.* **1991**, *65*, 337-358.

- [152] Bachmann, P.; Düll, F.; Späth, F.; Bauer, U.; Steinrück, H.-P.; Papp, C., A HR-XPS study of the formation of h-BN on Ni(111) from the two precursors, ammonia borane and borazine. *J. Chem. Phys.* **2018**, *149*, 164709.
- [153] Song, L.; Ci, L.; Lu, H.; Sorokin, P. B.; Jin, C.; Ni, J.; Kvashnin, A. G.; Kvashnin, D. G.; Lou, J.; Yakobson, B. I., et al., Large Scale Growth and Characterization of Atomic Hexagonal Boron Nitride Layers. *Nano Lett.* **2010**, *10*, 3209-3215.
- [154] Auwärter, W.; Kreutz, T. J.; Greber, T.; Osterwalder, J., XPD and STM investigation of hexagonal boron nitride on Ni(111). *Surf. Sci.* **1999**, *429*, 229-236.
- [155] Auwärter, W.; Muntwiler, M.; Osterwalder, J.; Greber, T., Defect lines and two-domain structure of hexagonal boron nitride films on Ni(111). *Surf. Sci.* **2003**, *545*, L735-L740.
- [156] Eichler, J.; Lesniak, C., Boron nitride (BN) and BN composites for high-temperature applications. *J. Eur. Ceram. Soc.* **2008**, *28*, 1105-1109.
- [157] Chen, Y.; Zou, J.; Campbell, S. J.; Caer, G. L., Boron nitride nanotubes: Pronounced resistance to oxidation. *Appl. Phys. Lett.* **2004**, *84*, 2430-2432.
- [158] Chunyi, Z.; Yoshio, B.; Chengchun, T.; Hiroaki, K.; Dimitri, G., Large-Scale Fabrication of Boron Nitride Nanosheets and Their Utilization in Polymeric Composites with Improved Thermal and Mechanical Properties. *Adv. Mater.* **2009**, *21*, 2889-2893.
- [159] Xuemei, L.; Jun, Y.; Jianxin, Z.; Wanlin, G., Large area hexagonal boron nitride monolayer as efficient atomically thick insulating coating against friction and oxidation. *Nanotechnology* **2014**, *25*, 105701.
- [160] Geim, A. K.; Novoselov, K. S., The rise of graphene. *Nat. Mater.* **2007**, *6*, 183.
- [161] Nagashima, A.; Tejima, N.; Gamou, Y.; Kawai, T.; Oshima, C., Electronic dispersion relations of monolayer hexagonal boron nitride formed on the Ni(111) surface. *Phys. Rev. B* **1995**, *51*, 4606-4613.
- [162] Solozhenko, V. L.; Lazarenko, A. G.; Petitet, J. P.; Kanaev, A. V., Bandgap energy of graphite-like hexagonal boron nitride. *J. Phys. Chem. Solids* **2001**, *62*, 1331-1334.
- [163] Watanabe, K.; Taniguchi, T.; Kanda, H., Direct-bandgap properties and evidence for ultraviolet lasing of hexagonal boron nitride single crystal. *Nat. Mater.* **2004**, *3*, 404.
- [164] Dean, C. R.; Young, A. F.; Meric, I.; Lee, C.; Wang, L.; Sorgenfrei, S.; Watanabe, K.; Taniguchi, T.; Kim, P.; Shepard, K. L., et al., Boron nitride substrates for high-quality graphene electronics. *Nat. Nanotechnol.* **2010**, *5*, 722.
- [165] Späth, F.; Gebhardt, J.; Düll, F.; Bauer, U.; Bachmann, P.; Gleichweit, C.; Görling, A.; Steinrück, H. P.; Papp, C., Hydrogenation and hydrogen intercalation of hexagonal boron nitride on Ni(1 1 1): reactivity and electronic structure. *2D Mater.* **2017**, *4*, 035026.
- [166] Späth, F.; Soni, H. R.; Steinhauer, J.; Düll, F.; Bauer, U.; Bachmann, P.; Hieringer, W.; Görling, A.; Steinrück, H.-P.; Papp, C., Oxygen Functionalization of Hexagonal Boron Nitride on Ni(111). *Chem. Eur. J.* **2019**.
- [167] Paine, R. T.; Narula, C. K., Synthetic routes to boron nitride. *Chem. Rev.* **1990**, *90*, 73-91.
- [168] Boese, R.; Maulitz, A. H.; Stellberg, P., Solid-State Borazine: Does it Deserve to be Entitled "Inorganic Benzene"? *Chem. Ber.* **1994**, *127*, 1887-1889.
- [169] Islas, R.; Chamorro, E.; Robles, J.; Heine, T.; Santos, J. C.; Merino, G., Borazine: to be or not to be aromatic. *Struct. Chem.* **2007**, *18*, 833-839.
- [170] Staubitz, A.; Robertson, A. P. M.; Manners, I., Ammonia-Borane and Related Compounds as Dihydrogen Sources. *Chem. Rev.* **2010**, *110*, 4079-4124.
- [171] B., M. T., Will We Soon Be Fueling our Automobiles with Ammonia-Borane? *Angew. Chem. Int. Ed.* **2007**, *46*, 8116-8118.
- [172] Peng, B.; Chen, J., Ammonia borane as an efficient and lightweight hydrogen storage medium. *Energ. Environ. Sci.* **2008**, *1*, 479-483.
- [173] Stephens, F. H.; Pons, V.; Tom Baker, R., Ammonia-borane: the hydrogen source par excellence? *Dalton Trans.* **2007**, *0*, 2613-2626.
- [174] Hausdorf, S.; Baitalow, F.; Wolf, G.; Mertens, F. O. R. L., A procedure for the regeneration of ammonia borane from BNH-waste products. *Int. J. Hydrog. Energy* **2008**, *33*, 608-614.

- [175] Smythe, N. C.; Gordon, J. C., Ammonia Borane as a Hydrogen Carrier: Dehydrogenation and Regeneration. *Eur. J. Inorg. Chem.* **2010**, *2010*, 509-521.
- [176] Davis, B. L.; Dixon, D. A.; Garner, E. B.; Gordon, J. C.; Matus, M. H.; Scott, B.; Stephens, F. H., Efficient Regeneration of Partially Spent Ammonia Borane Fuel. *Angew. Chem. Int. Ed.* **2009**, *48*, 6812-6816.
- [177] Sutton, A. D.; Davis, B. L.; Bhattacharyya, K. X.; Ellis, B. D.; Gordon, J. C.; Power, P. P., Recycle of tin thiolate compounds relevant to ammonia-borane regeneration. *Chem. Commun.* **2010**, *46*, 148-149.
- [178] Sutton, A. D.; Burrell, A. K.; Dixon, D. A.; Garner, E. B.; Gordon, J. C.; Nakagawa, T.; Ott, K. C.; Robinson, J. P.; Vasiliu, M., Regeneration of Ammonia Borane Spent Fuel by Direct Reaction with Hydrazine and Liquid Ammonia. *Science* **2011**, *331*, 1426-1429.
- [179] Yan, J.-M.; Zhang, X.-B.; Akita, T.; Haruta, M.; Xu, Q., One-Step Seeding Growth of Magnetically Recyclable Au@Co Core-Shell Nanoparticles: Highly Efficient Catalyst for Hydrolytic Dehydrogenation of Ammonia Borane. *J. Am. Chem. Soc.* **2010**, *132*, 5326-5327.
- [180] Gutowska, A.; Li, L.; Shin, Y.; Wang, C. M.; Li, X. S.; Linehan, J. C.; Smith, R. S.; Kay, B. D.; Schmid, B.; Shaw, W., et al., Nanoscaffold Mediates Hydrogen Release and the Reactivity of Ammonia Borane. *Angew. Chem. Int. Ed.* **2005**, *44*, 3578-3582.
- [181] Keaton, R. J.; Blacquiere, J. M.; Baker, R. T., Base Metal Catalyzed Dehydrogenation of Ammonia-Borane for Chemical Hydrogen Storage. *J. Am. Chem. Soc.* **2007**, *129*, 1844-1845.
- [182] Xu, Q.; Chandra, M., Catalytic activities of non-noble metals for hydrogen generation from aqueous ammonia-borane at room temperature. *J. Power Sources* **2006**, *163*, 364-370.
- [183] Chandra, M.; Xu, Q., A high-performance hydrogen generation system: Transition metal-catalyzed dissociation and hydrolysis of ammonia-borane. *J. Power Sources* **2006**, *156*, 190-194.
- [184] Kim, K. K.; Hsu, A.; Jia, X.; Kim, S. M.; Shi, Y.; Hofmann, M.; Nezich, D.; Rodriguez-Nieva, J. F.; Dresselhaus, M.; Palacios, T., et al., Synthesis of Monolayer Hexagonal Boron Nitride on Cu Foil Using Chemical Vapor Deposition. *Nano Lett.* **2012**, *12*, 161-166.
- [185] Shi, Y.; Hamsen, C.; Jia, X.; Kim, K. K.; Reina, A.; Hofmann, M.; Hsu, A. L.; Zhang, K.; Li, H.; Juang, Z.-Y., et al., Synthesis of Few-Layer Hexagonal Boron Nitride Thin Film by Chemical Vapor Deposition. *Nano Lett.* **2010**, *10*, 4134-4139.
- [186] Wideman, T.; Sneddon, L. G., Convenient Procedures for the Laboratory Preparation of Borazine. *Inorg. Chem.* **1995**, *34*, 1002-1003.
- [187] Preobrajenski, A. B.; Vinogradov, A. S.; Mårtensson, N., Monolayer of h-BN chemisorbed on Cu(111) and Ni(111): The role of the transition metal 3d states. *Surf. Sci.* **2005**, *582*, 21-30.
- [188] Jin, C.; Lin, F.; Suenaga, K.; Iijima, S., Fabrication of a Freestanding Boron Nitride Single Layer and Its Defect Assignments. *Phys. Rev. Lett.* **2009**, *102*, 195505.
- [189] Jiménez, I.; Jankowski, A. F.; Terminello, L. J.; Sutherland, D. G. J.; Carlisle, J. A.; Doll, G. L.; Tong, W. M.; Shuh, D. K.; Himpsel, F. J., Core-level photoabsorption study of defects and metastable bonding configurations in boron nitride. *Phys. Rev. B* **1997**, *55*, 12025-12037.
- [190] Usachov, D.; Adamchuk, V. K.; Haberer, D.; Grüneis, A.; Sachdev, H.; Preobrajenski, A. B.; Laubschat, C.; Vyalikh, D. V., Quasifreestanding single-layer hexagonal boron nitride as a substrate for graphene synthesis. *Phys. Rev. B* **2010**, *82*, 075415.
- [191] Li, H.; Li, H.; Dai, W.-L.; Wang, W.; Fang, Z.; Deng, J.-F., XPS studies on surface electronic characteristics of Ni-B and Ni-P amorphous alloy and its correlation to their catalytic properties. *Appl. Surf. Sci.* **1999**, *152*, 25-34.
- [192] Legrand, J.; Gota, S.; Guittet, M. J.; Petit, C., Synthesis and XPS Characterization of Nickel Boride Nanoparticles. *Langmuir* **2002**, *18*, 4131-4137.
- [193] Inamura, K.; Inoue, Y.; Ikeda, S.; Kishi, K., X-ray photoelectron spectroscopic study for the adsorption and the decomposition of alkylamines on nickel. *Surf. Sci.* **1985**, *155*, 173-186.
- [194] Pache, T.; Steinrück, H. P.; Huber, W.; Menzel, D., The adsorption of H₂O on clean and oxygen precovered Ni(111) studied by ARUPS and TPD. *Surf. Sci.* **1989**, *224*, 195-214.
- [195] Geanangel, R. A.; Rabalais, J. W., Evidence from mass spectra and X-ray photoelectron spectra concerning the structure of poly(aminoborane). *Inorg. Chim. Acta* **1985**, *97*, 59-64.

References

- [196] Russell, J. N.; Chorkendorff, I.; Lanzillotto, A. M.; Alvey, M. D.; Yates, J. T., Angular distributions of H₂ thermal desorption: Coverage dependence on Ni(111). *J. Chem. Phys.* **1986**, *85*, 6186-6191.

12. Acknowledgements – Danksagung

An dieser Stelle möchte ich allen danken, die zum Gelingen dieser Dissertation beigetragen haben.

Besonderer Dank gilt dabei Prof. Dr. Hans-Peter Steinrück für die Möglichkeit diese Arbeit an seinem Lehrstuhl, in einer sehr angenehmen Arbeitsumgebung, anzufertigen. Die gemeinsamen Diskussionen wissenschaftlicher Daten waren stets konstruktiv und motivierend. Auch abseits wissenschaftlicher Themen stand er mit Rat und Tat zur Seite.

Als nächstes möchte ich mich bei PD Dr. Christian Papp für die kompetente Betreuung und umfangreiche Unterstützung in allen Belangen bedanken. Als Leiter der Synchrotron-Arbeitsgruppe war er stets die erste Anlaufstelle für alle wissenschaftlichen und organisatorischen Angelegenheiten und eine große Hilfe bei deren Bewältigung.

Der Großteil der Daten in dieser Dissertation wurde am Synchrotron BESSY II in Berlin erzeugt. Der Aufwand, der hinter den dazugehörigen, mehrwöchigen Messzeiten steckt, ist nicht allein zu bewältigen, sondern erfordert Teamwork und Zusammenhalt in allen Belangen. Ich bedanke mich daher für die tatkräftige Unterstützung bei meinen Kollegen der Synchrotron-Arbeitsgruppe Dr. Udo Bauer, Dr. Florian Späth, Fabian Düll, Johann Steinhauer und Felix Hemauer.

Im Rahmen der Kooperation zu LOHC-Projekten, bedanke ich mich bei Prof. Dr. Peter Wasserscheid, Dr. Andreas Bösmann sowie Dr. Marlene Scheuermeyer und Dr. Konstantin Gärtner für die Synthese und Hydrierung von LOHCs. Ohne diese Substanzen wäre ein Großteil der Studien gar nicht erst möglich gewesen. Zudem bedanke ich mich bei Prof. Dr. Jörg Libuda und Dr. Matthias Schwarz für die Kooperation zum Indol-LOHC-System und dem Beitrag von IRAS Daten.

Während der Promotionsphase betreute ich die Anfertigung zweier Masterarbeiten von Johann Steinhauer und Felix Hemauer als auch die Anfertigung von fünf Bachelorarbeiten von Jonas Enghard, Felix Hemauer, Roman Eschenbacher, Sofie Mika und Samo Marcinko. Die dadurch gewonnenen Ergebnisse trugen teilweise zu einzelnen Themen dieser Dissertation bei. Diesbezüglich möchte ich mich für die Zusammenarbeit bedanken.

Das reibungslose Funktionieren einer Ultrahochvakuum-Anlage setzt regelmäßige Wartungen, Reparaturen und Spezialanfertigungen voraus. Insbesondere möchte ich mich daher bei Hans-Peter Bäumlner als Elektroniker, Bernd Kreß als Vakuum-Ingenieur, und Friedhold Wölfel als Werkstattleiter, sowie dem gesamten Werkstatt-Team für die umfangreiche Unterstützung, Anfertigung und Reparatur elektronischer und technischer Komponenten bedanken.

Außerdem bedanke ich mich bei allen, die den wissenschaftlichen Betrieb am Lehrstuhl organisieren und aufrechterhalten, insbesondere bei Andrea Meixner-Wolf, Susanna Kreß, Sabine Patzak-Fleck und Norman Anja Schmidt.

Abschließend möchte ich mich bei meinen Eltern Martina und Hartmut sowie meiner Partnerin Katharina bedanken, die mir in jeder Lebenslage beistanden und mich in allen Belangen bedingungslos unterstützten.

Appendix A: Supplementary Data

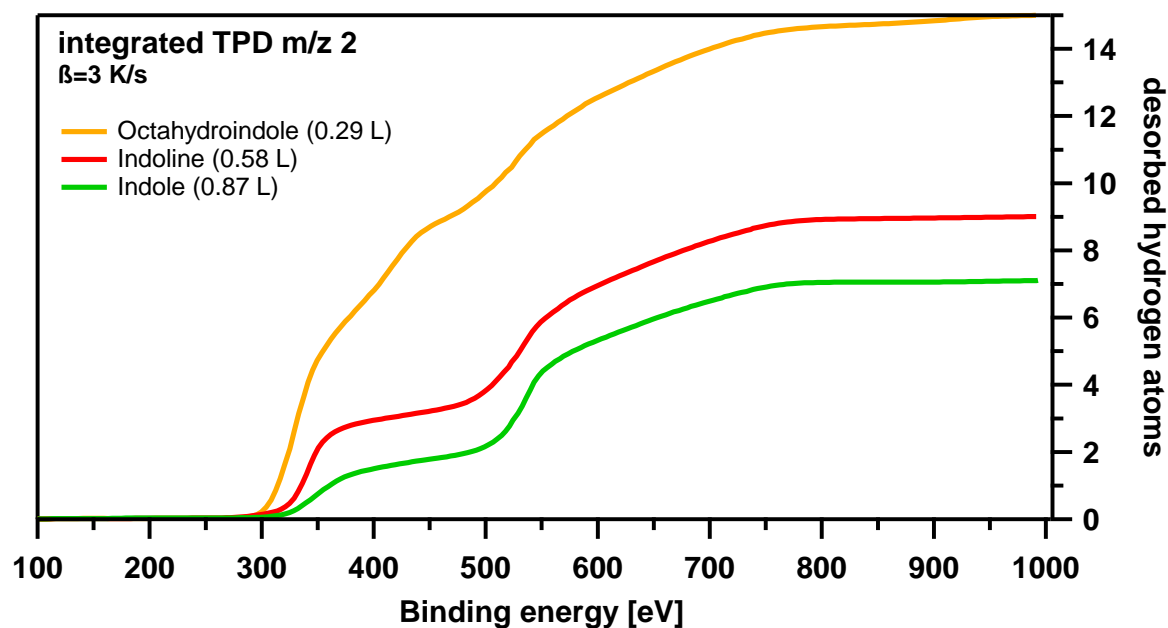


Figure A 1: Integrated H₂ (m/z=2) TPD spectra of indole, indoline and octahydroindole on Pt(111).

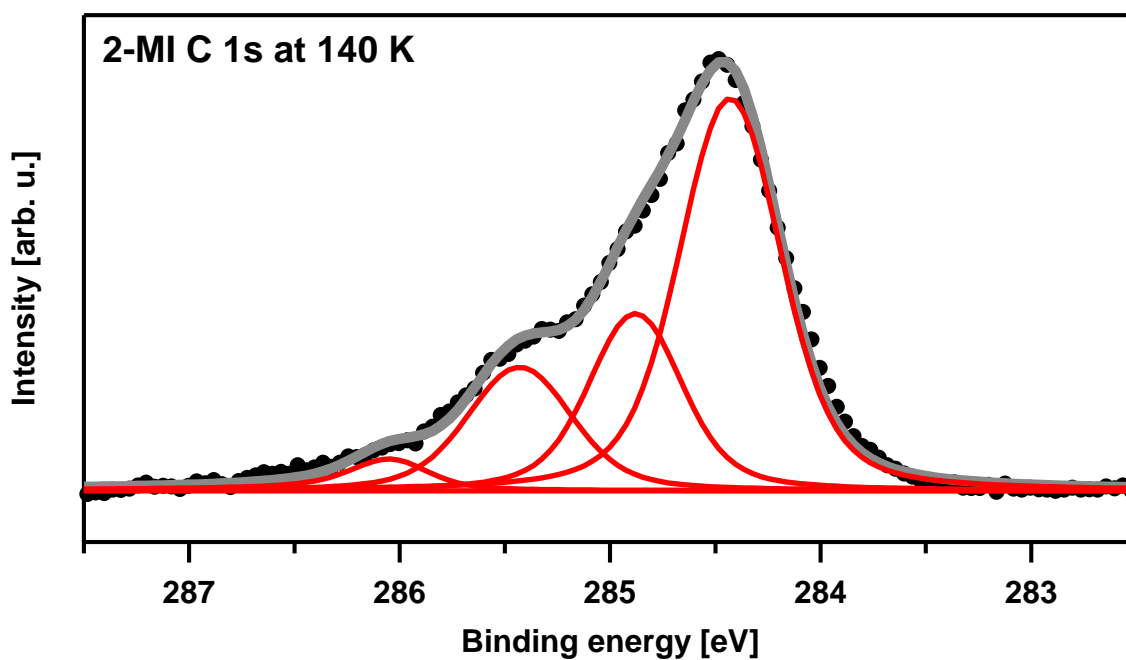


Figure A 2: Spectrum of 2-methylindole at 140 K on Pt(111), including fits.

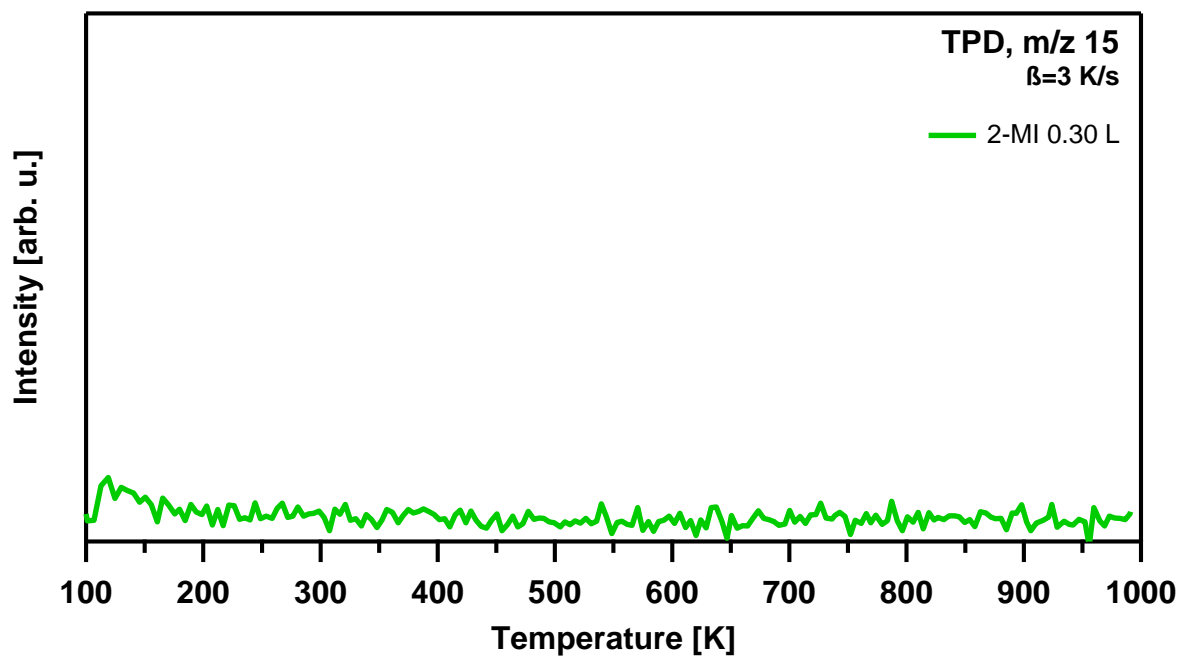


Figure A 3: TPD spectrum of m/z=15 of 2-methylindole. The small increase of the background signal from ~100-150 K is due to desorption from the sample holder.

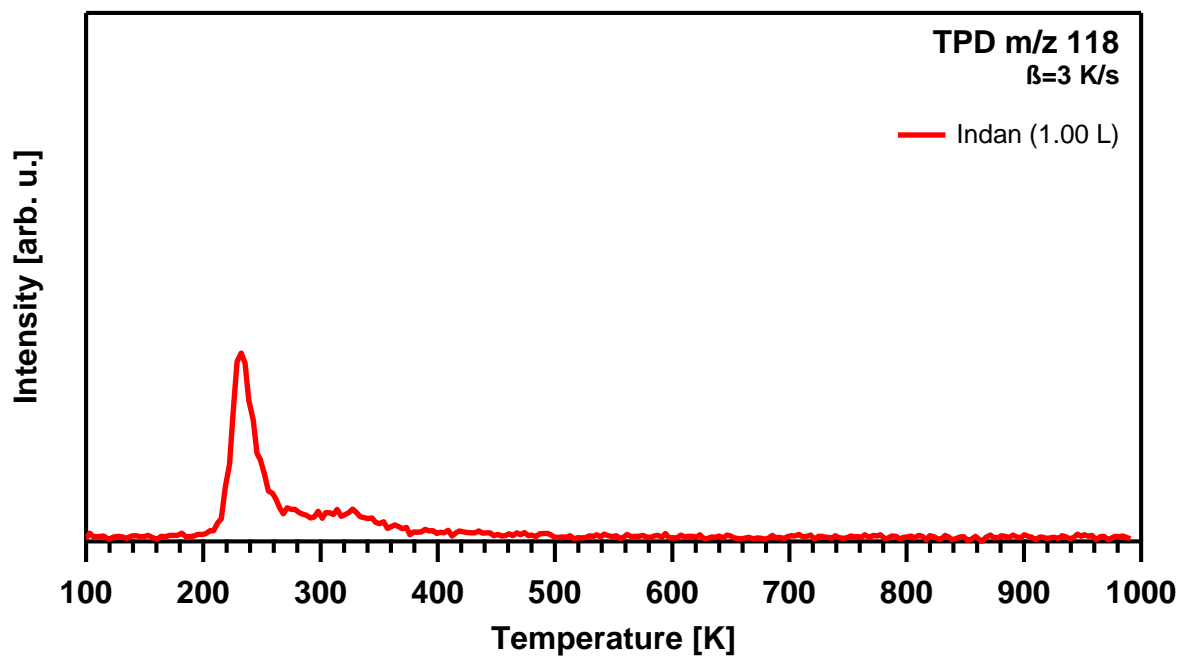


Figure A 4: TPD spectrum of m/z=118 of indan. Molecular desorption is observed with a peak maximum at 230 K.

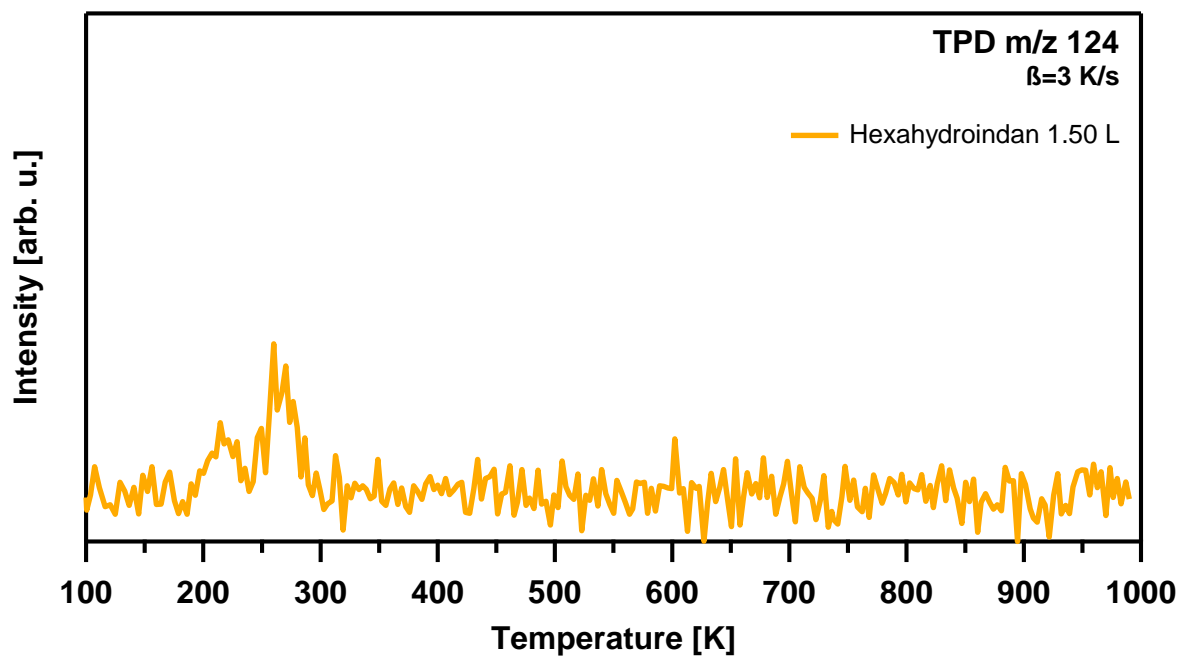


Figure A 5: TPD spectrum of $m/z=124$ of hexahydroindan. Molecular desorption is observed in the range from ~ 200 -300 K.

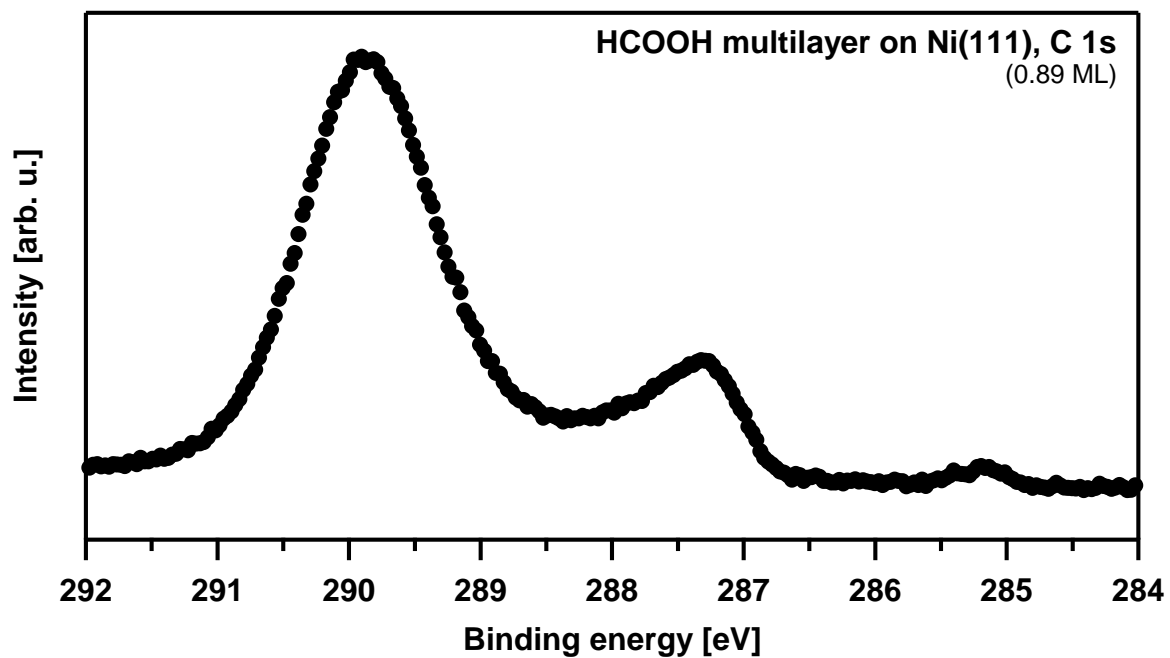


Figure A 6: C 1s spectrum of a formic acid multilayer on Ni(111).

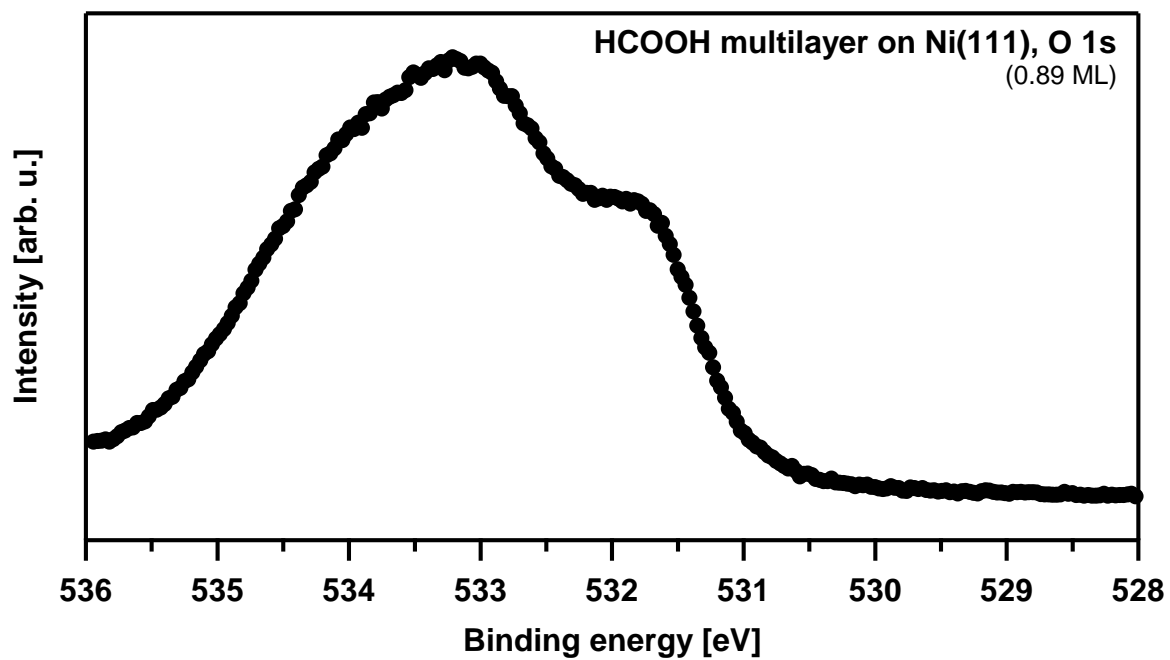


Figure A 7: O 1s spectrum of a formic acid multilayer on Ni(111).

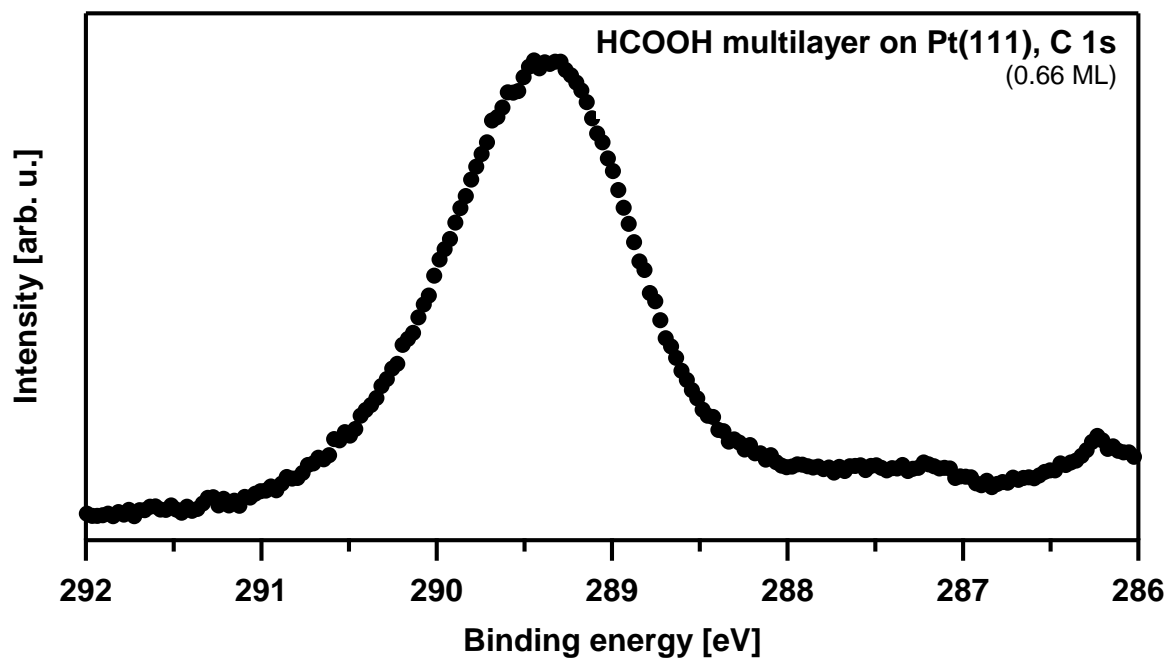


Figure A 8: C 1s spectrum of a formic acid multilayer on Pt(111).

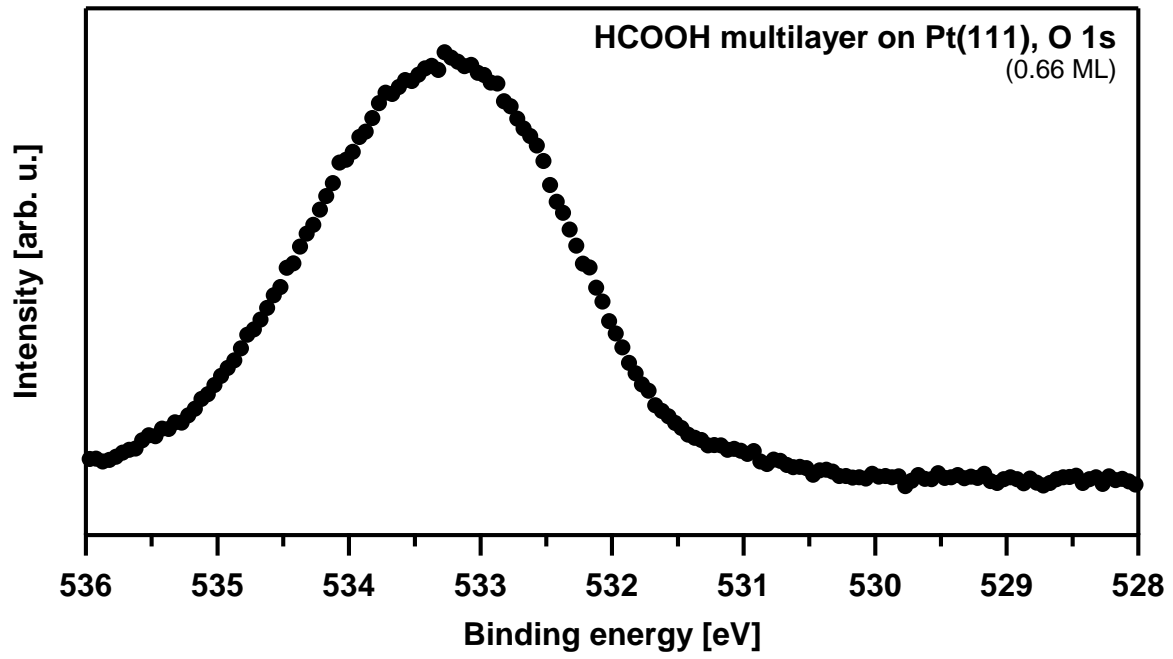


Figure A 9: O 1s spectrum of a formic acid multilayer on Pt(111).

Appendix B: Programs and Scripts

In the following, a short overview and documentation of helpful programs and scripts, written by me alongside the scientific part of this thesis, is given in order to serve as operation manual. The aim was to ease the acquisition, processing and evaluation of the collected data presented in this thesis. Some programs and scripts depend on third-party libraries and software packages and are marked accordingly.

All IGOR related programs/scripts were developed and tested with IGOR Pro 6.2.2.2. For the procedures to work, they must be placed in the “Igor Procedures” folder; the usual location is “C:\Users\XXX\Documents\WaveMetrics\Igor Pro 6 User Files\Igor Procedures”, where XXX is the username. LabVIEW programs were developed and tested on LabVIEW 17.0 (64-bit). The underlying operation system was Windows 10 (64-bit). The programs and scripts may exhibit bugs, especially with altered measurement setups and/or parameters. Therefore, simple code changes may be necessary from time to time.

IGOR scripts

B1.1 TPD.ipf

Dependencies: none

This procedure enables batch processing and imaging of TPD data acquired with the “Measurement” program of the “PFEIFFER VACUUM QUADSTAR 32-bit” software package. The binary TPD data must be converted to ASCII-format via “DispSav” before processing in IGOR. In order for TPD.ipf to successfully load TPD data, the header of the ASCII-file has to be in a specific format, which can be specified within “ParSet” (see Figure B1 for values and example header). The header must contain the highlighted lines in the depicted order or otherwise the import with this script will not work without code changes. In Figure B 2, the graphical user interface of the TPD procedure is shown with an example of processed TPD data above.

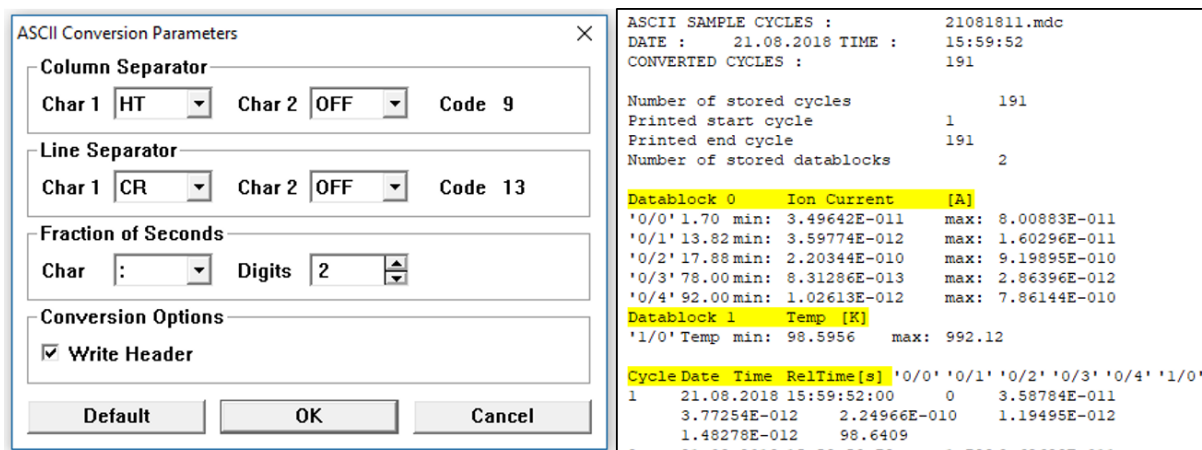


Figure B 1: ASCII setup within “ParSet” (left) and example of a resulting ASCII TPD-file header (right) with highlighted lines that must be present in this order for successful import in IGOR with the TPD procedure.

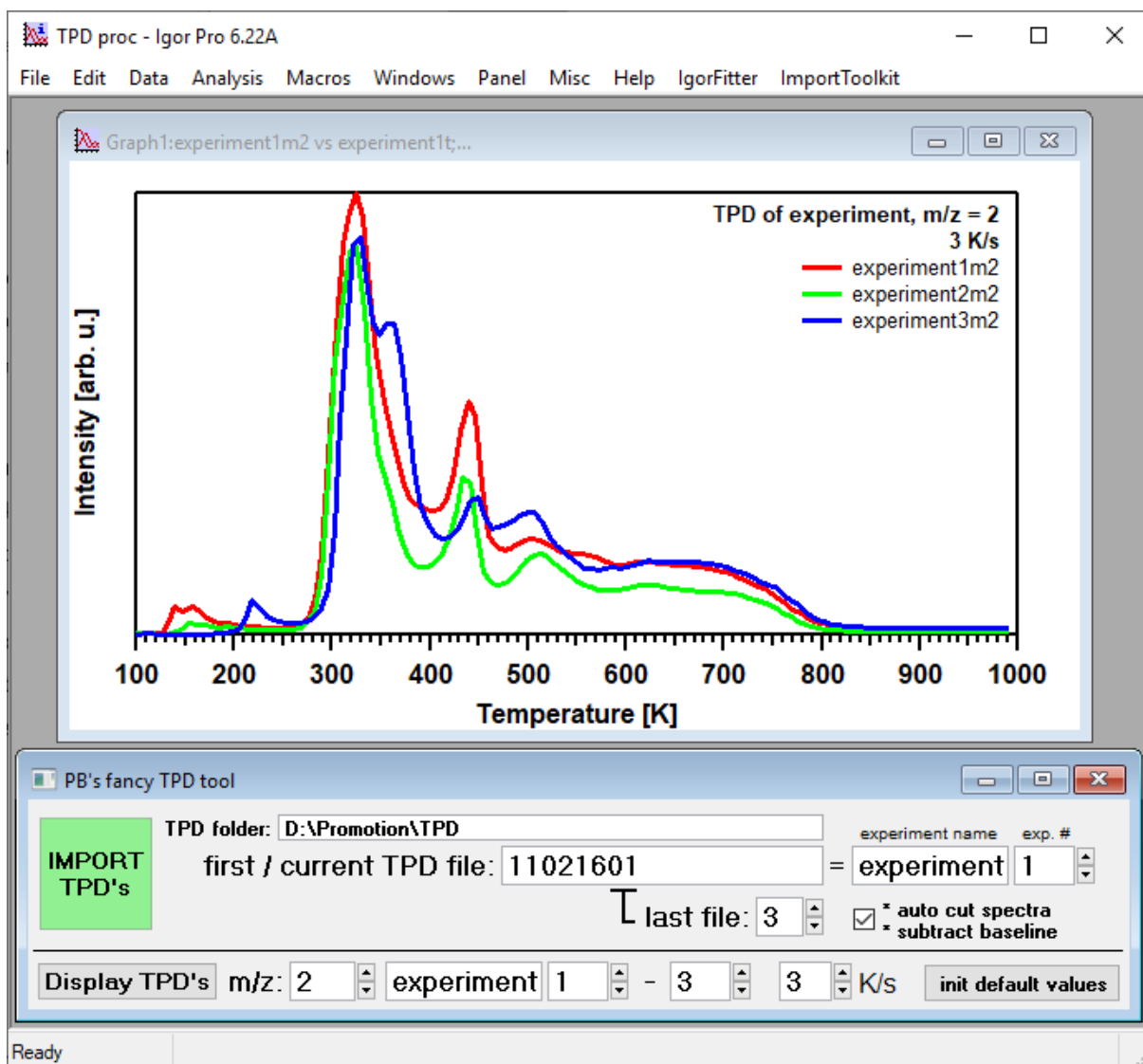


Figure B 2: Configuration window of the TPD procedure in IGOR and graph of example data after processing.

To process TPD data, follow these steps:

1. Open the “TPD tool” via the “Macros” menu, which then displays the interface shown in Figure B 2.
2. Insert the path to the folder containing the ASCII TPD-files in the “TPD folder” input field.
3. Specify the name of the first or current TPD file to import in the “first /current TPD file” input field. The filename should follow the naming scheme “ddMMyyxx” with ddMMyy as date and xx as enumerator. Specify the enumerator of the last file to import in “last file” input field.

(Names following the scheme “abcdefXX”, like experiment01, should also work.)

4. Insert the experiment name IGOR will use internally for the imported spectra into the “experiment name” input field.

In Figure B 2 “experiment” is used. Hint: Insert e.g. “CO”, if the imported data are CO TPD’s.

5. Insert the enumeration number of the experiment in the “exp. #” input field. This number will increase automatically during import, resulting in a new set of IGOR wave names for each imported TPD file.

Usually this number is 1 in the beginning, unless you import data from several dates and wish to enumerate them with the same experiment name. In this case first import your data from one date and then change the “current TPD file” and the “last file” to the next date. Furthermore, increase the experiment enumeration number by 1 to achieve a continuous, IGOR internal, experiment enumeration, e.g. experiment1, experiment2, ..., experiment8, without overriding data.

6. Checking “auto cut spectra / subtract baseline” will automatically remove excess acquired data points before reaching 100 K and after 1000 K. Furthermore, a baseline based on the lowest data point of the spectrum will be subtracted.
7. Press the button “IMPORT TPD’s” to import the specified files with the specified parameters.

The example in Figure B 2 would result in IGOR waves like experiment1mXX, experiment1t, experiment2mXX, experiment2t, experiment3mXX, experiment3t, with one temperature wave for each experiment and several waves per experiment ending with the measured m/z-ratio XX, e.g. experiment1m2, experiment1m18, experiment1m78.

8. Pressing the button “Display TPD’s” then visualizes the measured data in a graph window with experiment name-based labels. Therefore, specify the m/z-ratio with “m/z” and the experiment number range (e.g. “1-3” in Figure B 2). Optionally, the heating rate can be specified.
9. Pressing “init default values” will reset all user made changes in the user interface.

Default values, like “TPD folder”, can be adjusted by modifying the procedure.

B1.2 NEXAFS.ipf

Dependencies: nice.ipf

This procedure enables batch processing of NEXAFS data acquired at BESSY II with a Keithley amperemeter and EMP/2 as measurement software. It detects B, C, N and O K-edge regions, interpolates data, includes the decay of the ring current during measurement and enables the division/subtraction of reference spectra. For NEXAFS.ipf to successfully import raw data, the channel order inside EMP/2 and the generated files must be: “TIMER”, “Monoposition”, “Ringstrom”, “Keithley@XX”. Else, the procedure or EMP/2 configuration must be modified accordingly.

To process NEXAFS data follow these steps:

1. Open the “NEXAFS toolkit” via the “Macros” menu, which then displays the interface shown on the bottom of Figure B 3.
2. Insert the path to the folder containing the NEXAFS datafiles in “Path”.
3. Check “auto interpolate” if you wish to process your data further with the NEXAFS toolkit. Leave this option unchecked if you want to work with unprocessed raw data.

4. Usually, the supported scheme of NEXAFS filenames is “ddMMyy.XX” with “ddMMyy” as date and XX as enumerator. Insert the NEXAFS date into the input field behind “Set:” and the desired enumerator in the input field behind the “Load Data” button.
5. Press “Load Data” to load a single NEXAFS file. Press “Load from” to load multiple files, specified by the input fields right next to the button.
6. The buttons “Display”, “Append” and “Edit” allow you to either display the spectrum specified in the input field on the right, append it to an existing graph window or edit the associated raw data table.
7. “Append grazing ref (ig)” and “Append normal ref (in)” append the corresponding reference spectrum to the foremost graph window. Before appending, the enumeration number of the reference must be specified in the right input field.
8. If desired, the spectrum and the reference spectrum can be multiplied to each other via 2-point multiplication to compensate e.g. for intensity differences. First, select your spectrum number and the nature of your spectrum (grazing or normal), before pressing “Append cursors”. This will display 2 pairs of cursors A/C and B/D, which can be aligned to the desired part of the spectrum (usually at the lower or the higher end of the recorded binding energy) using either the direction keys of the keyboard or the input fields labelled “A/C” and B/D”. Pressing “Multiply to fit” performs the multiplication process. IMPORTANT: This step will modify your spectrum, to revert changes, you need to reload the spectrum (see 5.).

Your active graph window should now look like the top window in Figure B 3. Here A/C and B/C are set to the lower end of the spectrum. The spectrum and the reference have already been multiplied to fit each other.

9. Pressing “Divide Spec/Ref” divides the spectrum by the reference, while “Subtract Spec/Ref” subtracts the reference from the spectrum. This process does not modify the imported data and opens a new graph window with the result spectrum and automatic labels (see Figure B 3 middle).

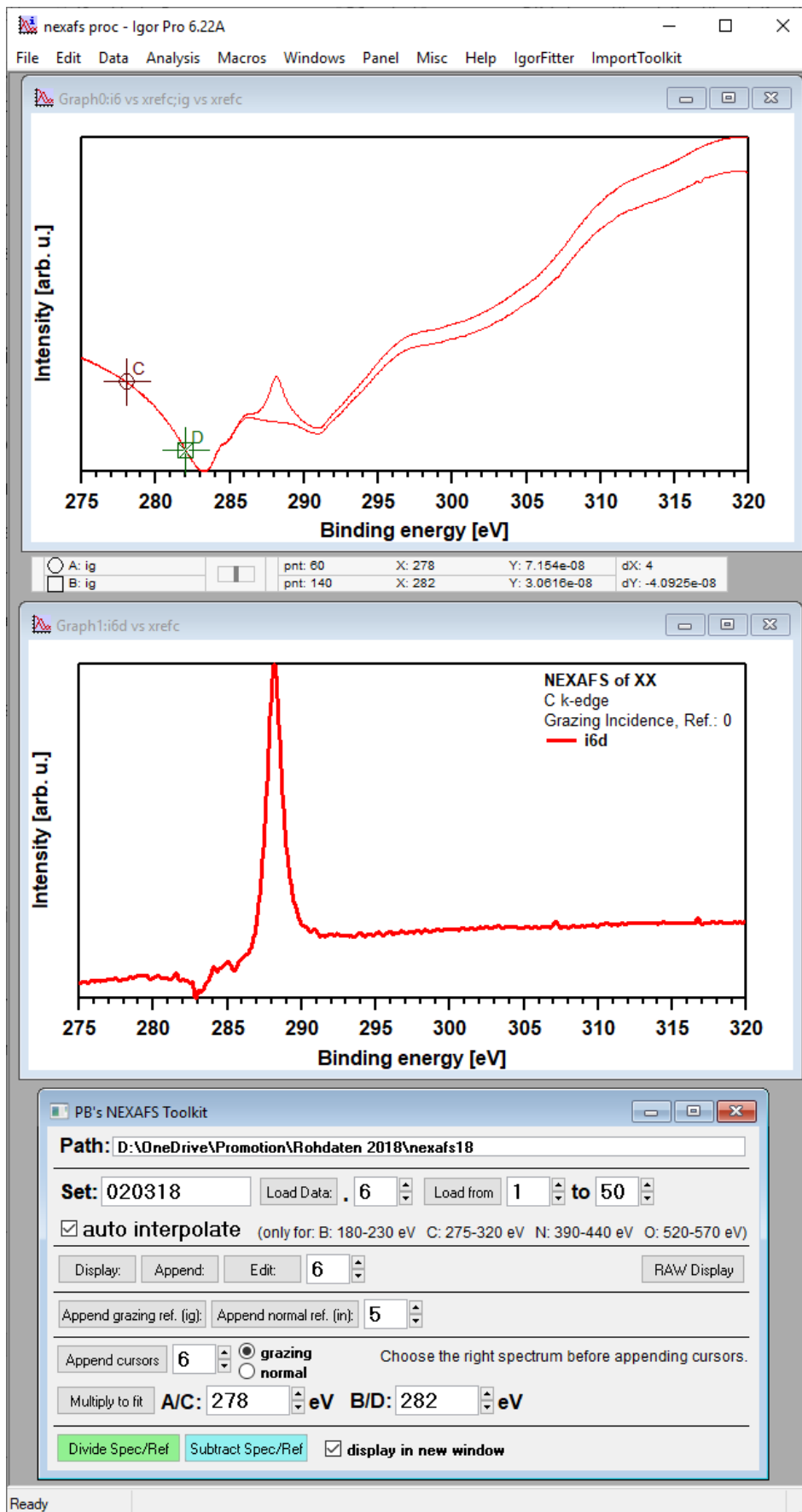


Figure B 3: Configuration window (bottom) of the NEXAFS procedure in IGOR and graphs of raw data (top) and final spectrum after processing (middle).

B1.3 nice.ipf

Dependencies: none

This procedure just modifies the appearance of graph windows, making them uniform and nice-looking for image exporting. In case of C 1s, N 1s and TPD spectra, it also aligns the binding energy/temperature range on the bottom axis to common values. Expanding the features for e.g. other core levels can be easily achieved by modifying the procedure.

To use the procedure, follow these steps:

1. Click “Nice” inside the “Macros” menu. The appearance of the foremost graph window will be modified. As there is no way in IGOR to easily revert the changes, duplicate your graph window before using this procedure.

B1.4 densplot.ipf

Dependencies: IgorFitter.ipf (C. Gleichweit)

This procedure displays a density plot of a set of XPS spectra, prior loaded into IgorFitter. It automatically detects C 1s and N 1s core level regions and adjusts the appearance of the resulting graph depending on the spectra belonging to an adsorption or TPXPS experiment.

To use the procedure, follow these steps:

1. Click “DensPlot” inside the “Macros” menu. A new graph window containing the density plot of the experiment will appear.

B1.5 densplotpeakpos.ipf

Dependencies: densplot.ipf, IgorFitter.ipf (C. Gleichweit)

This procedure overlays the binding energy of fitted peaks from IgorFitter in a prior generated density plot from densplot.ipf as colored markers.

To use the procedure, follow these steps:

1. Generate a density plot using densplot.ipf (see B1.4) and make sure it is the foremost graph window
2. Click “DensPlotPeakPos” inside the “Macros” menu to add colored peak positions for each XP-spectrum.

B1.6 fancyplot.ipf

Dependencies: IgorFitter.ipf (C. Gleichweit)

This procedure eases the process of making area plots by creating IGOR waves that are directly related to the provided coverage calibration instead of arbitrary integrals. Furthermore, it allows the concatenation of the coverages from single peaks into one area/species.

To use the procedure, follow these steps:

1. Open “Fancy Area Plot” via the “Macros” menu, which then displays the interface shown on the bottom of Figure B 4.
2. Specify the integral (wfitarea) of 1 ML of your desired core level reference in the input field next to “1 ML (CO wfitarea x2)”.

For the C 1s region on Pt(111), usually CO is used as reference molecule. The wfitarea of 0.5 ML CO amounts generally to 1.2, which then gives 2.4 for 1 ML. Monolayer values of different core levels can also be used; the axis labels of the produced graphs then just need to be updated.

3. Specify, whether the experiment is an adsorption or a TPXPS with the “Uptake” and “TPXPS” check boxes. This will adjust the bottom axis accordingly.
4. The input field “Divide by” enables the calculation of molecule monolayers, e.g. by division through the number of carbon atoms in the molecule.
5. Fill out the Area matrix with the peak numbers to be summarized. Each line results in one area in the result graph. Currently, a maximum of five peaks can be added up to give one area, with a maximum of seven areas in total. Leave the fields zero, when not in use.

6. Pressing “Do Areaplot” will produce a raw formatted area plot (see Figure B 4 top), which then can be further adjusted. The field “Start Coverage” will display the coverage value of the first spectrum of the area plot.

Optional: If “display AreaPlot” is unchecked, no new graph window will pop up. The values are still recalculated, and existing area plot graph windows will be updated.

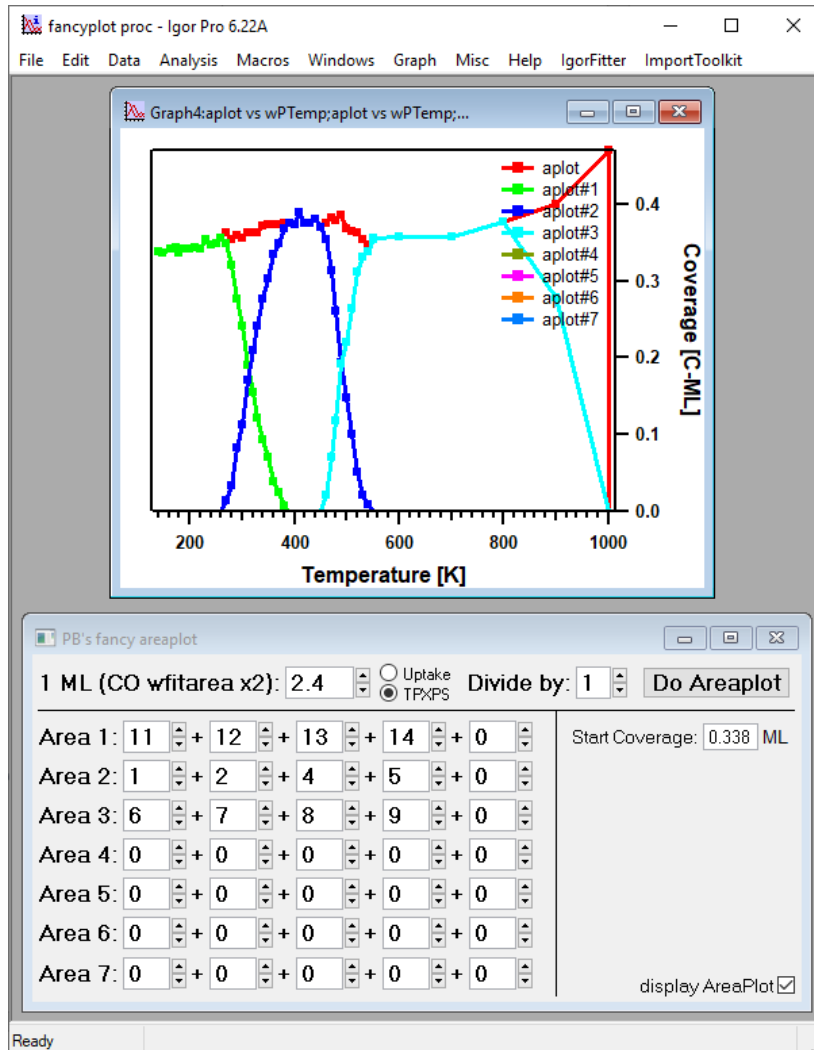


Figure B 4: Configuration window (bottom) of the fancyplot procedure in IGOR and resulting graph window (top) with added up peak areas.

B1.7 RIT (realtimeimporttoolkit.ipf, realtimeimporttoolkit_additions.ipf, watchfolder.ps1)

Dependencies: Windows PowerShell, IgorFitter.ipf (C. Gleichweit), Vernissage.exe (v2.3.3, Scienta Omicron)

This program utilizes a combination of scripts and programs to invoke the import of XPS files into IGOR utilizing the command line interface of Vernissage, which converts MATRIX (Scienta Omicron XPS Measuring Software) XPS files to ASCII format. Within the Realtime Import toolkit (RIT), XPS spectra can be displayed and transferred to IgorFitter for direct data evaluation. The functional schematic is given in Figure B 5 and the overview of the control interface is shown in Figure B 6.

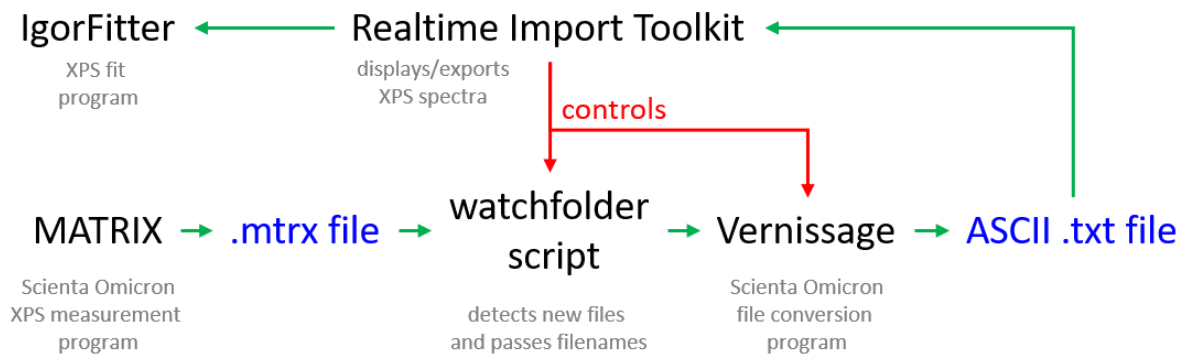


Figure B 5: Functional schematic of the Realtime Import Toolkit.

To use this program, follow these steps:

1. Make sure you have administrative rights on your Windows user account and install Vernissage v2.3.3 to the location below, otherwise this program will not work.

C:\Program Files (x86)\Scienta Omicron\Vernissage\V2.3.3

2. Click “Realtime Import Toolkit” inside the “ImportToolkit” menu in IGOR. The interface shown on the bottom of Figure B 6 will appear.
3. On first use, you need to press “Setup watchfolder” inside the advanced settings on the bottom right. This will setup the PowerShell script/profile. WARNING: This will rename any old default PowerShell profile in place.

4. Specify the folder in which MATRIX exports measurement data in the “MATRIX file folder” input field. Select a folder, where you want the ASCII files converted by Vernissage to be in the “OUTPUT folder” input field.
5. The buttons “Start watchfolder” and “Stop watchfolder” start or stop looking for new .mtrx files generated by MATRIX in the “MATRIX file folder”. If a new file is found, it will be converted automatically to an ASCII .txt file using the Vernissage command interface. “Batch convert MATRIX file folder” batch converts all available files in the “MATRIX file folder”.
6. Press “Get output filename sample” to automatically insert a sample filename into the “filename sample” input field. It can also be put in manually. A filename sample is needed to know the name structure of the files you want to import.

MATRIX usually generates filenames like the one seen in Figure B 6, which represents the default naming scheme. The scheme can be changed within MATRIX but the filename should always contain the part behind “iXPS--” in order to be importable in RIT.

7. Specify the excitation energy in with “Set hv” and the spectrum dwell time with “Set dwell time”. These settings are necessary, as Vernissage does not provide the options for ASCII file headers with supplementary measurement information and export is only possible with kinetic energy values.
8. Specify the enumeration number of the first spectrum you want to import with “start import with spectrum #”. In case you want to import loop recorded spectra, check “loop recording in MATRIX” and input the loop number to start with in “start loop #”. In case of loop spectra, you also need to specify the spectrum number in “start import with spectrum #”.

The MATRIX generated filenames always contain a string with the spectrum number and the loop number between the string “iXPS--” and the string “-Detector_Region”. In Figure B 6, this string is “15_1” in the “filename sample”. Consequently, the spectrum number is 15 and the loop number is 1. For normal XPS measurements, the spectrum number increases with each measured

spectrum. For loop recordings the spectrum number stays unchanged while the loop number increases with each spectrum.

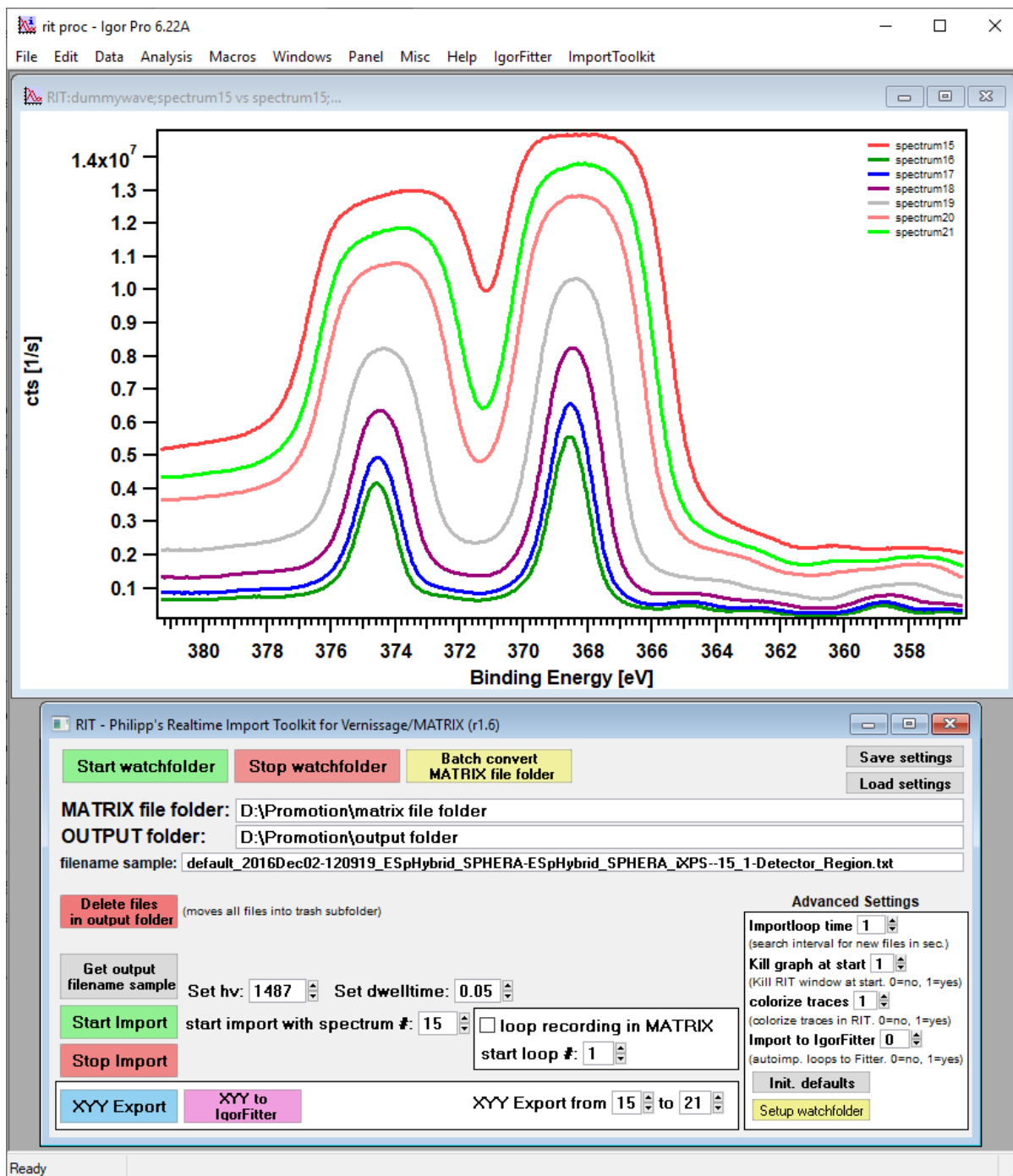


Figure B 6: Configuration window (bottom) of the Realtime Import Toolkit in IGOR and resulting graph window (top), which automatically displays newly imported spectra.

9. Click "Start Import" and "Stop Import" to start/stop importing ASCII files into IGOR, which were specified in the previous steps. The import function will try to import one spectrum file per second (on default settings, see "importloop time" in advanced settings) and increase the spectrum or loop number upon successful import of a

spectrum. It then waits for the next file to become available for input, until the import is stopped manually. “Start Import” will also open a graph window, automatically appending the imported spectra (see Figure B 6). Imported ASCII files will be moved to a subfolder inside the specified “OUTPUT folder” to remain a clean folder structure. If you wish to remove all files in the “OUTPUT folder” into a trash subfolder, click “Delete files in output folder”.

The example in Figure B 6 shows the import of spectrum 15 to 21 of the defined “filename sample” with the start settings for spectrum 15 put into the respective input fields. The import was stopped at spectrum 21.

10. To export the imported spectra, first specify the export spectrum range with “XYY Export from” input fields. Then select either “XYY Export” to export the selected spectra as .xyy file or “XYY to IgorFitter” to directly transfer the spectra in the corresponding IgorFitter matrices for direct data evaluation.
11. User made settings can be stored and loaded with “Save settings” and “Load settings”. Advanced settings allow further tweaks of the import process:
 - “Importloop time”: Changes the search interval for new ASCII files; unit: seconds.
 - “Kill graph at start”: Closes existing spectrum window upon “Start Import”.
 - “colorize traces”: Colorize new spectra to differentiate for better differentiation.
 - “Import to IgorFitter”: Automatic transfer of imported loop spectra to IgorFitter.
 - “Init. defaults”: Revert all settings to default.

LabVIEW programs

B1.8 MiniESCA Pressure (miniesca_v3.1.vi)

Dependencies: PV ActiveLine.lvlib (Pfeiffer Vacuum)

Prerequisites: Pfeiffer Vacuum DualGauge (tested: TPG262) connected to PC via RS232/USB

This program serves as secondary pressure display for Pfeiffer Vacuum Single or DualGauges. It enables the simultaneous readout of both pressure channels (DualGauge) and live, base pressure corrected, exposure calculation for the main channel. Furthermore, logfiles of pressure and exposure can be saved. The user interface is shown in Figure B 7.

To use this program, follow these steps:

1. Open the MiniESCA Pressure program and click on “Run” (white arrow top left).
2. Select the proper baud rate (usually 9600) and choose the right COM port (bottom right of the user interface). Pressure values should now be displayed in the Channel 1/Channel 2 fields and the graph window (check trace on the right panel).

If no pressure readings appear after this step, stop the program with the red button on the top left and restart it with the white arrow. In case the pressure is still not displayed, check the baud rate and COM port of the gauge and/or restart the gauge before trying to connect again. You might want to refer to Windows device manager to choose the right COM port.

3. The base pressure can be set using the button “Set BP” and will be displayed next to it.
4. Pressing “OFF” under “Exposure /Langmuir Channel 1” will change the indicator to “ON” and start displaying the calculated exposure in Langmuir next to it. Furthermore, the “Dosing Time [mm:ss]” and “Dosing Time [s]” clocks will start to count with their respective time units until the exposure calculation is turned off again. You must reset the time manually with “RESET” after each cycle. “CH 1 uncorr.” will display the exposure without base pressure subtraction.

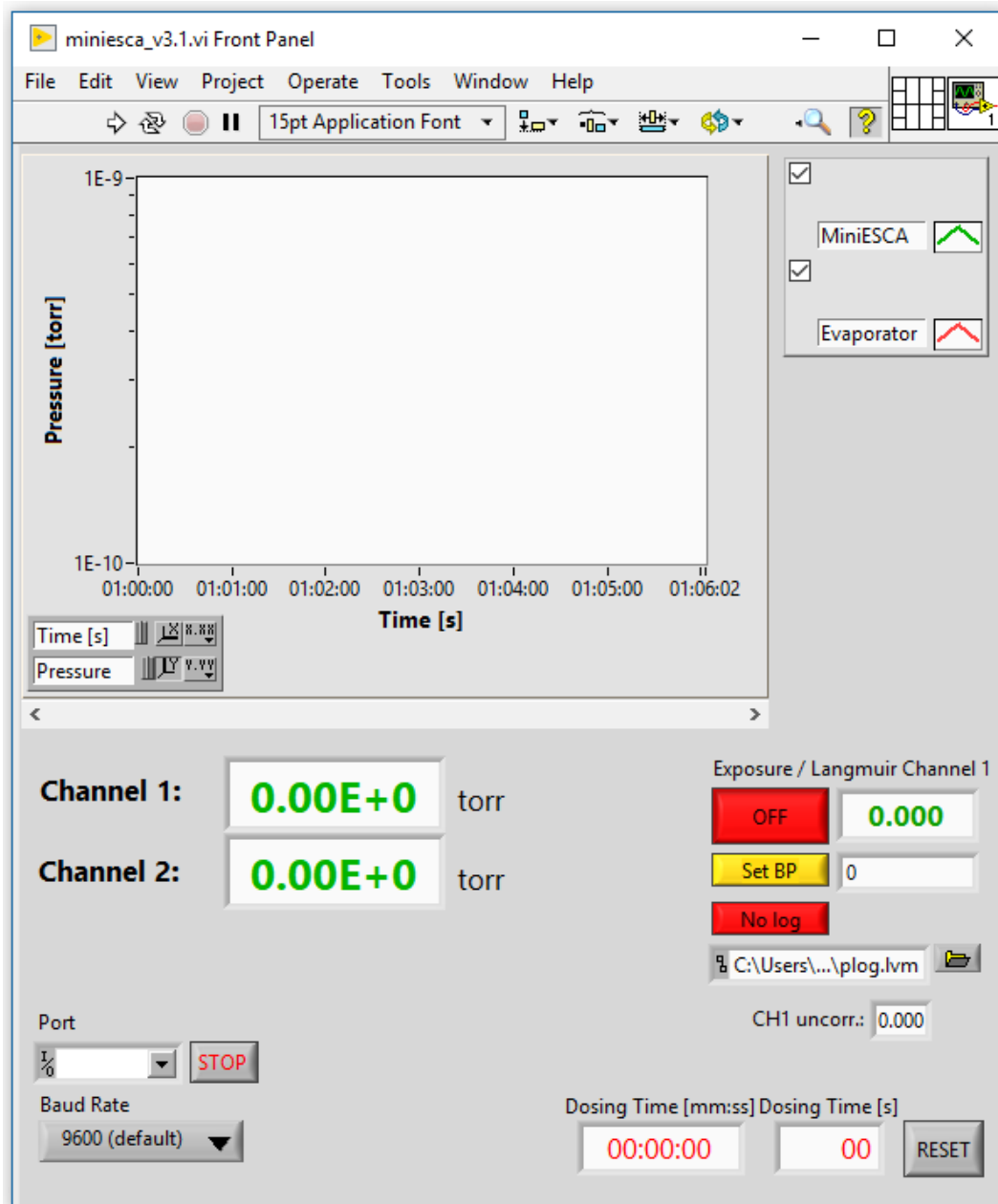


Figure B 7: LabVIEW interface of the MiniESCA Pressure program.

5. Optional: If you wish to log time, pressure and (uncorrected) exposure during exposure calculation press “No log” before turning on the calculation. The indicator will change to “Logging”. This will save a new enumerated logfile in the folder specified below for each exposure calculation cycle.

In the example in Figure B 8 the logfiles will be named plog.lvm, plog1.lvm, ..., plog9.lvm and so on. The filename can be adjusted at will.

6. To stop the program, press the red circle on the upper left. The “STOP” button next to the COM port selection will only disconnect the COM port from LabVIEW.

B1.8 Sync Pressure (sync_pressure_v2.vi)

Dependencies: PV ActiveLine.lvlib (Pfeiffer Vacuum), et24xx.llb (Eurotherm), vacom_main.vi, vacom_serial.vi

Prerequisites: VACOM MVC-3 gauges connected to PC via RS232/USB and/or Pfeiffer Vacuum gauges (tested: TPG261/262) connected to PC via RS232/USB

This program serves as central monitoring display for the most important pressure gauges connected to the synchrotron UHV machine. It enables the simultaneous readout of VACOM and Pfeiffer Vacuum Gauges and can additionally be connected to an Eurotherm for temperature readings. Furthermore, live, base pressure corrected, exposure calculation is available for the main channel (analysis chamber). Pressure and exposure values can be saved in logfiles. The user interface is shown in Figure B 8.

To use this program, follow these steps:

1. Connect all gauges to COM ports (using a serial to USB hub); configure all COM ports in the Windows device manager (might be necessary every time the hub is connected to a different USB port).
2. Open the Sync Pressure program and click on “Run” (white arrow top left).
3. Select the proper baud rates (default: 9600, changes can be made in the “Baud Rate” tab) and choose the right COM port for each gauge.
4. Toggle the red “OFF” button of the gauges (and channel) you want to activate to “ON”. Pressure values should now be displayed in respective fields and the graph window (check trace on the right panel). Channel and trace names can be adjusted in LabVIEW’s “edit mode”.

If no pressure readings appear after this step, stop the program with the red button on the top left and restart it with the white arrow. In case the pressure is still not displayed, check the baud rates and COM ports of the gauges and/or restart the gauges before trying to connect again. You might want to refer to Windows device manager to choose the right COM port.

5. Optional: To display the Eurotherm temperature, toggle the red “OFF” to “ON”.

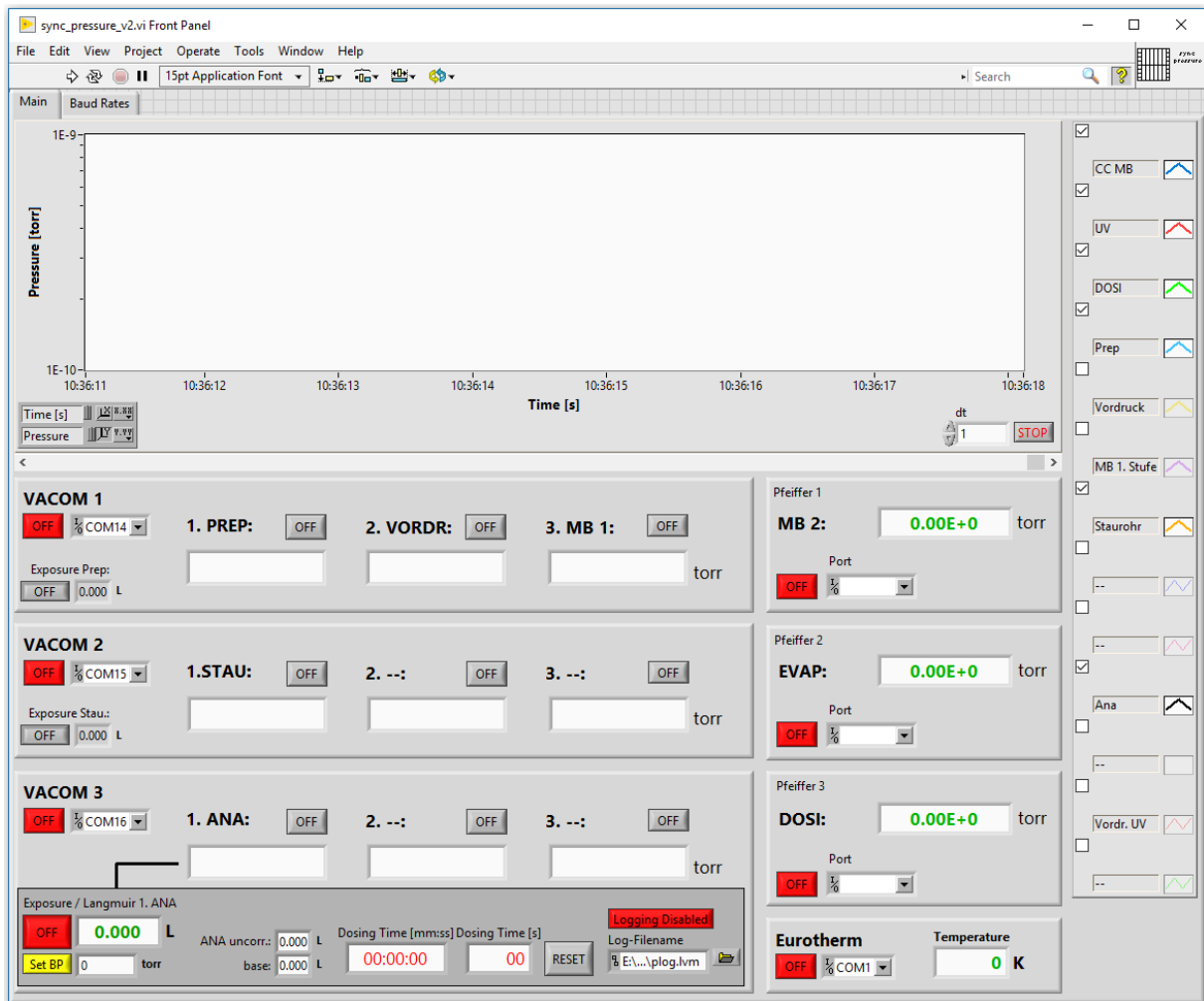


Figure B 8: LabVIEW interface of the Sync Pressure program.

6. The base pressure can be set using the button “Set BP” in the “Exposure / Langmuir 1. ANA” frame of the VACOM 3 control.
7. Pressing “OFF” in the “Exposure / Langmuir 1. ANA” frame will change the indicator to “ON” and start displaying the calculated exposure in Langmuir next to it. Furthermore, the “Dosing Time [mm:ss]” and “Dosing Time [s]” clocks will start to count with their respective time units until the exposure calculation is turned off again. You must reset the time manually with “RESET” after each cycle. “ANA uncorr.” will display the exposure without base pressure subtraction; “base” will display the neglected exposure of the base pressure.
8. Optional: If you wish to log time, pressure and (uncorrected) exposure during exposure calculation press “Logging disabled” before turning on the calculation. The indicator will change to “Logging enabled”. This will save a new enumerated logfile in the folder specified below for each exposure calculation cycle.

In the example in Figure B 8 the logfiles will be named plog.lvm, plog1.lvm, ..., plog9.lvm and so on. The filename can be adjusted at will.

9. To stop the program, press the red circle on the upper left.

B1.9 Beamline Control (bctrl_mini_v2.vi)

Dependencies: CA Lab 1.6.0.10 (Helmholtz Zentrum Berlin)

Prerequisites: CA Lab installed, PC must be inside HZB network

This program utilizes CA Lab to read/write EPICS variables which are used for beamline control at BESSY II. In particular, the energy, slit and harmonic of beamlines UE56-2 PGM 1 and PGM 2 can be controlled with this program. Configurable presets allow for fast switching of beam energies and thus fast measurement of different core levels. The program interface is shown in Figure B 9.

To use this program, follow these steps:

1. Install CA Lab 1.6.0.10 (or higher).
2. Add the following lines to your system and user environment variables of your PC; if you are using the PGM1 beamline, then replace “pgm2” with “pgm1”. Double check the value, otherwise you might end up controlling the other beamline and interrupting foreign experiments! After editing the Windows environment variables, you need to reboot the PC.

variable name	value
EPICS_CA_ADDR_LIST	ue562pgm2.blc.bessy.de
EPICS_CA_AUTO_ADDR_LIST	NO

3. Open the Beamline Control program, choose either “PGM 1” or “PGM 2” according to the beamline in the “Beamline UE56” field and click on “Run” in LabVIEW (white arrow top left).
4. The “Energy”, “Slit”, “Harmonic” and “Ring current” fields below “CURRENT” show the respective live values with stand-by indicators to the right.

The “Energy” standby indicator turns green, as soon as undulator and monochromator are in position for the desired beam energy. “Slit” and “Harmonic” standby indicators turn green, when the “CURRENT” values are equal to the corresponding “TARGET” values.

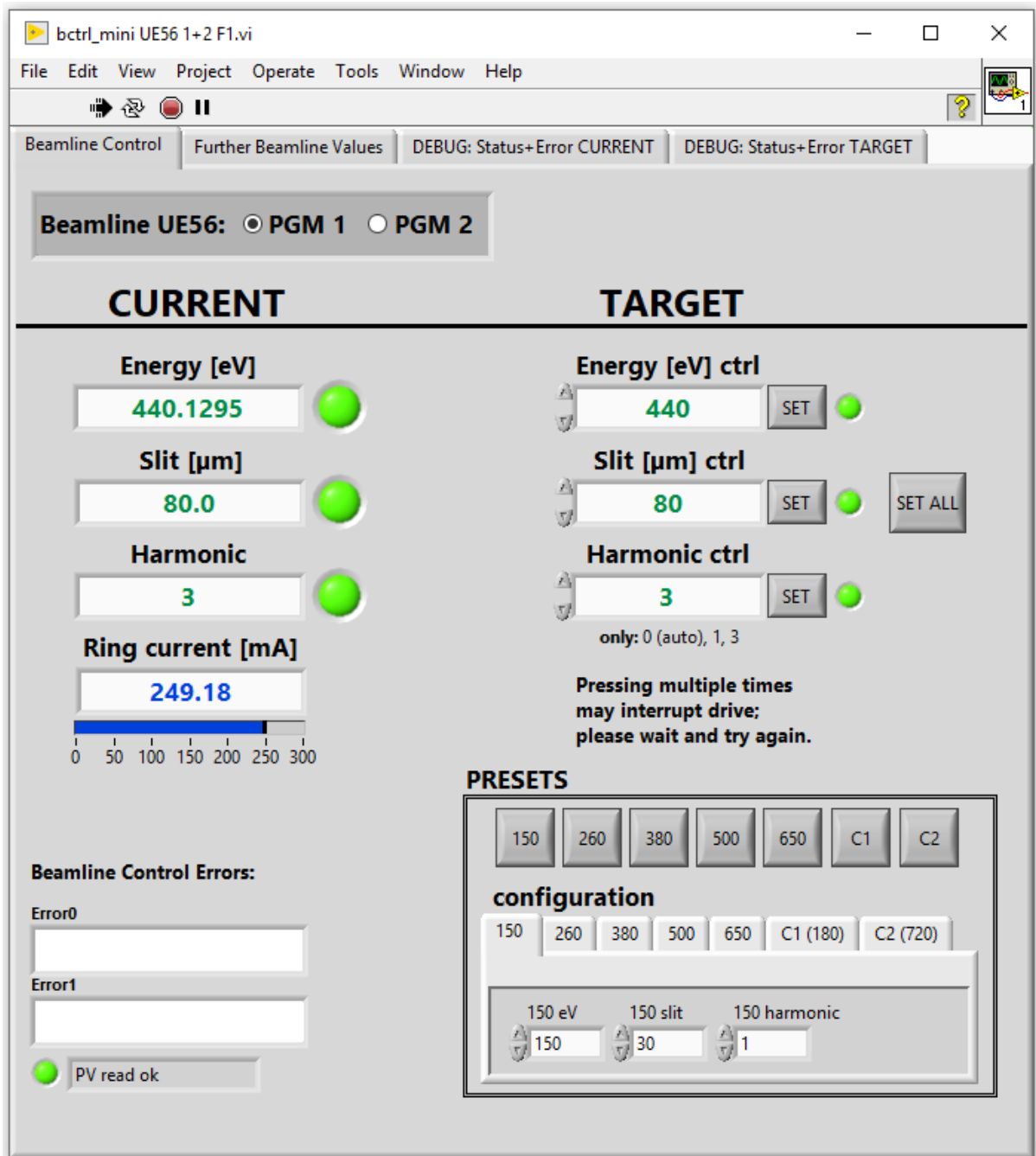


Figure B 9: LabVIEW interface of the Beamline Control program.

- The “Energy”, “Slit” and “Harmonic” input fields below “TARGET” allow the modification of the corresponding “CURRENT” values upon clicking on “SET” or “SET

ALL". The standby indicators to the right display errors in the signal transmission and should always be green.

6. Pressing a button in the "PRESETS" box, changes the "TARGET" values to a preconfigured set from the "configuration" tabs below.

By pressing e.g., the "150" button, the "TARGET" values are automatically updated to match the preconfigured values with 150 eV as "Energy", 30 μm as "Slit" and 1 as "Harmonic".

7. Potential beamline errors are displayed in the "Beamline Control Errors" fields. Further beamline values and debugging info is available within the corresponding tabs at the top of the user interface.

